



**HAL**  
open science

# Characterization of the Cabling on Industrial Power Networks for EMI Simulation

Tamiris Grossl Bade

► **To cite this version:**

Tamiris Grossl Bade. Characterization of the Cabling on Industrial Power Networks for EMI Simulation. Electric power. Communauté Université Grenoble Alpes, 2019. English. NNT : . tel-02409933

**HAL Id: tel-02409933**

**<https://hal.science/tel-02409933v1>**

Submitted on 13 Dec 2019

**HAL** is a multi-disciplinary open access archive for the deposit and dissemination of scientific research documents, whether they are published or not. The documents may come from teaching and research institutions in France or abroad, or from public or private research centers.

L'archive ouverte pluridisciplinaire **HAL**, est destinée au dépôt et à la diffusion de documents scientifiques de niveau recherche, publiés ou non, émanant des établissements d'enseignement et de recherche français ou étrangers, des laboratoires publics ou privés.

## THÈSE

Pour obtenir le grade de

**DOCTEUR DE LA COMMUNAUTE UNIVERSITE GRENOBLE  
ALPES**

**préparée dans le cadre d'une cotutelle entre la *Communauté  
Université Grenoble Alpes* et la « *Universidade Federal de  
Santa Catarina* »**

Spécialité : **Génie Électrique**

Arrêté ministériel : le 6 janvier 2005 – 25 mai 2016

Présentée par « **Tamiris GROSSL BADE** »

Thèse dirigée par « **James ROUDET** » et « **Patrick KUO-PENG** »  
codirigée par « **Jean-Michel GUICHON** » et « **Carlos Antônio  
FRANÇA SARTORI** »

préparée au sein des Laboratoires « **Laboratoire de Génie  
électrique de Grenoble (G2Elab)** » et « **Grupo de Concepção e  
Análise de Dispositivos Eletromagnéticos (GRUCAD)** »

dans l'École Doctorale « **Électrotechnique Électronique  
Automatique et Traitement du Signal** »

# **Caractérisation du câblage des réseaux industriels de puissance en vue de la simulation CEM**

Thèse soutenue publiquement le **10 juillet 2019**,  
devant le jury composé de :

**M. Hubert PIQUET**

Professeur à l'ENSEEIH - Laplace, Président

**M. Christian VOLLAIRE**

Professeur à l'ECL - Ampère, Rapporteur

**Mme. Viviane C. SILVA**

Professeure à l'USP, Rapporteuse

**Mme. Sylvie BARANOWSKI**

Maître de conférences à l'Université de Lille, Membre

**M. Sérgio S. MUHLEN**

Professeur à l'Unicamp, Membre

**M. Mário L. PEREIRA FILHO**

Docteur chercheur à l'IPT São Paulo, Membre

**M. James ROUDET**

Professeur à l'UGA - G2Elab, Directeur de Thèse

**M. Patrick KUO-PENG**

Professeur à l'UFSC - GRUCAD, Co-directeur de Thèse

**M. Jean-Michel GUICHON**

Maître de conférences à l'UGA - G2Elab, Invité

**M. Carlos Antônio FRANÇA SARTORI**

Professeur à l'USP, chercheur IPEN, Invité





Tamiris Grossl Bade

# CHARACTERIZATION OF THE CABLING ON INDUSTRIAL POWER NETWORKS FOR EMI SIMULATION

Dissertation submitted under a cotutelle agreement between the “Comunnauté Grenoble Alpes” and “Universidade Federal de Santa Catarina” for the obtention of the degree of Doctor in Electrical Engineering

Advisors: James Roudet and Patrick Kuo-Peng

Co-advisors: Jean-Michel Guichon and Carlos A.F. Sartori

Grenoble, 2019



Jury members:

**M. Hubert PIQUET**

Professor at the National Polytechnic Institute of Toulouse – Laplace,  
President

**M. Christian VOLLAIRE**

Professor at the Ecole centrale de Lyon – Ampère, Reviewer

**Mme. Viviane C. SILVA**

Professor at the University of São Paulo, Reviewer

**Mme. Sylvie BARANOWSKI**

Senior lecturer at University of Lille, Member

**M. Sérgio S. MUHLEN**

Professor at the University of Campinas, Member

**M. Mário L. PEREIRA FILHO**

Researcher at the IPT São Paulo, Member

**Prof. James ROUDET**

Professor at the University Grenoble Alpes – G2Elab, Thesis Advisor

**Prof. Patrick KUO-PENG**

Professor at the Federal University of Santa Catarina – GRUCAD,  
Thesis Co-advisor

**M. Jean-Michel GUICHON**

Senior lecturer at the University Grenoble Alpes – G2Elab, Invited

**M. Carlos A. F. SARTORI**

Professor at the University of São Paulo, Researcher at the IPEN, Invited

*our work should equip  
the next generation of women  
to outdo us in every field  
this is the legacy we'll leave behind*

*progress - rupi kaur*



# CONTENTS

ACKNOWLEDGMENTS	ix
ACRONYMS	xi
NOTATION	xiii
CIRCUIT SYMBOLS	xv
INTRODUCTION	1
1 CONTEXT AND PRELIMINARY CONCEPTS	3
1.1 INTRODUCTION . . . . .	4
1.2 MEDIUM FREQUENCY PHENOMENA IN A LARGE SYSTEM . . . . .	4
1.3 OBJECTIVES OF THE CABLING MODEL . . . . .	7
1.4 CONCLUSION . . . . .	8
2 TWO-CONDUCTOR CABLE FREQUENCY DOMAIN MODEL	9
2.1 INTRODUCTION . . . . .	10
2.2 TWO-CONDUCTOR TRANSMISSION LINES . . . . .	10
2.3 TWO-CONDUCTOR CABLE PARAMETER IDENTIFICATION . . . . .	15
2.4 FREQUENCY-DOMAIN MODEL EXPERIMENTAL VALIDATION . . . . .	27
2.5 NUMERIC ANALYSIS OF RESONANCE PHENOMENA . . . . .	38
2.6 CONCLUSION . . . . .	50
3 MULTICONDUCTOR CABLE FREQUENCY DOMAIN MODEL	51
3.1 INTRODUCTION . . . . .	52
3.2 MULTICONDUCTOR TRANSMISSION LINE MODEL . . . . .	52
3.3 MULTICONDUCTOR CABLE PARAMETER IDENTIFICATION . . . . .	64
3.4 FREQUENCY-DOMAIN MODEL EXPERIMENTAL VALIDATION . . . . .	66
3.5 EXTENSION OF RESONANCE SURFACES FOR MULTICONDUCTOR CABLES . . . . .	74
3.6 CONCLUSION . . . . .	85
4 TIME-DOMAIN MODEL	87
4.1 INTRODUCTION . . . . .	88
4.2 TIME-DOMAIN TRANSMISSION LINES MODELS . . . . .	88
4.3 FREQUENCY-DOMAIN MODEL RESULTS CONVERTED TO TIME DOMAIN . . . . .	95
4.4 TIME-DOMAIN VALIDATION . . . . .	99
4.5 QUALITATIVE ANALYSIS OF THE FREQUENCY DOMAIN MODEL . . . . .	108

4.6	CONCLUSION . . . . .	111
5	APPLICATIONS . . . . .	<b>113</b>
5.1	INTRODUCTION . . . . .	114
5.2	METHODOLOGY TO DETECT RESONANCE PROBLEMS IN A GIVEN SYSTEM . . . . .	114
5.3	INDUCTION MOTOR FED WITH ELECTRICALLY LONG CABLE . . . . .	115
5.4	DC LINK WITH ELECTRICALLY LONG CABLE . . . . .	123
5.5	FILTER DESIGN TAKING RESONANCE PHENOMENA INTO ACCOUNT . . . . .	135
5.6	CONCLUSION . . . . .	143
	CONCLUSION . . . . .	<b>145</b>
	PUBLICATIONS . . . . .	<b>153</b>
A	APPENDIX A . . . . .	<b>1</b>
B	APPENDIX B . . . . .	<b>3</b>
C	APPENDIX C . . . . .	<b>7</b>
C.1	COMPARISON BETWEEN THE RESONANCE BEHAVIOR OF TWO-CONDUCTOR CABLES OF DIFFERENT CROSS-SECTION . . . . .	7
C.2	COMPARISON OF THE RESONANCE BEHAVIOR OF THE SAME CABLE WITH DIFFERENT LENGTHS . . . . .	10
D	APPENDIX D . . . . .	<b>13</b>
E	APPENDIX E . . . . .	<b>15</b>
E.1	THE BALUN EXPERIMENTAL IDENTIFICATION . . . . .	15
E.2	DETERMINATION OF USEFUL FREQUENCY BAND . . . . .	17
F	APPENDIX F . . . . .	<b>19</b>
G	APPENDIX G . . . . .	<b>21</b>
H	APPENDIX H . . . . .	<b>23</b>
I	APPENDIX I . . . . .	<b>27</b>

---

## Acknowledgments

I would like to thank my advisers James Roudet, Jean-Michel Guichon, Patrick Kuo-Peng and Carlos Sartori for their guidance in the development of this work. Their contribution to this thesis was significant, and so was their contribution into my personal growth towards the research career I chose to follow.

I would also like to thank my thesis jury for the time invested on analyzing the results of this work, particularly to my reviewers Viviane Silva and Christian Vollaire for their report on my manuscript.

I thank the technical team of the G2Elab, particularly Alexix Derbey, for their support during the experimental phase of this work, support that was essential for the good progress of my research.

I thank the labmates for their friendship along these years, both those who left before me and those who will still finish their PhD.

I thank my family for their prayers and emotional support, which never failed me during the years in which I was invested in this PhD thesis. I thank my boyfriend, equally for his support during this period. I thank my parents for the attention and investment directed to my education, and for always motivating me to learn since my childhood. And I would like to thank God for all the blessings throughout my life.



---

## Acronyms

Acronyms:

---

<b>EMI</b>	Electromagnetic Interference
<b>EMC</b>	Electromagnetic Compatibility
<b>LISN</b>	Line Impedance Stabilization Network
<b>DM</b>	Differential Mode
<b>CM</b>	Common Mode
<b>MTL</b>	Multiconductor Transmission Lines
<b>p.u.l.</b>	per-unit-length
<b>PWM</b>	Pulse width modulation
<b>PE</b>	Protective Earth

---





---

## Notation

Physical and mathematical constants:

Name	Symbol	Value	Units
Speed of light in the vacuum	$c$	$3 \times 10^8$	$m/s$
Vacuum dielectric permittivity	$\epsilon_0$	$8.85 \times 10^{-12}$	$F/m$
Vacuum magnetic permeability	$\mu_0$	$4\pi \times 10^{-7}$	$H/m$
Complex identity	$j$	$\sqrt{-1}$	
Euler's number	$e$	2.72	

Variables :

Name	Symbol	Units
Spatial axis	$x$	$m$
Frequency	$f$	$Hz$
Angular frequency	$\omega$	$rad/s$
Voltage	$V$	$V$
Current	$I$	$A$
Voltage along a transmission line, frequency domain	$V(x) \equiv V(x, f)$	$V$
Current along a transmission line, frequency domain	$I(x) \equiv I(x, f)$	$A$
Voltage along a transmission line, time domain	$V(x, t)$	$V$
Current along a transmission line, time domain	$I(x, t)$	$A$
Impedance	$Z$	$\Omega$
Cable length	$\ell_c$	$m$
Number of conductors	$n + 1$	
Characteristic impedance	$Z_c$	$\Omega$
Modal characteristic impedance	$Z_d$	$\Omega$

Propagation constant	$\gamma = \alpha + j\beta$	$1/m$
Attenuation constant	$\alpha$	$Np/m$
Phase constant	$\beta$	$rad/m$
Propagation speed	$v$	$m/s$
Propagation delay	$T_D$	$s$
Reflection coefficient	$\Gamma$	
Wave length	$\lambda$	$m$
Per-unit-length impedance	$z = r + j\omega l$	$\Omega/m$
Per-unit-length admittance	$y = g + j\omega c$	$S/m$
Per-unit-length resistance	$r$	$\Omega/m$
Per-unit-length conductance	$g$	$S/m$
Per-unit-length inductance	$l$	$H/m$
Per-unit-length capacitance	$c$	$F/m$
Amplitude of a signal	$A$	$V, A$
Duty cycle	$d$	
DC bias	$b$	$V, A$
Period	$T$	$s$
Rise time	$t_r$	$s$
Fall time	$t_f$	$s$
Fourier series coefficient: amplitude	$C$	
Fourier series coefficient: phase	$\theta$	rad

Matrix variables:

All matrices are notated in **bold**.

Name	Symbol
Cable chain matrix	<b><math>\Phi</math></b>
Changing matrix to modal base	<b><math>\mathbf{T}</math></b>
Changing matrix to the common/differential modes base	<b><math>\mathbf{M}</math></b>
Characteristic impedance matrix	<b><math>\mathbf{Z}_c</math></b>
Characteristic admittance matrix	<b><math>\mathbf{Y}_c</math></b>

---

## Circuit Symbols

There are some differences between the European and American symbols in circuit schematics. For that reason, this section defines the conventions used in the circuit schematics along this document.

There are two different voltage representation in the two conventions, both are drawn in Fig. 1. Europeans traditionally use an arrow pointing to the higher potential (Fig. 1a), while Americans use the signals  $+$  and  $-$ , the plus signal indicating the higher potential (Fig. 1b).

The European representation of the voltage, shown in Fig. 1a, was chosen as default along this document.

A second point with great differences is the representation of voltages and current sources, which seem to differ considerably even among European countries. The symbols chosen to be used in this document are represented in Fig. 2

The following table resumes all the source symbols used in the document, along with other less known circuit symbols.

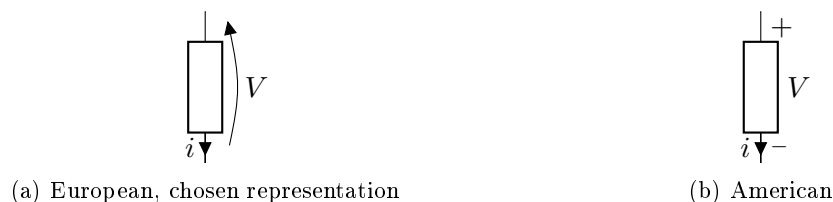


Figure 1 – The two most used voltage-current representation in circuit schematics

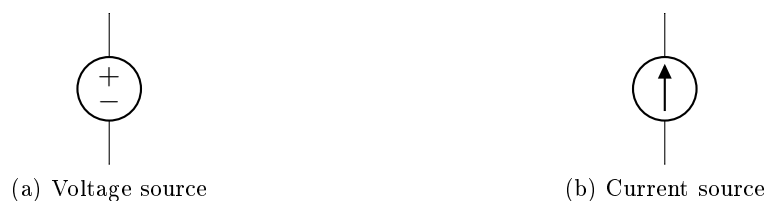
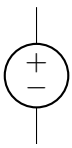
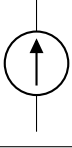
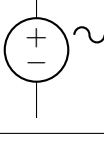
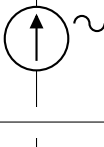
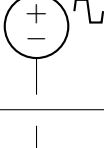
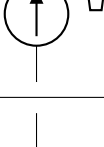
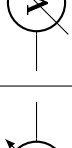

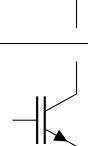



Figure 2 – Source symbols used in this document

Voltage Source	
Current Source	
Sinusoidal Voltage Source	
Sinusoidal Current Source	
Trapezoidal Voltage Source	
Trapezoidal Current Source	
Voltmeter	
Ammeter	
Transistor MOSFET	
Transistor IGBT	

---

## Introduction

Any electrical or electronic device commercialized nowadays has to comply with electromagnetic compatibility (EMC) standards. Among other characteristics, these standards define the maximum amplitude of conducted emissions the device is allowed. However, despite the requirements of the multiple standards, there are still EMI problems on a system level in large electric networks, such as cabling of buildings and industrial plant networks. These problems include conducted and inductively or capacitive coupled interferences.

Three main causes for the system level electromagnetic interference (EMI) problems can be identified. First, the conducted emissions of the device under test conditions are probably different from the ones that will take place when the device is connected to a large cabling network. Indeed, the conducted emissions test setup defined in these standards invariably have the device connected to a Line Impedance Stabilization Network (LISN), usually through a cable no longer than  $1.5\text{ m}$ . A LISN has stable input impedance values, which are either constant or varying of one order of magnitude in frequency band, while in a real network the impedance seen by the device varies within a much wider range of values, and ensemble of cabling connected to the device can be much longer.

Second, the stray signal injected in a complex cabling network by these devices might be amplified by the resonance phenomenon. For example, a power cabling network on industrial plants may have unshielded cables tens of meters long, inserted in a complex environment. These cables will behave as transmission lines at the frequencies of the stray signals emitted by devices such as power converters. It is not likely that the characteristic impedance of the cables are matched with the input impedances of the devices, what establishes stationary waves in the cabling leading to resonance-due amplification of the stray signals. Moreover, it is likely that stray currents will be induced in metallic cable paths and reinforced concrete walls. They are known as common-mode currents, and they are particularly dangerous parasitic signals.

Least of all, in a large cabling system, the electric potential reference is not the same along the cabling. Indeed, the copper conductor losses in medium frequencies (tens of  $kHz$  up to hundreds of  $MHz$ ) make it impossible for them to be considered as an equipotential surface. A second option to build an equipotential would be the potential reference given by grounding rods, but the electric potential of one rod may be different from the one of a second rod grounded tens of meters away because the ground is not perfectly conductive. This instability of the reference potential might cause dysfunctions in the electric devices connected to the cabling network.

From these reasons arises the need of a model able to represent the behavior of a complex cabling system for EMI simulations. Such model would allow the development of protective EMC

strategies in the design phase of a large cabling system, or even be the base on the design of filters to be included in an existing cabling network, to reduce the level of conducted emissions circulating on it.

The model should to be valid for a wide frequency band, computationally efficient, and take into account the propagation phenomenon to accurately predict the amplitude of the stray signals in any part of the cabling network. The cables to which the model will be applied to are unshielded power cables designed for 50/60 *Hz* industrial applications. Ideally, the complex environment in which the cables are inserted should also be represented.

This thesis is structured as follows:

Chapter 1 introduces the EMI phenomenon that may occur in a large electric system, and its potential to cause dysfunctions and damage to the devices connected to it. The difficulties in the EMI modeling of the cabling are discussed, and the objectives of the model developed in this work are detailed.

Chapter 2 defines a frequency domain simulator for two-conductor cables. It is based on the frequency domain solution of the telegrapher equations, and includes an experimental technique to identify the parameters of a given cable. The simulator is experimentally validated with measurements of the resonance-due voltage amplification in a two-conductor cable. Also, the behavior of the resonance phenomena is studied in detail.

Chapter 3 extends the simulator derived in chapter 2 to a multiconductor cable, using the multiconductor transmission line (MTL) theory. The experimental cable parameter identification technique is adapted to multiconductor cables, and the new version of the simulator is validated experimentally with a three-conductor cable. The tools developed in chapter 2 to characterize the resonance phenomenon in a cable are extended to the multiconductor cables.

Chapter 4 discusses the time domain modeling of long cables, and describes a method to obtain the time domain results using the frequency domain simulator developed in the two previous chapters. The proposed method is validated experimentally, with experiments including long cables in which resonance occurs.

In chapter 5, the simulation method proposed in this work is applied to practical examples of large systems, following a procedure built to completely predict the resonant behavior of each system. First, the case of an induction motor connected through a long cable to its drive is studied. Second, two DC-link structures are simulated and analyzed. Least of all, a new EMI filter design technique taking into account the resonance phenomena in long cables is proposed.

## Chapter 1

---

# Context and preliminary concepts

### CONTENTS

---

1.1	INTRODUCTION . . . . .	4
1.2	MEDIUM FREQUENCY PHENOMENA IN A LARGE SYSTEM . . . . .	4
1.3	OBJECTIVES OF THE CABLING MODEL . . . . .	7
1.4	CONCLUSION . . . . .	8

---

### Abstract

*In this chapter, the problematic motivating the characterization and modeling of large cabling network are discussed in detail. The EMI phenomena to be modeled are introduced, along with the difficulties to model them. The objectives of the EMI modeling are stated and justified.*



## 1.1 Introduction

The goal of this study is to accurately characterize a large cabling network, aiming an efficient EMI simulation. To that end, the behavior of low to medium frequency stray signals introduced in a large electric system by the devices connected to it have to be studied. This first chapter introduces and contextualizes the desired EMI model, presenting the problematic motivating this study and introducing the concepts that will be used along this document. Also, the objectives of the present work are detailed.

Among the power devices source of high levels of conducted emissions, power converters are the most common. Their applications have spread in the last decades in industrial and residential electric systems. Power converters invariably introduce switching harmonics in the network to which they are connected. The circulation of these harmonics in a large electric system might induce electromagnetic interference (EMI) problems, principally if communications and control circuits can be affected by the power circuit.

The EMI phenomena that may take place in a large electric system are discussed in section 1.2. In section 1.3 the objectives of the cabling model that is the goal of this work are listed and justified.

## 1.2 Medium frequency phenomena in a large system

As aforementioned, the power converters are the polluting devices more commonly found in industrial electric networks. For this reason, this EMI study will be focused on the conducted emissions generated by these devices.

Power converters are electronic devices able to change the characteristics of an electric signal using switches, which are built with semiconductor devices such as power diodes and power transistors (MOSFET, IGBT, etc..). The switches are controlled to convey a desired behavior to the output electric power. However, the switches in these structures impose high voltage and current variation ( $dV/dt$  and  $dI/dt$ ) at each switching event, i.e., at each change of the state of conduction of the semiconductor devices. The high variation of voltage and current introduces medium frequency (order of  $MHz$ ) harmonics to the system that usually need to be strongly filtered to guarantee the expected input and output signals, as well as its compatibility with the network to which it is connected.

Previous work studied the EMI behavior of power converters [10, 40, 44]. In these works, different EMI models for power converters were developed, with structural [40, 44] and black box [10] approaches. Particularly, in [44] is presented an interesting study of the envelope of a switched voltage spectrum in function of parameters of the switched voltage: duty cycle  $d$ , rise time  $t_r$  and fall time  $t_f$ . In this work, it is demonstrated that the harmonic spectrum of the switched voltage and current has an attenuation of  $-40, dB/dec$  for frequencies higher than  $\frac{1}{\pi t_m}$ , where  $t_m = \min(t_r, t_f)$ .

Based on this work, a frequency band for the cabling characterization and modeling aimed by this work can be defined. To ensure that the upper limit of the frequency band does not cut out relevant harmonics, it is safer to choose a cutoff frequency for the switching harmonics as  $f_{cut} = \frac{10}{\pi t_r}$ . This way, for frequency higher than  $f_{cut}$ , it is certain that the harmonics have been attenuated of at least  $-40 dB$ .

With semiconductors based on Silicon technology, typical rise and fall times are of the order of hundreds of  $ns$ , and the truncation frequency  $f_{cut}$  would be of the order of tens of  $MHz$ . For that reason, the model studied in this work is designed to fit for a frequency band going from DC up to tens of  $MHz$ .

Two other difficulties contribute to the establishment of this frequency upper limit:

- above tens of  $MHz$ , the models of the power transistors more commonly used (MOSFET, IGBT) are difficult to obtain;
- for frequencies much higher than tens of  $MHz$ , the characterization of the devices under study becomes complicated

For example, an induction motor of power of the order of  $10 kW$  can have dimensions around  $70 \times 50 \times 50 cm$ , and it is difficult to experimentally characterize such a large device over hundreds of  $MHz$ .

In large electric systems, such as the ones in buildings, industrial and generation plants, the cables connecting the multiple devices are often tens of meters long. The smallest wavelength  $\lambda$  in the frequency band chosen for this study (up to tens of  $MHz$ ) is of the order of tens of meters. In the literature, it is often considered that the propagation phenomenon in the voltage and current waves in a transmission line can be neglected if the length of the line is smaller than  $\lambda/10$ . Therefore, the cables of the concerned systems are long enough for the medium frequency harmonics to be subjected to the propagation phenomenon. In other words, the cables under study are electrically long, and propagation must be taken into account.

For that reason, the EMI model for the cabling in large system will take the propagation phenomena into account, by modeling the cables using the transmission line theory.

With the propagation, arises the risk of resonance phenomenon in the long cables. The resonance is a superposition of stationary waves in the line. There are specific frequencies in which these stationary waves interfere constructively, considerably amplifying the signal originally injected in the cable.

The stationary waves are present because of the reflection of the voltage and current waves at the cable terminals. The only case where the waves are not reflected at the line terminals is when the characteristic impedance of the line is identical to the input/output impedance of the device connected to the terminal. In this case, the line is matched, and the resonance phenomenon does not take place, independent of the cable length.

On the other hand, if the line is ended by an open end or short circuit, there is a full reflection of the voltage and current waves in the line terminal. In this case, the only factor limiting the resonance amplification are the losses on the cable. If the cable is lossless, the stationary waves are not attenuated along the cable, and their superposition creates an amplification that tends to infinity.

The large complex systems designed for the low frequency applications that are the concern of this study (buildings and industrial electric networks) are designed for  $50/60 Hz$  or DC. For that reason, cable impedance matching is not a concern in these systems, and even if it is, it would be considerably difficult to obtain. Indeed, the input impedances of the devices connected to these networks, which may be electric motors, power converters, etc..., vary with frequency and are not likely to be matched with the cable characteristic impedance. Therefore, it is likely that resonance phenomena will take place in the cabling of large electric systems, if the medium frequency harmonics generated by the power converters circulate in long cables.

Resonance phenomena has the potential to cause serious damage to a system. It can generate dangerous overvoltages and overcurrents that may cause insulation faults, thermal dysfunctions, and/or reduce the useful life of the devices composing the system. In consequence, it is vital that the resonance phenomenon is accurately represented by the model.

One well-known case where the resonance phenomenon may cause serious damage is the induction motor connected through a long cable to its drive. In such system, overvoltage may take place at the motor terminals, due to resonance phenomenon. This problem is well documented in the literature [20, 45, 52], the resonance-due overvoltages may cause insulation faults in the motor, and reduce the useful life of its bearings.

Other references to resonance problems in the literature are the resonance in the feeding network of electric trains [7], and at the cable connecting offshore wind turbines to the onshore substation [25, 43]. In [43], the authors proposed a narrow band notch filter to dump resonance-due amplifications at the resonance frequencies, and were challenged by the fact that resonance frequency is very sensitive to parameters that vary with temperature and with the cable aging.

Indeed, the resonance frequency is highly sensitive to variations of the cable parameters, particularly on the per-unit-length (p.u.l.) inductance  $l$  and capacitance  $c$  of the cable. Moreover, the amplitude of the resonance-due amplification of voltage and current waves is highly sensitive to the cable losses.

The cable losses are not negligible for the cables used in low frequency applications, such as the large industrial electric networks. These losses have a considerable impact of the voltage and current behavior in a cable, and vary with frequency due to phenomena such as the skin effect, the proximity effect and the dielectric loss dependence on the frequency.

To exemplify the impact of the cable losses in the resonance-due amplification of a voltage signal in a cable, the amplitude of the sinusoidal voltage in a two-conductor cable is plotted for three different loss characteristics, using the schematic in Fig. 1.1. In this schematic, the cable is open-ended. The plot is done for the voltage at  $x = \ell_c$ , in function of the frequency. The three loss characteristics attributed to this line are:

1. A realistic behavior of the losses, variable with frequency due to skin-effect, etc...
2. Losses constant with frequency, but non-zero
3. Lossless cable

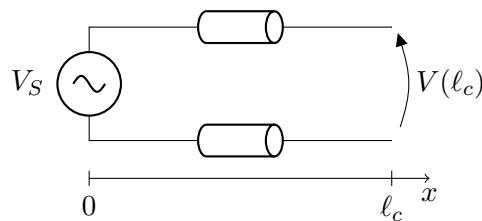


Figure 1.1 – Schematic to show the loss impact on resonance-due voltage amplification

The voltages  $V(\ell_c)$  obtained from each of these loss cable characteristics are plotted in Fig. 1.2.

In this figure, the first two resonances in the open-ended cable are visible. In the lossless case, the resonance-due voltage amplification tends to infinity. For the constant but non-zero losses, the

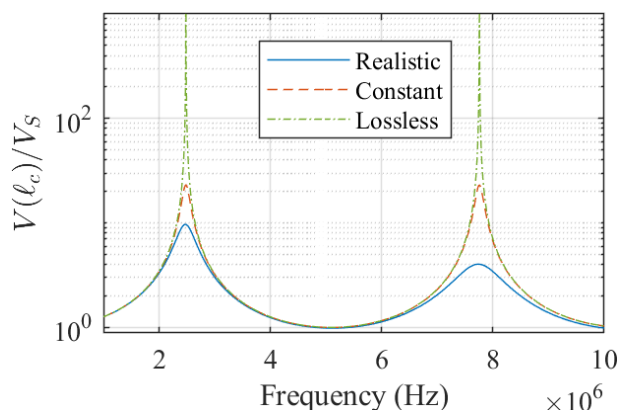


Figure 1.2 – Voltage amplification at  $x = \ell_c$  for three different loss characteristics

amplification is limited, and has the exact same amplitude for both of the resonance frequencies visible in the figure. Finally, in the voltage amplification for the realistic loss characteristics, the voltage amplitude is limited, and also different for each of the resonance visible in the figure. The amplification at the first resonance frequency is higher because at this frequency the cable losses are smaller.

Fig. 1.2 shows the importance of an accurate model of the losses in a cable designed for low frequencies applications. The variability of the losses with frequency has to be taken into account, or the resonant behavior of the cable cannot be accurately represented by the model.

The same way, the reactive elements of the cable model: p.u.l. inductance  $l$  and capacitance  $c$ , have to be accurately identified to guarantee the correct prediction of the resonance frequency in a long cable. Indeed, the skin effect has a second impact on the cable parameters: the p.u.l. inductance  $l$  also varies with frequency, and this behavior also has to be taken into account.

In conclusion, the cabling model aimed by this work has to be built from cable parameters accurately identified, and support the variation of these parameters with frequency.

### 1.3 Objectives of the cabling model

Based on the considerations made in the previous section, it is possible to define the requirements that the EMI cabling model must fulfill:

- The model must be valid for a frequency band from DC up to a few tens of  $MHz$ ;
- The model must be length-scalable: the cable length is a parameter of the model;
- The model must be able to represent the voltage and current wave propagation;
- The model must support the cable parameter variation with the frequency;
- The cable parameters must be accurately defined;
- The model must be computationally efficient, so it can be used for design ends;

The frequency band is chosen so the harmonics generated by power converters with rise/fall time as low as  $100\text{ ns}$  can be represented, a typical time for silicon-based power semiconductors.

It is specified that the model has to be length-scalable so a cabling network can be easily represented, and the length of the cable can also be a parameter in the design process of a system.

The propagation phenomenon in the cabling has to be taken into account, because the systems aimed by this work are large, and have electrically long cables for the chosen frequency band, i.e., the cable length is of the same order of magnitude or greater than the smallest wavelength circulating in the cable.

With the propagation phenomenon, resonance in the cable becomes possible, and even likely to happen, as in low frequency systems the impedances of the devices connected to a long cable terminals are not likely to be matched with the characteristic impedance of the cable.

The resonance phenomenon is very sensitive to the cable parameters, and an accurate prediction of the resonance frequency and resonance-due wave amplification requires an accurate identification of the parameters of a given cable. Moreover, to obtain the desired accuracy the parameter variation with the frequency has to be modeled, as has been shown in Fig. 1.2.

The model has to be computationally efficient because its goal is to aid the design phase of a large electric system, what requires multiple simulations. If the simulation time is too long, or if the memory cost simulation is too high, the model would not be useful to conception ends.

The development of the cabling model will be described in chapters 2 to 4, and is based on the transmission line theory. This theory is recalled from its basis because the industrial cabling networks are not usually represented by the existing transmission line models. Indeed, the fact that the cables are unmatched and susceptible to induce an alternative stray path requires a review on the hypothesis taken in these models, so an adapted simulator can be defined for this application.

This work will be limited to the study of radial networks, which is the structure of most buildings and industrial electrical networks. The case of networks with closed loops will not be considered.

## 1.4 Conclusion

In this chapter, the guidelines of the model aimed by this work are given. The frequency band of the study is defined based on the harmonic spectrum generated by power converters. The possibility of propagation and resonance phenomena in the long cabling for this frequency band is explained. The problems arising from the resonance phenomenon are exemplified. From these problems arises the need to correctly predict the resonance behavior in large cabling systems.

Therefore, the cabling model has to satisfactorily represent the voltage and current wave propagation in long cables and their resonant behavior. It has been demonstrated that the resonance behavior is highly sensitive to the cable parameters, including the cable losses. That demands the development of an accurate parameter identification technique for the cables under study.

Other requirements that the model has to meet are: it will be length-scalable and computationally efficient.

Cabling networks with closed loop are not studied here. However, the simulator developed in this work could be applied to closed-loop applications.

## Chapter 2

---

# Two-conductor cable frequency domain model

---

### CONTENTS

---

2.1	INTRODUCTION . . . . .	10
2.2	TWO-CONDUCTOR TRANSMISSION LINES . . . . .	10
2.2.a	The frequency domain model . . . . .	12
2.2.b	$Z_c$ and $\gamma$ dependance on frequency . . . . .	14
2.3	TWO-CONDUCTOR CABLE PARAMETER IDENTIFICATION . . . . .	15
2.3.a	Review of existing parameter identification techniques . . . . .	16
2.3.b	Experimental parameter identification using an Impedance Analyzer . . . . .	19
2.4	FREQUENCY-DOMAIN MODEL EXPERIMENTAL VALIDATION . . . . .	27
2.4.a	Resonance-based experiment validation . . . . .	27
2.4.b	Input Impedance Validation . . . . .	30
2.4.c	Examples of cable parameters identification . . . . .	33
2.5	NUMERIC ANALYSIS OF RESONANCE PHENOMENA . . . . .	38
2.5.a	Open-ended and short-circuited resonances . . . . .	38
2.5.b	Resonance in function of the load . . . . .	42
2.5.c	LC resonance versus transmission-line resonance . . . . .	48
2.6	CONCLUSION . . . . .	50

---

### Abstract

*In this chapter a frequency domain simulation tool for lossy two-conductor cables, with the conductors equally spaced from each other is developed. The cable parameters are obtained experimentally. The frequency band of the model goes from DC up to 30 MHz, limited by the equipment available for the experimental parameter identification. The parameter assessment, as well as the frequency domain simulation tool, are validated experimentally. The resonance phenomenon in the two-conductor transmission line is studied in detail, and its dependence on the cable losses is highlighted.*

## 2.1 Introduction

In this chapter, two-conductor cables commonly used on industrial and buildings cabling networks are studied. These cables will be characterized and modeled.

As mentioned in the previous chapter, the model of the building network must predict accurately the stray voltages and currents amplifications due to the resonance phenomenon. Indeed, the resonance on the cables in a building network can be dangerous to the devices connected to it. This phenomenon is not taken into account on the building networks design, which usually regards only  $50/60\text{ Hz}$  behavior of the system. The harmonics generated by the switching devices (battery chargers, network stabilizers, LED lights, etc...) based on silicon technology can go up to tens of  $\text{MHz}$ , frequency band in which the cables under study, which are frequently tens of meters long, will resonate. This is a problem trending to become critical with the advent of the new wide-band gap semiconductor technologies, which have much faster switching time and, as a consequence, introduce higher frequency harmonics into the network.

In a first approach, a hypothetical radial network will be modeled, representing a large cabling network (industrial plat, building, etc...). The first hypothesis taken is that this network has cables with the space between its conductors constant along the line. Of course, this is strong supposition, and certainly not true for all the portions of an industrial cabling system. However, a model based on this hypothesis still gives a good approximation, because the space between the wires in the cabling network does not change drastically. The losses in the cable must be accurately represented, because the resonance phenomenon is highly dependent on them, as was shown in section 1.2. In this chapter, the study is limited to two-conductors cables.

Section 2.2 introduces the theory of two-conductor transmission lines and the proposed modeling tool. Section 2.3 talks about experimental parameter identification of power cables, and proposes an impedance analyzer based parameter identification method. Section 2.4 validates with frequency domain experiments the simulation tool developed in section 2.2, with the parameters obtained in section 2.3. Section 2.5 studies the resonance phenomena in two-conductor transmission lines.

## 2.2 Two-conductor transmission lines

Consider the two-conductor transmission line represented in Fig. 2.1. The voltage and current along the line vary in function of  $x$ . Their behavior can be described by the telegrapher equations, obtained by representing the line as a series association of the basic cell presented in Fig. 2.2.

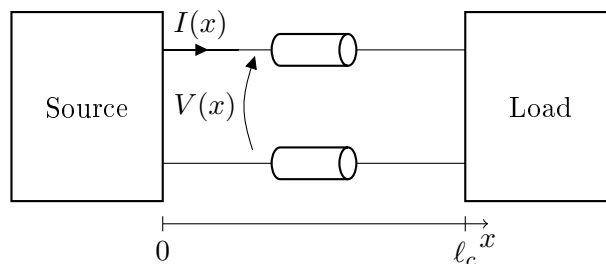


Figure 2.1 – Two-conductor transmission line, variable definition

The telegrapher equations in the frequency domain are written in (2.1), with the parameters

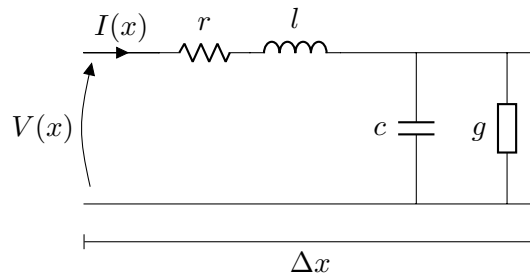


Figure 2.2 – Elementary cell of two-conductor transmission lines, with its per-unit-length parameters

$z$  and  $y$  given by (2.2), where  $j$  is the imaginary unit,  $\omega = 2\pi f$  is the angular frequency, and  $r$  ( $\Omega/m$ ),  $l$  ( $H/m$ ),  $c$  ( $F/m$ ) and  $g$  ( $S/m$ ) are the per-unit-length (p.u.l.) parameters of the line, represented in Fig. 2.2

$$\frac{\partial V(x)}{\partial x} = -zI(x) \quad (2.1a)$$

$$\frac{\partial I(x)}{\partial x} = -yV(x) \quad (2.1b)$$

$$z = r + j\omega l \quad (2.2a)$$

$$y = g + j\omega c \quad (2.2b)$$

The telegrapher equations can be decoupled if written in the second order partial derivative form, as in (2.3), where  $\gamma = \sqrt{zy}$

$$\frac{\partial^2 V(x)}{\partial x^2} = \gamma^2 I(x) \quad (2.3a)$$

$$\frac{\partial^2 I(x)}{\partial x^2} = \gamma^2 V(x) \quad (2.3b)$$

Equations 2.3 admit the solution (2.4):

$$V(x) = V^+ e^{-x\gamma} + V^- e^{x\gamma} \quad (2.4a)$$

$$I(x) = I^+ e^{-x\gamma} - I^- e^{x\gamma} \quad (2.4b)$$

Where constants  $V^+$ ,  $V^-$ ,  $I^+$ , and  $I^-$  must be defined using the boundary conditions of the differential equation problem. In this case, the boundary conditions are the voltage and current relations at the load ( $x = \ell_c$ ) and the source ( $x = 0$ ) ends. We can reduce the number of undetermined constants by defining the characteristic impedance in (2.7) as follows:

$$\frac{\partial I(x)}{\partial x} = -\gamma (e^{-x\gamma} I^+ + e^{x\gamma} I^-) = -yV(x) \quad (2.5)$$

$$V(x) = \underbrace{y^{-1}\gamma}_{Z_c} (e^{-x\gamma} I^+ + e^{x\gamma} I^-) \quad (2.6)$$

$$Z_c = \sqrt{\frac{z}{y}} \quad (2.7)$$



With this definition, the solution in (2.4) can be simplified to (2.8):

$$V(x) = Z_c (I^+ e^{-x\gamma} + I^- e^{x\gamma}) \quad (2.8a)$$

$$I(x) = I^+ e^{-x\gamma} - I^- e^{x\gamma} \quad (2.8b)$$

From (2.8), the use representation of the two-conductor line can be written as in (2.9). This representation is useful because it removes the dependence on the constants  $I^+$  and  $I^-$  (by introducing a dependence on  $V(0)$  and  $I(0)$ ), and concatenation can be easily performed, what will be useful to build the model of the radial network aimed by this study.

$$\begin{bmatrix} V(x) \\ I(x) \end{bmatrix} = \begin{bmatrix} \cosh(x\gamma) & -Z_c \sinh(x\gamma) \\ -\frac{1}{Z_c} \sinh(x\gamma) & \cosh(x\gamma) \end{bmatrix} \begin{bmatrix} V(0) \\ I(0) \end{bmatrix} \quad (2.9)$$

### 2.2.a The frequency domain model

For a hypothetical radial network, where cables with two-conductors equally spaced along the network connect multiple devices, equation (2.9) is valid for any continuous section of two-conductor cable. Moreover, assuming the hypothesis that all devices connected to the network are linear, any continuous portion of two-conductor cable can be modeled by the equivalent circuit in Fig. 2.3, from the Thévenin's theorem.

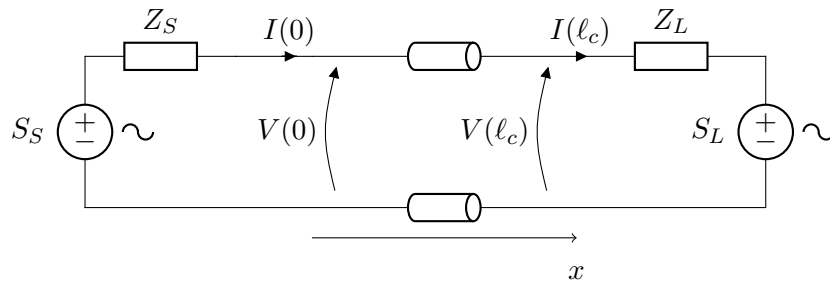


Figure 2.3 – Schematic of the generalized frequency domain model for two-conductor cables

So far, the voltages and currents have been represented as a function only of  $x$ . But, as the parameters  $Z_c$  and  $\gamma$  vary with frequency (cf. section 2.2.b), the voltages and currents along the line are also dependent on the frequency. In some sections of this document, the frequency dependence of these variables will be omitted, for simplicity, but, in any case, the definitions in (2.10) hold.

$$V(x) \equiv V(x, f) \quad (2.10a)$$

$$I(x) \equiv I(x, f) \quad (2.10b)$$

To determine the voltages and currents of the equivalent circuit of Fig.2.3, it is sufficient to solve the system of equations (2.11).

$$\begin{cases} \begin{bmatrix} V(\ell_c, f) \\ I(\ell_c, f) \end{bmatrix} = \Phi(\ell_c, f) \begin{bmatrix} V(0, f) \\ I(0, f) \end{bmatrix} & (2.11a) \\ V(0, f) = S_S - Z_S I(0, f) & (2.11b) \\ V(\ell_c, f) = S_L + Z_L I(\ell_c, f) & (2.11c) \end{cases}$$

Where matrix  $\Phi$  is defined as in (2.12)

$$\Phi(x, f) = \begin{bmatrix} \cosh(x\gamma(f)) & -Z_c(f) \sinh(x\gamma(f)) \\ -\frac{1}{Z_c(f)} \sinh(x\gamma(f)) & \cosh(x\gamma(f)) \end{bmatrix} \quad (2.12)$$

If the voltages and/or currents in a position of the line different from  $x = 0$  or  $x = \ell_c$  are needed, they can be determined with (2.13).

$$\begin{bmatrix} V(x, f) \\ I(x, f) \end{bmatrix} = \Phi(x, f) \begin{bmatrix} V(0, f) \\ I(0, f) \end{bmatrix} \quad (2.13)$$

The obtainment of parameters  $Z_c$  and  $\gamma$  is discussed in section 2.3. Once these parameters are determined, the cables on the hypothetical radial network aforementioned can be modeled by (2.11), by representing any devices, or cabling, connected to their terminals as a Thévenin/Norton equivalent circuit.

Equations (2.11) and (2.13) allow the conception of a frequency domain simulation tool able to model the generic system in 2.3, which calculates the voltages and currents along the two-conductor line under study.

Figure 2.4 shows the flowchart of the frequency domain simulation tool. The inputs of the simulator are described below.

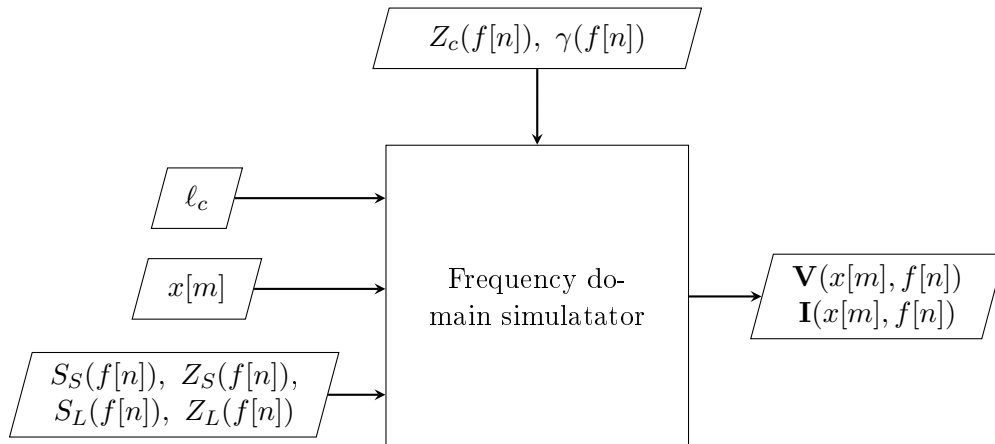


Figure 2.4 – Frequency domain simulation tool inputs and outputs — two-conductor cables

- $f[n]$  is the discretization of the variable frequency  $f$ , a vector containing the frequency points in which calculations will be performed.
- $Z_c(f[n])$  and  $\gamma(f[n])$  are the cable parameters in function of frequency, and their identification will be discussed in the next section;
- $\ell_c$  is the cable length;
- $x[m]$  is the discretization of the variable position along the line  $x$ . It contains the positions of the line where the voltage and currents are to be calculated;
- $S_S(f[n])$ ,  $Z_S(f[n])$ ,  $S_L(f[n])$ , and  $Z_L(f[n])$  are the elements of the Thévenin equivalent circuit representing the devices connected to the cable extremities (cf. Fig. 2.3).

The outputs are the voltages  $V(x[m], f[n])$  and currents  $I(x[m], f[n])$  calculated at the positions  $x[m]$  of the line for the frequency points in  $f[n]$ .

As the case where  $S_L = 0$  was often studied during the development of this model, an analytical solution to this specific case was implemented, it is described in appendix B.

Section 2.3 discuss different methods to obtain the cable parameters, but before entering this subject, it is interesting to analyze their behavior in the frequency domain.

### 2.2.b $Z_c$ and $\gamma$ dependance on frequency

The real and imaginary parts of  $\gamma$  are classically denominated as:

$$\gamma = \sqrt{(r + j\omega l)(g + j\omega c)} = \alpha + j\beta \quad (2.14)$$

Where  $\alpha$  is the attenuation constant, and  $\beta$  the phase constant.

For a lossless line,  $\alpha = 0$  and the cable parameters are reduced to  $Z_c = \sqrt{l/c}$  and  $\gamma = j\omega\sqrt{lc}$ , both constant with frequency. In this case, the propagation velocity  $v$ , defined by (2.15) [19], is constant with frequency and equal to  $v = \frac{1}{\sqrt{lc}}$ <sup>1</sup>.

$$v = \frac{\omega}{\beta} \quad (2.15)$$

However, for the cables used in buildings networks losses cannot be neglected. For lossy lines, the parameters  $Z_c$  and  $\gamma$  are not constant, as will be shown below.

For a preliminary analysis, the cable p.u.l. parameters are supposed constant, with values  $r = 10 \text{ m}\Omega/\text{m}$ ,  $l = 1 \mu\text{H}/\text{m}$ ,  $g = 10 \text{ nS}/\text{m}$ , and  $c = 100 \text{ pF}/\text{m}$ , all typical values for power cables. Using these values, the parameters  $Z_c$ ,  $\alpha$ , and  $v$  are plotted in function of frequency in figures 2.5 and 2.6.

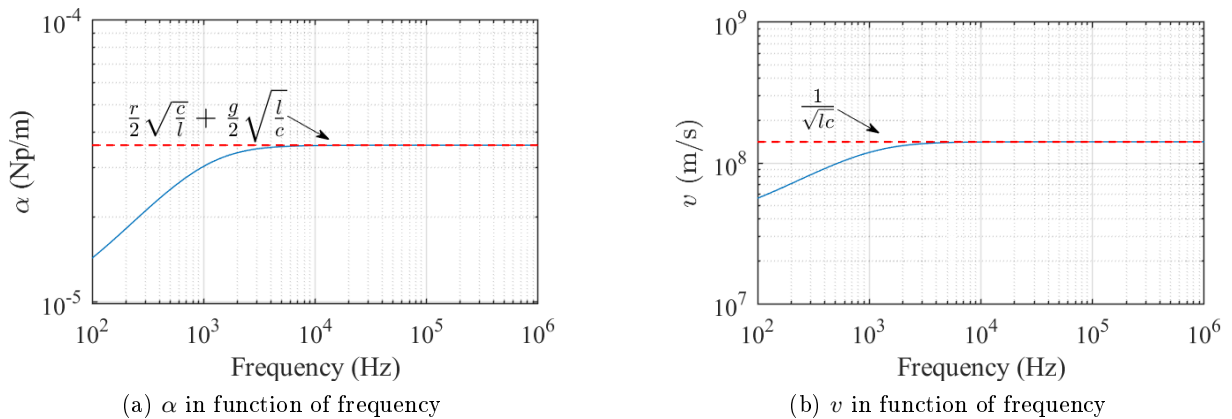
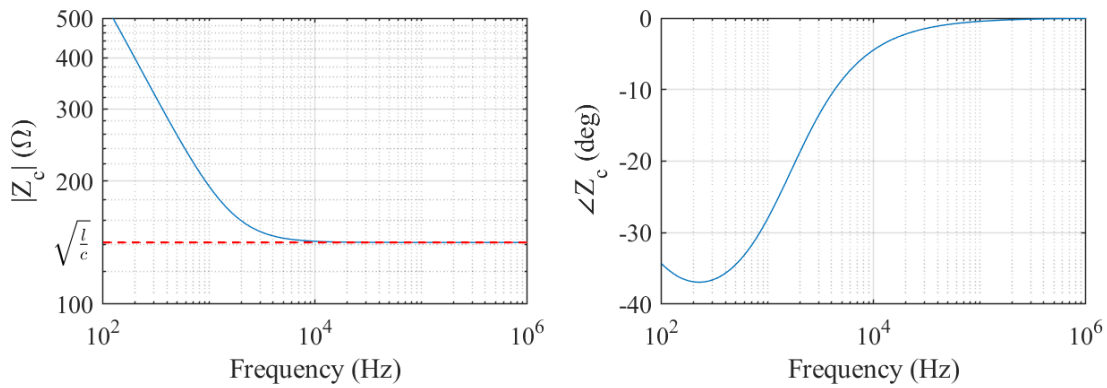


Figure 2.5 –  $\gamma = \alpha + j\frac{\omega}{v}$  in function of frequency

It can be seen that neither of the parameters plotted in Figs. 2.5 and 2.6 is constant, but they tend to a constant value for high frequencies.

The high frequency asymptote to  $Z_c$  can be obtained considering that, for high frequencies,

<sup>1</sup>These conclusions are also true for a line respecting the Heaviside condition, a case detailed in section 4.2.a

Figure 2.6 –  $Z_c$  in function of frequency

the approximations  $r \ll \omega l$  and  $g \ll \omega c$  are valid, which gives (2.16).

$$\lim_{\omega \rightarrow \infty} Z_c = \lim_{\omega \rightarrow \infty} \sqrt{\frac{r + j\omega l}{g + j\omega c}} = \sqrt{\frac{l}{c}} \quad (2.16)$$

The asymptotes to  $\gamma$  (real and imaginary parts) can be obtained using the binomial theorem truncated to the second term:  $(a+b)^{\frac{1}{2}} \approx a^{\frac{1}{2}} + \frac{b}{2}a^{-\frac{1}{2}}$  for  $a \ll b$ . With this identity, the asymptotes for high frequencies, where  $r \ll \omega l$  and  $g \ll \omega c$ , are determined with:

$$\begin{aligned} \lim_{\omega \rightarrow \infty} \gamma &= \lim_{\omega \rightarrow \infty} (r + j\omega l)^{\frac{1}{2}} (g + j\omega c)^{\frac{1}{2}} \approx \left[ (j\omega l)^{\frac{1}{2}} + \frac{r}{2}(j\omega l)^{-\frac{1}{2}} \right] \left[ (j\omega c)^{\frac{1}{2}} + \frac{g}{2}(j\omega c)^{-\frac{1}{2}} \right] \\ \lim_{\omega \rightarrow \infty} \gamma &= \frac{r}{2} \sqrt{\frac{c}{l}} + \frac{g}{2} \sqrt{\frac{l}{c}} + j\omega \sqrt{lc} \end{aligned} \quad (2.17)$$

This analysis shows that, in general, the propagation speed varies with frequency for a lossy cable, a conclusion that will be used further in this document.

For real cables these parameters will behave differently in high frequency, because the loss-related parameters  $r$  and  $g$  vary with frequency, due to skin and proximity effect, and the frequency-dependent behavior of the dielectric materials.

## 2.3 Two-conductor cable parameter identification

The model developed in section 2.2.a needs the cable parameters  $Z_c$  and  $\gamma$  to be determined. These parameters can be obtained with analytical, numerical, and experimental methods.

It was shown in 1.2 that the cable losses limit the resonance due amplifications. Therefore, they are essential to the complete prediction of the resonance behavior of a transmission line. For that reason, the ability of determining the cable losses is an important feature to be discussed in each parameter identification method.

Analytical solutions derived directly from Maxwell equations [33] are possible if the line geometry can be easily described in some coordinate system, which is not the case of the building cabling.

As for numerical methods, a variety of line parameters calculation methods is available in the literature, using formulations such as finite-element method (FEM) [8, 12, 14], finite-difference time-domain method (FDTD) [16], and boundary element method (BEM) [4]. The inconveniences of numerical methods are widely known: high computational effort, and the need of an

accurate description of the geometry and/or the physical constants linked to the problem

In fact, for both analytical and numerical methods, measurements are necessary to an accurate determination of the insulation parameters. For the low-frequency cables used in a building network, the experimental transmission-line parameter identification is not more complicated than measuring the relative permittivity of the cable insulation, for example.

For these reasons, and to avoid high computational effort, experimental parameter identification is the chosen approach to model the cables used in this work.

In this section, experimental methods to obtain these parameters are discussed. Section 2.3.a brings a review of the experimental parameter identification methods existing in the literature, and in section 2.3.b the parameter identification method chosen by the authors is described.

### 2.3.a Review of existing parameter identification techniques

The line parameters can be extracted directly from measurements either on time domain using a Time Domain Reflectometer (TDR) [1,3], or on frequency domain using Impedance Analyzers [6,24] or Vector-Network Analyzers (VNA) [23,54,55]. The parameter identification method for each of these devices will be shortly described in this section.

A TDR is a device that sends a square wave into the device under test (usually a cable) and measures the wave reflected back to the device output (Fig. 2.7b). The output impedance of the TDR device is normalized to  $50\Omega$ . The connector between the cable under test and the TDR output is a coaxial cable of characteristic impedance  $Z_0 = 50\Omega$ , usually about  $20\text{ cm}$  long. Fig. 2.7a shows a schematic explaining the reflections that take place in this measurement configuration.

From the first reflected wave that arrives at the TDR output (instant “2” in Fig. 2.7), it can determine the absolute value of the reflection coefficient  $\Gamma_1$ , defined in (2.18). From the second reflected wave that arrives at the TDR output (instant “3” in Fig. 2.7), the propagation time delay in the cable  $T_D$  can be determined.  $T_D$  is linked to the propagation velocity  $v$  by (2.19), where  $\ell_c$  is the cable length.

$$\Gamma_1 = \frac{Z_c - Z_0}{Z_c + Z_0} \quad (2.18)$$

$$T_D = \frac{\ell_c}{v} \quad (2.19)$$

Therefore, TDR parameter identification allows an easy determination of the absolute value of the characteristic impedance  $|Z_c|$  and the propagation velocity  $v$ . However, for the general case, parameters  $Z_c$  and  $\gamma$  are also frequency dependent (see section 2.2), and, in addition, cable losses also vary with frequency. The dependence of the propagation speed on the frequency (Fig. 2.5b) results in a different propagation time  $T_D$  for each harmonic that composes the square signal sent into the cable. As a result, the rise time of the reflected wave is degraded, as shown in Fig. 2.7b (zone 3). The loss-related parameters can be extracted from the deformation of the reflected wave using data-fitting algorithms as detailed in [49]. However, this makes the post-processing of the TDR data more cumbersome than for the other experimental methods.

A Vector Network Analyzer (VNA) can also be used to identify the parameters of low-frequency cables [55]. It is extensively used for connections on printed circuit boards. A VNA along with additional TDR measurements allows a more accurate determination of low-frequency parameters [23].

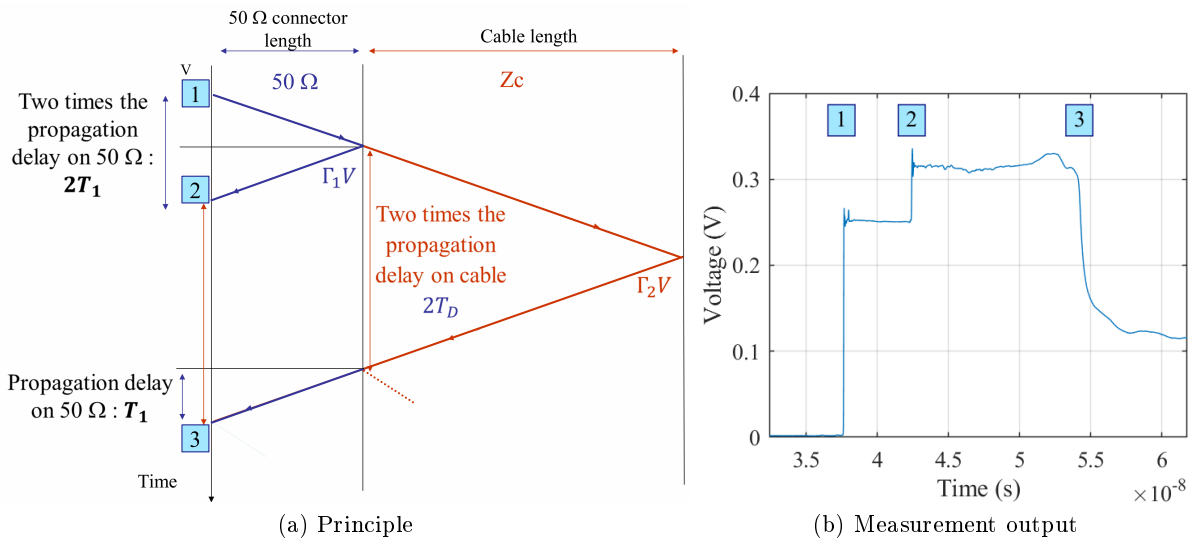


Figure 2.7 – Time-domain reflectometer (TDR)

A VNA device measures the S-parameters of the device under test, which are coefficients determined by the ratios of the wave reflected by the signal and the input wave (2.20), the waves are defined in Fig. 2.8a.

$$\begin{pmatrix} b_1 \\ b_2 \end{pmatrix} = \begin{pmatrix} S_{11} & S_{12} \\ S_{21} & S_{22} \end{pmatrix} \begin{pmatrix} a_1 \\ a_2 \end{pmatrix} \tag{2.20}$$

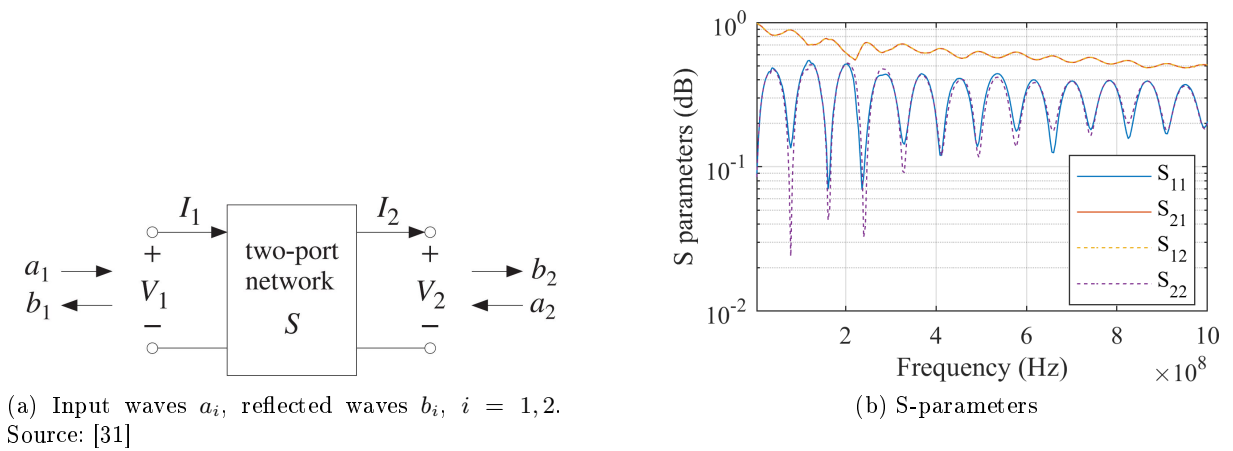


Figure 2.8 – VNA measurement

The S-parameters matrix can be converted to the use model introduced in section 2.2.a with (2.21) [11].

$$\begin{bmatrix} V(\ell_c) \\ I(\ell_c) \end{bmatrix} = \begin{bmatrix} \Phi_{11} & \Phi_{12} \\ \Phi_{21} & \Phi_{22} \end{bmatrix} \begin{bmatrix} V(0) \\ I(0) \end{bmatrix} \quad (2.21a)$$

$$\Phi_{11} = \frac{1}{2S_{12}}(1 - S_{11})(1 + S_{22}) + S_{12}S_{21} \quad (2.21b)$$

$$\Phi_{12} = -\frac{Z_0}{2S_{12}}(1 + S_{11})(1 + S_{22}) - S_{12}S_{21} \quad (2.21c)$$

$$\Phi_{21} = -\frac{1}{2S_{12}Z_0}(1 - S_{11})(1 - S_{22}) - S_{12}S_{21} \quad (2.21d)$$

$$\Phi_{22} = \frac{1}{2S_{12}}(1 + S_{11})(1 - S_{22}) + S_{12}S_{21} \quad (2.21e)$$

From the definition of matrix  $\Phi(\ell_c, f) = \begin{bmatrix} \Phi_{11} & \Phi_{12} \\ \Phi_{21} & \Phi_{22} \end{bmatrix}$  in (2.12), the cable parameters  $Z_c$  and  $\gamma$  can be deduced with (2.22).

$$Z_c = \sqrt{\frac{\Phi_{12}}{\Phi_{21}}} \quad (2.22a)$$

$$\gamma = \frac{1}{\ell_c} \ln(\Phi_{11} - Z_c\Phi_{21}) \quad (2.22b)$$

However, some considerations must be made about parameter identification from the VNA results. First, as the results are inaccurate around cable resonance (S-parameters tend to zero), the cable parameters are not precise for frequencies multiple of  $\lambda/2$ . Post-processing options to avoid this limitation are available in [23, 47, 55].

Second, VNA classical 2-port measurement is not adapted to our application. That is because the ground is connected to both ends of the cable, through the outer conductor of the probe coaxial cables. This identification setup gives parameters useful for applications such as printed-circuit strips [23], where the ground is an equipotential surface. However, for the building network application such configuration is unrealistic, because there is no equipotential along a large cabling network.

For the application under study, only a 4-point VNA measurement would be viable. It consists in measuring the cable S-parameters as if it was a 4-port device, connecting each extremity of the cable to the live point of each probe, leaving the outer conductors of the probe disconnected. However promising, this option to experimental parameter assessment was not pursued, because four-ports VNA were not available in any of the laboratories associated to our institution.

Impedance analyzer is the chosen method for the identification of the cable parameters in this work. It consists in extracting the cable parameters from two impedance measurements, usually the short-circuited and open-ended cable impedances. This method is detailed in the next subsection. Impedance analyzers are a good option for parameter identification from low to medium frequencies, which is the frequency band of interest.

The next subsection 2.3.b describes the input impedance based parameter identification, commenting on the choice of the cable length for an efficient identification in 2.3.b-i, and discussing the impact of the common mode on the measurements in 2.3.b-ii.

### 2.3.b Experimental parameter identification using an Impedance Analyzer

The theory of the cable parameter identification with impedance analyzer is resumed below. Consider the schematic shown in Fig. 2.9. The two-conductor line input impedance can be obtained from (2.9), and is given in (2.23).

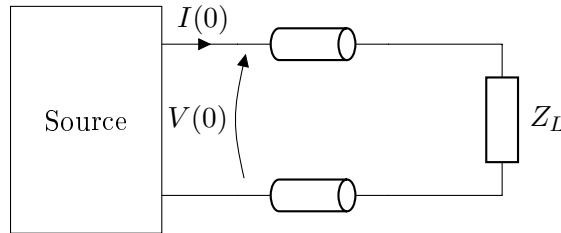


Figure 2.9 – The input impedance of the cable

$$Z(0) = \frac{V(0)}{I(0)} = Z_c \frac{Z_L + Z_c \tanh(\ell_c \gamma)}{Z_c + Z_L \tanh(\ell_c \gamma)} \quad (2.23)$$

The input impedance for the short-circuited line  $Z_{SC}$  and the open-ended line  $Z_{OC}$  are the following:

$$Z_{SC} = Z_c \tanh(\ell_c \gamma) \quad (2.24a)$$

$$Z_{OC} = Z_c \coth(\ell_c \gamma) \quad (2.24b)$$

From (2.24), the characteristic parameters of the line can be found from the input impedances with:

$$Z_c = \sqrt{Z_{SC} Z_{OC}} \quad (2.25a)$$

$$\gamma = \frac{1}{\ell_c} \tanh^{-1} \left( \sqrt{\frac{Z_{SC}}{Z_{OC}}} \right) \quad (2.25b)$$

The cable input impedances can be measured with an impedance analyzer.

Some precautions need to be taken on the impedance measurement of unshielded cables. They cannot be characterized in a bundle, or superpose themselves, as the stray capacitance and magnetic couplings between different portions of the cable would compromise the determination of the p.u.l. capacitance and inductance. Therefore, it is recommended to set up the cable over a non-conductive surface. However, a long extended cable may increase the common-mode currents circulating in the measurement circuit and even behave like an antenna, if it is open-ended and longer than  $\lambda/4$  (alternatively:  $f > v/4\ell_c$ ), point from which it behaves as a poor half-wave dipole.

These problems are exclusive to unshielded cables, as the geometry of shielded cables prevent them from inducing currents in nearby conductors, or behave as antennas.

The following subsections bring some considerations on how to determine a good length for the sample cable used in parameter identification and how to mitigate the common mode in the impedance measurements.

#### 2.3.b-i Choice of the sample cable length

The length of the sample cable used for the identification input impedance measurements has to be carefully chosen for unshielded cables. Indeed, long unshielded cables can behave as bipolar



antennas when open-ended, capturing electromagnetic signals even if its conductors are not spaced from each other. This phenomenon would not be significant for shielded cables, because their geometry does not favor radiation.

Therefore, if long sample cables are to be used in the parameter assessment, the input impedance measurements must be effectuated in an electromagnetically clean environment, e.g., a Faraday cage or an anechoic chamber. A second problem arises with the need of performing the measurements inside a metallic cage: the cable cannot be placed too close to any metallic surface during the measurements, otherwise the Foucault current induced in the metallic surface and the stray capacitance between the cable and the surface will interfere with the input impedance measurements, introducing a systematic error in the parameter assessment. Therefore, when the cable is placed in a metallic cage, it must be suspended by insulating supports.

To verify the possibility of identifying the cable parameters with a long sample cable, the input impedance measurements were performed inside an anechoic chamber for four sample cables of different lengths:  $6\text{ m}$ ,  $12\text{ m}$ ,  $24\text{ m}$ , and  $36\text{ m}$ . All the sample cables were kept apart from the metallic ground and walls, supported by insulating materials. The results are presented in Fig. 2.10.

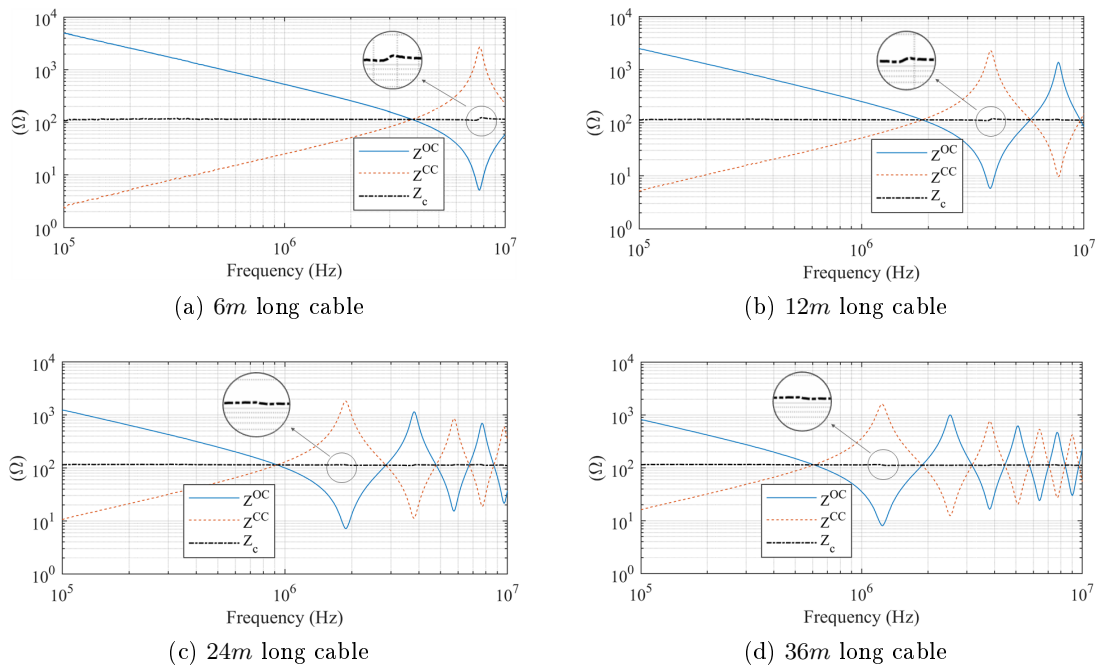


Figure 2.10 – Two-conductor cable characteristic impedance identification for different lengths

The figures 2.10 show distortions on the characteristic impedance absolute value, around the sample cables resonance and antiresonance frequencies. The largest distortion can be observed in Fig. 2.10a, it corresponds to the smallest of the chosen sample cables. Table 2.1 resumes the relative distortion of the characteristic impedance absolute value, relative to the experimental medium value for each cable. It shows that distortion is reduced for longer cables.

The characteristic impedance is calculated with  $Z_c = \sqrt{Z_{OC}Z_{SC}}$ , from (2.25). The distortion in its absolute value occurs around the cable resonance, because the resonances in  $Z_{OC}$  do not take place at the exact same frequency as the antiresonances in  $Z_{SC}$ , and vice-versa. The slight difference on the cables natural frequencies is due to the way the cable extremity was short

Table 2.1 – Characteristic Impedance Distortions Due to Resonance

Cable length	Average $ Z_c $	$\frac{\text{Min} Z_c }{\text{Av} Z_c }$	$\frac{\text{Max} Z_c }{\text{Av} Z_c }$
6m	114.12 $\Omega$	6.53%	7.62%
12m	114.23 $\Omega$	4.02%	3.98%
24m	114.64 $\Omega$	3.04%	2.43%
36m	114.01 $\Omega$	2.75%	2.12%

circuited. To short-circuit the cable, the extremities of the conductors are striped and twisted together, while for the open-ended cable these striped extremities are kept apart. That makes the effective cable length different for short-circuited and open-ended impedance measurements, what changes the cable natural frequencies.

Even though these natural frequencies difference is not big, it may cause important distortions on  $Z_c$ . Indeed, the characteristic impedance is the geometric mean value between the two impedances (SC and OC), and, around the cable natural frequencies, the impedance absolute values are either very high or very low. It may be easier to visualize this effect by taking the logarithm of the characteristic impedance expression:

$$\log(Z_c) = \frac{1}{2} (\log(Z_{SC}) + \log(Z_{OC})) \quad (2.26)$$

Because  $\log(Z_c)$  can be considered constant along the frequency, when the value of either  $\log(Z_{SC})$  or  $\log(Z_{OC})$  is very high for a given frequency, while the other is very low for a slight different frequency, the distortion be observed in  $Z_c$  can be important even for a really small difference in frequencies of maxima and minima of  $Z_{OC}$  and  $Z_{SC}$ .

The simplest way to avoid this distortion is to choose a cable sample considerably shorter than a quarter of the smallest wavelength in the measurement band ( $\ell_c \ll \lambda/4$ ), so that resonance will not occur [19] during the identification measurements. However, if such length is small when compared to the measurement circuit, it may compromise the accuracy of the parameter identification, and the cable sample should be longer.

If the use of a long sample cable is unavoidable, long enough to resonate in the identification frequency band, some precautions must be taken for unshielded cables:

- Any cable longer than  $\lambda/4$ , for the smallest wave length  $\lambda$  in the frequency band, may capture the electromagnetic noise of the media: the input impedance measurements must be effectuated inside a Faraday cage;
- The cable must be placed away from the metallic surfaces, suspended by insulating supports;
- The cable cannot superpose itself;
- The short circuit at the cable extremity must be carefully done to not substantially change the total cable length. For example, it can be done with massive copper plates.

Naturally, the longer the sample cable, less the quality of the short circuit will interfere in the results, as shown in table 2.1.

In this work, the frequency band is limited at  $30\text{ MHz}$ , and the parameter assessment measurements were effectuated with sample cables about  $1\text{ m}$  long, so resonance does not occur. The short circuit was made with the conductors extremities striped and twisted together, and pressed between two cooper plates.

### 2.3.b-ii Common-mode mitigation

In any impedance analyzer measurement, common-mode currents may flow outside of the measurement circuit, through its stray capacitance [21]. In such cases the impedance measurement is subjected to a systematic error. The fact that the cable under test has to be minimally long enhances the circulation of common-mode currents. The effects of the circulation of common mode during the parameter identification measurements will be shown in section 2.4.

The present section discusses common-mode mitigation methods, demonstrating the imprecision observed on the measured impedance value due to common-mode circulation, at the same time it introduces the proposed solution: use a balun transformer as interface between the impedance analyzer and the device under test (DUT), while the analyzer itself is powered through a LISN (Line Impedance Stabilization Network).

**Common-mode mitigation with ground plane:** In any impedance analyzer measurement, common-mode currents may flow outside of the measurement circuit, if there is a conductor nearby. The common-mode current circulates through the stray capacitances between the measurement circuit and the external conductor, as illustrated in Fig. 2.11.

Source: [21] page 3-15

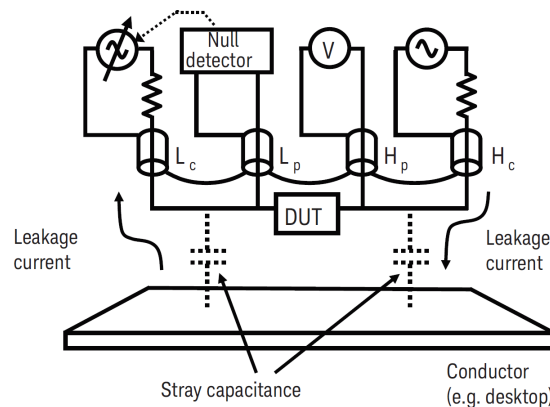


Figure 2.11 – Example of common-mode measurement corruption due to common-mode current [21]

The solution proposed by the Impedance Analyzer Handbook [21] is to insert a metallic plate connected to the outer conductors of the impedance analyzer output, as shown in Fig. 2.12. This way, the common-mode currents will be trapped by the metallic plate, and close a loop through the analyzer mass, having no influence in the impedance measurement.

However, such a solution is troublesome for the cable parameter identification. As aforementioned, the cable cannot be placed too close to a conducting surface, because in that case it would induce Foucault currents in the surface, interfering with the determination of the actual p.u.l.

Source: [21] page 3-15

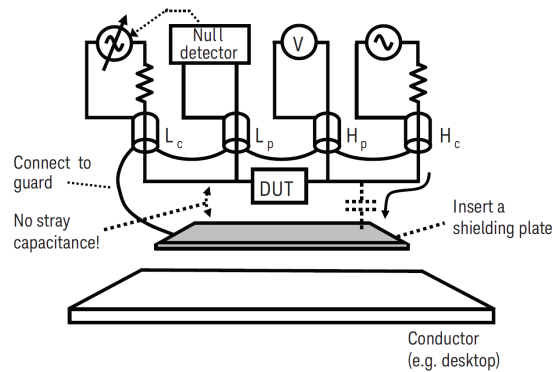


Figure 2.12 – Solution to avoid common-mode-due error [21]

inductance of the cable. Moreover, the stray capacitance between the cable conductors and the plate would interfere with the determination of the actual p.u.l. capacitance.

Therefore, another common-mode mitigation method is needed.

**Common-mode mitigation with balun:** The balance-to-unbalanced transformer, or balun, as it is known, is a high frequency transformer able to balance voltage signals by connecting the secondary winding middle point to the mass (cf. Fig. 2.13).

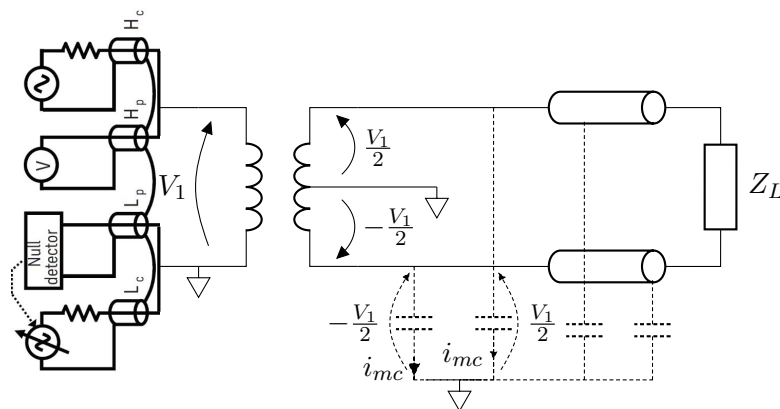


Figure 2.13 – Common-mode analysis of balun-isolated measurement

Having balanced voltages in a cable input generates identical common-mode currents in opposite directions, thus mitigating common mode during impedance measurement. This is shown in Fig. 2.13. The need to balance voltage on unshielded cables in order to guarantee the validity of the transmission line model has been mentioned since 1950 [19]. It is important to note that the common-mode currents from each conductor only cancel each other if the cable is also balanced, i.e., the stray capacitances between the conductors and mass are identical.

To demonstrate these assertions, an experiment was designed to evaluate the common mode, consisting in cable input impedance measurements performed with and without balun in the two setups listed below. In both configurations, cable and impedance analyzer were on a wooden table.

1. Configuration “A”: a recommended set for measurement, no other device, cable or metallic surface is closer than  $50\text{cm}$  to the cable under test (Fig. 2.14.);
2. Configuration “B”: a common-mode enhancing configuration, the cable was disposed so that it is parallel to the feeding cable of the impedance analyzer, with its extremity close to the analyzer electrical plug (Fig. 2.15).

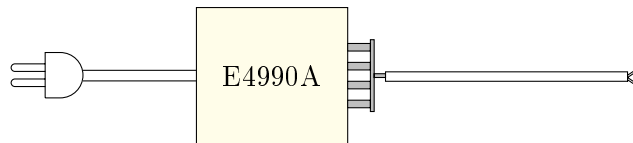


Figure 2.14 – Configuration “A”: avoids common-mode circulation

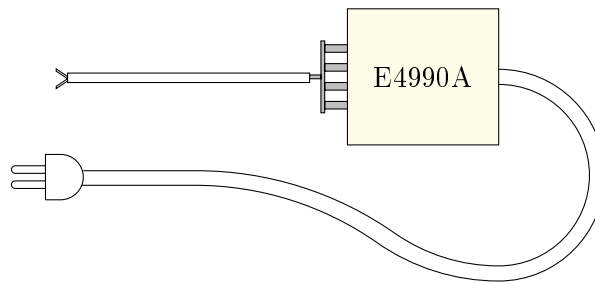


Figure 2.15 – Configuration “B”: common-mode enhancing configuration

This experiment was performed on a two-conductor cable composed of stranded copper wires of section  $0.75\text{ mm}^2$  surrounded by PVC sheaths, refer to Fig. 2.16 for its cross-section.

Source: <http://www.caledonian-cables.co.uk>

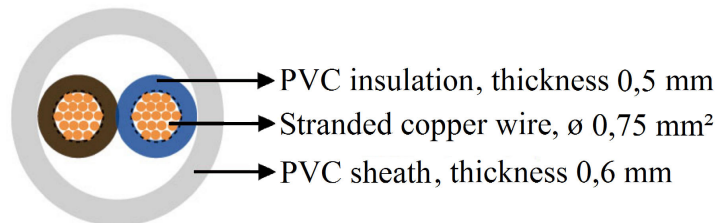


Figure 2.16 – Cross-section of the two-conductor  $0.75\text{ mm}^2$  cable

The connections between the impedance analyzer, balun transformer and the cable under test were made with printed circuit boards made in the laboratory, pictures of them are presented in Fig. 2.17. These connectors were compensated with the impedance analyzer internal three-measurements compensation (OPEN, SHORT, and LOAD) [21]. A study of the reliability of the impedance analyzer compensation of the balun is presented on appendix E. As the lab-made connectors are not certified measurement adapters, the accuracy of the measurement is difficult to predict. Therefore, the results on this section allow conclusions on the measurement precision, or repeatability, but not on its accuracy. The accuracy of the proposed experimental parameter identification protocol will be demonstrated in section 2.4.

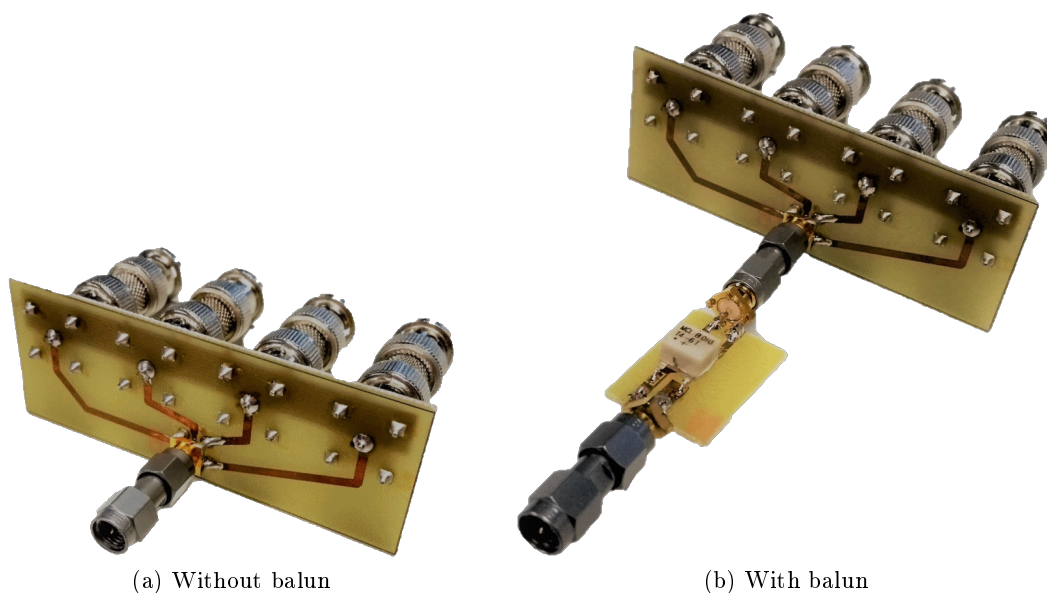


Figure 2.17 – E4990A adapter designed by the authors

The balun chosen for these measurements is the Minicircuits T6-4T. This experiment was performed for the frequency band from  $200\text{ kHz}$ , which is the lower limit balun in the printed circuit (cf. appendix E), up to  $30\text{ MHz}$ , which is the upper limit of the LISN frequency band (the LISN will be used in the next experiment).

The cable input impedance was measured for both configurations “A” and “B” with a balun in the interface between the impedance analyzer and the cable using the connector presented in Fig. 2.17b, and without a balun using the connector shown in Fig. 2.17a.

The differences between the impedance measured on the configurations A and B, relative to the impedance measured in configuration A, were calculated for every frequency point in which the impedance measurement was carried out (1000 points). Table 2.2 resumes the maximal relative difference values, for a short-circuited and an open-ended cable, and the frequency to which each maximum occurs.

Table 2.2 – Maximum difference between the impedance measured using configurations “A” and “B”, relative to the measurement in config. “A”

	Short circuit		Open end	
	Maximal relative difference	Frequency of the maximal difference	Maximal relative difference	Frequency of the maximal difference
With balun	0.79%	$10.7\text{ MHz}$	1.2%	$29.6\text{ MHz}$
Without balun	5.8%	$30\text{ MHz}$	2.7%	$2.4\text{ MHz}$

The differences between the measurements in configurations “A” and “B” without balun shows that common-mode current is effectively circulating in the measurement circuit.

Moreover, the difference between the two measurements is smaller when performed with a

balun. It proves that the balun mitigates the common mode.

Part of the disparities observed in table 2.2 may be due to external interference, conducted by the impedance analyzer feeding cable. To verify this possibly, this experiment was repeated with the impedance analyzer fed through a LISN.

**Impact of LISN filtering:** The experiment described above was repeated, but using a LISN as a filter in the impedance analyzer input. The cable input impedance was measured with and without balun in configurations “A” and “B”, and the differences between the measured impedance are resumed in table 2.3.

Table 2.3 – Maximum difference between the impedance measured in configurations A and B, relative to the impedance measured in config. “A”; impedance analyzer powered through a LISN

	Short circuit		Open end	
	Maximal relative difference	Frequency of the maximal difference	Maximal relative difference	Frequency of the maximal difference
With balun	0.42%	28.8 MHz	0.39%	30 MHz
Without balun	4.8%	29.5 MHz	1.18%	28.7 MHz

The previous conclusion can be confirmed: the balun mitigates the common-mode signals. Furthermore, the introduction of a LISN reduces the differences between the impedance measured in configurations “A” and “B” in all cases, with and without balun. It proves that interference conducted by the analyzer feeding cable was also present in the former experiment.

### 2.3.b-iii Conclusion on the cable parameter identification with impedance analyzer

In conclusion, it is recommended to perform the impedance measurements for the cable parameter identification taking into account the following rules:

- A balun should be used in the interface between the sample cable and the impedance analyzer, to mitigate common mode;
- The analyzer energy input should be filtered, with a LISN for example, to avoid perturbations from the building network;
- The short circuit should be carefully performed, preferably with massive copper terminals;
- It is better to avoid the sample cable resonances during the input impedance measurements, by choosing a small cable. If the sample cable resonates, additional recommendations apply:
  - The measurement should be performed inside a metallic cage;
  - The cable should be placed away from the metallic surfaces, suspended by dielectric materials.

The impedance analyzer parameter identification gives a couple  $Z_c$ ,  $\gamma$  for each frequency point in which the impedance measurement is effectuated. An interpolation of the results is enough to estimate these parameters for the other values in the frequency band.

The measurements for the cable parameter identification along this document were systematically performed with the maximum number of frequency points allowed by the Keysight E4990A Impedance Analyzer: 1600 frequency points.

## 2.4 Frequency-domain model experimental validation

The impedance analyzer-based parameter identification method presented in the former section provides the cable parameters  $\gamma$  and  $Z_c$ , which can then be inserted on the two-conductor cable frequency domain simulator described in section 2.2.a.

The proposed parameter identification will be validated with two experimental validation setups: the first based on the measurement of the resonance-due voltage amplifications along the line, and the second based on the input impedance measurement. Both setups use cables longer than the identification cable sample.

The cable length for the validation setups was chosen so resonance will occur in the frequency band from 1 MHz up to 10 MHz. As resonance is a phenomenon quite sensitive to the cable parameters, a resonant cable configures a worst-case scenario for validation purposes: it is at the resonance that the inaccuracy of the parameters will be the most visible.

The cable chosen for these validation experiments is a two-conductor cable composed of stranded copper wires of section  $0.75 \text{ mm}^2$  with outer PVC sheaths, refer to Fig. 2.18 for its cross-section.

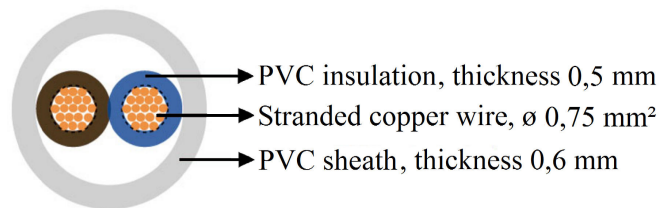


Figure 2.18 – Cross-section of two-conductor  $0.75 \text{ mm}^2$  cable

A 1 m long sample of this cable was used for the parameter identification measurements. Two sets of identification measurements were performed:

1. **With balun**, with the connector built in the laboratory (cf. Fig. 2.17b), and with the impedance analyzer powered through a LISN, as described in section 2.3.b;
2. **Without balun**, with the standard connector Keysight 16047E in a common-mode enhancing configuration: sample cable next to the impedance analyzer feeding cable, its extremity close to the analyzer electric outlet (Fig. 2.15).

The parameters of the two-conductor cable of section  $0.75 \text{ mm}^2$  are given in section 2.4.c.

The resonance-based validation experiment and the input impedance based validation experiment are described in the two following sections.

### 2.4.a Resonance-based experiment validation

The resonance-based experiment consists in the voltage measurement, for different excitation frequencies, at the position of the line  $x = x_M$  where the maximum voltage occurs once resonance is established. Fig. 2.19 shows the schematic of the experiment.



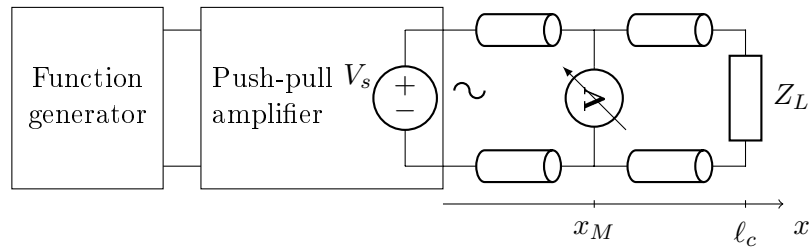


Figure 2.19 – Schematic of the validation resonance-based experiment

The voltage measurement was performed with a battery-powered scope, to avoid alternative current paths through the scope's feeding cable. It can be argued that the scope is not sufficiently precise for these measurements, but its use remains interesting because a conversion of the frequency domain results to time domain will be discussed and re-validated in chapter 4, and then the measurements of the voltage along the cable with a scope will be indispensable.

In an open-ended line, at any frequency, the maximum voltage is located at the line endpoint  $x_M = \ell_c$ . For the short-circuited line, the position of the maximum voltage changes with frequency, but for the first resonance, it occurs at the line midpoint  $x_M = \ell_c/2$ . As the measurement position  $x = x_M$  remained fixed for a given load, the maximum voltage was not necessarily measured for frequencies different from the cable natural frequencies.

In order to maximize voltage amplification, source and load reflection coefficient absolute value must be maximal, i.e.  $|\Gamma| = 1$ . To fulfill these conditions, firstly, in the load extremity, the experiments were performed either with a short-circuited or an open-ended line, and secondly, in the source extremity, an AB-class push-pull amplifier with closed loop was used to emulate a voltage source with very low output impedance.

The probe input impedance  $Z_{scope}$  was taken into account in the theoretical model because it slightly interferes on the measured voltage.  $Z_{scope}$  was measured with the impedance analyzer, and it is plotted in Fig. 2.21. The probe mass was connected with the spring connector adapted to it, shown in Fig. 2.20, to reduce the area of the loop of the mass connection. The cable and the scope were suspended with insulating supports to minimize common-mode currents during this experiment.



Figure 2.20 – Connection of the voltage probe along the line

The resonance experiment was performed with a two-conductor cable of length  $\ell_c = 11.87\text{ m}$ , with conductors of section  $0.75\text{ mm}^2$ . The cable and the scope were suspended with insulating supports, to mitigate common-mode currents.

Fig. 2.22 resumes the theoretical calculations performed for this validation, detailing the inputs needed for the theoretical calculation of  $V(x_M, f)$ . As aforementioned, two cable parameter sets are used: with and without balun.

To recall,  $\ell_c$  is the cable length,  $x_M$  is the voltage measurement point,  $Z_{scope}$  is the input

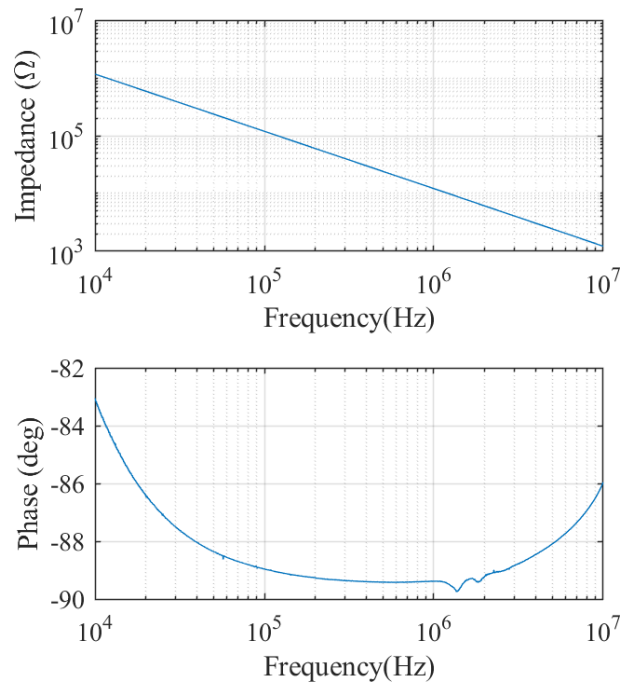


Figure 2.21 – Voltage probe input impedance

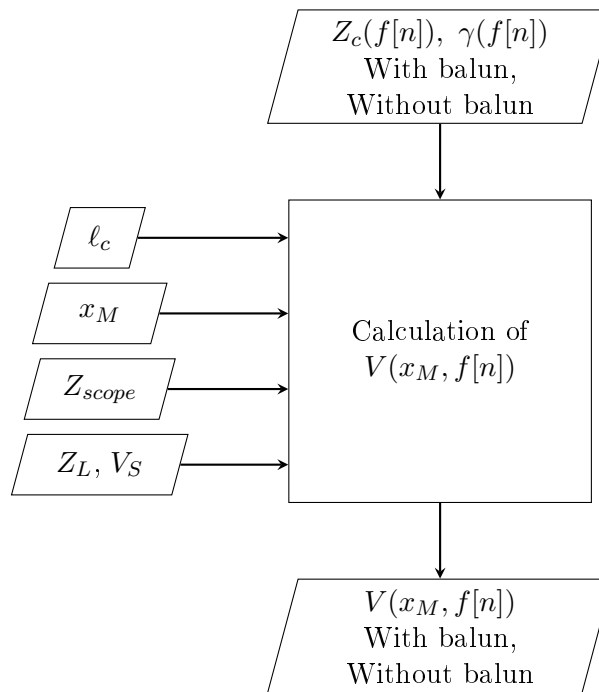


Figure 2.22 – Frequency domain voltage simulation

impedance of the scope probe,  $Z_L$  is the load connected at  $x = \ell_c$  (open and short circuit in this study),  $V_S$  is the input voltage, purely sinusoidal, of variable frequency, and  $f[n]$  is the discretization of the variable  $f$  frequency, a vector containing the points to which the calculations are performed.

The results of the validation experiment are presented in Fig. 2.23. Both theoretical and experimental data are plotted in terms of voltage amplification, i.e.  $V(x_M)/V(0)$ .

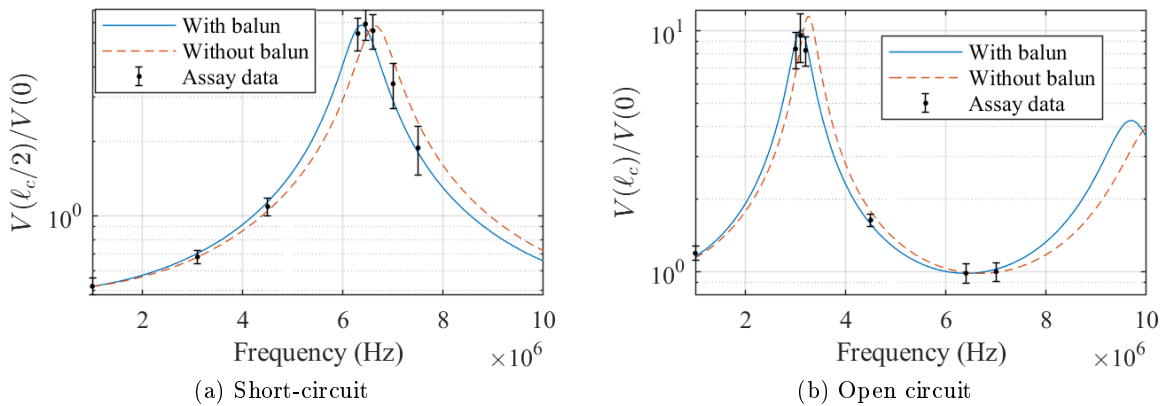


Figure 2.23 – Input impedance comparison

It is clear that the predicted resonance frequency and amplitude are closer to the experimental results for the balun isolated identification measurements; table 2.4 presents the relative errors between the theoretical and experimental results for both cases.

Table 2.4 – Frequency-Domain Model Resonance Frequency and Amplitude Relative Errors

	With balun		Without balun	
	Amplitude	Frequency	Amplitude	Frequency
Open-ended	5.5%	0.03%	20%	5.2%
Short-circuited	1.1%	1.2%	1.8%	2.9%

The experimental parameter identification with impedance analyzer described in section 2.3.b, following the experimental protocol recommended by 2.3.b-ii, is validated by this experiment.

### 2.4.b Input Impedance Validation

The second validation experiment consists in the input impedance measurement of a long cable, longer than the sample cable used for the parameter identification. The same cable from the former section was used, two-conductor of section  $0.75 \text{ mm}^2$  and  $11.87 \text{ m}$  long, cf. Fig 2.18 for its cross-section.

The input impedance was measured with the long cable open-ended and short-circuited. The measurement was performed inside a Faraday cage, to avoid radiated electromagnetic interference, with the cable suspended over cardboard boxes. The balun Minicircuits T4-6T (Fig. 2.17b) was used in the interface between impedance analyzer and cable, to filter the common-mode currents that may circulate through the metallic walls of the cage.

The theoretical impedance was predicted from equation (2.23), using two sets of parameters obtained with and without balun. Fig. 2.24 shows a practical schematic with the inputs and output of the theoretical cable input impedance calculation.

The theoretical results are plotted over the measured input impedance in Fig. 2.25

This validation experiment conducts to the same conclusion as the former: for the parameter identification without balun, the common mode on input impedance measurement compromises

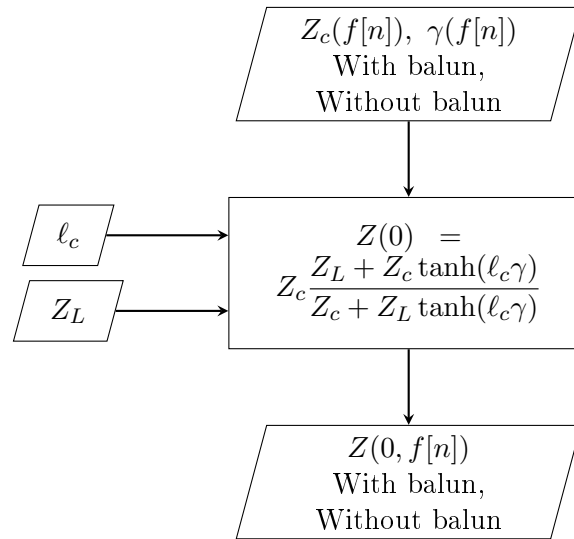


Figure 2.24 – Theoretical input impedance calculation

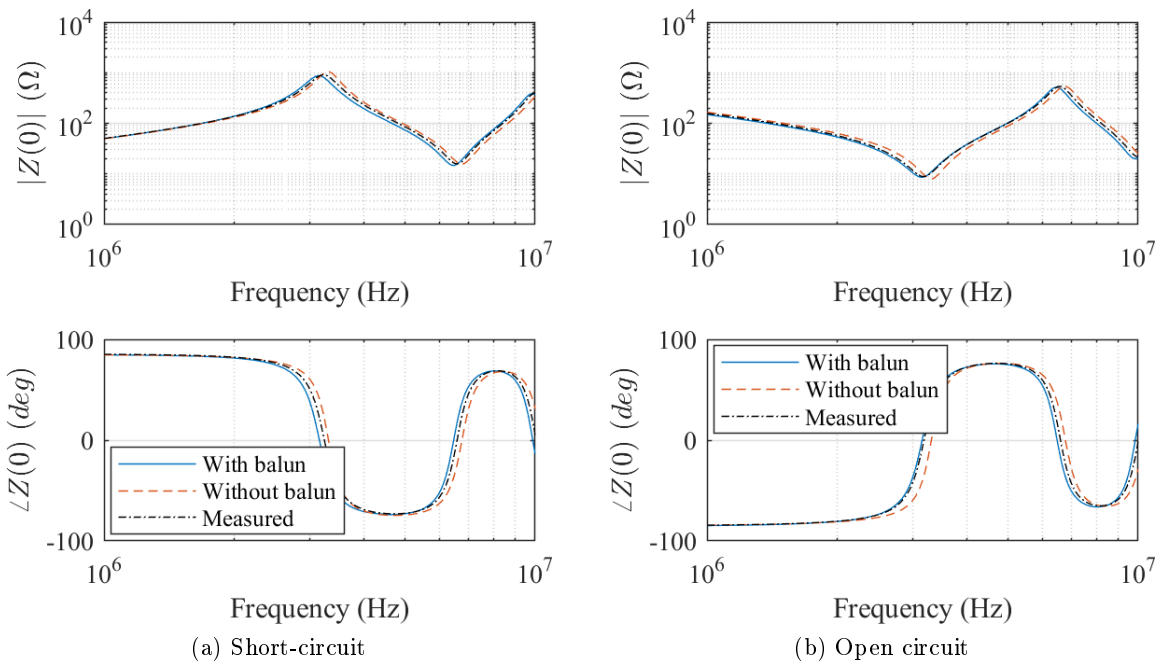


Figure 2.25 – Input impedance comparison, theoretical calculations using parameters obtained from identification with and without balun

the accuracy of the model. This error is reduced when the parameters issued from the identification with balun are used.

However, the use of a balun also introduces a measurement error, as its compensation by the analyzer is not perfect. It is possible that part of this error comes from flaws in the impedance analyzer connectors built in the laboratory. The compensation of these connectors using the OPEN, SHORT and LOAD compensation measurements proposed by the impedance analyzer is not ideal for a large frequency band, this is addressed in annex E. In any case, making the connectors in the laboratory was the only option, because the production of commercial impedance

analyzer terminals with balun (e.g. 16314A, 16315A) was discontinued in 2006 ([22]).

The error introduced by the balun can be verified by comparing its results to those using a parameter identification without balun in a configuration where no common mode circulates. Such a configuration was achieved by carrying out the input impedance measurements without balun as follows:

- The sample cable was put away from any device or metallic surface, placed over a wooden table;
- The impedance analyzer was fed through a LISN;
- The laboratory-made connector in Fig. 2.17a was used;

The identification input impedance measurements with balun were repeated, in the same configuration. The comparison between the long cable input impedance using the parameters from both of these identification measurement setups is presented in Fig. 2.25.

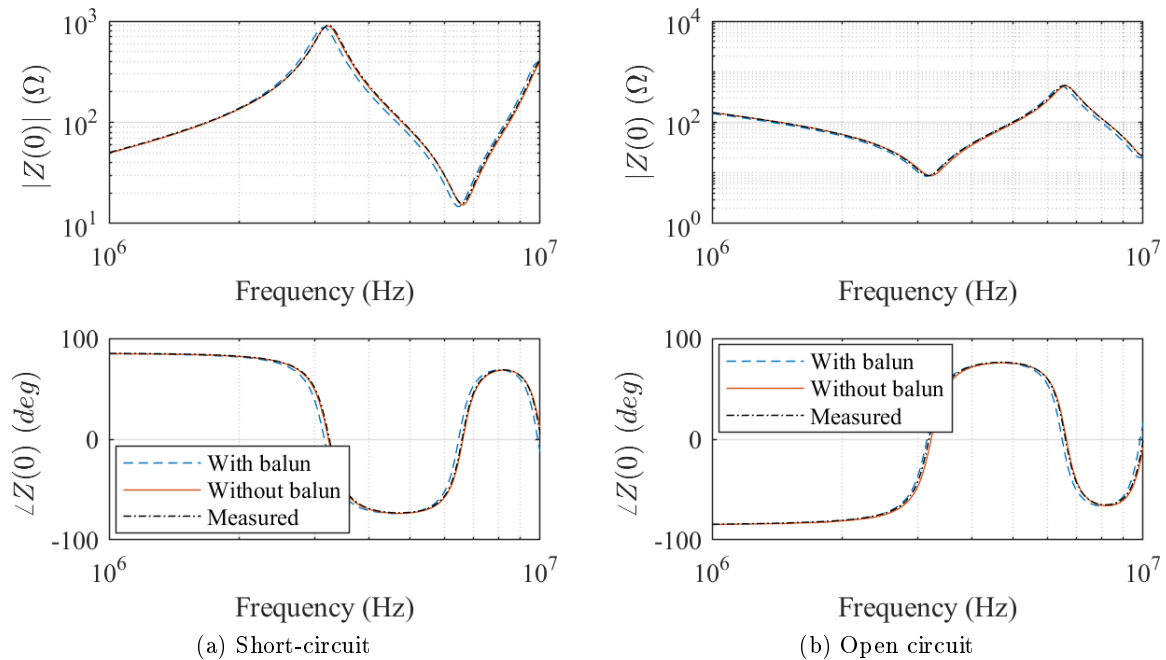


Figure 2.26 – Input impedance comparison, theoretical calculations using parameters obtained from identification with or without balun, identification without balun on ideal configuration

It can be seen that in this case the results using the parameter identification without balun are closer to the experimental data. It is proven that, for our specific configuration, no common-mode currents were circulating in the measurement circuit despite the absence of the balun, making the identification without balun more accurate because of the absence of the measurement errors introduced by the balun itself. The results in section 2.3.b-ii prove that a balun is necessary to guarantee the precision of the measurement, as it is usually difficult to predict the common-mode levels in any experimental setup. The balun guaranteed the repeatability of the results even under unfavorable configurations regarding the common-mode conducted emissions.

The results in Fig. 2.25 imply that the accuracy of the model could yet be improved if the balun was dispensable in the identification input impedance measurements. However, the

balun is only not necessary when one can be sure that no common mode will circulate in the identification measurement setup, on the desired frequency band.

### 2.4.c Examples of cable parameters identification

The experimental parameter identification techniques presented in section 2.3 recommends the use of a balun transformer. The problem of the balun is that its frequency band is limited. For example, the balun Minicircuits T4-6T used in the previous results has a useful frequency band from around  $100\text{ kHz}$  up to  $50\text{ MHz}$  according to its data-sheet (refer to annex E for details on the practical frequency band of the balun).

To characterize a cable for frequencies lower than  $100\text{ kHz}$ , the identification input impedance measurements had to be performed without balun. But, in this case, the balun is effectively dispensable, because in this setup the common mode is negligible at these frequencies.

Also, it is recommended to perform the low frequency parameter identification measurements with a considerably long cable, so the small values of  $r$  and  $g$  in low frequency are more accurately measured.

In the general case, to obtain the parameters of the cables of interest in a wide frequency band, including on direct current (DC), the three following setups for the identification measurements were combined:

1. For frequencies from  $f_{lim}$  up to  $30\text{ MHz}$ : measurements using an  $1\text{ m}$  long cable sample following the protocol in section 2.3, i.e., with a balun in the interface between the cable and the impedance analyzer, with LISN as line filter for the analyzer, without the protection of a Faraday cage because the length of the cable sample is a order of magnitude smaller than  $\lambda/4$ , i.e. there is no radiation phenomenon;
2. For frequencies lower than  $f_{lim}$ , DC excluded: measurements using a  $12\text{ m}$  long cable sample, extended on the floor, without balun and without LISN, on a non-protected environment because, again, the cable is too short to act as an antenna in this frequency band.
3. In DC: The p.u.l. resistance was obtained from a series of associated DC measurements of current and voltage in a  $12\text{ m}$  long conductor. The p.u.l. conductance was approximated by its value at  $20\text{ Hz}$ , measured with the impedance analyzer.

The frequency  $f_{lim}$  corresponds to the frequency of changing between the high and low frequency identification measurements. The parameter identification frequency band is limited on  $30\text{ MHz}$  because it is the upper limit of the LISN available for these measurements.

The p.u.l. parameters can be obtained from the characteristic impedance  $Z_c$  and the propa-

gation coefficient  $\gamma$  with the following equations:

$$r = \Re\{\gamma Z_c\} \quad (2.27a)$$

$$l = \frac{1}{j\omega} \Im\{\gamma Z_c\} \quad (2.27b)$$

$$g = \Re\left\{\frac{\gamma}{Z_c}\right\} \quad (2.27c)$$

$$c = \frac{1}{j\omega} \Im\left\{\frac{\gamma}{Z_c}\right\} \quad (2.27d)$$

$$(2.27e)$$

A convenient frequency limit  $f_{lim}$ , where the change between each of the characterization measurements occurs, has to be determined for each cable under study.

For example, considering the case of the two-conductor cable of section  $0.75 \text{ mm}^2$ , its cross-section described by Fig. 2.27.

Source: <http://www.caledonian-cables.co.uk>

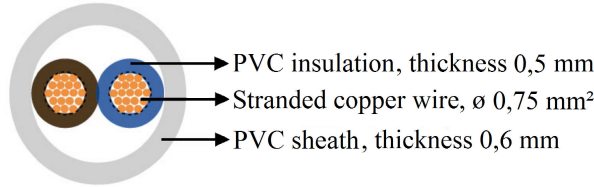


Figure 2.27 – Cross-section of the two-conductor  $0.75 \text{ mm}^2$  cable

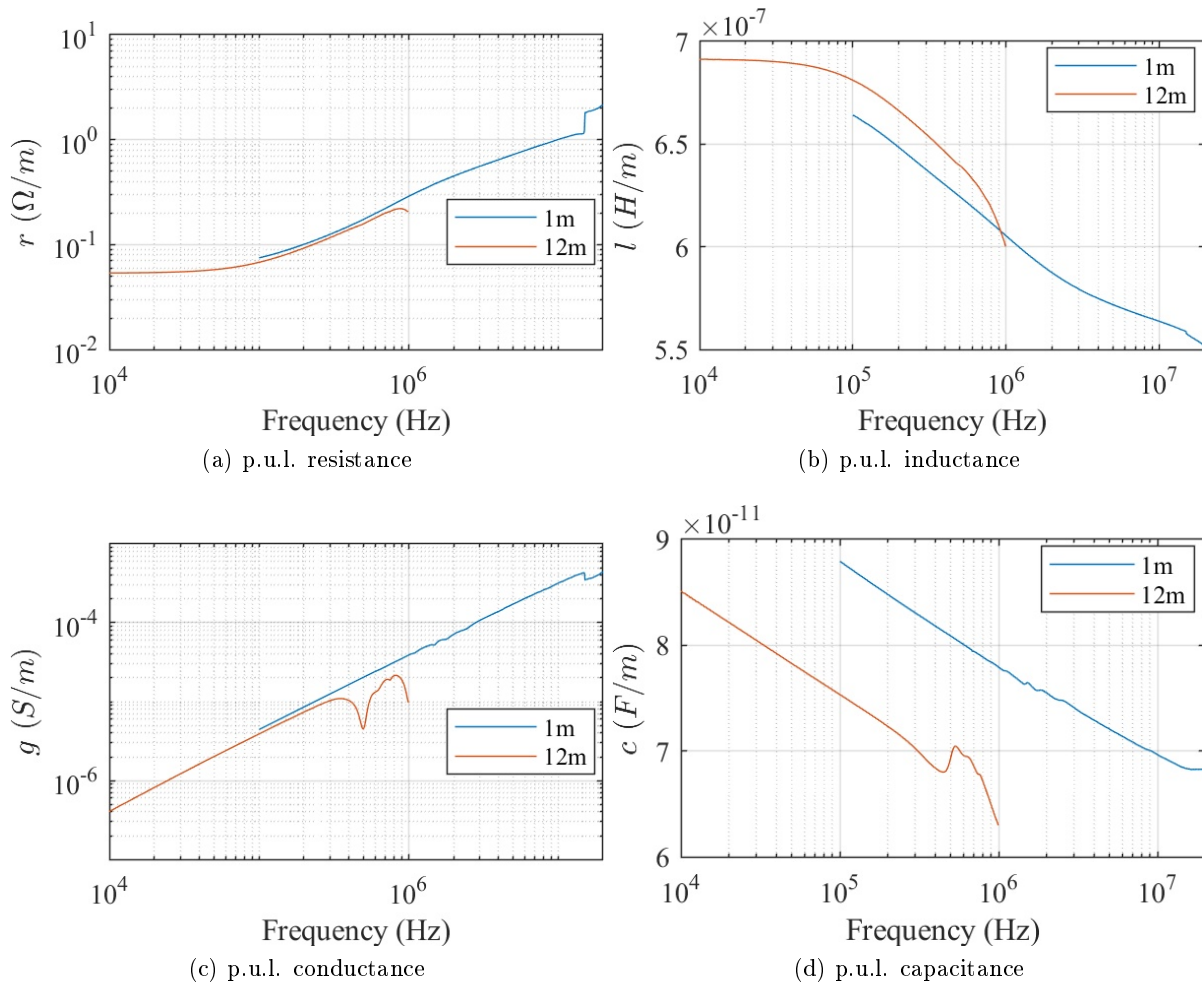
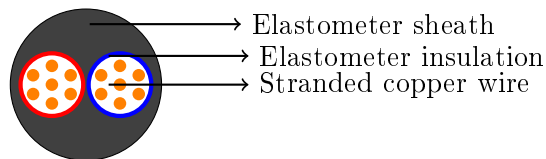
From the results presented in section 2.4.b, it is demonstrated that a self input impedance measurement of the  $1 \text{ m}$  long sample cable without balun yielded theoretical results closer to the validation experimental data than the parameter identification with balun. For this reason, in this specific case, the input impedance measurements without balun will be used to model this cable, as it has been proven that they are more precise. It is important to recall that the parameter identification input impedance measurements may contain significant errors if common mode circulates in the measurement circuit, and it has been proven in section 2.3.b-ii that the balun mitigates the common mode. Therefore, in the general case, the use of a balun is recommended.

In Fig. 2.28, the p.u.l. parameters of this cable obtained with the high frequency measurements of an  $1 \text{ m}$  long sample cable, without balun, are superposed with the parameters obtained with the low frequency measurements in a  $12 \text{ m}$  long sample cable. In this figure, it can be seen that the parameters from the two identification measurements do not coincide exactly, what will cause discontinuities in the wide band parameters of the cable. Also, for this cable, the frequency  $f_{lim} = 300 \text{ kHz}$  is the change frequency that will generate the smallest discontinuities between the low and high frequency parameter identification.

The parameters of the cable of section  $0.75 \text{ mm}^2$  are presented in Figs. 2.30 and 2.31 for a wide frequency band, using the frequency limit just defined.

The cable parameters obtained for a two-conductor cable of section  $2.5 \text{ mm}^2$ , its cross-section is presented by Fig. 2.29, are plotted in Fig. 2.32 and Fig. 2.33. The limit frequency chosen for the parameter identification of this cable is  $f_{lim} = 600 \text{ kHz}$ .

For both cables it can be seen that the propagation speed  $v$  increases with frequency, according

Figure 2.28 – Per-unit-length parameters of the  $0.75 \text{ mm}^2$  cableFigure 2.29 – Cross-section of the two-conductor  $2.5 \text{ mm}^2$  cable

to the theoretical behavior described in Section 2.2.b, but it does not seem to converge to a constant value.

The attenuation constant  $\alpha$  has a drastically different behavior. This is due to the fact that  $\alpha$  depends heavily on the loss-related parameters  $r$  and  $g$ , which change considerably with frequency. Indeed, this behavior is expected: the attenuation is a direct consequence of the cable losses. On the other hand, the propagation speed  $v$  depends principally on  $l$  and  $c$ , which have smaller variations with frequency.

The characteristic impedance in both cases has a small phase in the analyzed frequency-band, and its absolute value doesn't change drastically; both of these characteristics are in agreement with the theoretical prediction in 2.2.b



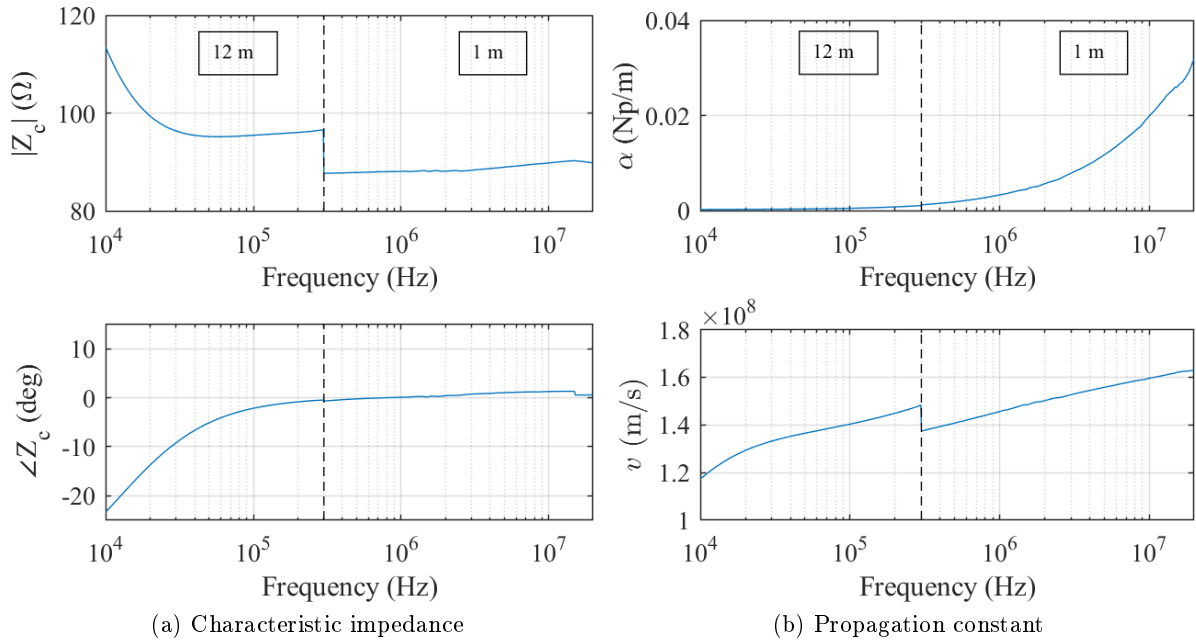


Figure 2.30 – Parameters of the cable of section  $0.75 \text{ mm}^2$

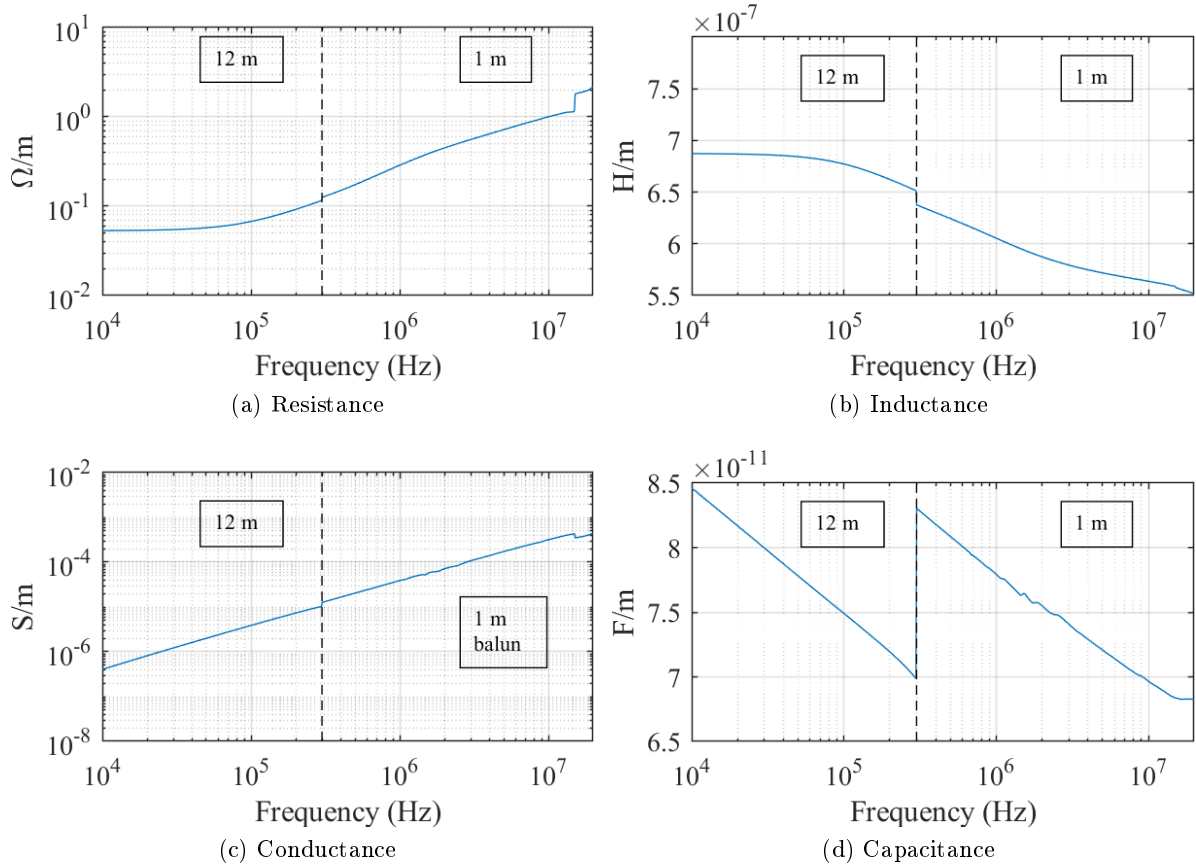


Figure 2.31 – Per-unit-length parameters of the cable of section  $0.75 \text{ mm}^2$

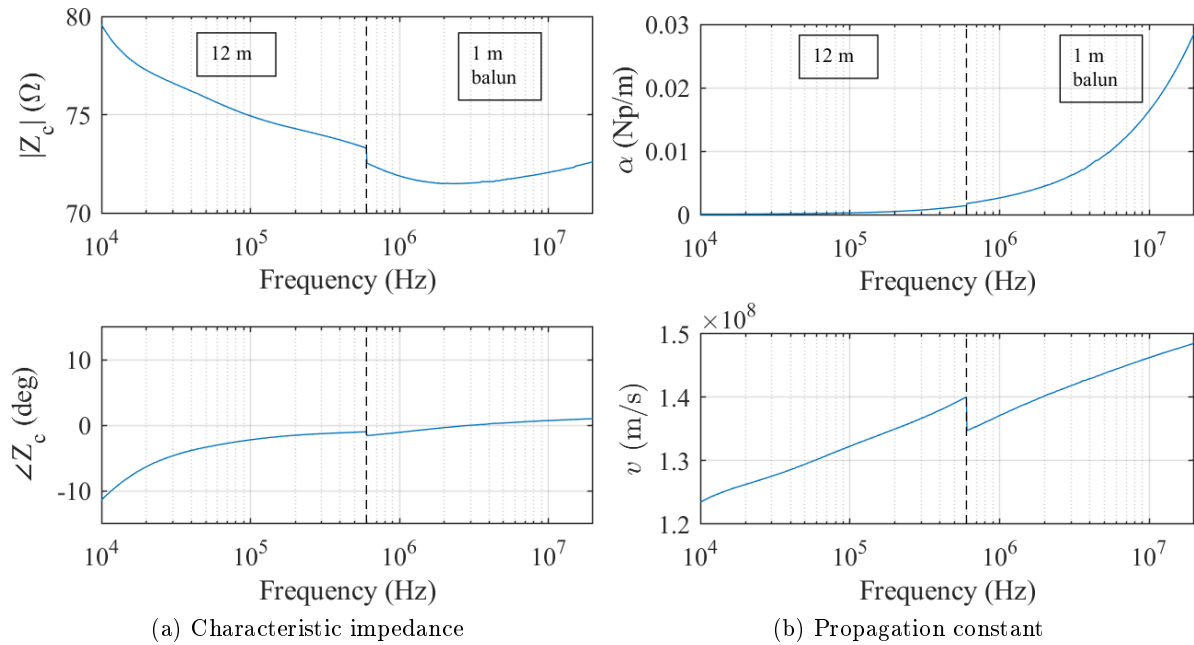


Figure 2.32 – Parameters of the cable of section  $2.5 \text{ mm}^2$

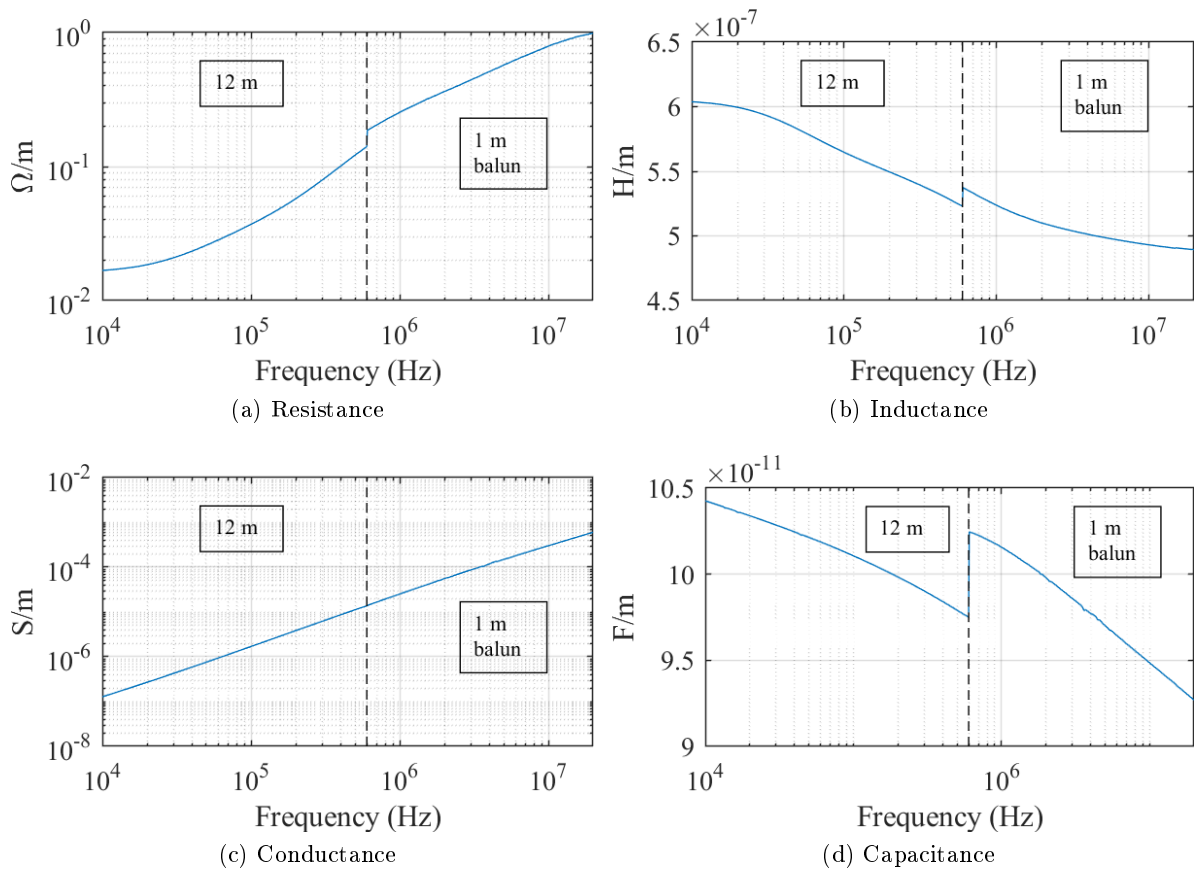


Figure 2.33 – Per-unit-length parameters of the cable of section  $2.5 \text{ mm}^2$

## 2.5 Numeric Analysis of Resonance Phenomena

As has been discussed in chapter 1, resonances on the building cables can be dangerous for the devices connected to its network. These resonances are trending to grow more dangerous with the advent of the wide band gap semiconductors technology, allowing lower switching delays and, as a consequence, harmonics of higher frequencies circulating in the building cabling.

The resonant behavior of a two-conductor cable was exemplified in section 2.4. To study this subject thoroughly, it is necessary to understand the resonance mechanism, and its conditions to occurrence. It is difficult to determine analytically the conditions under which resonances take place in lossy lines, as a consequence, qualitative and numerical analysis of the phenomena are developed in the next sections.

The next section, 2.5.a, describes the resonance of lossy lines short-circuited or open-ended, after that the resonance with a generic load  $Z_L$  connected to its extremity is studied in section 2.5.b. In section 2.5.c studies the difference between the transmission line resonance and the LC resonance of a model without propagation.

### 2.5.a Open-ended and short-circuited resonances

Consider the simplified schematics in Fig 2.34. In this first approach, we will study the resonant behavior of this cable for the cases where the load  $Z_L$  is either a short circuit (SC) or an open end (OC).

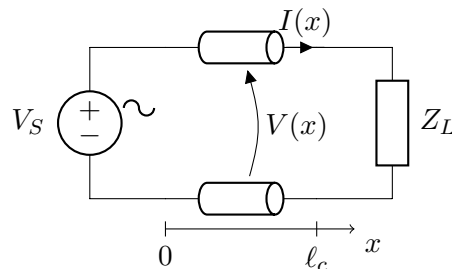


Figure 2.34 – Schematics for the resonance analysis

The resonance occurs because of the superposition of the traveling waves on the line, reflected on the line extremities. The propagating waves interfere constructively, thus amplifying the injected signal, if their frequency corresponds to one of the cable natural frequencies. With these frequencies, the line input impedance  $Z(0)$  assumes its minimum values.

The input impedances of the two-conductor transmission line for these cases is defined on (2.24), and repeated here for convenience:

$$Z_{SC} = Z_c \tanh(\ell_c \gamma) \quad (2.28)$$

$$Z_{OC} = Z_c \coth(\ell_c \gamma) \quad (2.29)$$

First, the short-circuited input impedance  $Z_{SC}$  is analyzed. The complex function “ $\tanh(c)$ ” has the roots  $c = jn\pi \forall n \in \mathbb{Z}$ . Therefore, the input impedance of a short-circuited line can only be zero for the lossless line case ( $\alpha = 0$ , where  $\gamma = \alpha + j\beta$ ), with  $\beta\ell_c = n\pi$ . This is true if the line is excited at the frequencies  $f_{SC}$  in (2.30a), in other words, when the line length is multiple

of half of a wavelength (2.30b).

$$f_{SC} = v \frac{n}{2\ell_c} \quad \forall n \in \mathbb{Z} \quad (2.30a)$$

$$\ell_c = n \frac{\lambda_{SC}}{2} \quad \forall n \in \mathbb{Z} \quad (2.30b)$$

For a lossy line,  $\alpha \neq 0$  and “ $\tanh(c)$ ” cannot be zero. However, its minima remain on the points of the complex plane where  $\Im\{c\} = jn\pi \quad \forall i \in \mathbb{Z}$ . Therefore, the resonance frequency of a lossy short-circuited line is the same as for the lossless line (2.30a).

The position of the voltage and current maxima on a short-circuited line varies with  $n$ . In Fig. 2.35 we plotted the voltage and current envelopes along an 11 m long line for if  $n = 1, 2, 3$ , using the parameters of the two-conductor cable of section  $2.5 \text{ mm}^2$  (cf. Fig. 2.33 for its parameters) and injecting a sinusoidal voltage of amplitude 1 V at the line input.

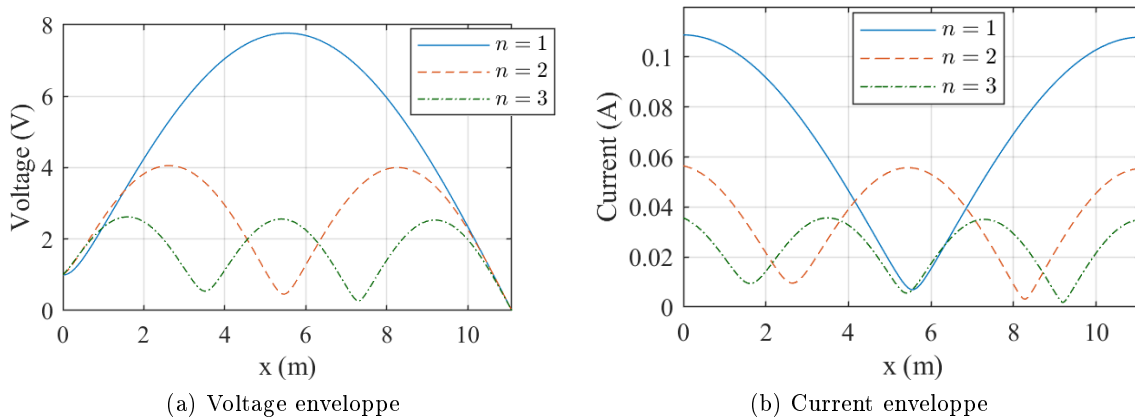


Figure 2.35 – Voltage and current envelopes of a short-circuited resonant line

Table 2.5 – Two-conductor  $2.5 \text{ mm}^2$  cable parameters, at the resonance frequencies of the short-circuited line (cf. Fig. 2.33)

$n$	$f$ (MHz)	$Z_c$ ( $\Omega$ )	$\gamma$ (1/m)
1	6.5	$71.8 + j0.64$	$0.012 + j0.28$
2	13.0	$72.2 + j1.06$	$0.020 + j0.56$
3	19.6	$72.6 + j1.28$	$0.028 + j0.83$

The current maxima take place in the line positions where the voltage is minimum, and vice-versa. That is easily explained with the energy conservation law: the instant power remains the same for any position  $x$ , except for the dissipation of Joule losses, and therefore the current must reach a minimum when the voltage amplification is maximum.

As the line is short-circuited, a current maximum will always take place at  $x = \ell_c$ . Also, the voltage at this extremity will always be  $V(\ell_c) = 0$ , a minimum. The voltage and current envelopes behave as sinusoidal functions, therefore their maxima take place  $\frac{\lambda}{4}$  away from their minima, as illustrated by Fig. 2.35. For the first harmonic  $n = 1$ ,  $\ell_c = \frac{\lambda}{2}$  and the maximum voltage amplification occurs  $\frac{\lambda}{4}$  away from the short-circuited extremity, at  $x = \frac{\ell_c}{2}$

Now, the open-ended input impedance  $Z_{OC}$  is analyzed. The complex function “ $\coth(c)$ ” has the real roots  $c = j\left(\frac{\pi}{2} + n\pi\right) \forall n \in \mathbb{Z}$ . Therefore, the input impedance of an open-ended line is null if  $\alpha = 0$  and  $\beta\ell_c = \frac{\pi}{2} + n\pi$ , what is true for lines excited at the frequencies  $f_{OC}$  in (2.31a), corresponding to the wavelength relation (2.31b).

$$f_{OC} = v \left( \frac{1}{4\ell_c} + \frac{n}{2\ell_c} \right) \forall n \in \mathbb{Z} \quad (2.31a)$$

$$\ell_c = \frac{\lambda}{4} + n\frac{\lambda}{2} \forall n \in \mathbb{Z} \quad (2.31b)$$

Again, for the lossy line ( $\alpha \neq 0$ ), the null impedance is not possible, but the minima of the function “ $\coth(c)$ ” remain on the points of the complex plane where  $\beta\ell_c = \frac{\pi}{2} + n\pi$ . Therefore, the natural frequency of a lossy open-ended line are the same as for the lossless case (2.31a).

The envelopes of the voltage and current along an 11 m long line are drawn for  $n = 1, 2, 3$  in Fig. 2.36, with the parameters of the two-conductor cable of section  $2.5 \text{ mm}^2$ . The maxima of the voltage envelope depend on the rang of the harmonic, but a voltage maxima it will surely occur at  $x = \ell_c$ , because  $I(\ell_c) = 0$ .

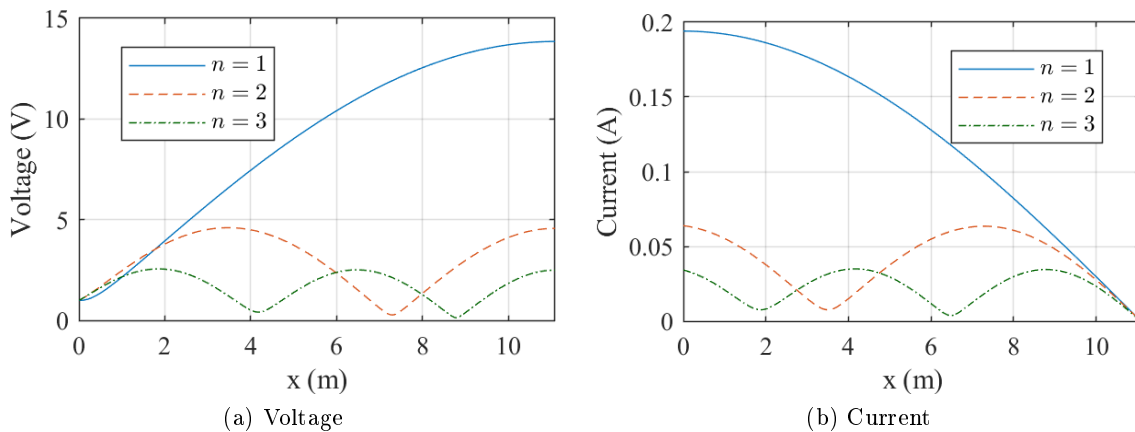


Figure 2.36 – Voltage and current envelopes of an open-ended resonant line

Table 2.6 – Two-conductor  $2.5 \text{ mm}^2$  cable parameters, at the resonance frequencies of the open-ended line (cf. Fig. 2.33)

$n$	$f$ (MHz)	$Z_c$ ( $\Omega$ )	$\gamma$ (1/m)
1	3.2	$71.54 + j0.059$	$0.0065 + j0.14$
2	9.3	$72.04 + j0.89$	$0.016 + j0.41$
3	16	$72.42 + j1.17$	$0.024 + j0.68$

By definition, the maxima of function “ $\tanh(c)$ ” occur at the same points of the minima of the function “ $\coth(c)$ ”, and vice-versa. The same behavior is observed between the short-circuited and open-ended line input impedances: for the frequencies where the open-ended line resonates, the short-circuited line will be at its maximum, i.e., an anti-resonance; and vice-versa.

The input impedance of a resonant line can be derived from (2.28) and (2.29). For example,

the short-circuited input impedance  $Z_{SC}$  at the cable natural frequencies is:

$$Z_{SC} = Z_c \tanh(\alpha l_c + jn\pi) = Z_c \tanh(\alpha l_c)$$

If  $\alpha l_c$  is small, the input impedance of the short-circuited resonant line can be approximated by:

$$Z_{res} = Z_c \alpha l_c \quad (2.32)$$

With a similar approach it can be deduced that the input impedance of the open-ended resonant line is also  $Z_{res}$  (2.32).

The maximum voltage amplification can be calculated for both cases:

$$\begin{aligned} V\left(\ell_c, \frac{v}{4\ell_c}\right)|_{Z_L \rightarrow \infty} &= V_s \cosh(\alpha l_c + j\frac{\pi}{2}) + \frac{V_s}{Z_c \alpha l_c} Z_c \sinh(\alpha l_c + j\frac{\pi}{2}) = \\ &= V_s j \left( \sinh(\alpha l_c) + \frac{1}{\alpha l_c} \cosh(\alpha l_c) \right) \end{aligned} \quad (2.33a)$$

$$\begin{aligned} V\left(\ell_c, \frac{v}{2\ell_c}\right)|_{Z_L=0} &= V_s \cosh(\alpha l_c + j\pi) + \frac{V_s}{Z_c \alpha l_c} Z_c \sinh(\alpha l_c + j\pi) = \\ &= -V_s \left( \cosh(\alpha l_c) + \frac{1}{\alpha l_c} \sinh(\alpha l_c) \right) \end{aligned} \quad (2.33b)$$

The dependence of the resonance amplification on the cable losses introduced in section 1.2 can now be confirmed. By applying  $\alpha = 0$  in these expressions, it can be shown that the voltage amplitude tends to infinity for lossless lines. Moreover, Fig. 2.37 shows that by computationally reducing the attenuation constant  $\alpha$  of the two-conductor cable of section  $2.5 \text{ mm}^2$  to  $\alpha/2$  and  $\alpha/5$ , with the cable short circuited, the resonance amplitude is higher.

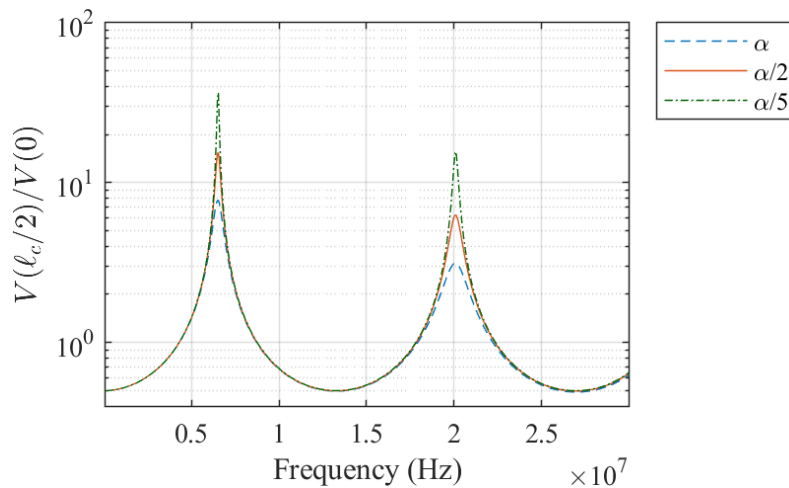


Figure 2.37 – Voltage envelope in function of frequency for the short-circuited two-conductor cable of section  $2.5 \text{ mm}^2$ , with variations on the attenuation constant  $\alpha$

The fact that the losses reduce the resonance amplification explain the different amplitudes observed in Figs. 2.35 and 2.36. As aforementioned, the losses of the cable increase with frequency, due to skin effect and the non-ideal behavior of the conductor insulation. Therefore, the amplitude of the first harmonic resonances ( $n = 1$ ) are higher because the losses at the first resonance frequency are lower.

For the same reason, the amplification of the first resonance for the open-ended cable is higher

than the amplification for the first resonance in a short-circuited cable. Indeed, for the two-conductor cable of section  $2.5\text{ mm}^2$ , the first open-ended resonance occurs at  $f_{OC} = 3,2\text{ MHz}$ , while the first short-circuited resonance occurs at  $f_{SC} = 6,5\text{ MHz}$ ; these values will be recalled in the next section

### 2.5.b Resonance in function of the load

To analyze the cable resonance in function of the load impedance, the same system described in the previous section, repeated in Fig. 2.38 for convenience, was studied. The cable is  $11\text{ m}$  long, having the parameters of the two-conductor cable of section  $2.5\text{ mm}^2$  plotted in Fig. 2.33. The source is considered ideal, i.e., with null output impedance, because it represents the worst case for the resonance phenomena: the traveling waves in the cable are completely reflected at  $x = 0$ .

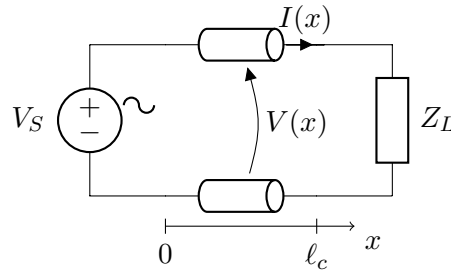


Figure 2.38 – Schematics for the resonance analysis

The resonance behavior of the system in Fig. 2.38 is analyzed with a numerical approach. To that end, multiple simulations of this system were performed, each for a different load impedance  $Z_L$ . The load is defined as  $Z_L = A + jB$ , and has logarithmic scaled values in the ranges listed in table 2.7. In this table are also listed the range of values in which the frequency of the source  $V_S$  was varied, also logarithmic scaled, as well as the positions  $x$  to which the variables were calculated.

Table 2.7 – Range of values used in the numerical analysis of the resonance

Variable	Range	Number of points	Scaling
$A$	$[0, 100]\text{ k}\Omega$	402	log
$B$	$[-100, 100]\text{ k}\Omega$	402	log
$f$	$[0.1, 10]\text{ MHz}$	5000	log
$x$	$[0, 11]\text{ m}$	23	linear

The maximum voltage  $V_{max}$  for each pair  $(A, B)$  among the different combinations of  $f$  and  $x$  was stored, along with the resonance frequency  $f_{max}$  that originated it, and the position  $x_{max}$  where it occurred.

The results are presented in Figs. 2.39 to 2.41. In the first figure (2.39), the maximum voltage  $V_{max}$  is plotted over the  $AxB$  plane. In Fig. 2.40, the frequency to which the maximum voltage occurred  $f_{max}$  is plotted. In Fig. 2.41, the position  $x_{max}$  in which the maximum voltage  $V_{max}$  takes place, for a line excited at frequency  $f_{max}$ , is plotted.

The figures were plotted in logarithmic scale. To make the negative part of the imaginary part  $B$  visible, the figures were split in two: One with the positive values of  $B$ , and other with

its negative values.

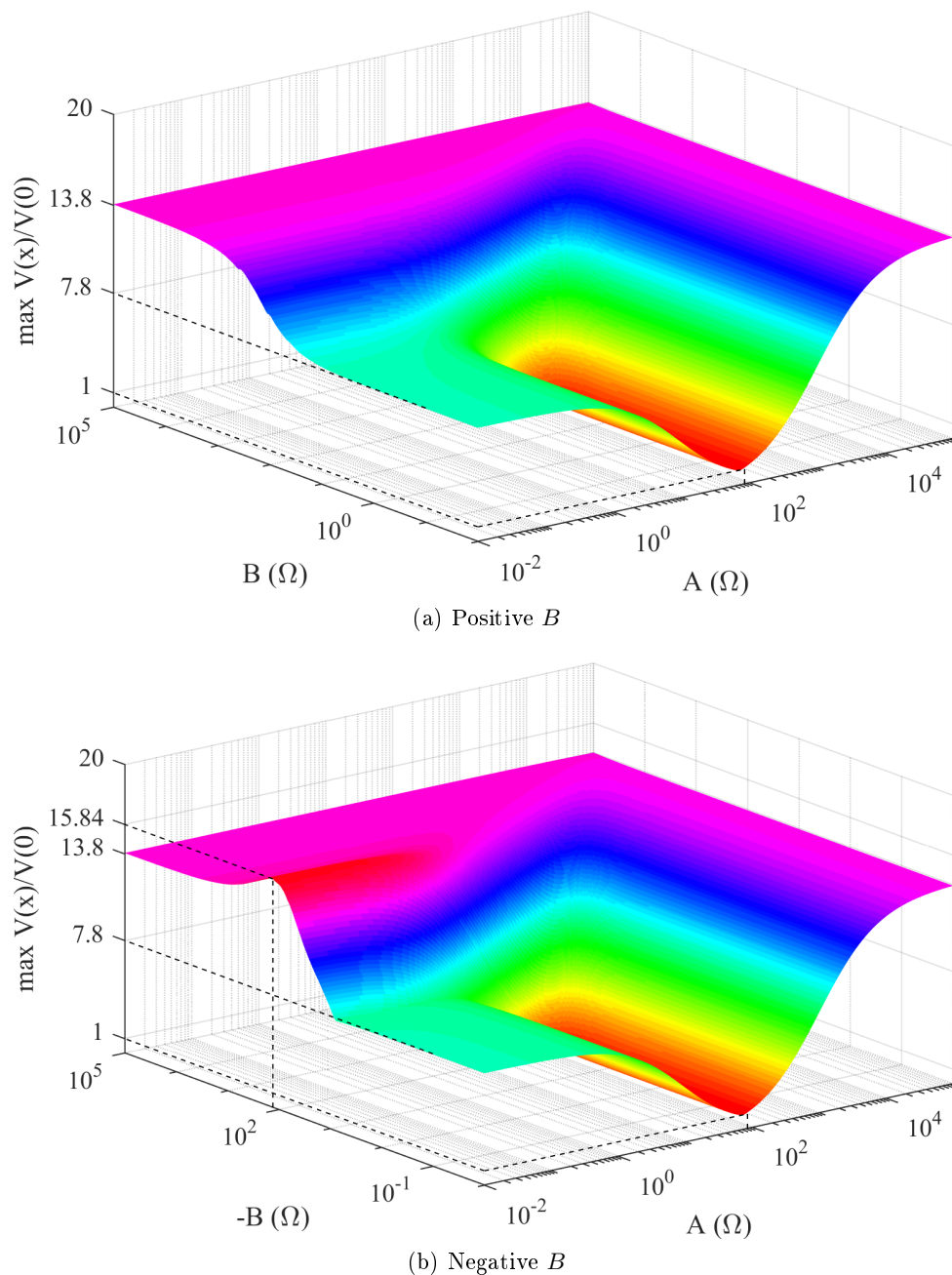


Figure 2.39 – Maximum voltage in function of  $Z_L = A + jB$ , positive and negative parts of  $B$

The surface in Fig. 2.39 is smooth, tending to 1 where  $A = |Z_c|$  and the absolute value of  $B$  is low. Indeed, if  $Z_L = Z_c$ , the termination of the line is matched, and as a consequence there are no wave reflections nor resonance amplifications.

Furthermore, the voltage amplification increase for high values of  $A$  and  $B$ , i.e., when  $Z_L$  tends to an open circuit. It is interesting to note that the maximum amplification occurs for a specific value:  $B = -130\ \Omega$  and small values of  $A$ , i.e., a purely capacitive load.

In Fig. 2.40, the frequencies for which the maxima in Fig. 2.39 occurs are plotted. It shows that for low values of  $A$  and  $B$  the resonance frequency is around  $6.5\text{ MHz}$ , the resonance



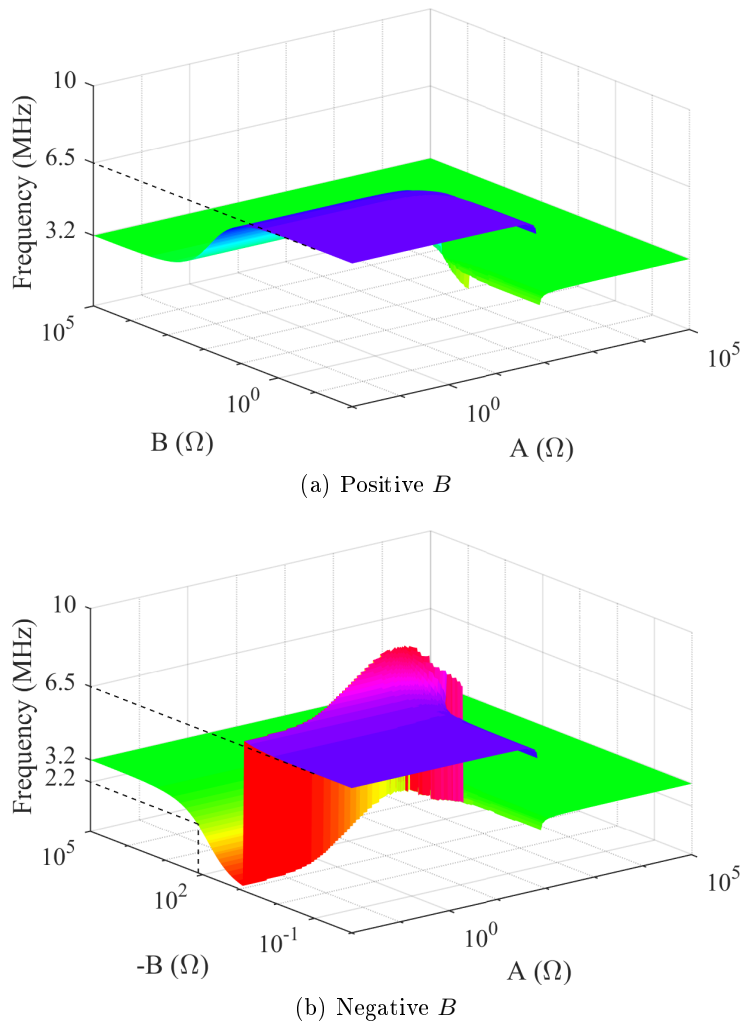


Figure 2.40 – Resonance frequency in function of  $Z_L = A + jB$ , positive and negative parts of  $B$

frequency of the short-circuited line. For high values of  $A$  and  $B$ , the resonance frequency drops to  $3.2\text{ MHz}$ , the open circuit resonance frequency. This explains the higher voltage amplification for higher  $A$  and  $B$ ; as the losses are smaller for  $3.2\text{ MHz}$  than for  $6.5\text{ MHz}$ .

For low values of  $B$  a discontinuity on the frequency surface is visible at  $A = |Z_c|$ . For this region the line is matched, and the resonance frequency is not defined.

The fall seen in the negative portion of  $B$ , while  $|B|$  increases, is a natural behavior of the line. It will be further addressed below.

In Fig. 2.41, the position  $x_{max}$  along the line where the maximum voltage occurs is plotted over the  $A \times B$  plane. The same tendency of the previous surfaces is seen here: for low values of  $A$  and  $B$  the resonance takes place at the middle of the line, the same position as for the short-circuited line resonance. Meanwhile, for high values of  $A$  and  $B$  the maximum voltage is at the end of the line, as for the open-ended line case.

The same discontinuity observed in Fig. 2.40 at  $Z_L = Z_c$  is present in this surface, because without resonance amplification, the position of maximum voltage is not defined.

The fall on the negative  $B$  plane for small  $A$  is also present here, as it was on the frequency surface, and can be better explained now. The rupture happens in the point where the ampli-

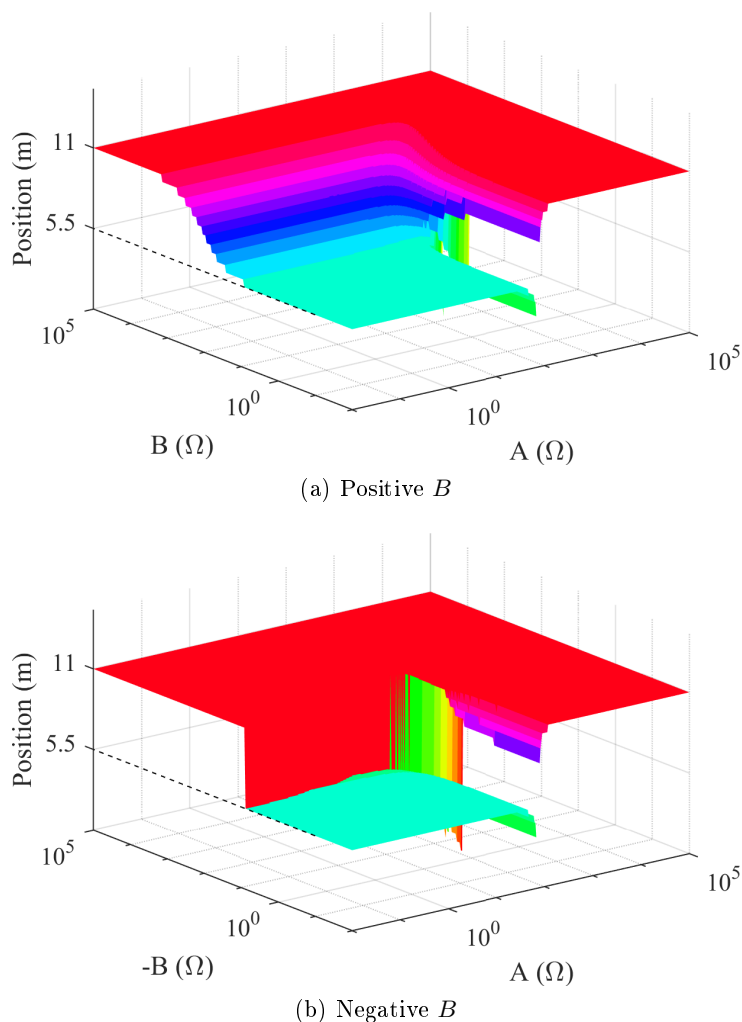


Figure 2.41 – Position of the maximum voltage in function of  $Z_L = A + jB$ , positive and negative parts of  $B$

fications at the end of the cable, which occur for lower frequencies, become less important than the amplifications taking place around the middle of the cable, at  $6\text{ MHz}$ . The low frequencies appearing just before the discontinuity correspond to wavelengths smaller than  $\lambda < 4\ell_c$ , and the voltage envelope doesn't assume its maximum value within the cable length. That is the reason why the maximal amplification doesn't take place for the lowest frequency: the wavelengths are too long in this frequency band.

The ensemble of the figures 2.39, 2.40 and 2.41 will be henceforth denominated “resonance surface response”.

In the two following sections are provided examples on how to extract the desired information from these surfaces. In 2.5.b-i the characterization of the resonant behavior of a cable for a given load is described. In section 2.5.b-ii a load is chosen to give the desired resonant behavior in a long cable. Other interesting analysis using the resonance surface response are performed in appendix C, where the surfaces are calculated for different types of cables, and for different cable lengths.

**2.5.b-i Characterizing the resonance behavior for a given load**

Using these surfaces the resonance frequency for a given load  $Z_L$  can be easily characterized, i.e., the frequency(s), the voltage amplification, and its position can be determined. For example, consider that the load in Fig 2.42 is connected at the extremity of the  $2.5\text{ mm}^2$  two-conductor cable.

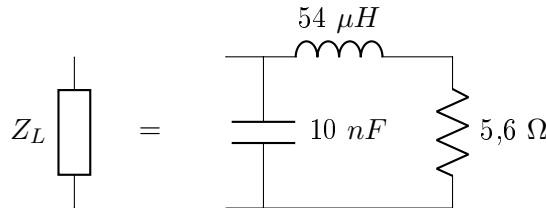


Figure 2.42 – The given RLC load

To characterize the cable resonance, first the evolution of the load with the frequency  $Z_L(f)$  must be plotted over the resonance frequency surface, as is done in Fig. 2.43.

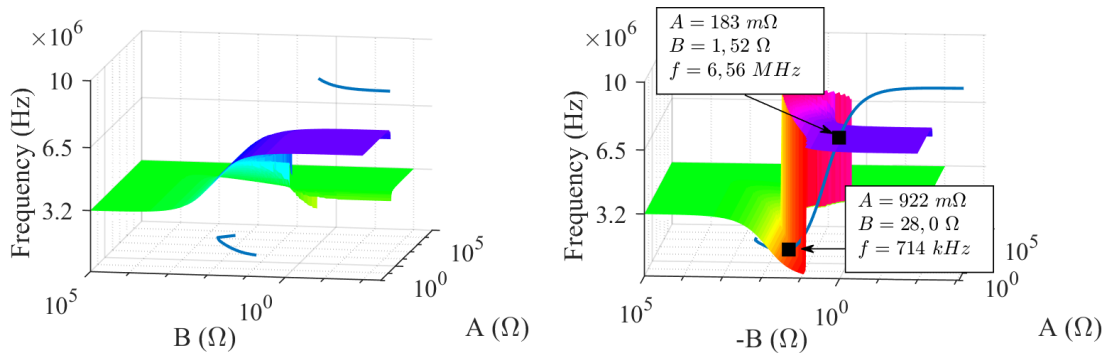


Figure 2.43 – The intersection of the load impedance and the resonance frequency surface

There are two intersections between  $Z_L(f)$  and the resonance frequency surface, what means that resonance will occur at two different frequencies, one at  $714\text{ kHz}$  and the other at  $6.56\text{ MHz}$ .

To determine the voltage amplification and its position for each of the resonances, the  $(A, B)$  pairs of the two intersections must be located in the voltage amplification surface and the position surface. This is done in Fig. 2.44

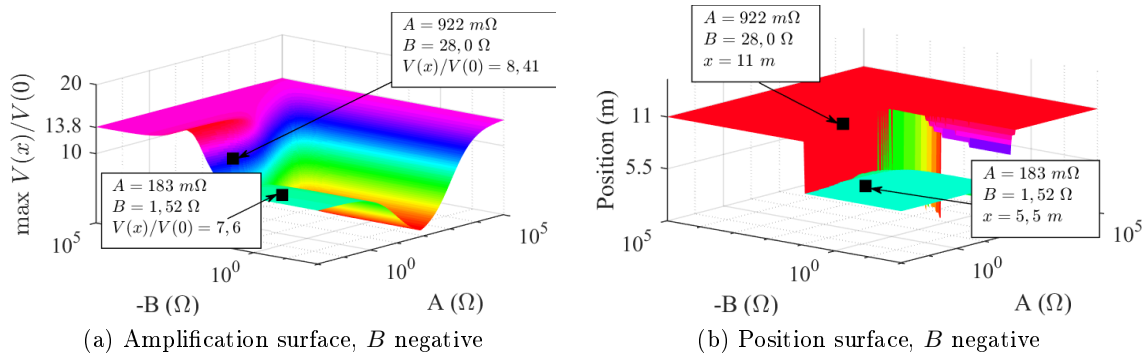


Figure 2.44 – Voltage amplifications and positions corresponding to the two intersections

The characteristics of the two detected resonances are resumed in table 2.8.

Table 2.8 – Characteristics of the predicted resonances

Resonance frequency	714 kHz	6.56 MHz
Amplification of the input voltage (single harmonic)	8.4	7.6
Maximal amplification position	$\ell_c$	$\ell_c/2$

**2.5.b-ii Choose a load in function of the resonance behavior**

On this second example of use of the resonance surfaces, a load will be chosen in function of a desired resonance behavior. We want to determine a practical load that would allow the biggest voltage amplification due to resonance. The point of maximum amplification is tagged in Fig 2.45.

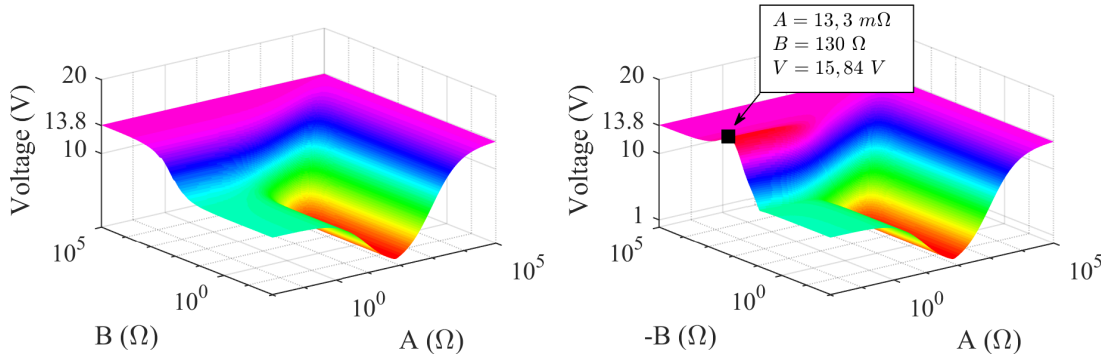


Figure 2.45 – The maximum voltage amplification possible due to resonance phenomena

The impedance value to which the desired voltage amplification takes place is  $Z_L = (0.0133 - j130.5)\Omega$ . This choice was done for the biggest real part  $A$  possible, without considerably reducing the maximal amplification.

Such a load can be represented by the series association of a resistor and a capacitor, as shown in Fig. 2.46. This configuration was chosen so the capacitor losses are represented by the resistance  $R_L$ .

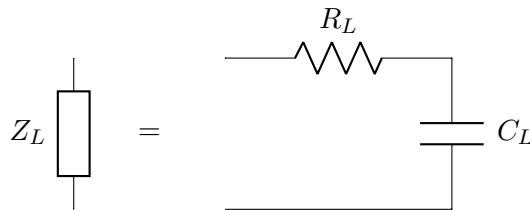


Figure 2.46 – A possible load for the desired voltage amplification

To determine the values of load components, the frequency in which the load must assume the desired impedance value must be known. This information is extracted from Fig. 2.47a.

The RC series association must assume the value  $Z_L = (0.0133 - j130.5)\Omega$  at 2.154 MHz.

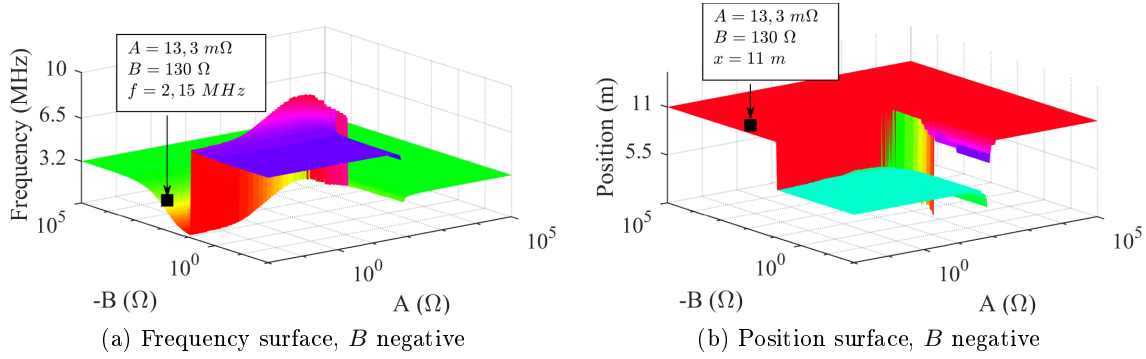


Figure 2.47 – The resonance frequency and maximum amplification position for the maximum amplification possible

That gives the following values for the load elements:

$$R_L < 13,3m\Omega$$

$$C_L = 566,2pF$$

In a practical case, it would be difficult to have a series resistance  $R_L$  as small as required, principally considering the scope of this work, where the load represents a device plugged somewhere in the building. Therefore, it is quite unlikely that the maximal voltage amplification will take place in a cable on an industrial cabling network.

### 2.5.c LC resonance versus transmission-line resonance

It is interesting to distinguish the transmission-line resonances due to propagation of waves in the line from the simpler LC-circuit resonance, which may also take place between a long cable and a reactive load.

To that end, consider the simplified transmission line model in figure 2.48, where the line is represented with only one cell. This representation is valid while the cable length is small when compared to the wavelength, i.e., the line is electrically short, whereas the transmission-line model is valid for any frequency.

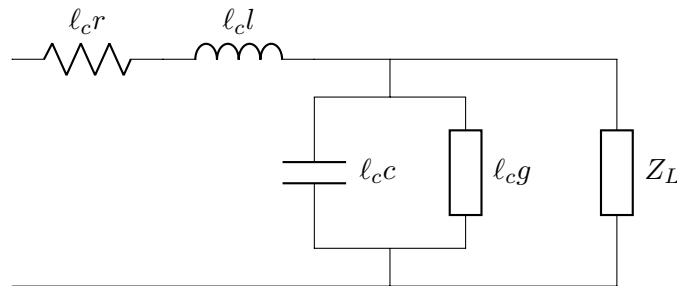


Figure 2.48 – Representation of an electrically short line, with load  $Z_L$

The case of a 5 m long cable is studied, with the load represented in Fig. 2.49 connected to the line extremity. Suppose that the cable parameters are fixed with the frequency, with the

following values:

$$\begin{aligned} r &= 0,8\Omega/m \\ l &= 0,57\mu H/m \\ g &= 213\mu S/m \\ c &= 73pF/m \end{aligned}$$

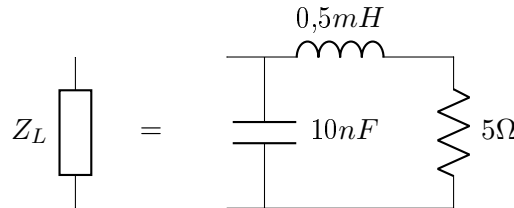


Figure 2.49 – The chosen load  $Z_L$

The input impedance of this line can be calculated, using the short line model, with:

$$Z_{short} = r\ell_c + j\omega l\ell_c + \frac{Z_L}{Z_L(g\ell_c + j\omega c\ell_c) + 1} \quad (2.34)$$

On the other hand, the input impedance of the line can be calculated for a large frequency band using the transmission line input impedance expression (2.23), repeated here for convenience.

$$Z(0) = Z_c \frac{Z_L + Z_c \tanh(\ell_c \gamma)}{Z_c + Z_L \tanh(\ell_c \gamma)} \quad (2.35)$$

The impedances calculated with both expressions (2.35) and (2.34) are plotted in Fig. 2.50. We can see that the two input impedance agree up to roughly  $2.5\text{ MHz}$ . At  $3\text{ MHz}$  the wavelength satisfies  $\lambda/10 \approx \ell_c$ . Before this limiting frequency, one resonance and one anti-resonance were correctly predicted by the short line model. This can be considered a simple LC circuit resonance, as a model that does not take the wave propagation into account can predict it. On the other hand, the resonances present on  $Z(0)$  for frequencies higher than  $3\text{ MHz}$  can only be predicted by the complete model, being caused by the wave propagation on the transmission-line.

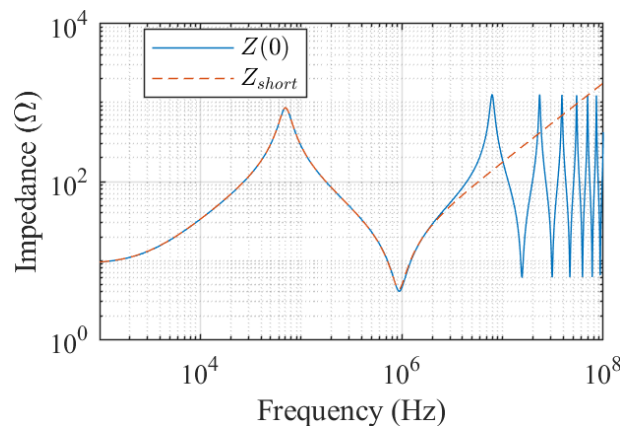


Figure 2.50 – Input impedance of the line under study

From Fig. 2.50 it can be concluded that even if the first resonance of a transmission line

connected to an LC load is predicted simply by circuit theory, the long transmission line model, with distributed parameters, is necessary to predict the complete resonance behavior of a cable.

In the case of open-ended and short-circuited cable the first resonance is not well represented by the short cable model. The input impedance of the open-ended cable calculated with expressions (2.35) and (2.34) is plotted in Fig. 2.51 as an example.

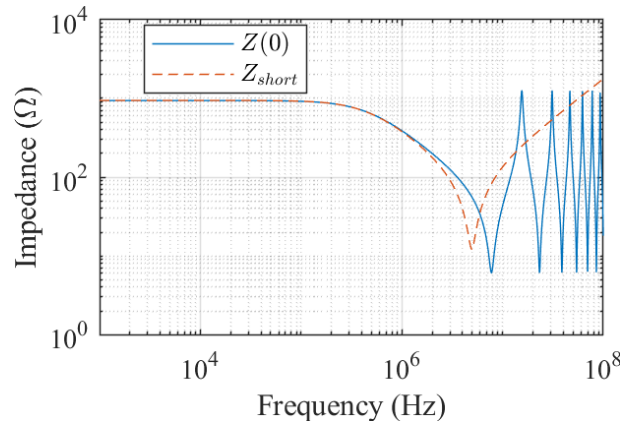


Figure 2.51 – Input impedance of the open-ended line

In conclusion, For a transmission line connected to an LC load the short line model, represented by the schematic in Fig. 2.48, can predict only the first resonance frequency of a system. If the line is open-ended or short-circuited, the short line model does not predict any of the resonances.

## 2.6 Conclusion

In this chapter the frequency domain model of transmission lines has been used for two-conductor applications, and frequency-domain simulation tool was built attending the demands described in chapter 1. The simulation tool is able to model a cable network where the conductors are equally spaced from each other. The cable parameters are experimentally identified with an impedance analyzer. The frequency band is only limited by the experimental parameter identification, and goes from DC up to 30 MHz with the equipment available during this work. The frequency domain simulation tool has been validated with experimental setups.

The simulated model meets the requirements listed in section 1.3. The transmission line model is length-scalable and models wave propagation and resonance. The cable parameter experimental identification with the impedance analyzer provides accurate parameters on the desired frequency-band. The frequency domain solution allows a computationally efficient simulation and an accurate representation of the cable losses.

The model predicts accurately the resonance frequencies, the voltage and current amplifications they may cause, and the position where the amplification take place in function of the load connected to the cable extremity. It was used to perform a numerical analysis of the resonance behavior in a given cable, what can be useful for design purposes.

The single cable model defined in section 2.2.a can be concatenated to model the hypothetical radial network defined in the introduction of this chapter.

## Chapter 3

---

# Multiconductor cable frequency domain model

### CONTENTS

---

3.1	INTRODUCTION . . . . .	52
3.2	MULTICONDUCTOR TRANSMISSION LINE MODEL . . . . .	52
3.2.a	General solution of the MTL telegrapher equations . . . . .	54
3.2.b	Solution with modal decomposition . . . . .	57
3.2.c	The frequency domain simulation tool . . . . .	58
3.3	MULTICONDUCTOR CABLE PARAMETER IDENTIFICATION . . . . .	64
3.4	FREQUENCY-DOMAIN MODEL EXPERIMENTAL VALIDATION . . . . .	66
3.4.a	Resonance-based experiment validation . . . . .	67
3.4.b	Input Impedance Validation . . . . .	69
3.4.c	Examples of cable parameter identification . . . . .	71
3.5	EXTENSION OF RESONANCE SURFACES FOR MULTICONDUCTOR CABLES . . . . .	74
3.5.a	Conditions for a three-conductor line to be balanced . . . . .	75
3.5.b	Numerical analysis of the resonance in a three-conductor balanced system . . . . .	77
3.5.c	Difficulties to generalize the resonance surfaces to any load matrix . . . . .	84
3.6	CONCLUSION . . . . .	85

---

### Abstract

*This chapter generalizes the simulation tool for two-conductor cables in the frequency domain developed in chapter 2 to multiconductor cables. The multiconductor cable parameters are identified experimentally, with an impedance analyzer-based identification method. The frequency band of the simulator goes from DC up to 30 MHz, limited by the equipment available for the experimental parameter assessment. The parameter identification, as well as the frequency domain simulation tool, are validated experimentally. The common and differential mode decomposition is studied, the conditions to the decoupling of the modes are demonstrated. The resonance of multiconductor transmission lines is studied, its dependence on cables losses is highlighted.*



### 3.1 Introduction

This chapter studies the multiconductor transmission-lines (MTL) model, aiming to generalize the frequency domain simulation tool developed for two-conductor cables in the previous chapter to multiconductor cables. The goal of this tool is to model of the propagation of stray current and voltages in buildings, up to the medium frequency band (tens of  $MHz$ ).

The simulation tool will model a hypothetical radial network, supposed to have  $n + 1$  conductors with the distance between each other constant along the line. As mentioned in the previous chapter, it cannot be guaranteed that the distance between the conductors is constant along line in an industrial cabling network. However, the model based on this hypothesis is still a good approximation of the cabling in a building, because the distance between the wires does not vary drastically.

Again, the frequency domain simulation tool must be able to correctly predict the resonance-due voltage and current amplifications on the cables, as well as the resonance frequency and position of the maximal amplification along the cable on the hypothetical radial network. To that end, the multiconductor cable parameters will be experimentally identified, as done in the previous chapter. The experimental parameter identification allows an accurate determination of the cable losses, a determinant factor of the amplitude of voltage and current resonances (2.5.a).

Section 3.2 introduces the multiconductor transmission line theory, and defines the structure of the frequency domain simulation tool under construction. Section 3.3 discusses the experimental identification of multiconductor transmission line parameters. Section 3.4 validates experimentally the frequency domain simulation tool developed in section 3.2, using the cable parameters obtained with the identification method proposed in section 3.3. Section 3.5 computes the resonance on multiconductor transmission lines.

### 3.2 Multiconductor transmission line model

The transmission line theory presented in the previous chapter for the two-conductor line case can be extended to the  $n + 1$  conductors case. This theory is known as multiconductor transmission line (MTL) model.

The MTL equations must take into account the voltages and currents in each of the conductors (Fig. 3.1), and are usually represented in matrix form. This form was first described by Louis Pipes in 1937 [37]. The telegrapher equations in matrix form are presented in (3.1). In this document, the matrices and vectors will be highlighted in bold.

$$\frac{\partial \mathbf{V}(x)}{\partial x} = -\mathbf{z}\mathbf{I}(x) \quad (3.1a)$$

$$\frac{\partial \mathbf{I}(x)}{\partial x} = -\mathbf{y}\mathbf{V}(x) \quad (3.1b)$$

In (3.1),  $\mathbf{V}(x)$  and  $\mathbf{I}(x)$  are the vectors of voltages and currents (3.2) along the line, respectively. The terms  $\mathbf{z}$  and  $\mathbf{y}$  are the per-unit-length (p.u.l) impedance and admittance matrices, respectively. They are defined in (3.3) [33], according to the p.u.l. parameters in Fig. 3.2. Again,  $j$  is the complex unit and  $\omega$  is the angular frequency,  $x$  is the axis parallel to the line.

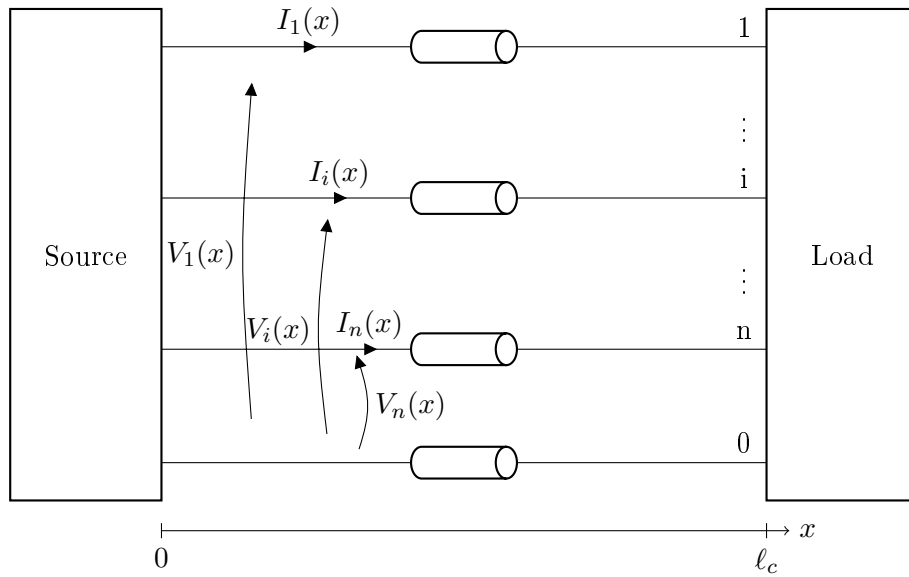


Figure 3.1 – Multiconductor transmission line, variables definition

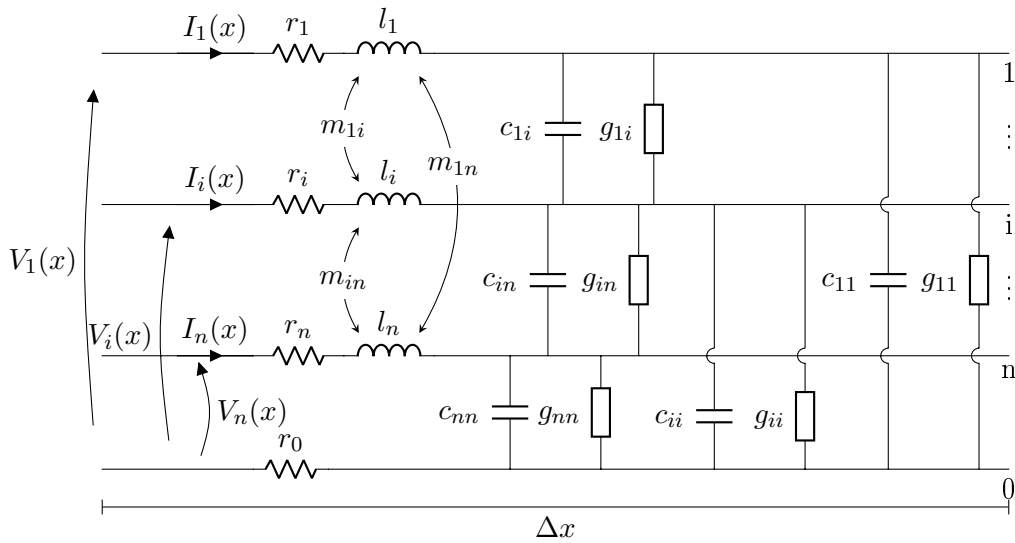


Figure 3.2 – Elementary cell of multiconductor transmission lines, with its p.u.l. parameters

$$\mathbf{V}(x) = \begin{pmatrix} V_1(x) \\ \vdots \\ V_i(x) \\ \vdots \\ V_n(x) \end{pmatrix} \quad \mathbf{I}(x) = \begin{pmatrix} I_1(x) \\ \vdots \\ I_i(x) \\ \vdots \\ I_n(x) \end{pmatrix} \quad (3.2)$$

$$\mathbf{z} = \mathbf{r} + j\omega\mathbf{l} \quad (3.3a)$$

$$\mathbf{y} = \mathbf{g} + j\omega\mathbf{c} \quad (3.3b)$$

$$\mathbf{r} = \begin{pmatrix} r_1 + r_0 & r_0 & \cdots & r_0 \\ r_0 & r_2 + r_0 & \cdots & r_0 \\ \vdots & \vdots & \ddots & \vdots \\ r_0 & r_0 & \cdots & r_n + r_0 \end{pmatrix} \quad (3.4a)$$

$$\mathbf{l} = \begin{pmatrix} l_1 & m_{12} & \cdots & m_{1n} \\ m_{12} & l_2 & \cdots & m_{2n} \\ \vdots & \vdots & \ddots & \vdots \\ m_{1n} & m_{2n} & \cdots & l_n \end{pmatrix} \quad (3.4b)$$

$$\mathbf{g} = \begin{pmatrix} \sum_{k=1}^n g_{1k} & -g_{12} & \cdots & -g_{1n} \\ -g_{12} & \sum_{k=1}^n g_{2k} & \cdots & -g_{2n} \\ \vdots & \vdots & \ddots & \vdots \\ -g_{1n} & -g_{2n} & \cdots & \sum_{k=1}^n g_{nk} \end{pmatrix} \quad (3.4c)$$

$$\mathbf{c} = \begin{pmatrix} \sum_{k=1}^n c_{1k} & -c_{12} & \cdots & -c_{1n} \\ -c_{12} & \sum_{k=1}^n c_{2k} & \cdots & -c_{2n} \\ \vdots & \vdots & \ddots & \vdots \\ -c_{1n} & -c_{2n} & \cdots & \sum_{k=1}^n c_{nk} \end{pmatrix} \quad (3.4d)$$

Matrices  $\mathbf{r}$ ,  $\mathbf{l}$ ,  $\mathbf{g}$  and  $\mathbf{c}$  are symmetric by definition, consequently so are  $\mathbf{z}$  and  $\mathbf{y}$ .

The inductive elements in Fig. 3.2 are relative to the loop between the concerned active conductor (1 to  $n$ ) and the reference conductor (0). Each self inductance  $l_{ii}$  represents the total inductance of the loop formed by the active conductor  $i$  and the reference conductor, while each mutual inductance  $m_{ij}$  represents the mutual inductance between the loops formed by the  $i^{th}$  conductor and the reference and the  $j^{th}$  conductor and the reference. Indeed, the drawback of this model is that it is not able to completely represent the magnetic effect of a parasitic current flowing only in the reference conductor, if the current is generated outside of the system to which the cable is connected.

Equations (3.1) must be decoupled to be solved, and their decoupling can be performed in different forms. Two decoupling methods are described in the two following subsections: The general solution resumed in [33] in section 3.2.a, and the modal decomposition of the line in section 3.2.b. Both of these methods will be used further down in this document.

### 3.2.a General solution of the MTL telegrapher equations

The telegrapher equation can be rewritten on second order differential equations as follows:

$$\frac{\partial^2 \mathbf{V}(x)}{\partial x^2} = \mathbf{z}\mathbf{y}\mathbf{V}(x) \quad (3.5a)$$

$$\frac{\partial^2 \mathbf{I}(x)}{\partial x^2} = \mathbf{y}\mathbf{z}\mathbf{I}(x) \quad (3.5b)$$

To decouple these equations, the matrices  $\mathbf{z}\mathbf{y}$  and  $\mathbf{y}\mathbf{z}$  must be diagonalized. Let  $\mathbf{T}_\mathbf{I}$  be the matrix composed by the eigenvectors of  $\mathbf{y}\mathbf{z}$  and  $\mathbf{T}_\mathbf{V}$  be the matrix composed of the eigenvectors

of  $\mathbf{zy}$ . Because  $\mathbf{z}$  and  $\mathbf{y}$  are symmetric, we have  $(\mathbf{zy})^T = \mathbf{y}^T \mathbf{z}^T = \mathbf{yz}$ , therefore the eigenvalues of  $\mathbf{yz}$  and  $\mathbf{zy}$  are the same and can be obtained with (3.6)

$$\Lambda = \mathbf{T}_V^{-1} \mathbf{zy} \mathbf{T}_V = \mathbf{T}_I^{-1} \mathbf{yz} \mathbf{T}_I \quad (3.6)$$

By using the change of variables as defined in (3.7), and by defining  $\gamma^2 = \Lambda$  the equations (3.5) can be rewritten as in (3.8).

$$\mathbf{V}(x) = \mathbf{T}_V \mathbf{V}_m(x) \quad (3.7a)$$

$$\mathbf{I}(x) = \mathbf{T}_I \mathbf{I}_m(x) \quad (3.7b)$$

$$\frac{\partial^2 \mathbf{V}_m(x)}{\partial x^2} = \gamma^2 \mathbf{V}_m(x) \quad (3.8a)$$

$$\frac{\partial^2 \mathbf{I}_m(x)}{\partial x^2} = \gamma^2 \mathbf{I}_m(x) \quad (3.8b)$$

$\mathbf{V}_m$  and  $\mathbf{I}_m$  are the vectors of modal voltages and currents, respectively, and  $\gamma$  is the diagonal matrix containing the propagation constants of each mode of the line, and will be henceforth denominated modal propagation matrix.

The definition of the matrix exponential is needed to continue with this reasoning. The expression  $e^{\mathbf{A}}$ , where  $\mathbf{A}$  is a square matrix is defined as follows:

$$e^{\mathbf{A}} = \sum_{k=0}^{\infty} \frac{\mathbf{A}^k}{k!} \quad (3.9)$$

From (3.9) the functions cosh and sinh can be defined for matrices, as follows:

$$\cosh(\mathbf{A}) = \frac{1}{2} (e^{\mathbf{A}} + e^{-\mathbf{A}}) = \sum_{k=0}^{\infty} \frac{\mathbf{A}^{2k}}{(2k)!} \quad (3.10a)$$

$$\sinh(\mathbf{A}) = \frac{1}{2} (e^{\mathbf{A}} - e^{-\mathbf{A}}) = \sum_{k=0}^{\infty} \frac{\mathbf{A}^{2k+1}}{(2k+1)!} \quad (3.10b)$$

Equation (3.8) admits the solution (3.11), already transformed back to the original base.

$$\mathbf{V}(x) = \mathbf{T}_V (e^{-\gamma x} \mathbf{V}_m^+ + e^{\gamma x} \mathbf{V}_m^-) \quad (3.11a)$$

$$\mathbf{I}(x) = \mathbf{T}_I (e^{-\gamma x} \mathbf{I}_m^+ - e^{\gamma x} \mathbf{I}_m^-) \quad (3.11b)$$

Coefficients  $\mathbf{V}_m^+$ ,  $\mathbf{V}_m^-$ ,  $\mathbf{I}_m^+$  and  $\mathbf{I}_m^-$  are vectors of size  $n$ , each element is to be determined with the boundary conditions of the problem: voltages and currents relations at the line terminals. As for the two-conductor case, the number of unknown coefficients can be reduced with the definition of the characteristic impedance, establishing a relationship between voltages and currents along the line (3.13).

$$\frac{\partial \mathbf{I}(x)}{\partial x} = -\mathbf{T}_I \gamma (e^{-\gamma x} \mathbf{I}_m^+ + e^{\gamma x} \mathbf{I}_m^-) = -\mathbf{y} \mathbf{V}(x) \quad (3.12)$$

$$\mathbf{V}(x) = \underbrace{\mathbf{y}^{-1} \mathbf{T}_I \gamma \mathbf{T}_I^{-1}}_{\mathbf{Z}_c} \mathbf{T}_I (e^{-\gamma x} \mathbf{I}_m^+ + e^{\gamma x} \mathbf{I}_m^-) \quad (3.13)$$

By defining the characteristic impedance matrix as (3.14), the simplified form of the solution

can be written as in (3.15)

$$\mathbf{Z}_c = \mathbf{y}^{-1} \mathbf{T}_I \boldsymbol{\gamma} \mathbf{T}_I^{-1} \quad (3.14)$$

$$\mathbf{V}(x) = \mathbf{Z}_c \mathbf{T}_I (\mathbf{e}^{-\gamma x} \mathbf{I}_m^+ + \mathbf{e}^{\gamma x} \mathbf{I}_m^-) \quad (3.15a)$$

$$\mathbf{I}(x) = \mathbf{T}_I (\mathbf{e}^{-\gamma x} \mathbf{I}_m^+ - \mathbf{e}^{\gamma x} \mathbf{I}_m^-) \quad (3.15b)$$

In the previous chapter a use representation of the two-conductor transmission line was introduced, because it is practical to represent the voltages and currents along the line in function of the voltages and currents at its input. A similar representation can be developed for the multiconductor transmission line, using a  $2n \times 2n$  matrix to represent the connection between the vector of voltages and currents along the line  $\begin{bmatrix} \mathbf{V}(x) \\ \mathbf{I}(x) \end{bmatrix}$  in function of the vector of voltages and currents at its input  $\begin{bmatrix} \mathbf{V}(0) \\ \mathbf{I}(0) \end{bmatrix}$ .

This representation is given in (3.16), and can be called  $2(n+1)$ -pole representation. The matrix  $\boldsymbol{\Phi} = \begin{bmatrix} \boldsymbol{\Phi}_{11}(x) & \boldsymbol{\Phi}_{12}(x) \\ \boldsymbol{\Phi}_{21}(x) & \boldsymbol{\Phi}_{22}(x) \end{bmatrix}$  is denominated ‘‘chain matrix’’ in [33].

$$\begin{bmatrix} \mathbf{V}(x) \\ \mathbf{I}(x) \end{bmatrix} = \begin{bmatrix} \boldsymbol{\Phi}_{11}(x) & \boldsymbol{\Phi}_{12}(x) \\ \boldsymbol{\Phi}_{21}(x) & \boldsymbol{\Phi}_{22}(x) \end{bmatrix} \begin{bmatrix} \mathbf{V}(0) \\ \mathbf{I}(0) \end{bmatrix} \quad (3.16a)$$

$$\boldsymbol{\Phi}_{11}(x) = \mathbf{Z}_c \mathbf{T}_I \cosh(x\boldsymbol{\gamma}) \mathbf{T}_I^{-1} \mathbf{Y}_c \quad (3.16b)$$

$$\boldsymbol{\Phi}_{12}(x) = -\mathbf{Z}_c \mathbf{T}_I \sinh(x\boldsymbol{\gamma}) \mathbf{T}_I^{-1} \quad (3.16c)$$

$$\boldsymbol{\Phi}_{21}(x) = -\mathbf{T}_I \sinh(x\boldsymbol{\gamma}) \mathbf{T}_I^{-1} \mathbf{Y}_c \quad (3.16d)$$

$$\boldsymbol{\Phi}_{22}(x) = \mathbf{T}_I \cosh(x\boldsymbol{\gamma}) \mathbf{T}_I^{-1} \quad (3.16e)$$

In (3.16),  $\mathbf{Y}_c = \mathbf{Z}_c^{-1}$ .

The  $2(n+1)$ -pole representation in (3.16) can still be simplified if rewritten in function the of p.u.l. matrices  $\mathbf{y}$  and  $\mathbf{z}$ . To that end, we establish the following relations:

$$\boldsymbol{\gamma}^2 = \mathbf{T}_I^{-1} \mathbf{y} \mathbf{z} \mathbf{T}_I \quad (3.17)$$

$$\mathbf{y} \mathbf{z} = \mathbf{T}_I \boldsymbol{\gamma}^2 \mathbf{T}_I^{-1} \quad (3.18)$$

$$\mathbf{y} \mathbf{z} = \mathbf{T}_I \boldsymbol{\gamma} \mathbf{T}_I^{-1} \mathbf{T}_I \boldsymbol{\gamma} \mathbf{T}_I^{-1} \quad (3.19)$$

$$\sqrt{\mathbf{y} \mathbf{z}} = \mathbf{T}_I \boldsymbol{\gamma} \mathbf{T}_I^{-1} \quad (3.20)$$

With a similar manipulation, we can find  $\sqrt{\mathbf{z} \mathbf{y}} = \mathbf{T}_V \boldsymbol{\gamma} \mathbf{T}_V^{-1}$ . Matrices  $\sqrt{\mathbf{y} \mathbf{z}}$  and  $\sqrt{\mathbf{z} \mathbf{y}}$  are the equivalent to the propagation constant  $\boldsymbol{\gamma}$  in the MTL case, and will be henceforth denominated propagation matrix  $\sqrt{\mathbf{y} \mathbf{z}}$  and propagation matrix  $\sqrt{\mathbf{z} \mathbf{y}}$ .

The characteristic impedance matrix can also be redefined, as in (3.21)

$$\mathbf{Z}_c = \mathbf{y}^{-1} \sqrt{\mathbf{y} \mathbf{z}} = \sqrt{\mathbf{z} \mathbf{y}}^{-1} \quad (3.21)$$

With these definitions, we can write (3.22) [33]:

$$\begin{pmatrix} \mathbf{V}(x) \\ \mathbf{I}(x) \end{pmatrix} = \begin{pmatrix} \Phi_{11}(x) & \Phi_{12}(x) \\ \Phi_{21}(x) & \Phi_{22}(x) \end{pmatrix} \begin{pmatrix} \mathbf{V}(0) \\ \mathbf{I}(0) \end{pmatrix} \quad (3.22a)$$

$$\Phi_{11}(x) = \mathbf{Z}_c \cosh(x\sqrt{\mathbf{y}\mathbf{z}}) \mathbf{Y}_c \quad (3.22b)$$

$$\Phi_{12}(x) = -\mathbf{Z}_c \sinh(x\sqrt{\mathbf{y}\mathbf{z}}) \quad (3.22c)$$

$$\Phi_{21}(x) = -\sinh(x\sqrt{\mathbf{y}\mathbf{z}}) \mathbf{Y}_c \quad (3.22d)$$

$$\Phi_{22}(x) = \cosh(x\sqrt{\mathbf{y}\mathbf{z}}) \quad (3.22e)$$

The  $2(n+1)$ -pole representation in (3.22) provides a direct description of the MTL avoiding the calculation of the matrix  $\mathbf{y}\mathbf{z}$  eigenvectors. Because of its simplicity, this formulation was chosen for the frequency domain simulation tool for multiconductor transmission lines. For the same reason, it is used in the generalization of the experimental parameter identification for the MTL proposed in 2.3.b.

### 3.2.b Solution with modal decomposition

In the previous section a general solution was presented. It uses matrix decomposition in modal quantities only as a step of the mathematical manipulation, leading to a general model written in function of full parameter matrices ( $\mathbf{Z}_c$  and  $\sqrt{\mathbf{y}\mathbf{z}}$ ). However, it is possible, and useful, to completely decompose the  $n+1$  conductor line problem in  $n$  propagation modes where each one behave as a two-conductor line, independent of the other conductors, as long as the eigenvalues of  $\mathbf{y}\mathbf{z}$ , or  $\mathbf{z}\mathbf{y}$ , are distinct [34].

To that end, the modal decomposition of the propagation matrices presented in the previous section is necessary along with a modal decomposition of the characteristic impedance matrix  $\mathbf{Z}_c$ , so that each mode will be associated to a modal propagation constant  $\gamma_i$ , from which the modal propagation velocity can be extracted, as well as to a modal characteristic impedance  $Z_{ci}$ . The definition of the modal characteristic impedance is not unique, as well explicated in [13], depending on the eigenvectors matrices  $\mathbf{T}_I$  and  $\mathbf{T}_V$  normalization, as well as on the physical relation used as definition of the characteristic impedance. In this document, the definition denominated as Voltage-Current by the authors in [13] is chosen.

The equations (3.1) can be rewritten in a modal base with the variable change defined in (3.23), what gives (3.24).

$$\mathbf{V}(x) = \mathbf{T}_V \mathbf{V}_m(x) \quad (3.23a)$$

$$\mathbf{I}(x) = \mathbf{T}_I \mathbf{I}_m(x) \quad (3.23b)$$

$$\frac{\partial \mathbf{V}_m(x)}{\partial x} = -\mathbf{T}_V^{-1} \mathbf{z} \mathbf{T}_I \mathbf{I}_m(x) \quad (3.24a)$$

$$\frac{\partial \mathbf{I}_m(x)}{\partial x} = -\mathbf{T}_I^{-1} \mathbf{y} \mathbf{T}_V \mathbf{V}_m(x) \quad (3.24b)$$

It is shown in [13,34] that matrices  $\mathbf{z}_m$  and  $\mathbf{y}_m$  in (3.25) are diagonal if the eigenvalues of  $\mathbf{y}\mathbf{z}$  and  $\mathbf{z}\mathbf{y}$  are distinct. Therefore, the system (3.26) is decoupled if this condition is valid.

$$\mathbf{z}_m = \mathbf{T}_V^{-1} \mathbf{z} \mathbf{T}_I \quad (3.25a)$$

$$\mathbf{y}_m = \mathbf{T}_I^{-1} \mathbf{y} \mathbf{T}_V \quad (3.25b)$$

$$\frac{\partial^2 \mathbf{V}_m(x)}{\partial x^2} = \mathbf{z}_m \mathbf{y}_m \mathbf{V}_m(x) \quad (3.26a)$$

$$\frac{\partial^2 \mathbf{I}_m(x)}{\partial x^2} = \mathbf{y}_m \mathbf{z}_m \mathbf{I}_m(x) \quad (3.26b)$$

The modal propagation matrix  $\gamma$  is defined similarly to the previous section

$$\begin{aligned} \gamma^2 &= \mathbf{z}_m \mathbf{y}_m = \mathbf{T}_V^{-1} \mathbf{z} \mathbf{y} \mathbf{T}_V = \\ &= \mathbf{y}_m \mathbf{z}_m = \mathbf{T}_I^{-1} \mathbf{y} \mathbf{z} \mathbf{T}_I \end{aligned} \quad (3.27)$$

Equations (3.26) admit the solution:

$$\mathbf{V}_m(x) = e^{-\gamma x} \mathbf{V}_m^+ + e^{\gamma x} \mathbf{V}_m^- \quad (3.28a)$$

$$\mathbf{I}_m(x) = e^{-\gamma x} \mathbf{I}_m^+ - e^{\gamma x} \mathbf{I}_m^- \quad (3.28b)$$

The modal characteristic impedance  $\mathbf{Z}_d$  will be defined as a relation between the voltages and currents of the line, as shown by (3.29) and (3.30). Its definition is explicit in (3.31).

$$\frac{\partial \mathbf{I}(x)}{\partial x} = -\gamma (e^{-\gamma x} \mathbf{I}_m^+ + e^{\gamma x} \mathbf{I}_m^-) = -\mathbf{y}_m \mathbf{V}_m(x) \quad (3.29)$$

$$\mathbf{V}_m(x) = \underbrace{\mathbf{y}_m^{-1} \gamma}_{\mathbf{Z}_d} (e^{-\gamma x} \mathbf{I}_m^+ + e^{\gamma x} \mathbf{I}_m^-) \quad (3.30)$$

$$\begin{aligned} \mathbf{Z}_d &= \mathbf{y}_m^{-1} \gamma = \mathbf{y}_m^{-\frac{1}{2}} \mathbf{z}_m^{\frac{1}{2}} = \\ &= (\mathbf{T}_V^{-1} \mathbf{y}^{-1} \mathbf{T}_I \mathbf{T}_V^{-1} \mathbf{z} \mathbf{T}_I)^{\frac{1}{2}} \end{aligned} \quad (3.31)$$

The solution to the modal voltages and currents along the line can then be simplified as (3.32).

$$\mathbf{V}_m(x) = \mathbf{Z}_d (e^{-\gamma x} \mathbf{I}_m^+ + e^{\gamma x} \mathbf{I}_m^-) \quad (3.32a)$$

$$\mathbf{I}_m(x) = e^{-\gamma x} \mathbf{I}_m^+ - e^{\gamma x} \mathbf{I}_m^- \quad (3.32b)$$

This is a system of matrix equations where all the matrices are diagonal (if a diagonal  $\mathbf{Z}_d$  can be obtained), therefore completely decoupled. That allows the solution (3.32) to be rewritten in  $n$  systems of scalar equations, one for each propagation mode. Also, each of these systems of equations can be written in the quadrupole form, as done to a two-conductor transmission line. The use modal representation for an  $n + 1$  conductors line with independent  $n$  propagation modes is expressed in (3.33).

$$\begin{pmatrix} V_{m_i}(x) \\ I_{m_i}(x) \end{pmatrix} = \begin{bmatrix} \cosh(\gamma_i x) & -Z_{d_i} \sinh(\gamma_i x) \\ -\frac{1}{Z_{d_i}} \sinh(\gamma_i x) & \cosh(\gamma_i x) \end{bmatrix} \begin{bmatrix} V_{m_i}(0) \\ I_{m_i}(0) \end{bmatrix} \quad \forall i = 1, 2, \dots, n \quad (3.33)$$

The superposition of each mode describes the complete behavior of the multiconductor transmission lines.

### 3.2.c The frequency domain simulation tool

This section describes the general frequency domain simulation tool, able to model a hypothetical radial network where multiconductor cables with conductors equally spaced along the network connect multiple devices. It is obtained with the generalization of frequency domain simulation

tool presented in section 2.2.a to the multiconductor case.

First, the simulation tool must be as generic as possible. To that end, the devices (or systems) connected to the cable terminals have to be represented with the most generic model possible. In other words, the models of the source and the load connected to the cable must be a generalization of the Thévenin's or Norton's theorem for  $(n + 1)$ -port devices.

Such generalizations can be found in [17], where it is proven that any linear  $(n + 1)$ -port system can be reduced to an equivalent circuit. The equivalent circuit is built with a graph containing sources or impedances in its branches, respecting the rules below:

1. **Impedances:** A branch containing an impedance must connect each two-ports of the device terminal, forming what is called a complete graph,
2. **Sources:** The branches containing sources cannot form loops, and every terminal node must be connected to a source branch, forming what is called a complete tree.

That gives an equivalent graph with  $\frac{n(n+1)}{2}$  impedances and  $n$  sources. The equivalent graph is not unique, but the rules just described guarantee it will be minimal. Fig. 3.3 shows a possible equivalent circuit for a device with  $(n + 1)$  terminals.

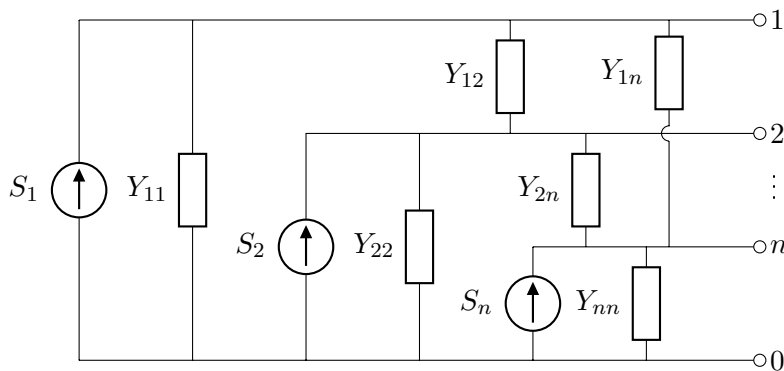


Figure 3.3 –  $(n + 1)$ -port equivalent circuit

Such an equivalent graph can be put in equation form as in (3.34a) [17]. In this equation, the voltages and currents at the device output are organized in vectors  $\mathbf{V}$  and  $\mathbf{I}$  and the current



sources are organized in vector  $\mathbf{S}$ , as in (3.34b). The admittance matrix  $\mathbf{Y}$  is defined in (3.34c).

$$\mathbf{I} = \mathbf{Y}\mathbf{V} + \mathbf{S} \quad (3.34a)$$

$$\mathbf{V} = \begin{bmatrix} V_1 \\ V_2 \\ \vdots \\ V_n \end{bmatrix}, \quad \mathbf{I} = \begin{bmatrix} I_1 \\ I_2 \\ \vdots \\ I_n \end{bmatrix}, \quad \mathbf{S} = \begin{bmatrix} S_1 \\ S_2 \\ \vdots \\ S_n \end{bmatrix} \quad (3.34b)$$

$$\mathbf{Y} = \begin{bmatrix} \sum_{k=1}^n Y_{1k} & -Y_{12} & \cdots & -Y_{1n} \\ -Y_{12} & \sum_{k=1}^n Y_{2k} & \cdots & -Y_{2n} \\ \vdots & \vdots & \ddots & \vdots \\ -Y_{1n} & -Y_{2n} & \cdots & \sum_{k=1}^n Y_{nk} \end{bmatrix} \quad (3.34c)$$

With the generalized multi-port equivalent circuit just described, we can define the generalized frequency domain model for multiconductor transmission lines. Consider the MTL presented in Fig. 3.4, supposing both source and load are represented by the equivalent circuit of Fig. 3.3.

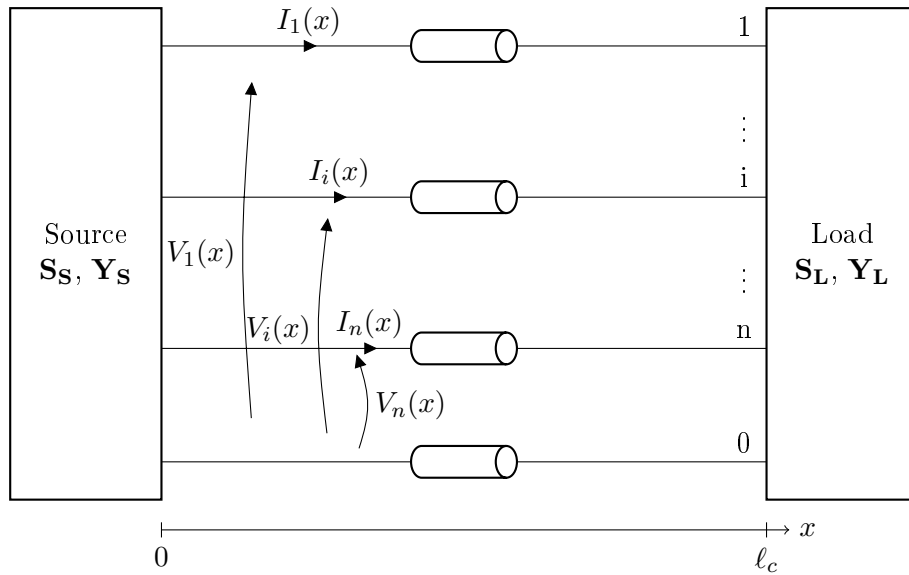


Figure 3.4 – Multiconductor transmission line, variables definition

The definition of the matrix used in the  $2(n+1)$ -pole model of an MTL is recalled here, it has been derived in section 3.2.a. It is more interesting to write it in the general solution in the

full matrix form:

$$\Phi(x, f) = \begin{pmatrix} \Phi_{11}(x, f) & \Phi_{12}(x, f) \\ \Phi_{21}(x, f) & \Phi_{22}(x, f) \end{pmatrix} \quad (3.35a)$$

$$\Phi_{11}(x, f) = \mathbf{Z}_c(f) \cosh(x\sqrt{\mathbf{y}\mathbf{z}}(f))\mathbf{Y}_c(f) \quad (3.35b)$$

$$\Phi_{12}(x, f) = -\mathbf{Z}_c(f) \sinh(x\sqrt{\mathbf{y}\mathbf{z}}(f)) \quad (3.35c)$$

$$\Phi_{21}(x, f) = -\sinh(x\sqrt{\mathbf{y}\mathbf{z}}(f))\mathbf{Y}_c(f) \quad (3.35d)$$

$$\Phi_{22}(x, f) = \cosh(x\sqrt{\mathbf{y}\mathbf{z}}(f)) \quad (3.35e)$$

Using the MTL model matrix  $\Phi$  in (3.35), the voltages and currents at the extremities of the line  $\mathbf{V}(0, f)$ ,  $\mathbf{V}(\ell_c, f)$ ,  $\mathbf{I}(0, f)$  and  $\mathbf{I}(\ell_c, f)$  can be obtained by solving the system of equations (3.36):

$$\begin{cases} \begin{bmatrix} \mathbf{V}(\ell_c, f) \\ \mathbf{I}(\ell_c, f) \end{bmatrix} = \Phi(\ell_c, f) \begin{bmatrix} \mathbf{V}(0, f) \\ \mathbf{I}(0, f) \end{bmatrix} \end{cases} \quad (3.36a)$$

$$\mathbf{I}(0, f) = \mathbf{S}_S(f) - \mathbf{Y}_S(f)\mathbf{V}(0, f) \quad (3.36b)$$

$$\mathbf{I}(\ell_c, f) = \mathbf{S}_L(f) - \mathbf{Y}_L(f)\mathbf{V}(\ell_c, f) \quad (3.36c)$$

Once this system of equations solved, the voltages and currents can be calculated anywhere along the line with (3.37)

$$\begin{bmatrix} \mathbf{V}(x, f) \\ \mathbf{I}(x, f) \end{bmatrix} = \Phi(x, f) \begin{bmatrix} \mathbf{V}(0, f) \\ \mathbf{I}(0, f) \end{bmatrix} \quad (3.37)$$

Equations (3.36) and (3.37) allow the conception of a frequency domain simulation tool able to model the generic system in 3.1, i.e, a generic multiconductor transmission-line simulator.

Figure 3.5 shows the input/output schematic of the frequency domain simulation tool. The inputs of the simulator are described below.

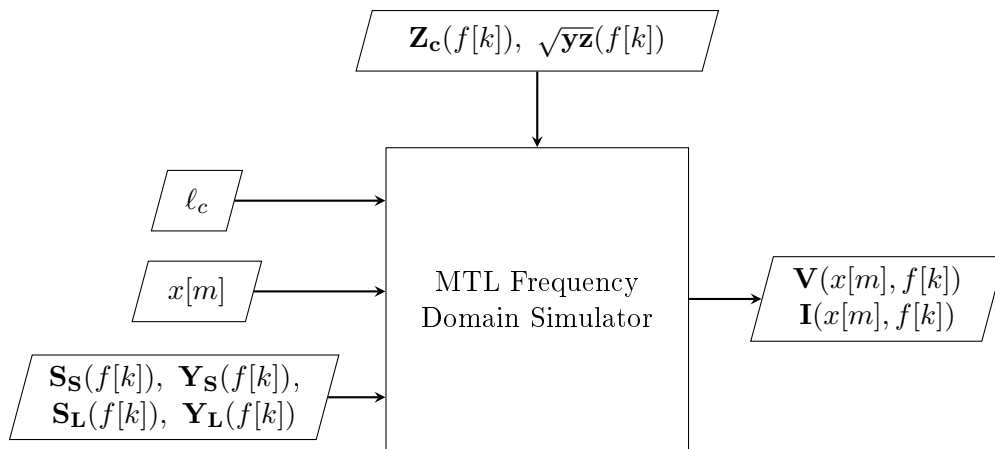


Figure 3.5 – Frequency domain simulation tool inputs and outputs — multiconductor cables

- $f[k]$  is the discretization of the variable frequency  $f$ , a vector containing the frequency points in which calculations will be performed.
- $\mathbf{Z}_c(f)$  and  $\sqrt{\mathbf{y}\mathbf{z}}(f)$  are the cable parameters obtained from the impedance analyzer-based parameter identification;

- $\ell_c$  is the cable length;
- $x[m]$  is discretization of the variable  $x$  position along the line, a vector containing the positions where the voltage and currents are calculated;
- $\mathbf{S}_S(f)$ ,  $\mathbf{Y}_S(f)$ ,  $\mathbf{S}_L(f)$ , and  $\mathbf{Y}_L(f)$  are the elements of the equivalent circuit representing the devices connected to the cable terminals.

The outputs are the voltages  $\mathbf{V}(x, f)$  and currents  $\mathbf{I}(x, f)$  calculated at the positions  $x[m]$  of the line in function of frequency  $f$ .

Figure 3.6 shows the programmable flowchart of the simulator developed for this work. It details the work-flow of the box “Frequency domain simulation tool MTL” in Fig. 3.5.

To resume, the frequency domain simulation tool algorithm consists in repeating the following steps for every frequency point of vector  $f$ :

1. Solve the system of equations in (3.36) to obtain the voltages and currents at the line extremities  $\mathbf{V}(0, f)$ ,  $\mathbf{V}(\ell_c, f)$ ,  $\mathbf{I}(0, f)$ ,  $\mathbf{I}(\ell_c, f)$ .
2. Voltages and currents at positions different from  $x = 0$  and  $x = \ell_c$  can be calculated with eq. (3.37), using the stored input voltages  $\mathbf{V}(0, f)$  and currents  $\mathbf{I}(0, f)$ .

The next section will discuss the experimental identification of the parameters of multiconductor cables, to obtain the cable parameters required by the simulator just described.

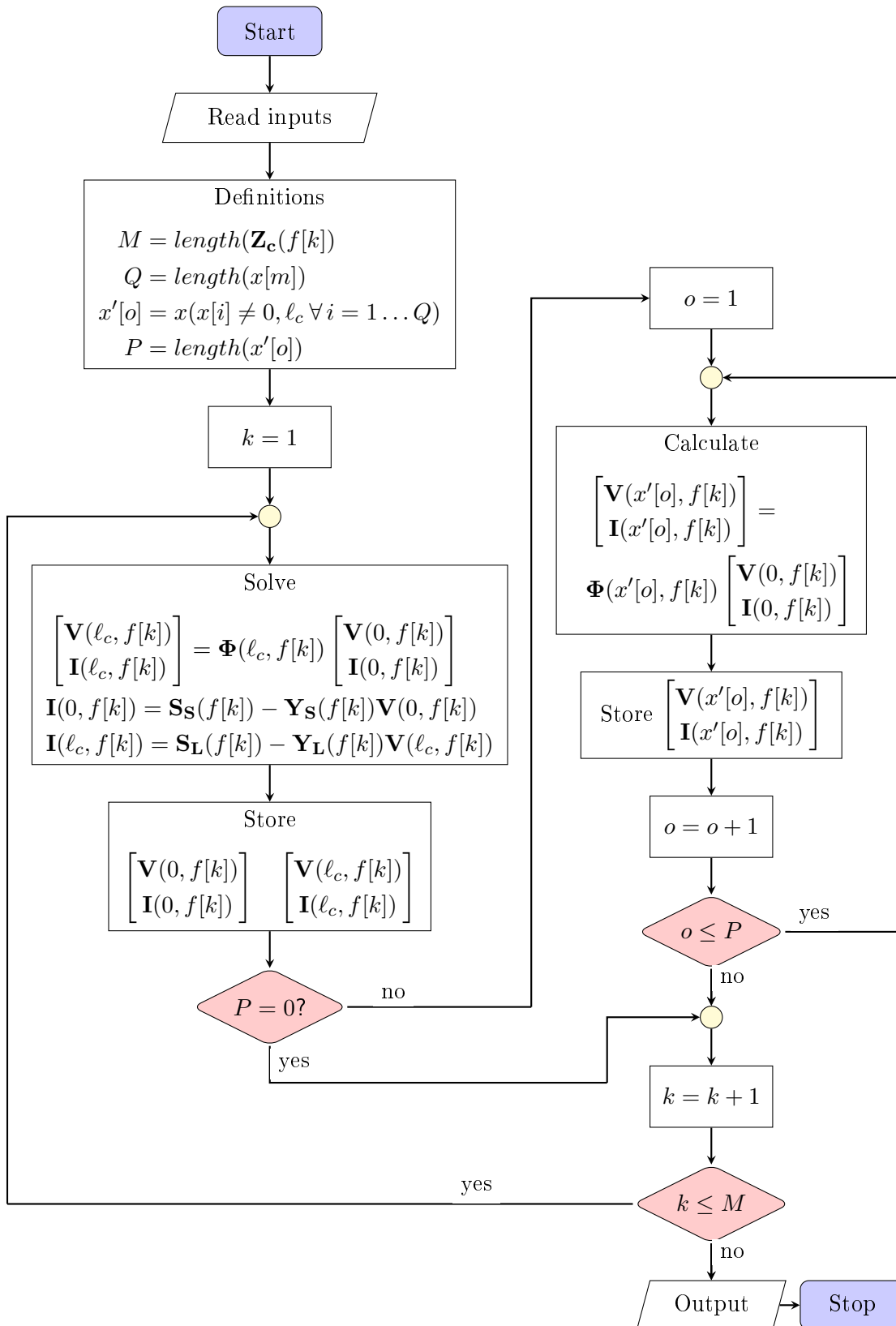


Figure 3.6 – Program flowchart of the frequency domain simulation tool — multiconductor cables

### 3.3 Multiconductor cable parameter identification

The MTL simulation tool described in the previous section, takes as input the cable parameters matrices: the characteristic impedance  $\mathbf{Z}_c$  and the propagation matrix  $\sqrt{\mathbf{y}\mathbf{z}}$ . These parameter matrices can be obtained with an impedance analyzer-based parameter identification method analog to the one presented in section 2.3, but now adapted to multiconductor cables.

This section describes an experimental technique adapted to identify the parameters of a multiconductor transmission line using measurements of its input impedance. To begin, the input impedance of a multiconductor transmission line must be defined.

Consider that a load with  $n + 1$  ports described by its input impedance matrix  $\mathbf{Z}_L$ , defined as in (3.38), is connected to the multiconductor transmission line at  $x = \ell_c$ .

$$\mathbf{V}(\ell_c) = \mathbf{Z}_L \mathbf{I}(\ell_c) \quad (3.38)$$

Consider also that the MTL input impedance  $\mathbf{Z}(0)$  is defined as:

$$\mathbf{V}(0) = \mathbf{Z}(0) \mathbf{I}(0) \quad (3.39)$$

By evaluating the  $2(n + 1)$ -pole representation of the MTL in (3.22) at  $x = \ell_c$ , the input impedance matrix  $\mathbf{Z}(0)$  can be expressed by (3.40)

$$\mathbf{Z}(0) = \mathbf{Z}_c [\mathbf{Z}_L \sinh(\ell_c \sqrt{\mathbf{y}\mathbf{z}}) + \mathbf{Z}_c \cosh(\ell_c \sqrt{\mathbf{y}\mathbf{z}})]^{-1} [\mathbf{Z}_c \sinh(\ell_c \sqrt{\mathbf{y}\mathbf{z}}) + \mathbf{Z}_L \cosh(\ell_c \sqrt{\mathbf{y}\mathbf{z}})] \quad (3.40)$$

Note that for a two-conductor case ( $n = 1$ ), this equation reduces to the input impedance of a two-conductor transmission-line (2.23), repeated here for convenience (note:  $\gamma \equiv \sqrt{zy}$ ).

$$Z(0) = Z_c \frac{Z_L + Z_c \tanh(\ell_c \gamma)}{Z_c + Z_L \tanh(\ell_c \gamma)}$$

For a short-circuited (SC) and an open-ended (OC) multiconductor line, the input impedance in (3.40) reduces to (3.41) (3.42) [2, 24]:

$$\mathbf{Z}^{SC}(0) = \mathbf{Z}_c [\cosh(\ell_c \sqrt{\mathbf{y}\mathbf{z}})]^{-1} \sinh(\ell_c \sqrt{\mathbf{y}\mathbf{z}}) \quad (3.41)$$

$$\mathbf{Z}^{OC}(0) = \mathbf{Z}_c [\sinh(\ell_c \sqrt{\mathbf{y}\mathbf{z}})]^{-1} \cosh(\ell_c \sqrt{\mathbf{y}\mathbf{z}}) \quad (3.42)$$

Finally, the characteristic impedance matrix  $\mathbf{Z}_c$  and the propagation matrix  $\sqrt{\mathbf{y}\mathbf{z}}$  can be deduced from open and short circuit input impedance with:

$$\mathbf{Z}_c = \left\{ \mathbf{Z}^{SC}(0) [\mathbf{Z}^{OC}(0)]^{-1} \right\}^{-1/2} \mathbf{Z}^{SC}(0) \quad (3.43)$$

$$[\cosh(\ell_c \sqrt{\mathbf{y}\mathbf{z}})]^{-1} \sinh(\ell_c \sqrt{\mathbf{y}\mathbf{z}}) = \mathbf{Z}_c^{-1} \mathbf{Z}^{SC}(0) \quad (3.44)$$

(3.44) can be solved numericalally to obtain  $\sqrt{\mathbf{y}\mathbf{z}}$ .

The input impedance matrix  $\mathbf{Z}(0)$  of a  $n + 1$  conductor cable can be measured as described in [24]. The measurement technique proposed by them is resumed below.

The input impedance  $\mathbf{Z}(0)$  can be measured for any load connected to its terminal: open circuit, short circuit or arbitrary known load  $\mathbf{Z}_L$ <sup>1</sup>. By choosing an open and short-circuited terminal the line parameters can be obtained from (3.43) and (3.44).

<sup>1</sup>If the arbitrary load is precisely characterized in the whole frequency band, eq. (3.40) can be used.

The diagonal terms of  $\mathbf{Z}(0)$  (self impedance) can be determined with:

$$Z_{ii}(0) = \left. \frac{V_i(0)}{I_i(0)} \right|_{I_{k \neq i}(0)=0} \quad (3.45)$$

With the setup shown in Fig. 3.7, the measured impedance corresponds to  $Z_{ii}$  if all conductor currents are zero at  $x = 0$ , except for the conductor under test. Electrically insulating the open extremities of the conductors is a good practice to guarantee this condition.

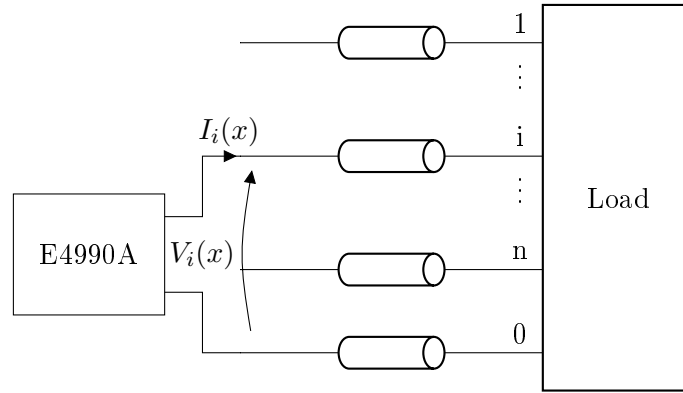


Figure 3.7 – Self impedance measurement setup

Because impedance analyzers do not measure mutual impedance, i.e. measuring voltage and injecting current on different ports, a mathematical approach is used to obtain the non-diagonal elements of  $\mathbf{Z}(0)$ . Using the measurement setup shown in Fig. 3.8, the measured impedance  $Z_{Mij}$  is:

$$\begin{aligned} Z_{Mij} &= \left. \frac{V_i(0) - V_j(0)}{I_i(0)} \right|_{I_{k \neq i, j}(0)=0} = \\ &= \frac{Z_{ii}(0)I_i(0) + Z_{ij}(0)I_j(0) - Z_{ji}(0)I_i(0) - Z_{jj}(0)I_j(0)}{I_i(0)} \quad (3.46) \end{aligned}$$

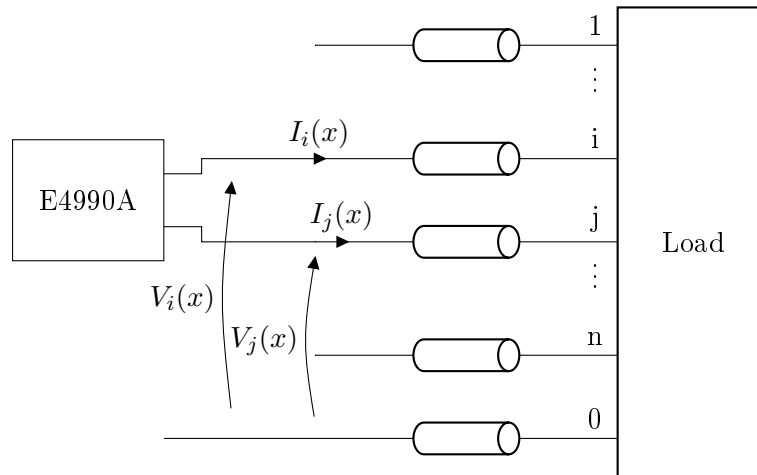


Figure 3.8 – Mutual-impedance measurement setup

As  $I_j(0) = -I_i(0)$  and using the fact that  $\mathbf{Z}(0)$  is symmetric, the mutual impedance  $Z_{ij} = Z_{ji}$

can be calculated with:

$$Z_{ij}(0) = \frac{1}{2}(Z_{ii}(0) + Z_{jj}(0) - Z_{Mij}) \quad (3.47)$$

Once every possible combination of two distinct active conductors (conductors 1 to  $n$  in Fig. 3.8) has been measured, the input impedance matrix can be filled. In the general case,  $n$  self-impedance and  $n(n-1)/2$  mutual-impedance measurements are required to complete it. If special conditions such as circular symmetry – case in which the elements of  $\mathbf{Z}(0)$  repeat cyclically [33] – are verified, the number of measurements required can be reduced.

An equivalent methodology to obtain the input admittance matrix is described in [24]. Admittance measurement requires the input extremities of the conductors to be short-circuited except for the conductor under test, instead of open-ended as just described. Directly measuring the input admittance matrix avoids a matrix inversion when solving (3.43). However, considering the good stability and accuracy of linear equation solvers when determining the product  $\mathbf{Z}^{SC}(0)[\mathbf{Z}^{OC}(0)]^{-1}$  in (3.43), the measurement of input admittance matrix instead of impedance is not mandatory, and not recommended for cases where it is difficult to guarantee neat short circuits on the cable input.

The precautions needed to perform the input impedance measurements described in section 2.3.b also apply for multiconductor power cables. Refer to the aforementioned section for a detailed description of the recommended measurement protocol.

### 3.4 Frequency-domain model experimental validation

The frequency domain model described in section 3.2.c was built for a three-conductor cable with conductors of section  $2.5 \text{ mm}^2$ , its cross-section is represented in Fig. 3.9. The cable parameters were obtained with the impedance analyzer identification described in the previous section, with a sample cable  $0.9 \text{ m}$  long, with balun in the interface between the impedance analyzer and the cable, and with the analyzer fed through a LISN.

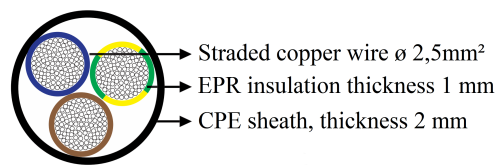


Figure 3.9 – Three-conductor cable cross-section

To show the effect of the common mode during the input impedance measurements, a second set of measurements was performed, with the same sample cable, using the Keysight impedance analyzer connector E16047A, and without the LISN, in a common-mode enhancing configuration: with the sample cable next to the feeding cable of the analyzer, its extremity close to the plug of the analyzer. The parameter resultant from these identification measurements will be identified as “without balun” in the next two subsections.

As was done for the two-conductor validation on Section 2.4, two validation experiments are performed. The first consists in the voltage measurement on a resonant cable and is described in section 3.4.a. The second, consisting in the measurement of the input impedance of a long cable, is described in section 3.4.b.

### 3.4.a Resonance-based experiment validation

The three-conductor resonance-based experiment is equivalent to the one performed for the two-conductor cable in section 2.4: a long three-conductor cable was fed with a sinusoidal source with variable frequency, and the voltage was measured in the position  $x = x_M$  where the maximum voltage resonance amplification occurs when the excitation source is at the natural frequency of the cable. A schematic of the resonance experiment is drawn in Fig. 3.10, the voltage  $V_1(x)$  was chosen to be measured. The voltage measurement position  $x_M$  remained fix for each load termination, and for the frequency points where no resonance occurs, the maximal voltage may occur elsewhere.

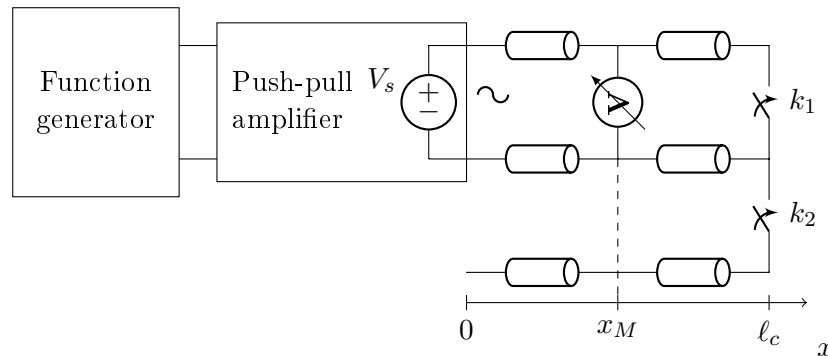


Figure 3.10 – Schematic: resonance-based validation experiment

The voltage measurements were performed with a battery-powered scope, to avoid an alternative current path via the mass of the scope. The use of a scope for this measurement, which is not the most accurate option, is justified because time domain measurements will be necessary in chapter 4. The probe equivalent impedance was taken into account in the theoretical modeling. The loop of the mass connection of the voltage probe was minimized, using the “spring” mass connector in Fig. 3.11.



Figure 3.11 – Connection of the voltage probe along the line

The resonance experiment was effectuated for two different load configurations (cf. Fig. 3.10):

- Configuration 1 :  $k_1$  and  $k_2$  closed
- Configuration 2 :  $k_1$  opened,  $k_2$  closed.

The complete open-circuit extremity was not used because our experiments showed that the behavior of the line in this case is really similar to a two-conductor open-ended line.

Both configurations 1 and 2 maximize the reflection coefficient in the load end  $\Gamma_L$ . The total reflection on the source end was ensured by feeding the long cable via the AB class push-pull



amplifier with closed loop, and near-zero output impedance, the same used for the two-conductor resonance-based validation.

For both load configurations, the position  $x_M$  of the maximum amplification of  $V_1$  was determined numerically. For configuration 1, complete short-circuit, the maximum occurs at  $x_M = \ell_c/2$ , and for configuration 2 at  $x_M = \ell_c$ .

The experiment was performed with a 11.98 m long cable. The cable and the scope were suspended with insulating supports, to mitigate common-mode currents.

Two cable parameter sets are used: the first obtained with balun, following the protocol 2.3.b-iii, and the second without balun in a common-mode enhancing configuration. The schematic in Fig. 3.12 resumes the theoretical calculations performed for this validation, detailing the inputs needed for the theoretical calculation of  $V_1(x_M, f)$ .

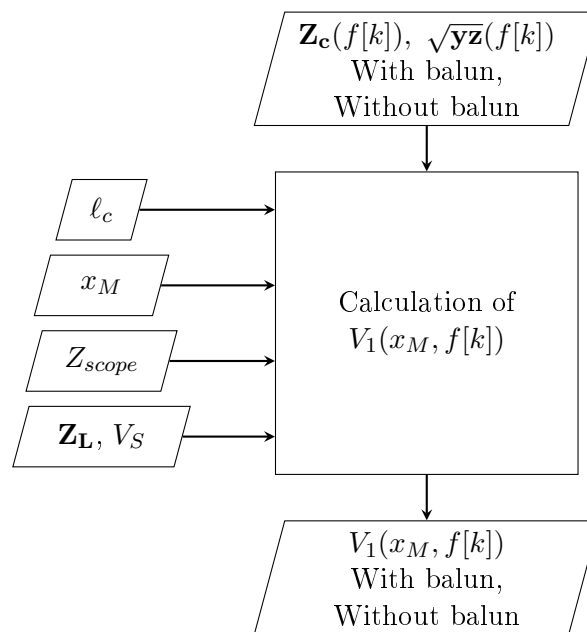


Figure 3.12 – Frequency domain voltage simulation

To recall,  $\ell_c$  is the cable length,  $x_M$  is the voltage measurement point,  $Z_{scope}$  is the input impedance of the scope probe,  $\mathbf{Z}_L$  is the load connected at  $x = \ell_c$  (open and short circuit in this study),  $V_S$  is the input voltage, purely sinusoidal, of variable frequency.  $f[k]$  is the discretization of the frequency  $f$ .

The results are presented in Fig. 3.13, where both theoretical and experimental data are plotted in terms of voltage amplification  $V_1(x_M)/V(0)$ .

Table 3.1 – Frequency-Domain Model Resonance Frequency and Amplitude Relative Errors

	With balun		Without balun	
	Amplitude	Frequency	Amplitude	Frequency
Config. 1	5.9%	0.1%	21%	1.8%
Config 2.	10.6%	1.7%	43.4%	3.7%

The results of the theoretical model using the parameters issued from the identification with

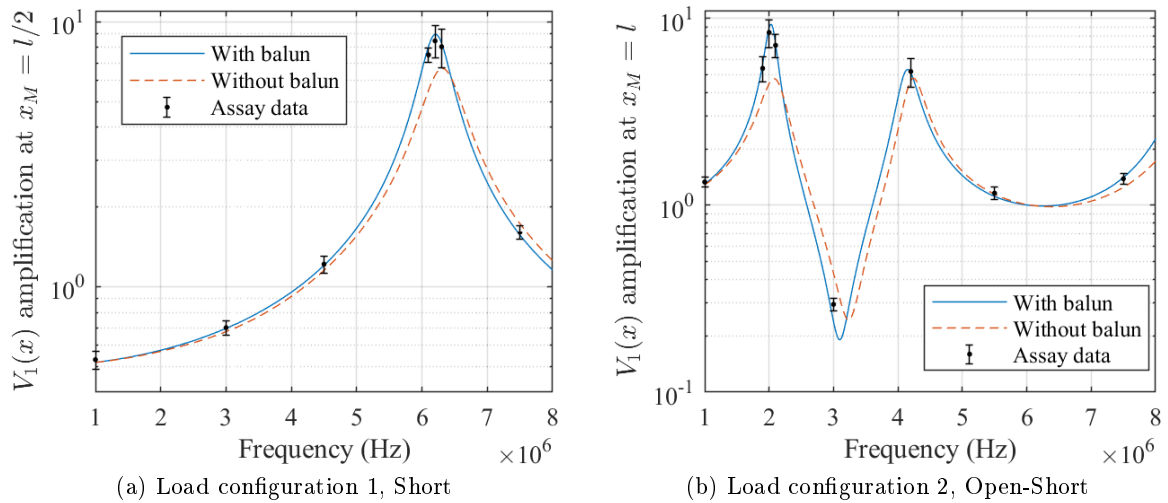


Figure 3.13 – Experimental validation : resonance-due voltage amplification

balun present a good agreement with the experimental data. It is shown in table 3.1 that the errors are more important for the parameter identification without balun in a common-mode enhancing configuration, as expected. Indeed, in this case the error goes up to 43% on configuration 2, due to the common-mode currents in the identification measurements.

### 3.4.b Input Impedance Validation

The same cable used in the previous section, of length  $11.98\text{ m}$ , was used for an input impedance validation. This validation consists in the measurement of the input impedance of a long cable, to be compared to the theoretical impedance predicted by (3.40), using the two sets of cable parameters obtained from the identification measurements with and without balun, as aforementioned. A schematic of the input impedance measurement setup is drawn in Fig. 3.14. The input impedance is measured between the conductors “1” and “0”.

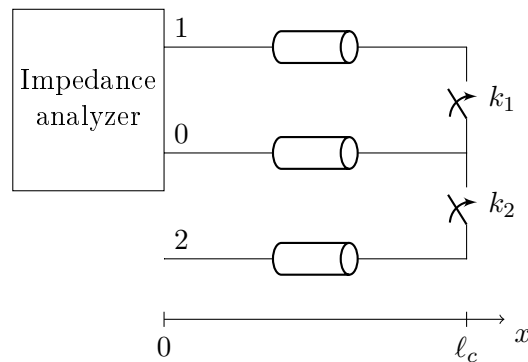


Figure 3.14 – Schematic: input impedance validation experiment

The input impedance matrix of a three-conductor transmission line is a  $2 \times 2$  matrix. The impedance measured with the schematic in Fig. 3.14 corresponds to the element in position (1,1) of  $\mathbf{Z}(0)$ , denominated hereafter  $Z_{11}$ .

A schematic illustrating the steps to calculate the theoretical input impedance is presented in

Fig. 3.15. The cable parameters  $\mathbf{Z}_c(f[k])$ ,  $\sqrt{\mathbf{y}\mathbf{z}}(f[k])$  are issued from a parameter identification with balun for the first calculation, and without balun for the second.

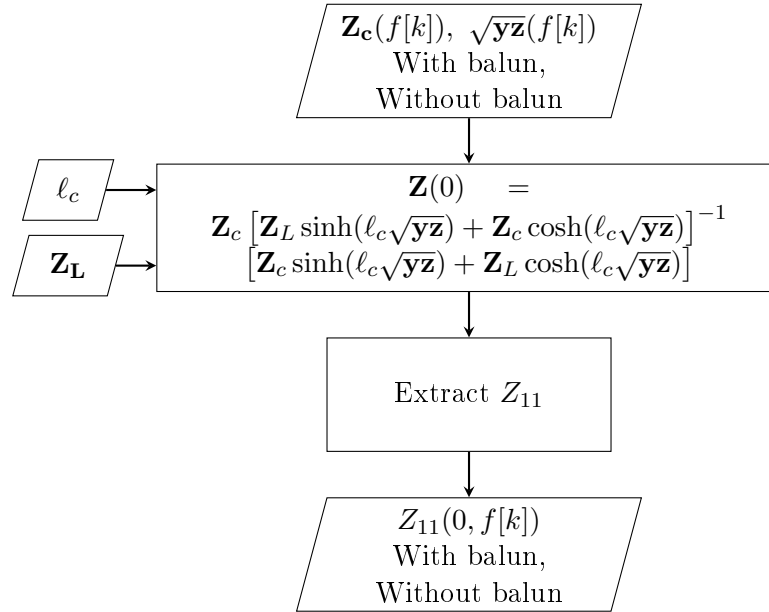


Figure 3.15 – Theoretical input impedance calculation

Two measurements were performed, one for each of the following load configurations:

- Configuration 1 :  $k_1$  and  $k_2$  closed
- Configuration 2 :  $k_1$  opened,  $k_2$  closed.

The long cable input impedance, in both cases, was measured with the cable suspended by insulating supports, and with a balun on the interface between the cable and the impedance analyzer, to avoid the circulation of common-mode currents. The results are presented in Fig. 3.16.

As expected, the input impedance predicted using the parameters obtained from the adequate parameter identification, i.e., with balun and using a LISN as line filter, present a good agreement with the experimental data. The results obtained from the parameter calculated from measurements without balun in a common-mode enhancing configuration present considerable errors.

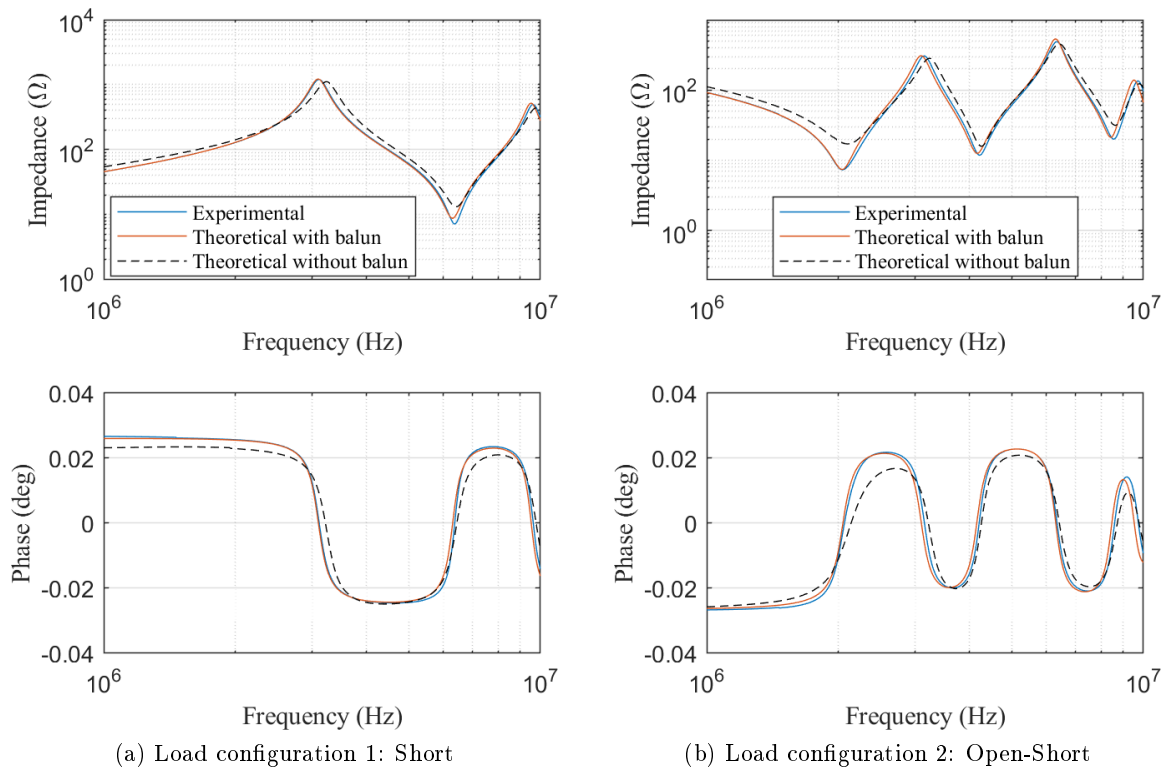
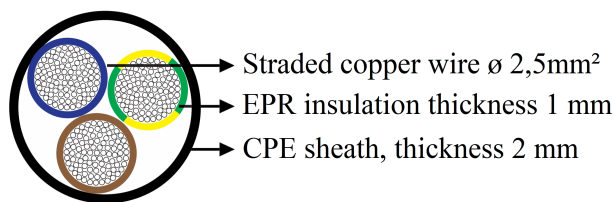


Figure 3.16 – Experimental validation : input impedance

### 3.4.c Examples of cable parameter identification

In this section, the parameters of the  $2.5 \text{ mm}^2$  section three-conductor cable are presented. The wide band parameters were obtained with the methods described in section 2.4.c, where the low frequency parameters are obtained from the input impedance measurements of a longer sample cable, in this case a  $12 \text{ m}$  long sample, and the high frequency parameters are obtained from a short sample cable identification, in this case  $1 \text{ m}$  long. Refer to section 2.4.c for the justification of this proceeding.

Source: <http://www.caledonian-cables.co.uk>

Figure 3.17 – Cross-section of the three-conductor  $2.5 \text{ mm}^2$  cable

The matrix parameters  $\mathbf{Z}_c$  and  $\sqrt{\mathbf{y}\mathbf{z}}$  of three-conductor cables are matrices of dimension  $2 \times 2$ . The parameters of the cable in Fig. 3.17 are plotted in Fig. 3.18. As the cable is symmetric circular, the diagonal elements of the matrices  $\mathbf{Z}_c$  and  $\sqrt{\mathbf{y}\mathbf{z}}$  are the same.

The p.u.l. parameter matrices  $\mathbf{r}$ ,  $\mathbf{l}$ ,  $\mathbf{g}$ , and  $\mathbf{c}$  can be obtained from the characteristic impedance

matrix  $\mathbf{Z}_c$  and the propagation matrix  $\sqrt{\mathbf{y}\mathbf{z}}$  with the following equations:

$$\mathbf{r} = \mathbb{R} \{ \mathbf{Z}_c \sqrt{\mathbf{y}\mathbf{z}} \} \quad (3.48a)$$

$$\mathbf{l} = \frac{1}{j\omega} \mathbb{I} \{ \mathbf{Z}_c \sqrt{\mathbf{y}\mathbf{z}} \} \quad (3.48b)$$

$$\mathbf{g} = \mathbb{R} \left\{ \sqrt{\mathbf{y}\mathbf{z}} (\mathbf{Z}_c)^{-1} \right\} \quad (3.48c)$$

$$\mathbf{c} = \frac{1}{j\omega} \mathbb{I} \left\{ \sqrt{\mathbf{y}\mathbf{z}} (\mathbf{Z}_c)^{-1} \right\} \quad (3.48d)$$

The p.u.l. parameters of the three-conductor cable in Fig. 3.17 are represented in Fig. 3.19. These parameters correspond to the p.u.l. elements of the MTL cell defined in Fig. 3.2.

These parameters will be used in other applications along this document.

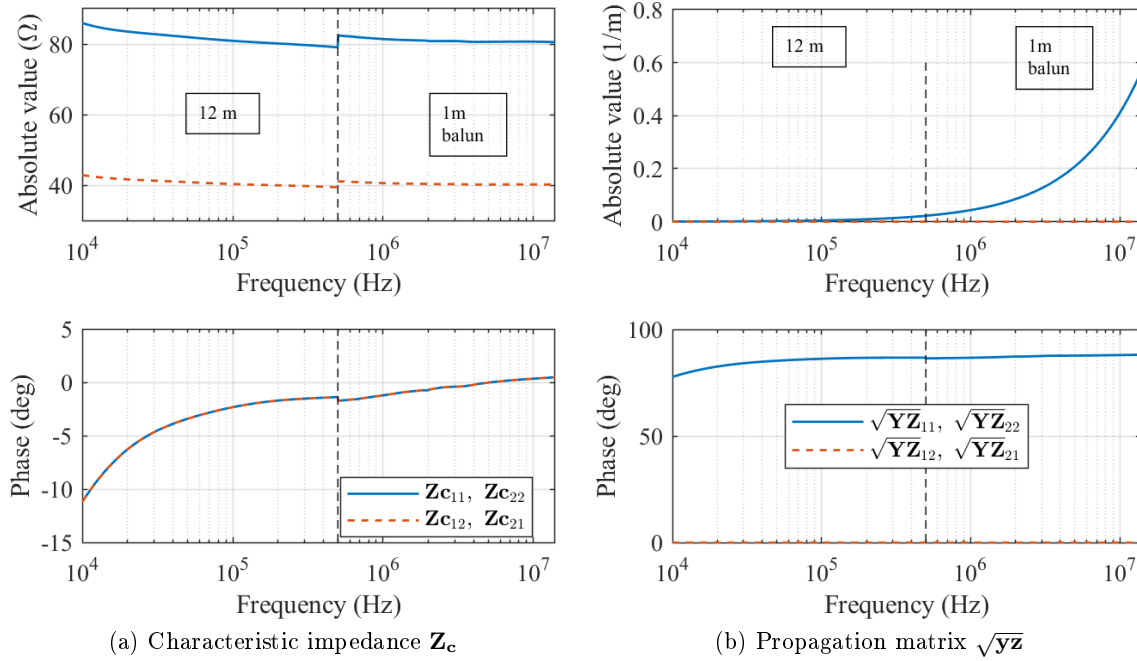


Figure 3.18 – Three-conductor cable complex parameters

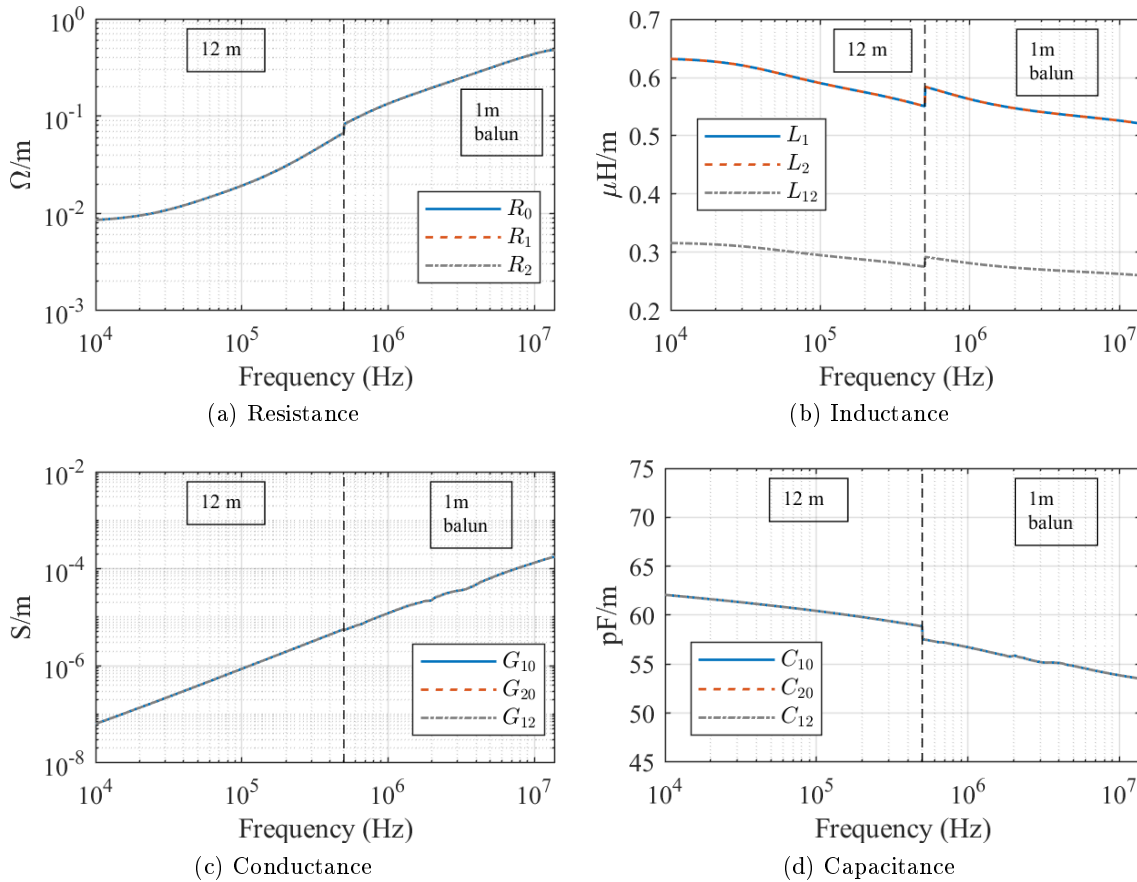


Figure 3.19 – Three-conductor p.u.l. parameters

### 3.5 Extension of Resonance surfaces for multiconductor cables

In section 2.5 the resonance phenomenon has been numericalallly analyzed, a study that led to the plotting of the three 3-dimensional surfaces describing the resonance behavior of a two-conductor transmission line in function of the load (cf. Figs. 2.39 to 2.41). In the first surface, the maximal amplification due to resonance is plotted in function of the load impedance (cf. Fig. 2.39). The two other surfaces contain the correspondent resonance frequency (cf. Fig. 2.40) and position of the maximal voltage along the line (cf. Fig. 2.41) for each maximal amplification point in Fig. 2.39.

This approach allows a visualization of the resonance behavior of a cable of a given length, and the easy prediction of the resonance behavior of the cable in a system (cf. section 2.5.b-i).

It would be interesting to extend the same analysis to multiconductor cables. Principally considering that, in a real single phase system, common-mode currents will circulate through alternative paths, and a two-conductor model cannot take them into account.

However, the generalization of the resonance surfaces to multiconductor transmission lines is troublesome. For example, consider the system with a three-conductor cable in Fig. 3.20.

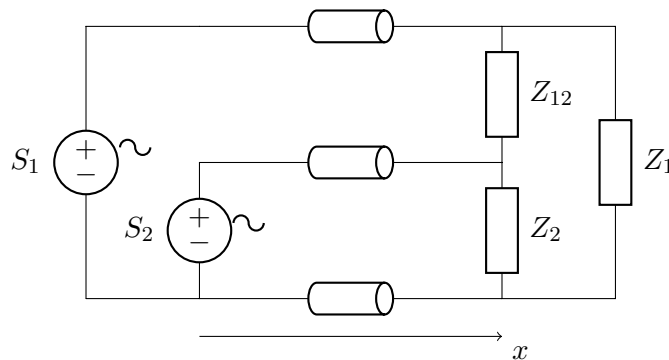


Figure 3.20 – Schematic for numerical resonance analysis

The load connected to cable at  $x = \ell_c$  can represent any generic passive load (cf. section 3.2.c, [17]). If the same approach used in section 2.5 was to used here, we would need to plot a 7-dimensional surface: 6 dimensions are needed to represent the real and imaginary parts of the three load impedances, and a 7<sup>th</sup> dimension is needed for the variable of interest (voltage amplification, resonance frequency or maximal amplification position). This 7-dimensional surface can be defined mathematically, but its visual representation is not possible.

Some simplifications can be used to reduce the number of dimensions of the surface to three, but they limit the group of multiport impedances that can be represented by the surface. In other words, for some specific cases, these surfaces can be plotted in three dimensions.

A first possibility of simplification is to set two of the three load impedances to constant values, for example  $Z_1$  and  $Z_2$ , and vary real and imaginary parts of the third, for example  $Z_{12}$ . This would be equivalent to vary the differential-mode load impedance, while its parasitic common-mode impedance remain unchanged. Note that this restriction applies to their frequency behavior as well: the fixed impedances cannot vary on frequency either, what is not realistic because stray capacitances will always interfere in any physical system, and their reactances are frequency dependent. Therefore, this option is not useful.

A second possibility is to diagonalize the load impedance matrix, using its own eigenvectors,

representing the system in an algebraic basis where the load impedance matrix is a diagonal matrix. That way, a 3-dimensional resonance surface can be plotted for each of the load matrix eigenvalues, since they are decoupled in the new basis.

However, some difficulties arise from this approach. They will be discussed in detail in section 3.5.c, and they come mainly from the fact that there is no matrix that can diagonalize any load impedance matrix, and different diagonalization matrices would be needed for each frequency point.

An alternative to that problem is to restrict the analysis to balanced systems. As will be explained in detail in sections 3.5.a and 3.5.b, a balanced system is a system with symmetric common-mode impedances, what causes the common and differential mode to be decoupled. If these two modes are decoupled, they can be modeled separately by two independent two-conductor systems, and the resonance surfaces for each mode can be visualized.

Section 3.5.a demonstrate the condition that three-conductor lines have to meet to be balanced. In section 3.5.b, the surfaces resultant from the numerical analysis of a balanced system are presented. After that, in section 3.5.c, the difficulties of generalizing this representation to all possible load impedance matrices are discussed.

### 3.5.a Conditions for a three-conductor line to be balanced

The decomposition of the voltages and currents of a single phase system in differential and common modes is widely used in the EMC field. This decomposition is useful because usually it allows to separate the stray voltage/current (on common mode) from the voltage and currents that are intended to circulate in the system (on differential mode).

For most cases, this decomposition is only useful if the modes are decoupled, i.e., differential voltages depend exclusively on differential-mode currents, and the same for the common mode. When the modes are decoupled, the complete system can be represented by two subsystems, one in differential mode and another in common mode. This representation simplifies the designing of filters, the measurements of the perturbation generated by the systems, among other applications.

In this section, we will determine the characteristics that a three-conductor cable has to meet to be balanced, so that the decoupling between common and differential mode is possible.

The common/differential mode decomposition consists in a changing of variables, mathematically similar to what was done in section 3.2, although restricted to three-conductor lines.

An example of definition of differential and common-mode currents and voltages is in (3.49), corresponding to the currents in Fig. 3.21.

$$V_{DM} = V_1 - V_2 \quad I_{DM} = \frac{I_1 - I_2}{2} \quad (3.49a)$$

$$V_{CM} = \frac{V_1 + V_2}{2} \quad I_{CM} = I_1 + I_2 \quad (3.49b)$$

However, as the definition of common and differential mode vary considerably in the literature, a more generic decomposition will be studied here, using (3.50) as definition to common and differential mode:

$$V_{DM} = \frac{V_1 - V_2}{k_1} \quad I_{DM} = \frac{I_1 - I_2}{k_3} \quad (3.50a)$$

$$V_{CM} = \frac{V_1 + V_2}{k_2} \quad I_{CM} = \frac{I_1 + I_2}{k_4} \quad (3.50b)$$



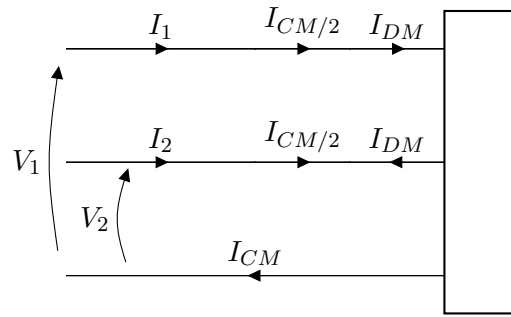


Figure 3.21 – Differential and common-mode currents

The constants  $k_1$ ,  $k_2$ ,  $k_3$ , and  $k_4$  are real, usually equal to 1 or 2, depending on the chosen definition.

The change of variables defined in the (3.50) can be expressed in matrix form, as shown in eqs. (3.51) to (3.53).

$$\mathbf{V}(x) = \mathbf{M}_V \mathbf{V}_M(x) \quad \mathbf{I}(x) = \mathbf{M}_I \mathbf{I}_M(x) \quad (3.51)$$

$$\mathbf{V}_M(x) = \begin{pmatrix} V_{DM}(x) \\ V_{CM}(x) \end{pmatrix} \quad \mathbf{I}_M(x) = \begin{pmatrix} I_{DM}(x) \\ I_{CM}(x) \end{pmatrix} \quad (3.52)$$

$$\mathbf{M}_V = \frac{1}{2} \begin{pmatrix} k_1 & k_2 \\ -k_1 & k_2 \end{pmatrix} \quad \mathbf{M}_I = \frac{1}{2} \begin{pmatrix} k_3 & k_4 \\ -k_3 & k_4 \end{pmatrix} \quad (3.53)$$

This formulation has the same structure as the modal decomposition defined by equation (3.23), rewritten hereafter:

$$\frac{\partial \mathbf{V}_M(x)}{\partial x} = -\mathbf{M}_V^{-1} \mathbf{z} \mathbf{M}_I \mathbf{I}_M(x) \quad (3.54a)$$

$$\frac{\partial \mathbf{I}_M(x)}{\partial x} = -\mathbf{M}_I^{-1} \mathbf{y} \mathbf{M}_V \mathbf{V}_M(x) \quad (3.54b)$$

From these equations, the modal impedance and admittance p.u.l. matrices can be defined, as follows:

$$\mathbf{z}_M = \mathbf{M}_V^{-1} \mathbf{z} \mathbf{M}_I \quad (3.55a)$$

$$\mathbf{y}_M = \mathbf{M}_I^{-1} \mathbf{y} \mathbf{M}_V \quad (3.55b)$$

From equations (3.54) and (3.55), it can be seen that common and differential mode will be decoupled if the modal matrices  $\mathbf{z}_M$  and  $\mathbf{y}_M$  are diagonal.

Suppose that the p.u.l. matrices  $\mathbf{z}$  and  $\mathbf{y}$  have the following generic structure:

$$\mathbf{z} = \begin{bmatrix} z_a & z_c \\ z_c & z_b \end{bmatrix} \quad \mathbf{y} = \begin{bmatrix} y_a & y_c \\ y_c & y_b \end{bmatrix}$$

Where  $z_a$ ,  $z_b$ ,  $z_c$ ,  $y_a$ ,  $y_b$ ,  $y_c$  are complex numbers. Recall that these matrices are symmetric

by definition. Then, matrices  $\mathbf{z}_M$  and  $\mathbf{y}_M$  will have the following structure:

$$\mathbf{z}_M = \begin{bmatrix} \frac{k_3}{2k_1}(z_a + z_b - 2z_c) & \frac{k_4}{2k_1}(z_a - z_b) \\ \frac{k_3}{2k_2}(z_a - z_b) & \frac{k_4}{2k_2}(z_a + z_b + 2z_c) \end{bmatrix} \quad (3.56a)$$

$$\mathbf{y}_M = \begin{bmatrix} \frac{k_1}{2k_3}(y_a + y_b - 2y_c) & \frac{k_2}{2k_3}(y_a - y_b) \\ \frac{k_1}{2k_4}(y_a - y_b) & \frac{k_2}{2k_4}(y_a + y_b + 2y_c) \end{bmatrix} \quad (3.56b)$$

From equations (3.56), it is demonstrated that the matrices  $\mathbf{z}_M$  and  $\mathbf{y}_M$  are diagonal if  $z_a = z_b$  and  $y_a = y_b$ , i.e., if the diagonal elements of matrices  $\mathbf{z}$  and  $\mathbf{y}$  are equal. In a cable where this condition is satisfied, common and differential mode will be decoupled, and the cable is balanced.

From (3.4), we can rewrite the balancing condition for three-conductor cables as follows:

- The p.u.l. resistance and self inductance of the active conductors (conductors 1 to  $n$ , reference conductor 0 excluded) must be the same;
- The sum of the p.u.l. conductance and capacitance between all the conductors must be same.

In conclusion, for a cable to be balanced, the diagonal elements of its p.u.l. parameter matrices  $\mathbf{z}$  and  $\mathbf{y}$  must be equal. It is equivalent to say that matrices  $\mathbf{z}$  and  $\mathbf{y}$  must be circular symmetric. For example, it is the case for three-conductor power cables with identical conductors equally spaced from each other, e.g. the three-conductor  $2.5 \text{ mm}^2$  cable used in the validation experiments (cf. section 3.4).

These conclusions are used to define a numerical analysis of the resonance in three-conductor cables, in the following section.

### 3.5.b Numerical analysis of the resonance in a three-conductor balanced system

A balanced system is a system in which the source, the cable and the load have decoupled common and differential mode, and each mode can be simulated individually [48].

Balanced systems are an interesting case of study because conceiving balanced common-mode filters is one of the most commonly used techniques to mitigate electromagnetic interference (EMI) problems, as it is a way to mitigate the common mode.

For this reason, and because their symmetry allows a visual representation of their resonant behavior, such systems are studied in this section. Recalling, the resonant surfaces of multiconductor cables can be determined mathematically for any system, but cannot be visually represented because they occupy more than three dimensions.

In the specific case of balanced systems, the resonant behavior of each mode (common and differential) will be computed and represented separately, as the modes are decoupled.

The system represented in Fig. 3.22, is balanced if the three-conductor transmission line is balanced (cf. section 3.5.a), and if the load connected at  $x = \ell_c$  is also balanced.

A balanced three-conductor cable has circulant impedance and admittance p.u.l. matrices  $\mathbf{z}$  and  $\mathbf{y}$ , as follows:

$$\mathbf{z} = \begin{bmatrix} z_1 & z_2 \\ z_2 & z_1 \end{bmatrix} \quad \mathbf{y} = \begin{bmatrix} y_1 & y_2 \\ y_2 & y_1 \end{bmatrix} \quad (3.57)$$

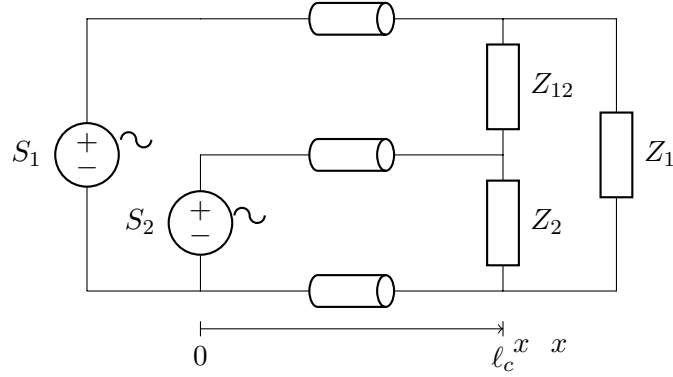


Figure 3.22 – Schematic for numerical resonance analysis,  $\ell_c = 12\text{ m}$

The  $2.5\text{ mm}^2$  three-conductor cable used in section 3.4, which has the parameters plotted in Fig. 3.19, is balanced. Its resonant behavior is analyzed in this section.

The mathematical change from the physical basis to the common/differential modes base is defined as follows:

$$\mathbf{V}(x) = \mathbf{M}_V \mathbf{V}_M(x) \quad (3.58)$$

$$\mathbf{I}(x) = \mathbf{M}_I \mathbf{I}_M(x) \quad (3.59)$$

$$\mathbf{M}_V = \frac{1}{2} \begin{bmatrix} 1 & 2 \\ -1 & 2 \end{bmatrix} \quad \mathbf{M}_I = \frac{1}{2} \begin{bmatrix} 2 & 1 \\ -2 & 1 \end{bmatrix} \quad (3.60)$$

The modal voltages  $\mathbf{V}_M(x)$  and currents  $\mathbf{I}_M(x)$  are defined in (3.61), where  $V_{DM}$  and  $I_{DM}$  are respectively the differential-mode voltage and current, and  $V_{CM}$  and  $I_{CM}$  the common-mode voltage and current along the line.

$$\mathbf{V}_M(x) = \begin{bmatrix} V_{DM}(x) \\ V_{CM}(x) \end{bmatrix} \quad \mathbf{I}_M(x) = \begin{bmatrix} I_{DM}(x) \\ I_{CM}(x) \end{bmatrix} \quad (3.61)$$

The impedance matrix of the load in Fig. 3.20 is written below; it was obtained considering  $\mathbf{V}(\ell_c) = \mathbf{Z}_L \mathbf{I}(\ell_c)$ :

$$\mathbf{Z}_L = \frac{1}{Z_1 + Z_2 + Z_{12}} \begin{bmatrix} Z_1(Z_2 + Z_{12}) & Z_1 Z_2 \\ Z_1 Z_2 & Z_2(Z_1 + Z_{12}) \end{bmatrix} \quad (3.62)$$

The modal load impedance matrix that meets  $\mathbf{V}_M(x) = \mathbf{Z}_{LM} \mathbf{I}_M(x)$ , can be determined as follows:

$$\mathbf{Z}_{LM} = \mathbf{M}_V^{-1} \mathbf{Z}_L \mathbf{M}_I \quad (3.63a)$$

$$\mathbf{Z}_{LM} = \frac{1}{Z_1 + Z_2 + Z_{12}} \begin{bmatrix} Z_{12}(Z_1 + Z_2) & \frac{1}{2} Z_{12}(Z_1 - Z_2) \\ \frac{1}{2} Z_{12}(Z_1 - Z_2) & \frac{1}{4} Z_{12}(Z_1 + Z_2) + 4Z_1 Z_2 \end{bmatrix} \quad (3.63b)$$

The common and differential mode are decoupled in the load if the matrix  $\mathbf{Z}_{LM}$  is diagonal. That is true if  $Z_1 = Z_2$ , i.e. if the load is balanced.

For a balanced load  $\mathbf{Z}_{\mathbf{L}_M}$  has only two diagonal elements  $Z_{L_{DM}}$  and  $Z_{L_{CM}}$ :

$$\mathbf{Z}_{\mathbf{L}_M} = \begin{bmatrix} Z_{L_{DM}} & 0 \\ 0 & Z_{L_{CM}} \end{bmatrix} = \begin{bmatrix} \frac{2Z_1 Z_{12}}{Z_{12} + 2Z_1} & 0 \\ 0 & \frac{Z_1}{2} \end{bmatrix} \quad (3.64)$$

With the load modal decomposition, we can separate the common and differential mode of the system in Fig. 3.22 into two independent systems, having each an equivalent two-conductors cable, using formulation presented in section 3.2.b. It results in the two subsystems: (3.65) for the differential mode and (3.66) for the common mode. The definitions (3.67) and (3.68) are also used.

$$\left\{ \begin{array}{l} \begin{pmatrix} V_{DM}(\ell_c) \\ I_{DM}(\ell_c) \end{pmatrix} = \begin{bmatrix} \cosh(\gamma_{DM}\ell_c) & -Z_{c_{DM}} \sinh(\gamma_{DM}\ell_c) \\ -\frac{1}{Z_{c_{DM}}} \sinh(\gamma_{DM}\ell_c) & \cosh(\gamma_{DM}\ell_c) \end{bmatrix} \begin{pmatrix} V_{DM}(0) \\ I_{DM}(0) \end{pmatrix} \\ V_{DM}(0) = S_{DM} \\ V_{DM}(\ell_c) = Z_{L_{DM}} I_{DM}(\ell_c) \end{array} \right. \quad (3.65a)$$

$$(3.65b)$$

$$(3.65c)$$

$$\left\{ \begin{array}{l} \begin{pmatrix} V_{CM}(\ell_c) \\ I_{CM}(\ell_c) \end{pmatrix} = \begin{bmatrix} \cosh(\gamma_{CM}\ell_c) & -Z_{c_{CM}} \sinh(\gamma_{CM}\ell_c) \\ -\frac{1}{Z_{c_{CM}}} \sinh(\gamma_{CM}\ell_c) & \cosh(\gamma_{CM}\ell_c) \end{bmatrix} \begin{pmatrix} V_{CM}(0) \\ I_{CM}(0) \end{pmatrix} \\ V_{CM}(0) = S_{CM} \\ V_{CM}(\ell_c) = Z_{L_{CM}} I_{CM}(\ell_c) \end{array} \right. \quad (3.66a)$$

$$(3.66b)$$

$$(3.66c)$$

$$Z_{c_{DM}} = 2\sqrt{\frac{z_1 - z_2}{y_1 - y_2}} \quad \gamma_{DM} = \sqrt{(z_1 - z_2)(y_1 - y_2)} \quad (3.67)$$

$$Z_{c_{CM}} = \frac{1}{2}\sqrt{\frac{z_1 + z_2}{y_1 + y_2}} \quad \gamma_{CM} = \sqrt{(z_1 + z_2)(y_1 + y_2)} \quad (3.68)$$

The resonance surface response can be plotted for each of the systems with eqs. (3.65) and (3.66). Multiple simulations were performed to calculate the maximal amplifications of the modal voltages  $V_{DM}$  and  $V_{CM}$  due to resonance in function of the modal impedances  $Z_{L_{DM}} = A_{DM} + jB_{DM}$  and  $Z_{L_{CM}} = A_{CM} + jB_{CM}$ , respectively, in the range values presented in table 3.2. The maximum voltage amplification for each load among the different values of  $f$  and  $x$  was stored, along with the frequency  $f_{max}$  and the position  $x_{max}$  to which it took place.

Table 3.2 – Range of values used in the numerical analysis of the resonance

Variable	Range	Number of points	Scaling
$A_{DM}, A_{CM}$	$[0, 100] k\Omega$	401	log
$B_{DM}, B_{CM}$	$[-100, 100] k\Omega$	401	log
$f$	$[0.01, 10] MHz$	5000	log
$x$	$[0, 12] m$	25	linear

The surfaces maximal voltage amplification of each mode are plotted in Fig. 3.23, the frequency to which each of the maximal amplification take place are represented plotted in Fig. 3.24 and the position where they occur is plotted in the surfaces in Fig. 3.25.

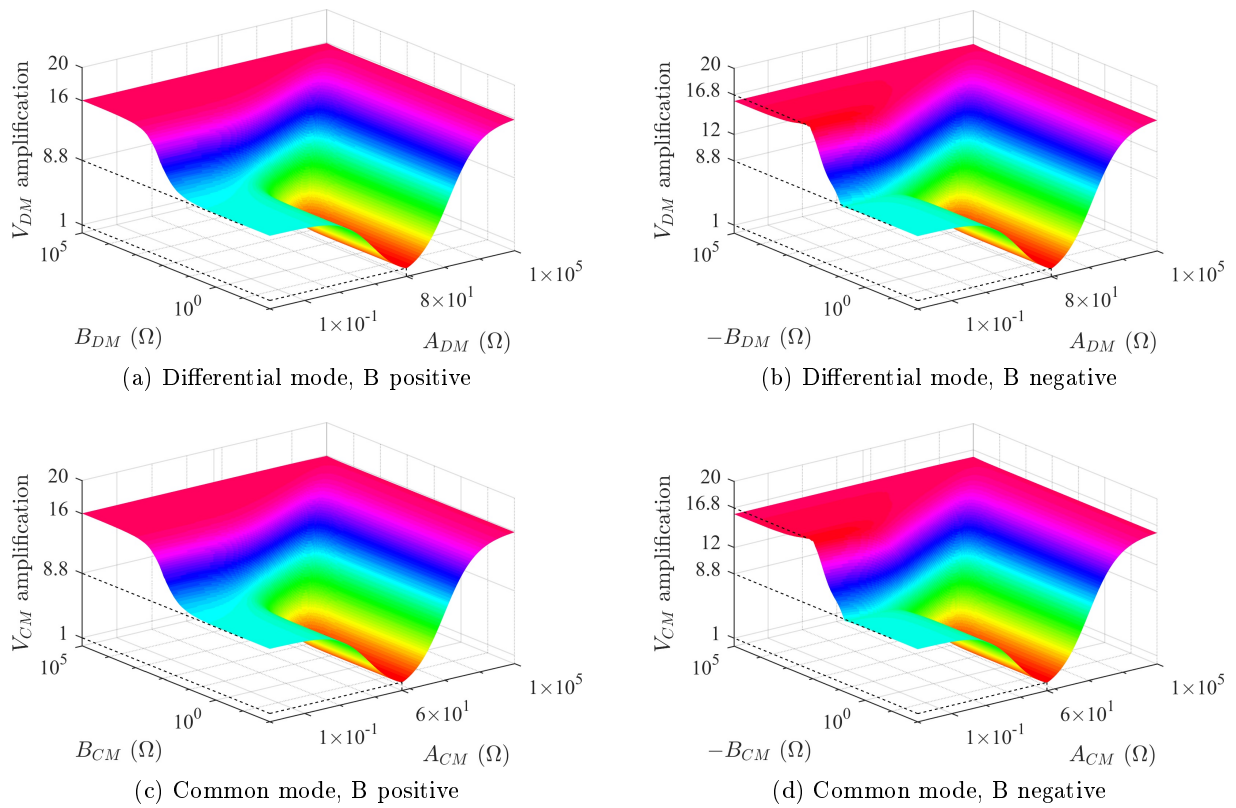


Figure 3.23 – Voltage amplification due to resonance on the three-conductor cable, in differential and common mode, in function of the modal load

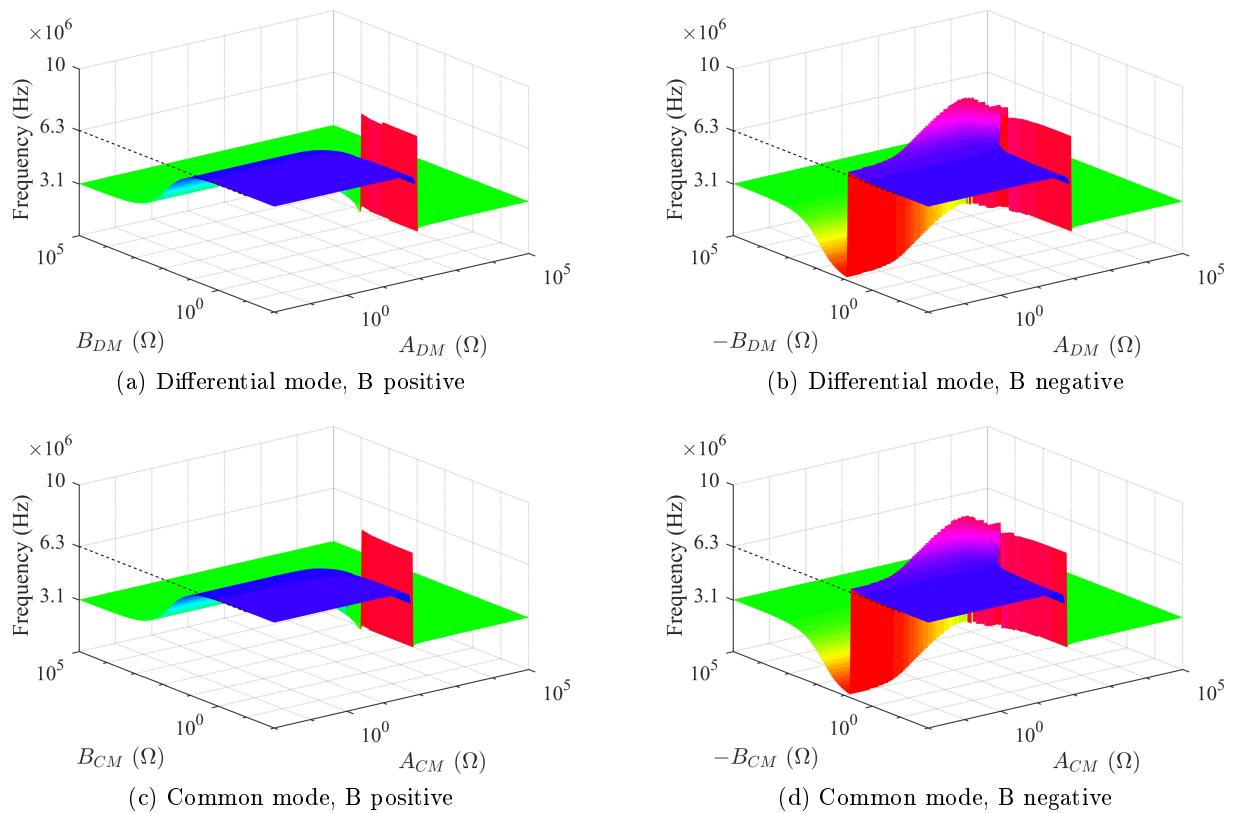


Figure 3.24 – Resonance frequencies of the three-conductor cable, in differential and common mode, in function of the modal load

There are few differences between the differential and common-mode surface, the main one being the position of the minimal amplification. The differential-mode characteristic impedance is around  $Z_{c_{DM}} = 80 \Omega$ , while the common-mode characteristic impedance is around  $Z_{c_{CM}} = 60 \Omega$ . The voltage amplification tends to 1 for the regions where  $Z_{L_{DM}} \approx Z_{c_{DM}}$ , or  $Z_{L_{CM}} \approx Z_{c_{CM}}$ .

The maximal amplification, in both modes, seems to happen for a specific negative value of  $B$ , with very low values for  $A$ , i.e., the maximal resonance occurs for a capacitive load.

As expected, in most cases the higher amplifications areas in Figs. 3.23 correspond to the lower resonance frequencies in Figs. 3.24. The voltage amplification dependence on the cable losses is yet again demonstrated.

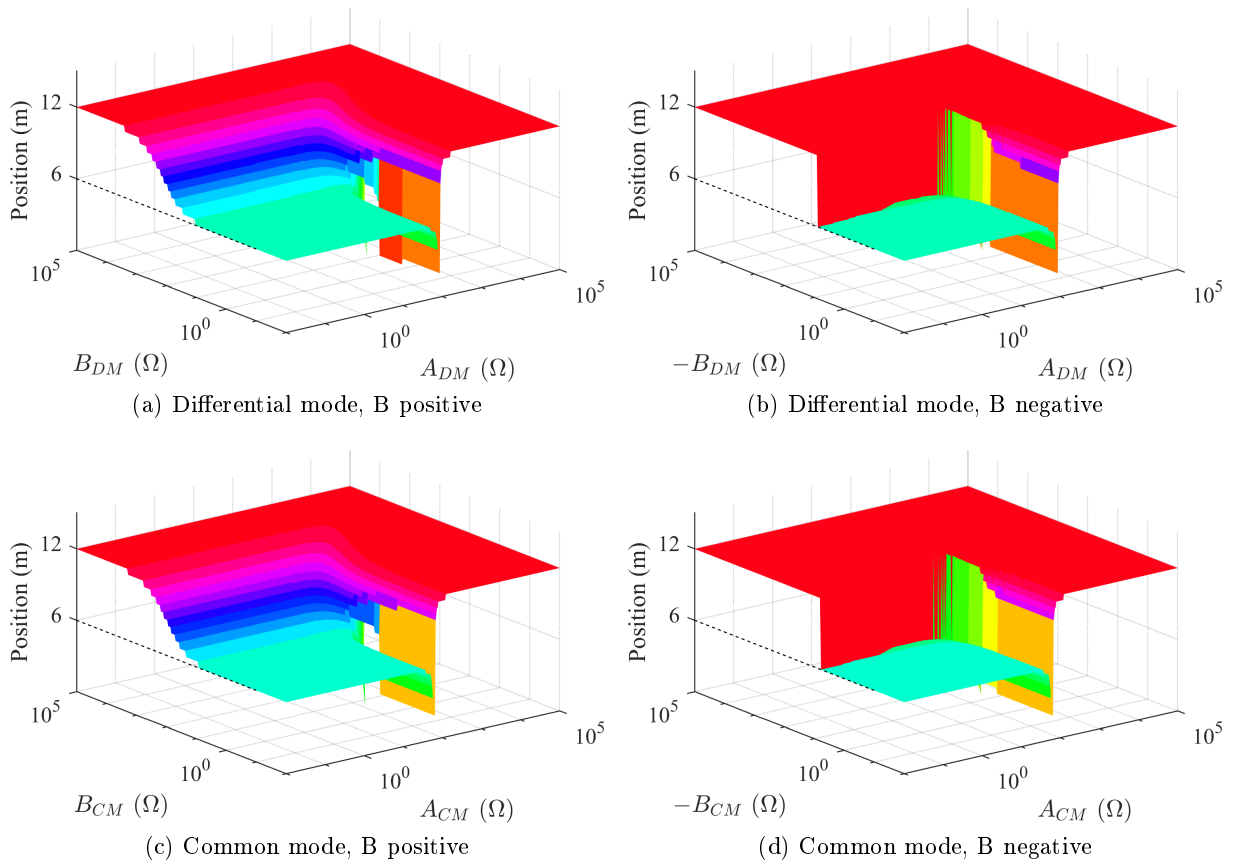


Figure 3.25 – Position of the maximal voltage amplification on the three-conductor cable, in differential and common mode, in function of the modal load

The maximal amplification tends to occur at  $x = \ell_c$  for the resonance frequencies around  $3.1 \text{ MHz}$ , and at  $x = \ell_2/2$  for the resonance frequencies around  $6.3 \text{ MHz}$ .

In general, figures 3.23 to 3.25 present the same behavior as the two-conductor cables studied in section 2.5.b and in appendix C. It corresponds to our expectations, as the decoupled differential and common mode effectively behave as two separated two-conductor transmission-lines.

However, because the surface of voltage amplification is plotted on the common/differential modes mathematical base, the predicted amplifications do not correspond to the amplifications in voltages  $V_1(x)$  and  $V_2(x)$ .

This characteristic will be exemplified below, in a study of the resonant behavior of the cable for a given load.

**Identifying the resonance behavior of the cable for a given load:** As an example of application of the resonance surfaces plotted in this section, the resonant behavior of the three-conductor cable will be studied for the load presented in Fig. 3.26. The complete system under study is represented by the schematic in Fig. 3.20, where the cable length is  $\ell_c = 12 m$

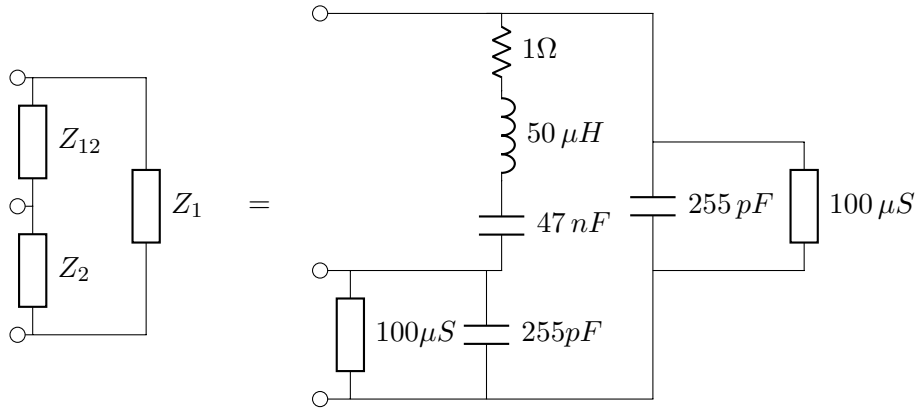


Figure 3.26 – Load used for this example

Note that the chosen load is balanced.

The impedance matrix of this load is calculated and converted to the modal base with (3.63a), and its modal impedances are plotted over the resonance frequency surfaces in Fig. 3.27

There is one intersection point per mode between the load impedance in function of frequency and the resonance surface. The frequencies to which these intersections occur are the resonance frequencies of the system.

To determine the voltage amplification each of these resonance frequencies will generate, in the modal base, we identified the correspondent points on the voltage amplification surfaces, in Fig. 3.28. The same way, to identify where along the line these voltage amplifications will take place, we identified the intersection points on the position surfaces, in Fig. 3.29.

With this analysis, the resonance behavior of each mode is identified. The characteristics of each resonance are resumed in table 3.3.

Table 3.3 – Resonance characteristics - modal base

	Frequency	Voltage Amplification	Position
Differential mode	2.92 MHz	15.2	12 m
Common mode	2.29 MHz	14.3	12 m

For both modes, the maximal amplification occurs at  $x = \ell_c$ . The amplification of the differential and common-mode voltage at  $x = \ell_c$  are plotted in function of the frequency in Fig. 3.30

The voltages can be represented in the regular, or physical, basis using (3.58), from which the voltage conversion can be more simply written (3.69).

$$V_1 = \frac{V_{MD}}{2} + V_{MC} \quad (3.69a)$$

$$V_2 = -\frac{V_{MD}}{2} + V_{MC} \quad (3.69b)$$

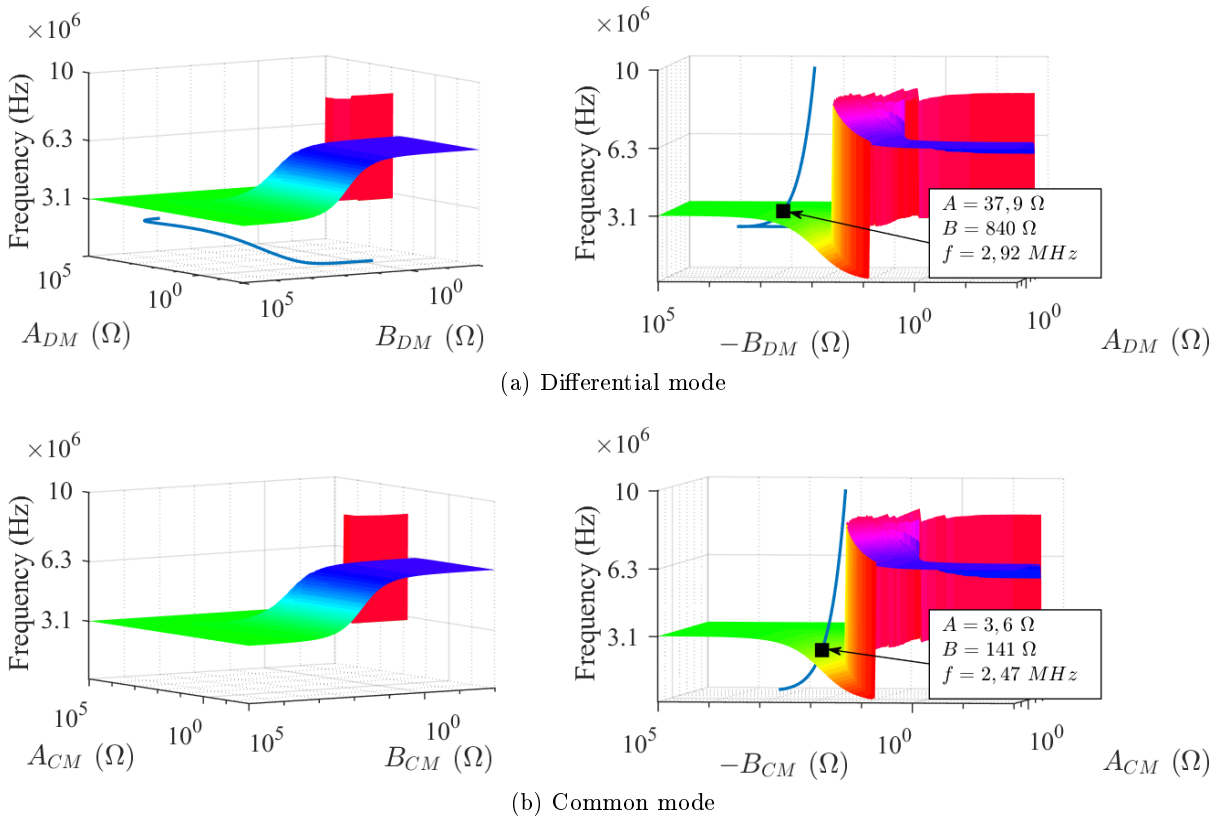


Figure 3.27 – Intersection of the modal impedances with the resonance frequency surfaces.

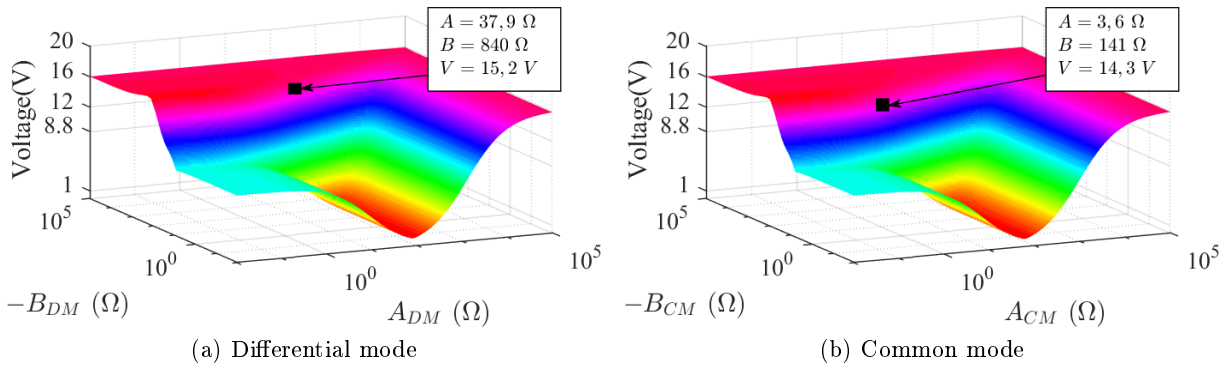


Figure 3.28 – Points of intersection on the voltage amplification resonance surfaces

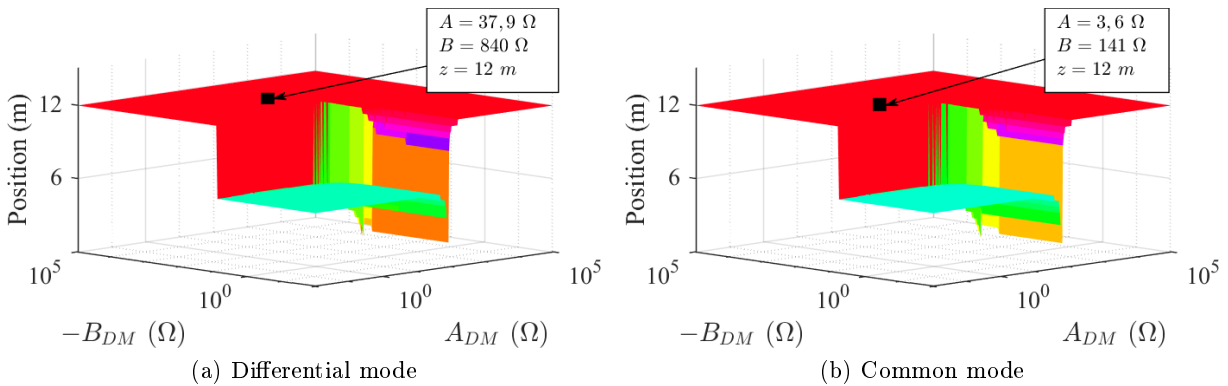


Figure 3.29 – Points of intersection on the position of maximal amplification due to resonance surfaces



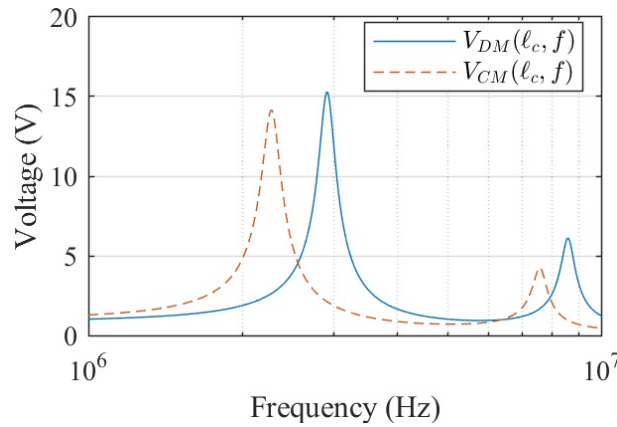


Figure 3.30 – Voltage at  $x = \ell_c$ , common/differential modes

For example, from (3.69) it can be seen that the resonance-due voltage amplification from the differential-mode resonance will be divided by two. Also, because the voltages  $V_1(x)$  and  $V_2(x)$  are a linear combination of both common and differential modes, they will be amplified at the resonance frequencies of both modes.

This behavior is confirmed in Fig. 3.31, where the voltages  $V_1(\ell_c)$  and  $V_2(\ell_c)$  are plotted in function of the frequency.

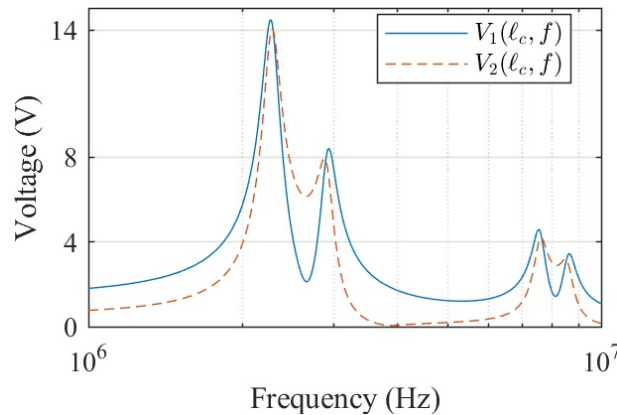


Figure 3.31 – Voltage at  $x = \ell_c$ , physical base

In conclusion, the surfaces characterizing the resonance behavior of a three-conductor balanced cable, connected to balanced source and load, can be used the same way as the resonance surfaces of the two-conductor cable presented in section 2.5.b. However, because the maximal voltage amplification is plotted on the modal base, its values do not correspond to the physical voltage amplification that will take place in the cable. Indeed, the physical voltages  $V_1(x)$  and  $V_2(x)$  are a linear combination of the modal voltages  $V_{DM}(x)$  and  $V_{CM}(x)$ .

### 3.5.c Difficulties to generalize the resonance surfaces to any load matrix

The results in the previous sections are only valid for balanced systems.

It would be interesting to extend the proposed analysis to any system. However, a strong difficulty arises in this attempt: there is no generic transformation that can diagonalize any matrix.

As a consequence, in the general case, an unbalanced device is represented by an impedance/admittance matrices that have different orthonormal eigenvectors for different frequencies.

The surfaces plotted in the previous section only make sense if the transformation matrix  $\mathbf{M}$  is kept constant. Therefore, if we choose a fixed diagonalization matrix  $\mathbf{M}$ , only a portion of all the possible load matrices will be diagonalized by it: the group of symmetric matrices having the eigenvectors in  $\mathbf{M}$ . This is a group of matrices as limited as the group of circulant symmetric matrices (balanced systems).

It is important to highlight that numerical resonance analysis with a generic multi-port load can be mathematically performed, despite these difficulties. After all,  $n$ -dimensional spaces exist mathematically, the difficulties only arise on the attempts to graphically represent them. In other words, the difficulties brought here only restrain the handy 3D representation of the resonant behavior of multiconductor cables.

In conclusion, even if 3-dimensional plots cannot thoroughly represent the resonance behavior of an unbalanced system, a purely mathematical approach can give the same results. It can be an interesting tool to be developed, but it is not treated in the scope of this work.

## 3.6 Conclusion

In this chapter the multiconductor transmission lines (MTL) were studied, and a frequency domain simulation tool for MTL has been developed. The simulation tool is valid for a radial network of multiconductor cables in which the distance between the conductors does not change along the cables. Multiconductor cables parameters were identified experimentally, from DC up to  $30\text{ MHz}$ . The upper limit of the frequency is imposed by the frequency limits of the devices available for experimental parameter identification. The cable parameters were injected on simulator, and the simulation results were validated with two different validation experiments.

As for the two-conductor case, the model proposed here respects the requirements listed in section 1.3. The MTL model in the frequency domain is length-scalable and models wave propagation and resonance, and allows an accurate representation of the cable parameters, which are frequency dependent. These parameters are determined using an impedance analyzer in the desired frequency-band. The frequency domain simulation is computationally efficient, and can represent the hypothetical radial network by concatenating the MTL model.

The losses of the cables were correctly predicted, what allows the developed tool to predict with accuracy the resonance-due amplifications anywhere in the network. Also, the frequency to which resonance occurs and the position along the cabling where the maximum voltage/current will take place can be predicted.

Also, the resonance behavior of a balanced system, using a three-conductor long cable, was computed, and represented in a 3-dimensional surface. However, this approach cannot be easily generalized to a generic system. Despite that, the approach described to obtain the resonance surfaces can be used to develop a numerical optimization tool to characterize the resonance behavior of a given system, but without the visual aid proportioned by the plotting of the resonance surfaces.



## CONTENTS

---

4.1	INTRODUCTION . . . . .	88
4.2	TIME-DOMAIN TRANSMISSION LINES MODELS . . . . .	88
4.2.a	Analytical solution: the Heaviside condition . . . . .	89
4.2.b	Time-domain equivalent circuits . . . . .	92
4.3	FREQUENCY-DOMAIN MODEL RESULTS CONVERTED TO TIME DOMAIN . . . . .	95
4.3.a	Periodic signals transform . . . . .	95
4.3.b	Generalized transform . . . . .	96
4.3.c	Time domain transform of the frequency domain solution . . . . .	96
4.4	TIME-DOMAIN VALIDATION . . . . .	99
4.4.a	Two-conductor cable validation . . . . .	101
4.4.b	Three-conductor cable validation . . . . .	105
4.5	QUALITATIVE ANALYSIS OF THE FREQUENCY DOMAIN MODEL . . . . .	108
4.5.a	Impact of the frequency dependence of the parameters . . . . .	109
4.5.b	The wave traveling delay . . . . .	110
4.5.c	Advantages of the frequency domain model . . . . .	111
4.6	CONCLUSION . . . . .	111

---

### Abstract

*This chapter aims to build a time domain simulation tool for multiconductor transmission lines. Many options for the transmission line simulations in time domain are available in the literature. These option will be discussed, and a time domain simulation based on the frequency domain model developed in the previous chapters will be proposed, and experimentally validated. The cable parameters are obtained experimentally, as done in the previous chapters.*

## 4.1 Introduction

The telegrapher equations do not yet have a general solution for lossy cables on time domain. Despite that, many modeling techniques are available in the literature, the most accurate of them represent the frequency dependence of the losses on time domain. They may consist in equivalent circuits that emulate the behavior of the cable losses, or in numerical solutions of the telegrapher equations, with approximated functions representing the losses. These techniques can predict the line behavior with a good accuracy if the equivalent models/approximations are valid. They will be more extensively discussed along this chapter.

The goal of this chapter is to choose a time domain modeling technique, from which will be built a simulation tool, as done in the previous chapters. The tool will model a hypothetical radial network composed of multiconductor cables, in which the characteristics of the conductors and the distance between them remains the same along the line. Indeed, industrial and building networks are radial, and the hypothesis that the distance between the conductors does not vary along the line is strong, but reasonable, because it does not vary drastically for wires inside electrical conduits, and the results of the model based on this hypothesis will represent a good approximation of the behavior of the line.

The line model must correctly predict the resonance phenomena anywhere in the network, as for the frequency domain model developed in the previous chapters. Accordingly, the cable parameters will be obtained experimentally, and the modeling of the cable losses must be accurate. We recall, the resonance amplifications are limited mainly by the losses in the cable.

Section 4.2 discusses several techniques found in the literature to model transmission lines on time domain. Section 4.3 introduces the chosen time domain modeling technique, and describes the structure of the time domain simulation tool. Section 4.4 shows the experimental validation of the simulation tool built in section 4.3. Section 4.5.c highlights the advantages of the proposed time domain modeling technique related to usual modeling techniques found in the literature.

## 4.2 Time-domain transmission lines models

An analytical time domain model of a generic transmission line is not yet found in the literature. Indeed, transforming the frequency domain solutions described in the precedent chapters to time domain presents complicated mathematical challenges. The analytical transform of the frequency domain solution to the telegrapher equations of time domain has two main obstacles:

1. The analytical inverse Laplace transform of  $e^{\sqrt{s}}$  is not known;
2. The per-unit-length loss-related parameters  $r$  and  $g$  are highly frequency dependent, and cannot be approximated by constants without compromising the generality of the model. They need causal analytical equivalent models  $r(s)$  and  $g(s)$  for the inverse Laplace transform to be possible.

An example of Causal analytical models approximating the per-unit-length (p.u.l.) parameters  $r(s)$ ,  $l(s)$ ,  $g(s)$ , and  $c(s)$  are defined in [57]. They could be a first step in the analytical inverse Laplace transform, if the first problem in the list above could be solved.

The telegrapher equations themselves can be written on time domain, but they assume a complicated form of second order differential equations to which no analytical solution is known.

For these reasons, at present, there is no time domain analytical solution for the transmission line problem in the general case.

A well-known analytical solution for lossless lines is described in [33], and an analytical time domain solution for lines respecting the Heaviside condition is derived in section 4.2.a, as an example of the analytical solution of the telegrapher equations.

To work around this issue, there are multiple time domain transmission line models available in the literature, using different approximations to represent the time domain behavior of the transmission line.

One of them is a numerical solution using a finite-differences time domain solution described in [33]. It is an efficient method, but it requires an expression of  $r(s)$  and  $g(s)$  that can be transformed by the inverse Laplace transform, what is usually done with asymptotic approximations; leading to a loss in the accuracy of the results [33].

Another well-known representation of lossy lines on time domain are the series association of elementary transmission-line cells associated with T-ladder networks, to emulate the high-frequency behavior of the line losses. This modeling method is discussed in section 4.2.b.

The method chosen for this work consists in representing the system under analysis on frequency domain, via Fourier Series or Fourier Transform, solving the problem on frequency domain and transform only the results back to time domain. This method is formally described in section 4.3.

#### 4.2.a Analytical solution: the Heaviside condition

The analysis of a possible analytical solution of the telegrapher equations in the time domain is discussed in this section. It is useful only for lossless and/or analogical communication cables, and serves as example of an analytical solution to time domain.

The two-conductor line frequency domain solution in (2.4) can be analytically transformed to time domain via the Laplace inverse transform if the Heaviside condition (4.1) is respected.

$$\frac{r}{g} = \frac{l}{c} \quad (4.1)$$

Note that the lossless line ( $r = 0$  and  $g = 0$ ) is a special case that respects the Heaviside condition. Power cables do not respect this condition in the medium frequencies band, mainly because of the dependence of the parameters  $r$  and  $g$  with the frequency (cf. sections 2.4.c and 3.4.c).

As will be seen below (cf. eq. (4.4)), the Heaviside condition guarantees that the propagation speed will be constant with frequency, thus avoiding distortions in the signal in time domain. This condition was postulated by Oliver Heaviside in the XIXth century.

If the Heaviside condition is respected, the propagation coefficient  $\gamma$  and the characteristic

impedance  $Z_c$  of a two-conductor transmission line can be rewritten as follows:

$$\begin{aligned}\gamma &= \sqrt{(r + j\omega l)(g + j\omega c)} = \\ &= \sqrt{l c} \sqrt{\left(\frac{r}{l} + j\omega\right) \left(\frac{g}{c} + j\omega\right)} = \sqrt{l c} \left(\frac{r}{l} + j\omega\right)\end{aligned}\quad (4.2)$$

$$\begin{aligned}Z_c &= \sqrt{\frac{r + j\omega l}{g + j\omega c}} = \\ &= \sqrt{\frac{l}{c}} \sqrt{\frac{\left(\frac{r}{l} + j\omega\right)}{\left(\frac{g}{c} + j\omega\right)}} = \sqrt{\frac{l}{c}}\end{aligned}\quad (4.3)$$

Therefore, for a line respecting this condition, the propagation speed is independent of frequency ( $\beta = \mathbb{I}\{\gamma\}$ ):

$$v = \frac{\omega}{\beta} = \frac{1}{\sqrt{l c}}\quad (4.4)$$

The solution of the telegrapher equations in the frequency domain in eq. (2.4) can be written using coefficients  $V^+$  and  $V^-$  in function of the frequency, which are, we recall, coefficients issued from the differential equation solution, to be determined from the boundary conditions. Eq. (2.4) can be rewritten as:

$$V(x, \omega) = V^+(\omega)e^{-x\gamma} + V^-(\omega)e^{x\gamma}\quad (4.5a)$$

$$I(x, \omega) = \frac{V^+(\omega)}{Z_c}e^{-x\gamma} - \frac{V^-(\omega)}{Z_c}e^{x\gamma}\quad (4.5b)$$

Using the transformation  $j\omega \rightarrow s$  equations (4.5) can be written in the Laplace space, and the line propagation constant can be simplified to  $\gamma = \sqrt{\frac{c}{l}r + s\sqrt{l c}} = \alpha + \frac{s}{v}$ .

$$V(x, s) = V^+(s)e^{-x(\alpha + \frac{s}{v})} + V^-(s)e^{x(\alpha + \frac{s}{v})}\quad (4.6a)$$

$$I(x, s) = \frac{V^+(s)}{Z_c}e^{-x(\alpha + \frac{s}{v})} - \frac{V^-(s)}{Z_c}e^{x(\alpha + \frac{s}{v})}\quad (4.6b)$$

The term  $e^{-x(\alpha + \frac{s}{v})}$  in equations (4.6) has an analytical Inverse Laplace Transform using the delay theorem.

To obtain the complete Inverse Transform, the expressions of  $V^+(s)$  and  $V^-(s)$  must be determined.

Take the schematic of the general model in 2.3, where a Thévenin equivalent is connected to both ends of the line. By evaluating  $V(x, s)$  and  $I(x, s)$  at  $x = 0$  and  $x = l$ , we have:

$$V(0, s) = V_S - Z_S I(0, s)\quad (4.7)$$

$$I(\ell_c, s) = V_L + Z_L I(\ell_c, s)\quad (4.8)$$

$$V^+(s) + V^-(s) = V_S - \frac{Z_S}{Z_c} (V^+(s) - V^-(s))\quad (4.9)$$

$$V^+(s)e^{-\ell_c(\alpha + \frac{s}{v})} + V^-(s)e^{\ell_c(\alpha + \frac{s}{v})} = V_L - \frac{Z_L}{Z_c} (V^+(s)e^{-\ell_c(\alpha + \frac{s}{v})} - V^-(s)e^{\ell_c(\alpha + \frac{s}{v})})\quad (4.10)$$

By manipulating equations (4.7) to (4.10) and including the reflection coefficients, redefined

below (4.11), an expression to  $V^+(s)$  and  $V^-(s)$  can be written as in (4.12)

$$\Gamma_S = \frac{Z_S - Z_c}{Z_S + Z_c} \quad \Gamma_L = \frac{Z_L - Z_c}{Z_L + Z_c} \quad (4.11)$$

$$V^+(s) = \frac{e^{\ell_c \alpha} e^{\ell_c \frac{s}{v}}}{e^{2\ell_c \alpha} e^{2\ell_c \frac{s}{v}} + 1} \left( \frac{Z_c}{Z_S + Z_c} e^{\ell_c \alpha} e^{\ell_c \frac{s}{v}} V_S(s) + \frac{Z_c}{Z_L + Z_c} \Gamma_S V_L(s) \right) \quad (4.12a)$$

$$V^-(s) = \frac{1}{e^{2\ell_c \alpha} e^{2\ell_c \frac{s}{v}} + 1} \left( \frac{Z_c}{Z_S + Z_c} \Gamma_L V_S(s) + \frac{Z_c}{Z_L + Z_c} e^{\ell_c \alpha} e^{\ell_c \frac{s}{v}} V_L(s) \right) \quad (4.12b)$$

Recalling the delay theorem: the Laplace transform of a function with a time delay  $a$  is:

$$\mathcal{L}[f(t+a)u(t+a)] = F(s)e^{as}$$

Using this theorem, the inverse Laplace transform of  $V(x, s)$  and  $I(x, s)$  can now be obtained:

$$\begin{aligned} V(x, t) &= \\ &= \frac{Z_c}{Z_S + Z_c} e^{-x\alpha} \sum_{n=1}^{\infty} (\Gamma_S \Gamma_L)^{n-1} e^{-\ell_c \alpha (2n-2)} V_S \left[ t - \frac{x}{v} - (2n-2)T_D \right] + \\ &+ \frac{Z_c}{Z_L + Z_c} e^{-x\alpha} \Gamma_S \sum_{n=1}^{\infty} (\Gamma_S \Gamma_L)^{n-1} e^{-\ell_c \alpha (2n-1)} V_L \left[ t - \frac{x}{v} - (2n-1)T_D \right] + \\ &+ \frac{Z_c}{Z_S + Z_c} e^{x\alpha} \Gamma_L \sum_{n=1}^{\infty} (\Gamma_S \Gamma_L)^{n-1} e^{-\ell_c \alpha 2n} V_S \left[ t + \frac{x}{v} - 2nT_D \right] + \\ &+ \frac{Z_c}{Z_L + Z_c} e^{x\alpha} \sum_{n=1}^{\infty} (\Gamma_S \Gamma_L)^{n-1} e^{-\ell_c \alpha (2n-1)} V_L \left[ t + \frac{x}{v} - (2n-1)T_D \right] \end{aligned} \quad (4.13a)$$

$$\begin{aligned} I(x, t) &= \\ &= \frac{1}{Z_S + Z_c} e^{-x\alpha} \sum_{n=1}^{\infty} (\Gamma_S \Gamma_L)^{n-1} e^{-\ell_c \alpha (2n-2)} V_S \left[ t - \frac{x}{v} - (2n-2)T_D \right] + \\ &+ \frac{1}{Z_L + Z_c} e^{-x\alpha} \Gamma_S \sum_{n=1}^{\infty} (\Gamma_S \Gamma_L)^{n-1} e^{-\ell_c \alpha (2n-1)} V_L \left[ t - \frac{x}{v} - (2n-1)T_D \right] + \\ &- \frac{1}{Z_S + Z_c} e^{x\alpha} \Gamma_L \sum_{n=1}^{\infty} (\Gamma_S \Gamma_L)^{n-1} e^{-\ell_c \alpha 2n} V_S \left[ t + \frac{x}{v} - 2nT_D \right] + \\ &- \frac{1}{Z_L + Z_c} e^{x\alpha} \sum_{n=1}^{\infty} (\Gamma_S \Gamma_L)^{n-1} e^{-\ell_c \alpha (2n-1)} V_L \left[ t + \frac{x}{v} - (2n-1)T_D \right] \end{aligned} \quad (4.13b)$$

These equations model the propagation of the reflected waves in the line, representing in written form what is usually described with the lattice diagram for transmission lines. The first sum term in each equation corresponds to the input voltage waveform  $V_S(t)$  propagating in the  $+x$  direction in the line, while the third sum term corresponds to the same waveform  $V_S(t)$  propagating in the  $-x$  direction. The second and fourth terms correspond to the waveform of  $V_L(t)$  propagating in the  $+x$  and  $-x$  directions, respectively.

There are no known time domain solution of the telegrapher equations more generic than the one derived here. Still, it cannot be used for the building cabling, because the concerned cables do not respect the Heaviside condition in the general case. Therefore, other options must be investigated to model these cables in the time domain.



### 4.2.b Time-domain equivalent circuits

There are transmission line models in the literature that can be simulated on time domain, with any 0D circuit simulator. The most common of these models are based on the fact that the Multiconductor Transmission Line (MTL) model is built with the series association of the basic cell represented in Fig. 3.2. The modeling equations assembled in section 3.2.c, to describe the MTL simulation tool, is equivalent to a series association of an infinite number of these cells, each of infinitesimal length  $dx$ . Of course, the series association of the finite number of these cells can also represent the behavior of the transmission line within an acceptable accuracy, if the length of each cell is considerably small when compared to the smallest wavelength that propagates in the line. A commonly used empiric rule is to guarantee that each cell represents a portion of the line smaller than  $\lambda/10$ .

Therefore, a transmission line can be simulated in the time domain with a series association of a number of cells sufficiently high to properly represent the transmission line in question.

However, the simple association of the cells in Fig. 3.2 does not allow the representation of phenomena such as the skin effect and the proximity effect, and the frequency behavior of the dielectric material insulating the MTL conductors. As mentioned before, in the frequency domain, these phenomena are represented by the evolution in function of the frequency of the p.u.l. parameters  $\mathbf{r}$ ,  $\mathbf{l}$ , and  $\mathbf{g}$ . If the basic cell in Fig. 3.2 is used for a time domain simulation, the values of these parameters have to be fix.

It is possible to walk around this problem by representing the aforementioned parameters in form of equivalent circuits that emulate their dependence with the frequency [18,27,33,53].

The dependence of the p.u.l. resistance with the frequency can be modeled with a RL T-ladder network, as the one represented in Fig. 4.1a [56]. The impedance of the inductance on each step will increase with frequency, and with  $\omega \rightarrow \infty$  the equivalent impedance of the network is the resistance  $r_0$ . On the other hand, when  $\omega = 0$  the equivalent impedance will be the parallel association of all the resistances in the ladder. Therefore,  $r_0$  should represent the high frequency value of the p.u.l. resistance, and the association  $r_0 \parallel r_1 \parallel \dots \parallel r_n$  the DC p.u.l. resistance.

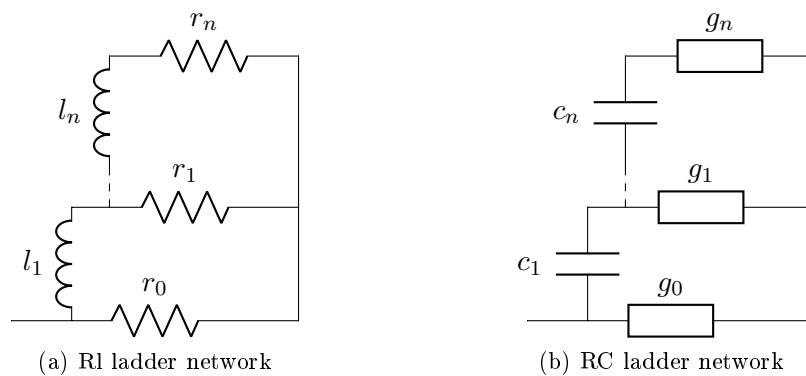


Figure 4.1 – T-ladder network to represent the cable losses

Similarly, the evolution of the p.u.l. conductance with frequency can be represented by the RC ladder association in Fig. 4.1b [18,53]. With a similar analysis, it can be shown that the low level conductance  $g_0$  corresponds to the DC p.u.l. conductance value, and the parallel association  $g_0 \parallel g_1 \parallel \dots \parallel g_n$  corresponds to the high frequency P.u.l. conductance.

Similarly, the frequency dependence of the p.u.l. self inductance can be represented by the equivalent circuit in Fig. 4.2. The p.u.l. inductances vary with frequency due to skin and proximity effect. The mutual p.u.l. are also frequency dependent, but their variation cannot be represented with this model.

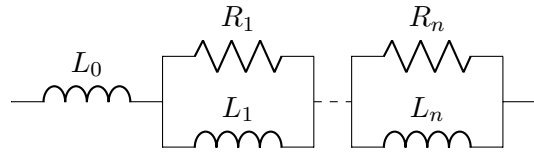


Figure 4.2 – Equivalent network to represent the cable inductance

The ladder networks described in Fig. 4.1 can be placed in the position of the variable resistances and conductances in the new basic cell of the MTL represented in Fig. 4.3.

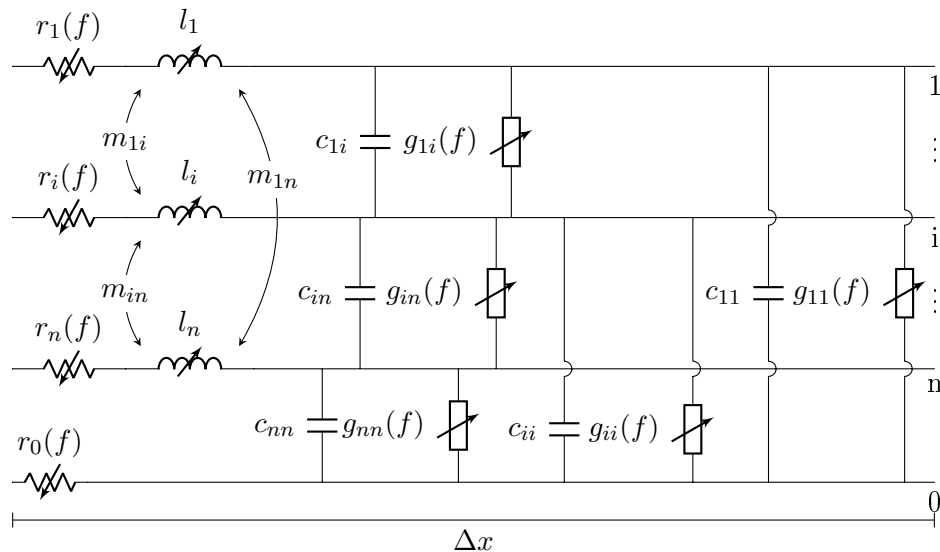


Figure 4.3 – Basic cell for time domain simulation of a MTL, parameter variable on frequency

The parameters that compose each ladder network can be calculated with vector fitting methods [30]. There are specific softwares, such as “APLAC RF Design Tool” that have built-in methods calculate them [18].

Many commercial circuit simulation software have built-in models of transmission lines that represent the line on time domain using the methods described in this section. The modeling methods of the most frequent software are discussed below.

**PSpice** The open-source PSpice software is widely used. It has many models of transmission lines for different applications, which should be chosen taking into account the cable characteristics, as well as the smallest rise/fall time in the system [38]. For the modeling of building cables, the model must be valid for long and lossy transmission lines. The PSpice model corresponding to these exigences is called “TLOSSY”, a distributed parameter model. Its entries are the cable length  $\ell_c$ , and p.u.l. parameters  $r$ ,  $l$ ,  $c$ ,  $g$ , all constants. The model does not represent the evolution of  $r$  and  $g$  with frequency. The model builds automatically a series association of the basic transmission cell. The number of cells is determined with the smallest fall/rise time in the

system. As the number of cells can easily grow big, the simulation time may become considerably long.

**Simplorer** Ansoft’s Simplorer circuit simulator has embedded models for coaxial cables, and single-phase and three-phase transmission lines for power systems. These models take as entry the characteristic impedance  $Z_c$ , the propagation speed  $v$ , the cable length  $\ell_c$  and the p.u.l. resistance  $r$ , all real constants. The model builds a lossless transmission line with distributed parameters from entries  $Z_c$ ,  $v$  and  $\ell_c$ . The resistance is associated in series with the distributed model [5]. The accuracy of such approximation decreases when the line length increases, and the software documentation recommends representing a “long” line with a series association of smaller transmission lines. Moreover, as the cable parameters are constant, this model is also not able to represent the frequency-dependent behavior of the cable losses, and propagation speed.

**APLAC** National Instruments’ APLAC software is dedicated to RF simulations. It has two built-in models for transmission-lines. The first model, denominated “Tline”, models the line with distributed parameters, all with a fixed value. The second model, denominated “TlineDisp”, models a lossy transmission line, using the ladder networks presented in Fig. 4.1 to represent the frequency dependence of the loss related parameters of the cable. The number of cells in both models is chosen by the software, in function of its length and a maximum frequency of the simulation, both defined by the user.

**EMTP** Powersys’ software EMTP is widely used for power systems simulations, and has many transmission line models, specific for the power cables used in energy transmission. The most complete of these models is denominated “FD m-phase”, and is able to take into account the frequency dependence of the cable parameters [9]. The modeling technique used by EMTP is detailed in [28], and, briefly, consists in the approximation of the cable parameters  $Z_c$  and  $\gamma$  by rational expressions in function of the frequency. These expressions can then be decomposed in partial fractions, for which the inverse Fourier/Laplace transform is defined, what allows the definition of an approximate model on time domain.

These are a few examples of time domain transmission line models available in commercial software, surely many others can be found. The disadvantage of simulating transmission lines on time domain using the series association of their basic cells is that the simulation time can be too high if the cable is electrically long (longer than the minimum wavelength to be accounted for), factor that would engender the need of a great number of cells for an accurate representation of the line.

Considering that this work aims to deal with harmonics of frequency up to  $30\text{ MHz}$ , and that the propagation velocity on the power cables characterized so far is around  $v = c/2$ , where  $c$  is the speed of light in vacuum, the minimal wavelength to be taken into account is around  $5\text{ m}$ . The length of the cables on industrial or building cabling network can be easily 10 times bigger than this value. Therefore, the approach described here is too cumbersome to model the industrial cabling network, because the simulations can easily take too long to complete. Indeed, this problem is even more critical considering the need of concatenation of the cable model, if a system with multiple cable portions need to be simulated.

The cable modeling technique on time domain considered fit for the industrial cabling modeling is described in the next section.

### 4.3 Frequency-domain model results converted to time domain

Chapters 2 and 3 introduced a frequency domain model for power cables, capable of modeling any piece of the radial network studied here. In this model, big portions of the network can be modeled as Thévenin/Norton equivalent circuits, and the piece of cable under study can be modeled by the generic frequency domain simulation tool described in section 3.2.c.

The attempt to transform of the model itself to time domain presents important difficulties, as has been discussed in section 4.2. However, if the system under study can be represented in the frequency domain, it can be simulated in the frequency domain with the aforementioned tool, and the results can be easily transformed to time domain using the Fourier Series in association with the phasor transform, or the Fourier Transform itself.

Indeed, in a time domain application where the devices connected to the cables terminals can be represented by Thévenin/Norton equivalent, it is sufficient to represent the equivalent voltage/current source(s) on frequency domain via one of the transforms mentioned above. Once this step is performed, the system can be solved for each frequency individually. Then, the time domain waveform can be computed with the inverse transform of the solution in the frequency domain.

In the next two subsections, the theory of time to frequency domain transform is discussed, and in the last subsection 4.3.c the algorithm built for time domain applications using this modeling technique is presented.

#### 4.3.a Periodic signals transform

If the sources in a given system are periodic, a Fourier Series in association with the phasor transform can be used to represent it in the frequency domain, and an analysis in the sinusoidal steady state can be performed. This is the case for systems in which the sources are switching structures, such as power converters.

In such cases, the Thévenin/Norton equivalent sources are periodic and can be represented by a Fourier series, as in (4.14).

$$s(t) = C_0 + \sum_{n=1}^N C_n \cos[(2\pi f_0 n)t + \theta_n] \quad (4.14)$$

By applying the phasor transform to equation (4.14), the frequency domain representation of a periodical source is obtained, and is written in phasor notation below:

$$S(f_n) = C_n e^{j\theta_n} \quad (4.15a)$$

$$S(0) = C_0 \quad (4.15b)$$

This representation of a periodic signal in the frequency domain is possible if the Fourier Series of  $s(t)$  exists, what is true for any practical signal [26].

The frequency domain representation of periodic signal is discrete on frequency, having a null value for frequencies non-multiples of the fundamental frequency  $f_1$ .

Once the system is represented on frequency domain, the voltages and currents along the line can be simulated for each harmonic. The frequency domain results can be converted back to time domain using equation (4.14).

### 4.3.b Generalized transform

If the source is not periodic, the Fourier series cannot be defined. For example, the case of the parasitic voltage pulse induced by lightning in the cabling network.

In such cases, the Fourier transform can be used to obtain a frequency domain representation of the Thévenin/Norton equivalent sources (4.16).

$$s(t) \Leftrightarrow S(\omega) \quad (4.16)$$

The Fourier transform is defined for continuous functions on time domain, and continuous spectra on frequency domain. As the model will be implemented on computers, the Discrete Fourier Transform (DTF) should be used, via the Fast Fourier Transform (FFT) algorithm for example. This transform is possible for any practical signal.

Once the DTF  $S(2\pi f[k])$  of the time domain signal is obtained, it can be inserted in the frequency domain model, for a steady state analysis of the system. As the spectrum resultant of the DFT represents a continuous spectrum, it must be interpolated if its value is needed for frequency values different from the frequency samples given by the FFT algorithm.

The results of the frequency domain-model calculated from a Fourier Transform can be transformed back to time domain via the inverse FFT.

Even though interesting, the representation of a system in the frequency domain via the Fourier transform will not be studied in this work. The algorithm described in the following section is exclusive to systems with periodic sources.

### 4.3.c Time domain transform of the frequency domain solution

The chosen technique to model transmission lines on time domain consists of the frequency domain simulation of the system, using the Fourier series along with the phasor transform as the bridge between time and frequency domains. In this work, time domain analysis of the transmission line is limited to systems where the line is excited with periodic sources.

Consider the generalized frequency domain model described in section 3.2.c. It models equivalent system in Fig. 4.4, repeated here for convenience, where generic multiport equivalent circuits are used to represent the devices connected to the line terminals.

The “source” and “load” boxes represent the devices connected to the cable terminals, and can be represented by a  $(n + 1)$ -port equivalent circuit, as described in section 3.2.c. This equivalent circuit allows the representation of any linear  $(n + 1)$ -port device with a  $n \times n$  admittance matrix  $\mathbf{Y}$  and  $n$  current sources  $\mathbf{S}$  that can be arranged in a column vector  $\mathbf{S}$ . Then, the voltages and currents at the device output are related by equation (4.17) (cf. section 3.2.c):

$$\mathbf{I}(f) = \mathbf{S}(f) - \mathbf{Y}(f)\mathbf{V}(f) \quad (4.17)$$

Both of the devices, “source” and “load”, can generate high frequency harmonics, therefore the “load” device may have current sources on its equivalent circuit, representing the stray signal injected by the “load” in the cable. Their names refer to the main function of the devices.

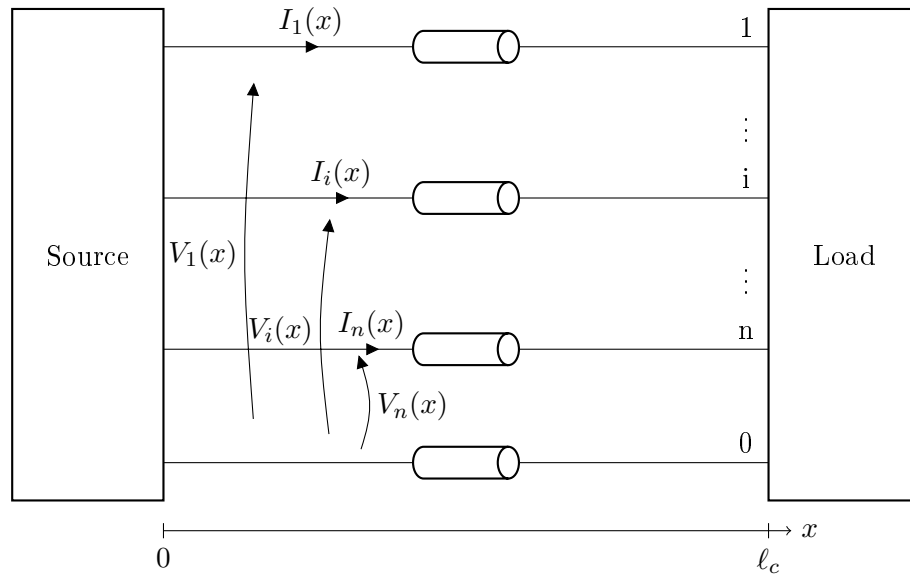


Figure 4.4 – Schematic of the multiconductor transmission line

The first step to simulate the system on frequency domain is to represent the equivalent circuit described by (4.17) on frequency domain. The first hypothesis taken is that the sources in the equivalent circuits corresponding to the boxes “source” and “load” are periodical. The current sources representing the “source” device are denominated  $\mathbf{S}_S(t)$ , and their period is  $T_S$ . The current sources representing the “load” device are denominated  $\mathbf{S}_L(t)$ , and are periodical with the period  $T_L$ . Because we took the hypothesis the sources are periodic, these sources can be represented in the frequency domain with the Fourier Series followed by the phasor transform (cf. section 4.3.a). The frequency domain representation of these vectors of sources are denominated  $\mathbf{S}_S(f)$  for the source and  $\mathbf{S}_L(f)$  for the load. The equation (4.17) can be rewritten for each one of the devices at the cable terminals as follows:

$$\mathbf{I}(0, f_S) = \mathbf{S}_S(f_S) - \mathbf{Y}_S(f_S)\mathbf{V}(0, f_S) \quad (4.18a)$$

$$\mathbf{I}(\ell_c, f_L) = \mathbf{S}_L(f_L) - \mathbf{Y}_L(f_L)\mathbf{V}(\ell_c, f_L) \quad (4.18b)$$

In the general case, the periods  $T_S$  and  $T_L$  are not necessarily the same. The vector  $f_S$  is defined as the group of frequencies multiple of  $1/T_S$ , the fundamental frequency of the stray signals injected in the line at  $x = 0$ , and  $f_L$  is the vector containing the multiples of  $1/T_L$ , the fundamental frequency of the stray signals injected at  $x = \ell_c$ .

Because of this possible discrepancy between the fundamental frequencies at each extremity of the cable, the frequency vectors  $f_S$  and  $f_L$  have to be merged into a single vector  $f$ , for the system to be completely simulated at once. In this process, the vectors  $\mathbf{S}_S(f)$  and  $\mathbf{S}_L(f)$  must be created: as mentioned in section 4.3.a, they must be zero in the frequency points that are not multiple of their fundamental frequency. i.e.,  $\mathbf{S}_S(f_L) = 0$  and  $\mathbf{S}_L(f_S) = 0$ .

Then, the merged voltage/current relations can be written as follows:

$$\mathbf{I}(0, f) = \mathbf{S}_S(f) - \mathbf{Y}_S(f)\mathbf{V}(0, f) \quad (4.19a)$$

$$\mathbf{I}(\ell_c, f) = \mathbf{S}_L(f) - \mathbf{Y}_L(f)\mathbf{V}(\ell_c, f) \quad (4.19b)$$

Once the vector  $f$  is known, the cable parameters must be determined for each of the frequency

points in  $f$ . That is done by interpolating directly the input impedance measurements used for the cable parameter identification. The real and imaginary parts of the input impedances of the sample cable are interpolated to  $f$ , after what the cable parameters are calculated for these frequencies.

After these steps, the frequency domain simulation tool described in section 3.2.c can be used to determine the voltage and currents along the line, and its results can be converted back to time domain using equation (4.14).

The process just described is represented by the flowchart in Fig. 4.5. The blue box represents the “time domain computing tool” developed for the modeling of the building cabling, based in the frequency-domain simulation tool described in section 3.2.c.

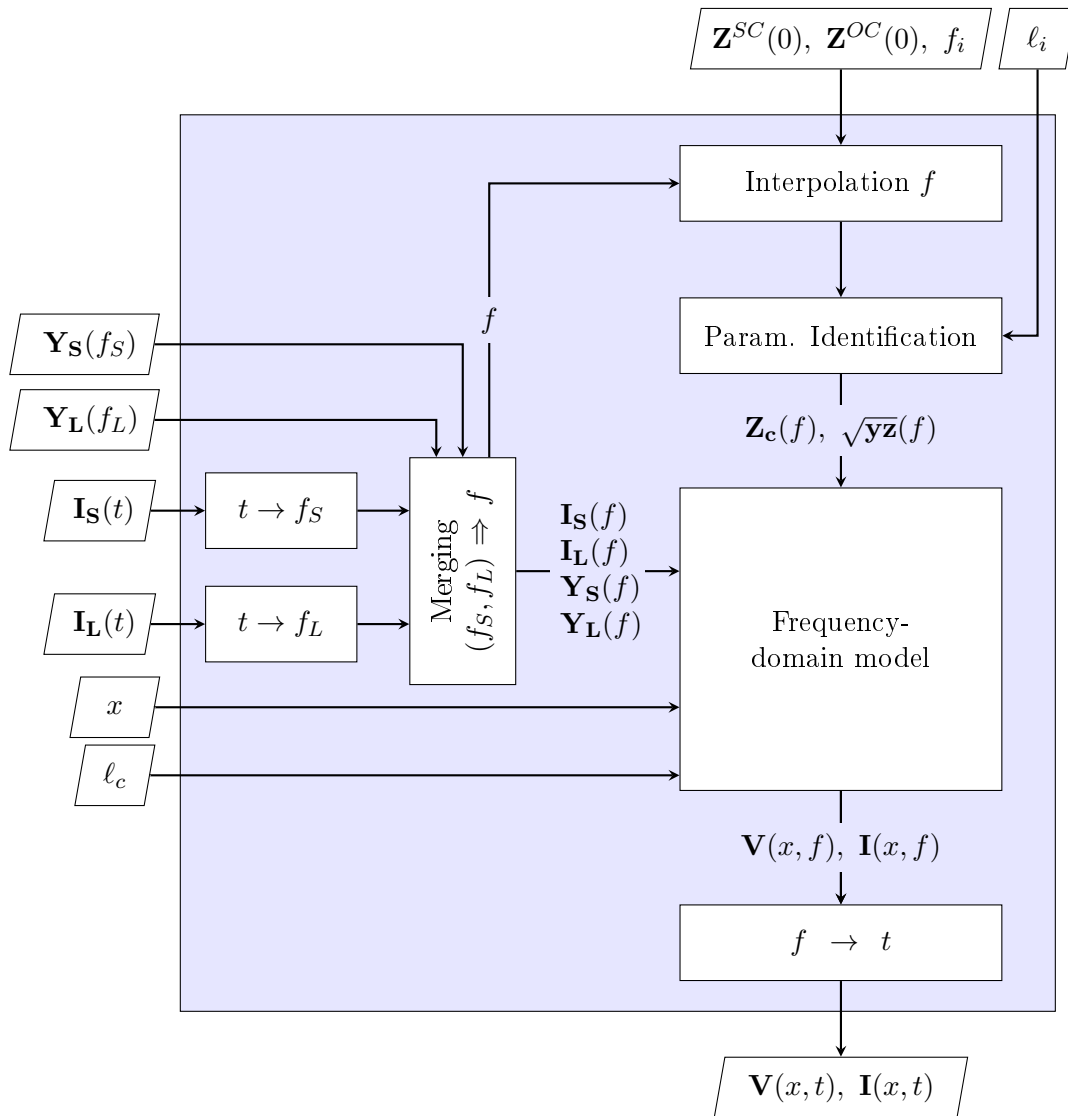


Figure 4.5 – Flowchart of the complete model

The tool takes as inputs the cable length  $\ell_c$ , the points  $x$  where the variables are to be calculated, the parameters of the equivalent circuits of the devices connected to each terminal  $\mathbf{Y}_S$ ,  $\mathbf{Y}_L$ ,  $\mathbf{I}_S(t)$ , and  $\mathbf{I}_L(t)$ , and the cable parameter identification data: the cable input impedance in short circuit  $\mathbf{Z}^{SC}(0)$  an open-ended  $\mathbf{Z}^{OC}(0)$ , the frequency to which these measurements were

performed  $f_i$ , and the sample cable length  $\ell_i$ .

At the left of the flowchart, the representation of the equivalent circuits of the devices connected to cable terminals is treated, aiming to obtain the parameters in the equation (4.19). First, the time domain current sources of the equivalent circuits  $\mathbf{I}_S(t)$  and  $\mathbf{I}_L(t)$  must be converted to frequency domain, using the Fourier series followed by the phasor transform. Then, as the frequency domain representation of these sources is obtained for the frequency points of their harmonics:  $f_S$  and  $f_L$ , respectively, the parameters  $\mathbf{I}_S(f_S)$ ,  $\mathbf{I}_L(f_L)$ ,  $\mathbf{Y}_S$ , and  $\mathbf{Y}_L$ , must be merged into a common frequency vector  $f$ , containing all the values in both  $f_S$  and  $f_L$ . Then, the parameters in function of  $f$  are inserted in the frequency domain model, and the vector  $f$  is used to the interpolation of the cable parameters.

On the top of the flowchart, the cable parameters computation for the frequency points in  $f$  is described. The frequency-vector  $f$  is used to interpolate  $\mathbf{Z}^{SC}(0)$  and  $\mathbf{Z}^{OC}(0)$ . The interpolated cable input impedances, as well as the length of the sample cable  $\ell_s$ , are used to obtain the cable parameters  $\mathbf{Z}_c(f)$  and  $\sqrt{\mathbf{y}\mathbf{z}}(f)$ .

The frequency domain model take as inputs the vector of positions  $x$  where the values of voltages and currents are demanded, the cable length  $\ell_c$ , the cable parameters  $\mathbf{Z}_c(f)$  and  $\sqrt{\mathbf{y}\mathbf{z}}(f)$ , and the frequency domain relations between the voltages and currents on the cable terminals described by eqs. (4.19). The outputs are the voltages and currents of the line in function of frequency  $f$ , at the positions on vector  $x$ , can then be converted to time domain using the Fourier series (4.14), as described on section 4.3.a.

The flowchart of the frequency domain model is shown in Fig. 3.6, refer to section 3.2.c for details.

The accuracy of the results of this time domain computing tool will be shown with the validation experiments in the next section.

## 4.4 Time-domain validation

The results of the time domain computing tool in section 4.3.c were validated experimentally with three different setups, two of them using two-conductor cables and the third using a three-conductor cable.

For all the experiments, a trapezoidal source with near zero output impedance was used. The trapezoidal source is periodic, and therefore can be decomposed in a Fourier Series, to be injected on the frequency-domain model after the phasor transform (cf. section 4.3.a). The Fourier Series decomposition of a periodic trapezoidal signal can be expressed as in (4.20), in function of the parameters defined in Fig. 4.6, and with  $\beta_r = \frac{t_r}{T_0}$ ,  $\beta_f = \frac{t_f}{T_0}$ , and  $\text{sinc}(a) = \frac{\sin(a)}{a}$ .

$$C_0 = Ad + b \tag{4.20a}$$

$$C_n = \frac{A}{n\pi} \sqrt{\text{sinc}^2(n\pi\beta_r) + \text{sinc}^2(n\pi\beta_f) + 2\text{sinc}(n\pi\beta_r)\text{sinc}(n\pi\beta_f) \cos(n\pi 2d)} \tag{4.20b}$$

$$\theta_n = -\text{atan} \left( \frac{\beta_f \sin(2n\pi\beta_r) + \beta_r (\sin(p) - \sin(q))}{-\beta_f (1 - \cos(2n\pi\beta_r)) + \beta_r (\cos(p) - \cos(q))} \right) \tag{4.20c}$$

$$p = n\pi(2d - \beta_f + \beta_r)$$

$$q = n\pi(2d + \beta_f + \beta_r)$$



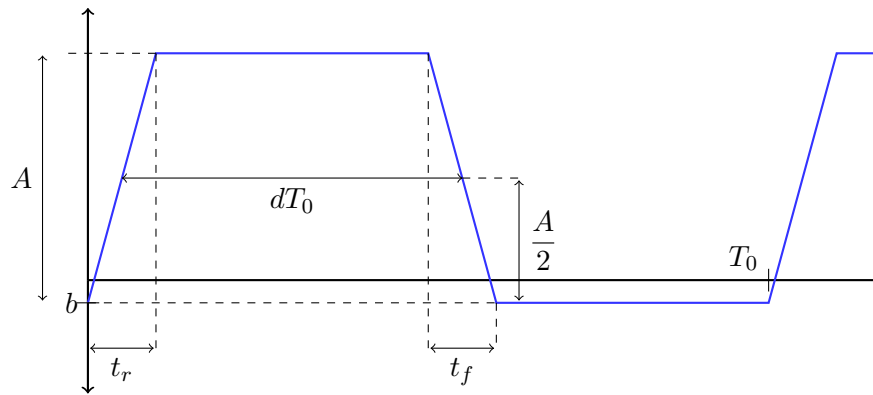


Figure 4.6 – Parameters of periodical trapezoidal source

As mentioned in section 1.2 , the spectrum of the series given by (4.20) is attenuated with  $-40 \frac{dB}{dec}$  from the frequency  $f = \frac{1}{\pi \min(t_r, t_f)}$ , and is truncated at  $f_{end} = \frac{10}{\min(\pi t_r, t_f)}$  in the time domain computation tool.

Some precautions have been taken to avoid alternative paths to the high frequency currents during the experiment. All the experiments were performed with the cables suspended by insulating materials, as is well shown in Fig. 4.7. The scope used to measure the voltage along the cable was fed through a battery, to avoid an alternative path to the current via the mass of the scope. The scope itself was placed over a cardboard box, as well as the load connected to the cable extremity.



Figure 4.7 – Photo of the experimental setup

The following subsections describe the validation experimental setup for each of the experiments, and present the validation results.

#### 4.4.a Two-conductor cable validation

The time domain computing tool is validated for two-conductor cables with the setup described in Fig. 4.8.

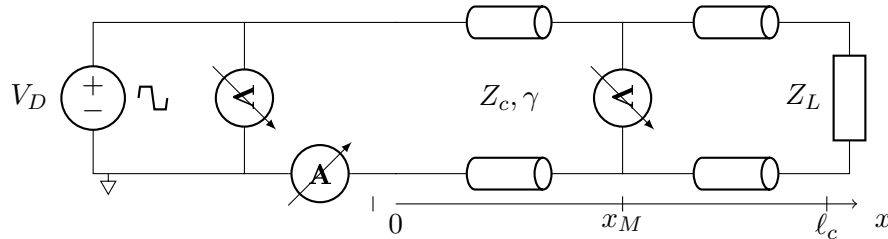


Figure 4.8 – Schematic for the time domain validation experiment

A long two-conductor cable is fed with a low output impedance trapezoidal source, and a known load is connected to the other extremity of the cable. Resonances will take place, according to the chosen load, and the voltage and current will be measured on the points of interest, i.e., the position  $x_M$  along the line where resonance-due amplifications are maximal.

The voltage is measured with scopes. One scope is constantly connected to the cable input, to verify the voltage imposed by the source behaves as expected, and another is connected to the point along the line where resonance-due voltage amplification is maximal. The scope that measures the voltage along the line is fed by battery. The scope connected to the cable input is directly connected to an electric plug, and, consequently, the input of the cable is connected to its mass.

A split-core current probe measures the resonance-due current amplification at the cable input. As discussed in section 2.5.a, the resonance-due current amplification arrives at the positions along the line where the voltage amplification is minimum, because the power is constant along the line, except for the Joule losses. As the voltage in the cable input is fixed by the voltage source on this case-study, the input is a point of minimum voltage amplification ( $V(0) = V_S$  for any frequency) and, therefore, of a maximum current amplification.

The voltage probe input impedance was taken into account on the system modeling. The voltage probe mass was connected to the cable using the adapted spring connector shown in Fig. 4.9.



Figure 4.9 – Connection of the voltage probe along the line

##### 4.4.a-i Two-conductor $2.5 \text{ mm}^2$ cable, RL series load

The first validation experiment was performed for the two-conductor cable of section  $2.5 \text{ mm}^2$ , cf. Fig. 2.29 for its cross-section, connected to the load in Fig. 4.10. The cable length is  $\ell_c = 11.09 \text{ m}$ .

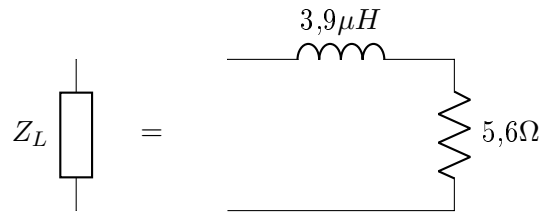


Figure 4.10 – The RL series load chosen for the experimental validation

The load in Fig. 4.10 was built with a power resistor mounted on a heat sink, in series with a coreless solenoid in Litz wire (Fig. 4.11).



Figure 4.11 – The RL series load connected to the two-conductor  $2.5\text{ mm}^2$  cable

The behavior of the resonance phenomena in the line with the load just described was studied with the method described in section 2.5.b-i. One resonance point is predicted, at the frequency  $f_n = 2.4\text{ MHz}$ , its characteristics are resumed in table 4.1.

Table 4.1 – Characteristics of the predicted resonance

Resonance frequency	$4.4\text{ MHz}$
Amplification of the input voltage (single harmonic)	6.8
Maximal amplification position	$8\text{ m}$

The trapezoidal source parameters that best describe the voltage imposed on the line input are listed in table 4.2.

Table 4.2 – Trapezoidal source parameters

$A$	$50.5\text{ V}$	$d$	$25.3\%$	$t_r$	$25\text{ ns}$
$b$	$-0.9\text{ V}$	$T_0$	$5\text{ }\mu\text{s}$	$t_f$	$25\text{ ns}$

The voltage was measured at  $x_M = 8\text{ m}$  with the battery powered scope, and current was measured at the cable input with a split-core probe.

The data obtained with these measurements is plotted over the correspondent theoretical prediction in Figs. 4.12a and 4.12b. The limits of the accuracy of the measurements are also plotted, given by the scope manual [50], so that the validity of the model can be verified.

The theoretical voltage and current present a good agreement with the experimental data, the theoretical results are within the accuracy gap of the measurements. Thus, the accuracy of the time domain computing tool is validated.

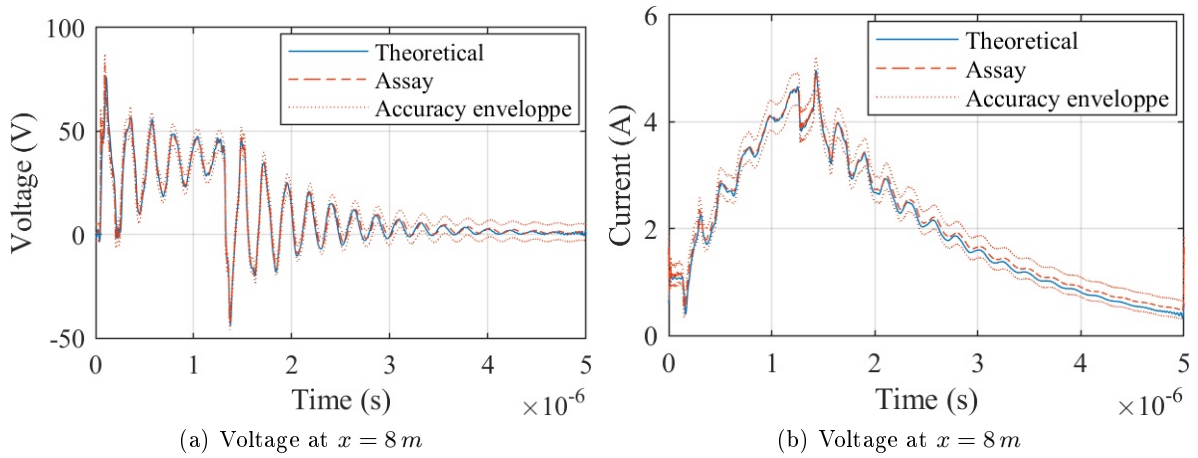
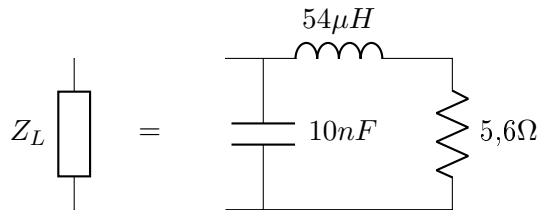


Figure 4.12 – Results of the validation experiment with series RL load

#### 4.4.a-ii Two-conductor $0,75\text{mm}^2$ cable, RL series C parallel load

The second setup for the two-conductor time domain validation uses the two-conductor  $0.75\text{mm}^2$  section cable, the cross-section described by Fig. 2.16, with length  $\ell_c = 11.98\text{m}$ . The load in Fig. 4.13. is connected to the cable extremity.

Figure 4.13 – RL series C parallel load connected to the  $0.75\text{mm}^2$  cable

To build this load, a power resistor was chosen, and mounted on a heat sink. The inductor was built with Litz wire, on a close loop ferrite core with an air gap, the capacitor is ceramic. A photo of this load is shown in Fig. 4.14.

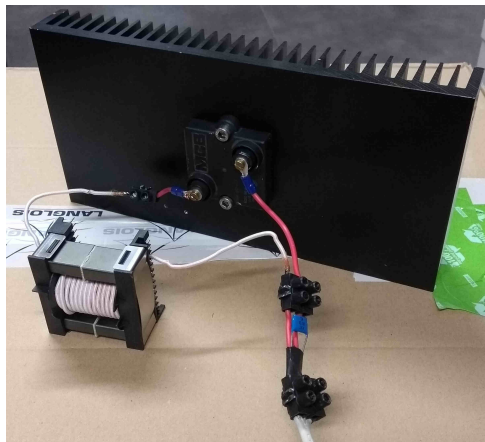


Figure 4.14 – Load used in the three-conductor cable time domain validation experiment

The trapezoidal source parameters were determined to best represent the voltage imposed by the source at the line input, they are listed in table 4.3.

Table 4.3 – Trapezoidal source parameters

$A$	$98.16 V$	$d$	$0.2475$	$t_r$	$106.2 ns$
$b$	$-0.5 V$	$T_0$	$25.004 \mu s$	$t_f$	$151.56 ns$

The resonance behavior of the cable connected to this load was evaluated as described in section 2.5.b-i. Two resonance frequencies were identified, and the characteristics of each one of them are resumed in table 4.4.

Table 4.4 – Characteristics of the predicted resonances

Resonance frequency	$660 kHz$	$6.4 MHz$
Amplification of the input voltage (single harmonic)	7.4	5.8
Maximal amplification position	$\ell_c$	$\ell_c/2$

The first resonance, at  $660 kHz$ , can be modeled with short line model, as described in section 2.5.c: for this frequency cable and load behave as an LCL resonant circuit. This can be shown by representing the line with a single cell, which gives the circuit in Fig. 4.15; the p.u.l. parameters correspond to  $f = 660 kHz$ . The resonance frequency of the LCL circuit in Fig. 4.15 is  $\frac{1}{2\pi} \sqrt{\frac{\ell_c 0.6 \mu + 54 \mu}{(\ell_c 70 p + 10 n) \ell_c 0.6 \mu 54 \mu}} = 609 kHz$ , close to the predicted resonance frequency

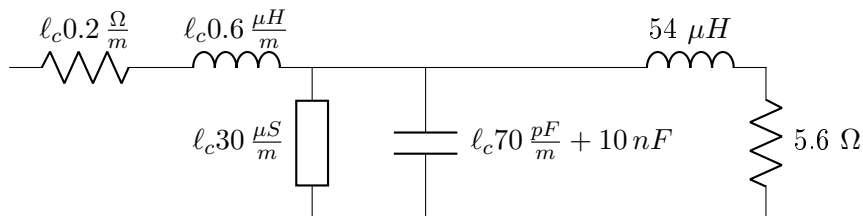


Figure 4.15 – Short line model of the system, valid for low frequencies

The resonance taking place at  $6.4 MHz$  is a propagation-due resonance. For that reason, we choose to measure the voltage where this resonance is maximum, i.e.,  $x_M = \ell_c/2$ . At this position, the  $660 kHz$  voltage amplification is also present, but its amplitude is not as high as at  $x = \ell_c$ . This is shown in Fig.4.16, where the frequency domain result for the voltage along the line is plotted in function of the frequency for three different positions of the line.

The voltage at  $x = \ell_c/2$  and the current at  $x = 0$  were obtained with the time domain computation tool, and compared to the experimental data in Fig. 4.17. The error limits of the scope measurement, obtained from the limits of accuracy given by the scope manual [50], are also plotted over the experimental data.

The resonance at  $6.4 MHz$  is attenuated much before the LCL resonance at  $660 kHz$ , and it is difficultly visible on the figures containing the whole period  $T_0$ . The high frequency resonance effect is more visible in Fig. 4.18, zoomed around the switching point  $dT_0$ .

The time domain computing tool predicts correctly the voltages and currents in this experiment, its values remaining within the accuracy gap of the scope.

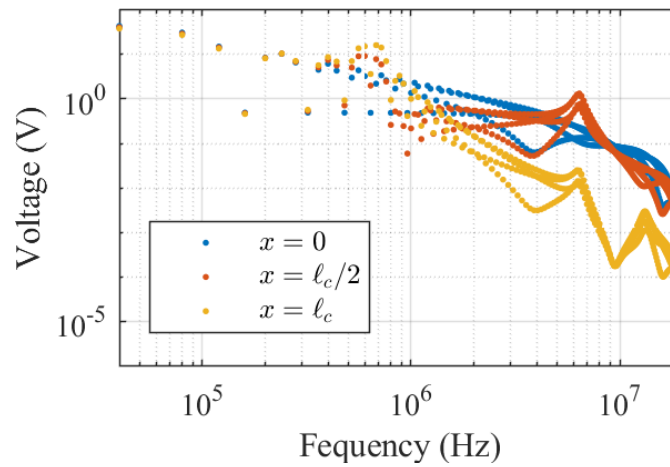


Figure 4.16 – The voltage along the line on the frequency domain

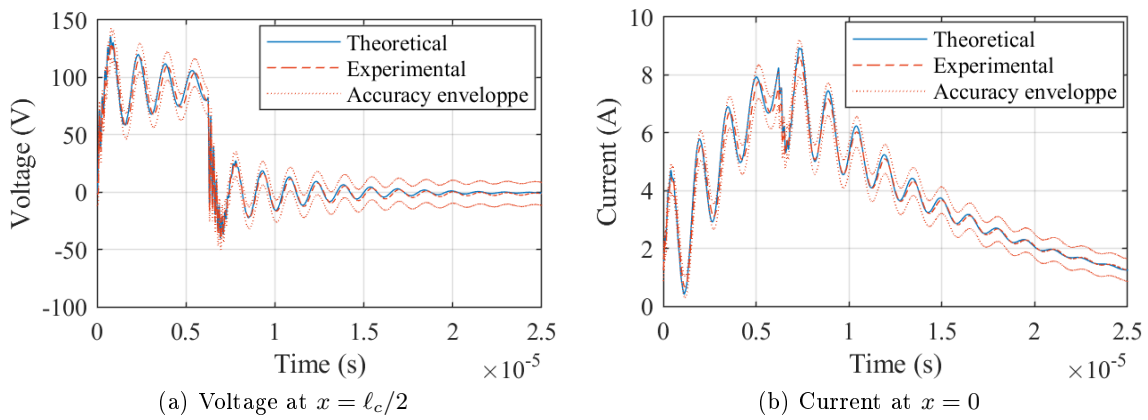


Figure 4.17 – Validation results for the RL series C parallel load

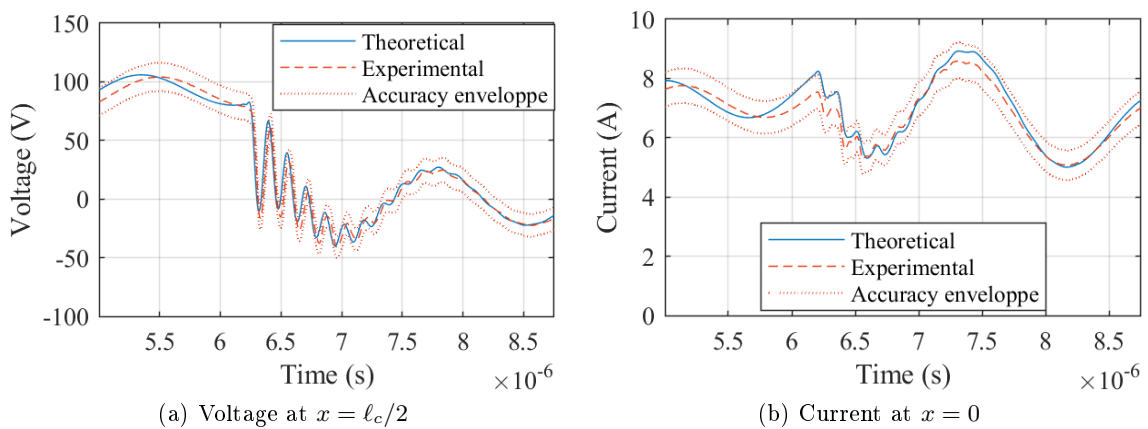


Figure 4.18 – Validation results for the RL series C parallel load, zoom on the 6,4MHz resonance

#### 4.4.b Three-conductor cable validation

A similar experiment has been designed to validate the proposed transmission line modeling technique for multiconductor cables.

A three-conductor cable, with  $2.5\text{ mm}^2$  stranded copper conductors insulated with polymer sheaths is used, its cross-section is repeated in Fig. 4.19 for convenience.

Source: <http://www.caledonian-cables.co.uk>

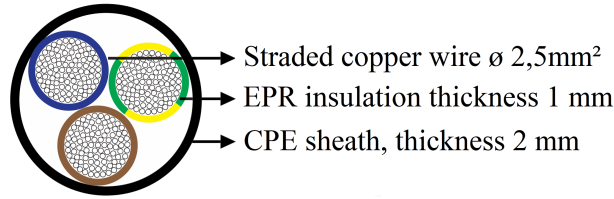


Figure 4.19 – Cross-section of the three-conductor  $2.5\text{ mm}^2$  cable

The experiment was designed to represent a single-phase system, with common-mode currents circulating through the third conductor. Its schematic is drawn in Fig. 4.20

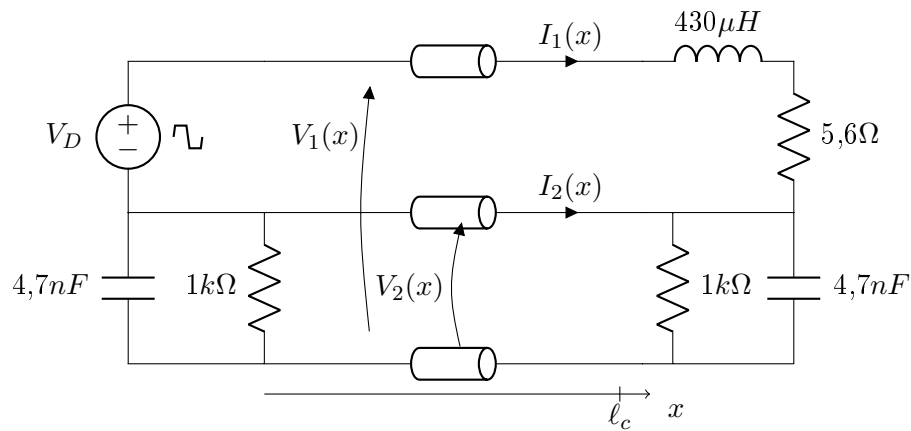


Figure 4.20 – Schematic for the three-conductor cable time domain validation experiment

A trapezoidal source feeds the system in differential mode. The differential mode load is a RL series association, and the third conductor is connected through a RC parallel association, representing the common-mode stray capacitance and conductance. The RC parallel association is oversized, so the current circulating through the third conductor, considered common mode in this analysis, is higher than the actual common-mode currents in the experimental set.

The RL series association was built with a power resistor mounted over a heat sink, in series with a solenoid on Litz wire around a closed loop ferrite core with an air gap. The RC parallel association were built with ceramic components. A photo of this load is presented in Fig. 4.21.

The differential source connected to the cable input imposes a trapezoidal voltage with the parameters listed in table 4.5.

Table 4.5 – Trapezoidal source parameters

$A$	$98.17\text{ V}$	$d$	$0.1867$	$t_r$	$108.0\text{ ns}$
$b$	$-0.5\text{ V}$	$T_0$	$20\text{ }\mu\text{s}$	$t_f$	$117.2\text{ ns}$

In this system, the voltage maximal amplifications due to resonance take place at  $x = \ell_c$ . As aforementioned, current maximal amplification due to resonance take place at  $x = 0$  because the voltage is imposed at the line input.

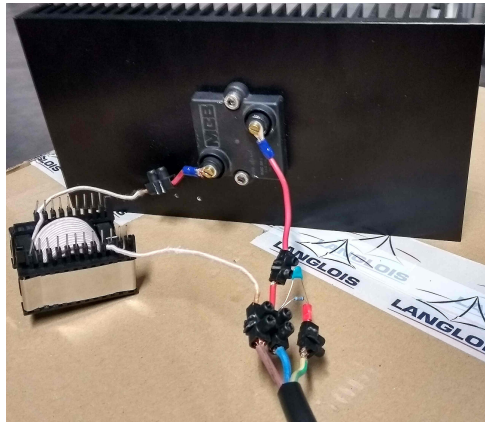


Figure 4.21 – Load used in the three-conductor cable time domain validation experiment

The resonant voltage and current were measured on time domain each at turn, i.e., the voltage or current probes were only connected to perform the measurement. This way no other probe was connected to the system during any of the measurements. The impact of the current probe was negligible, but the voltage probe input impedance had to be included in the theoretical model to guarantee the equivalency between the model results and the measurements.

The measured voltages and currents are compared to the model results in Figs. from 4.22 to 4.25.

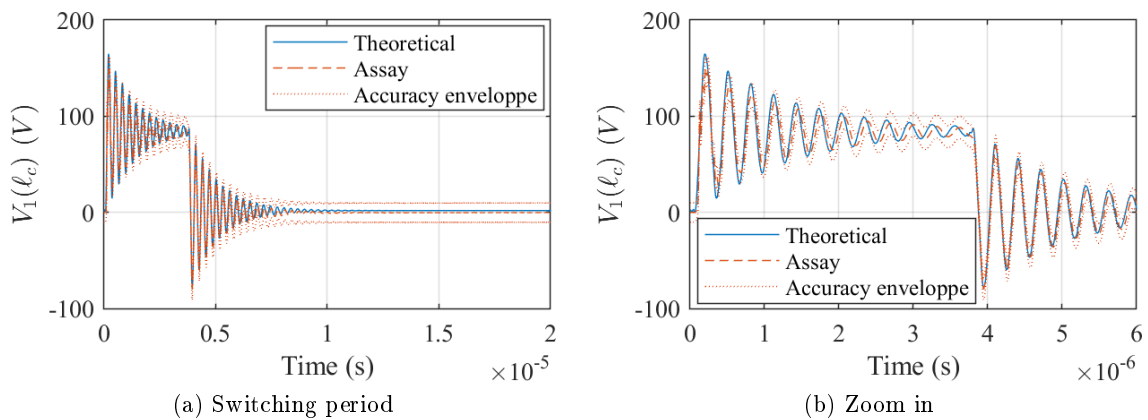
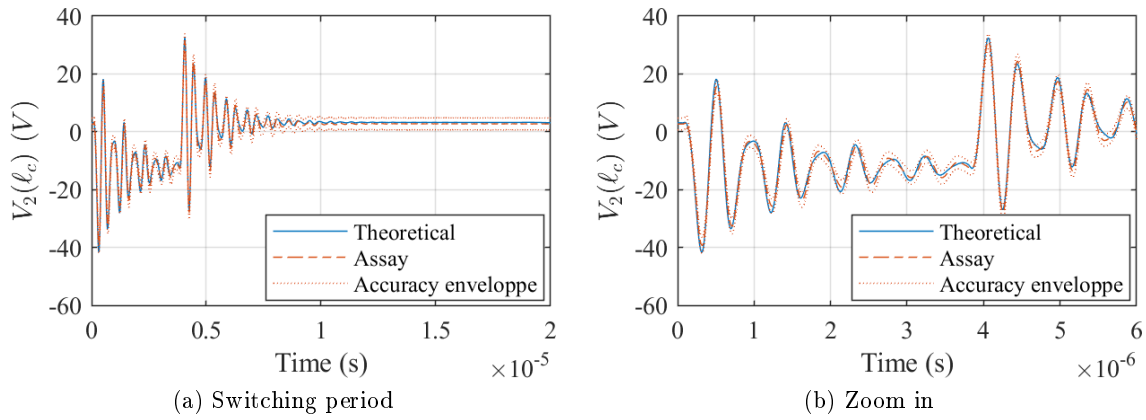
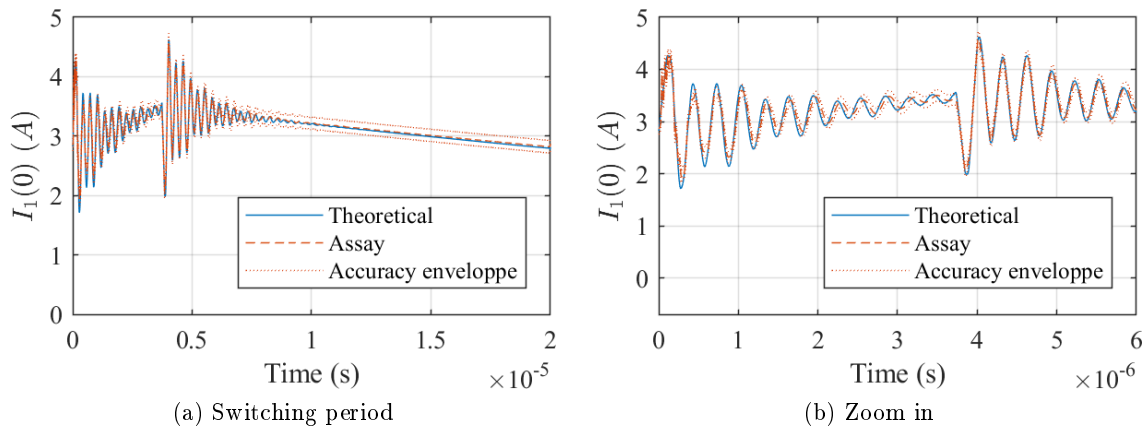
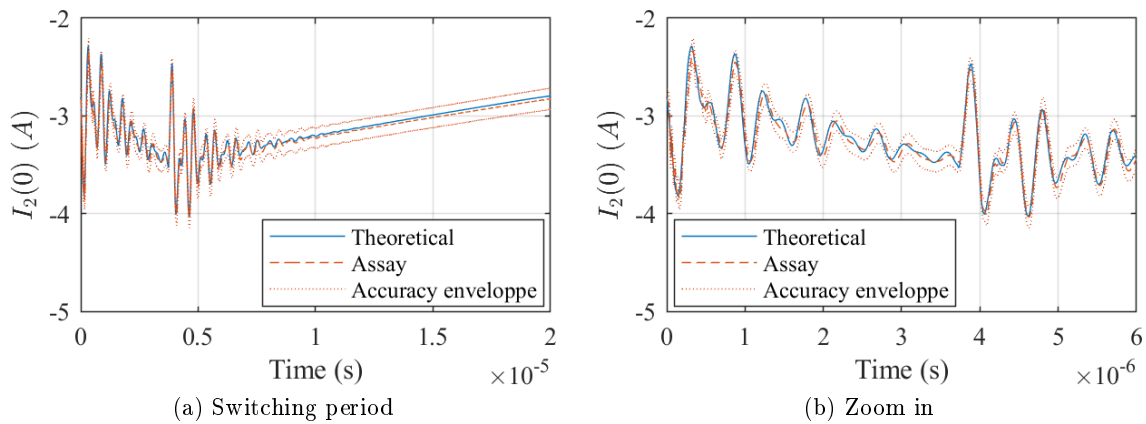


Figure 4.22 – Voltage  $V_1(\ell_c)$

The model agrees acceptably with the experimental data, thus validating the proposed cable modeling on time domain also for multiconductor cables.



Figure 4.23 – Voltage  $V_2(\ell_c)$ Figure 4.24 – Current  $I_1(0)$ Figure 4.25 – Current  $I_2(0)$ 

## 4.5 Qualitative analysis of the frequency domain model

The advantages of the simulation tool proposed in this work are analyzed in this section. In section 4.5.a the impact of the frequency dependent loss-related parameters is analyzed, and in

section 4.5.b the modeling of the time delay of a traveling wave in a long cable is studied. The conclusions on the performance of the simulator are made in section 4.5.c.

#### 4.5.a Impact of the frequency dependence of the parameters

In this section, the frequency domain simulation with conversion to time domain will be used to determine the importance of representing the frequency dependence of the parameters, regarding the accuracy of the time domain results.

This analysis is based on the system used for the three-conductor cable time domain validation in section 4.4.b, its setup is represented in Fig. 4.20. The cable is the unshielded three-conductor cable with conductors of section  $2.5 \text{ mm}^2$ , its cross-section is represented in Fig. 4.19.

To determine the importance of frequency dependent parameters, two sets of cable parameters constant along the frequency were defined, they are denominated “LF” (low frequency) and “HF” (high frequency), the self elements of the p.u.l. parameter matrices are detailed in Table 4.6. The “LF” has the DC values of the loss-related parameters  $\mathbf{r}$  and  $\mathbf{g}$  and the reactive parameters  $\mathbf{l}$  and  $\mathbf{c}$  are evaluated at  $50 \text{ kHz}$ , while the “HF” set has all the parameters evaluated at  $20 \text{ MHz}$ .

Table 4.6 – Fixed cable parameters for resonance analysis

	$r_i$	$l_{ii}$	$g_{ii}$	$c_{ii}$
LF (DC, $50 \text{ kHz}$ )	13.4 m $\Omega$ /m	547 nH/m	1 nS/m	58 pF/m
HF ( $20 \text{ MHz}$ )	487 m $\Omega$ /m	512 nH/m	238 $\mu$ S/m	54 pF/m

The simulation of the systems in Fig. 4.20 was performed for each of these sets, and for the complete model with variable cable parameters. The results for the output voltage are plotted in Fig. 4.26.

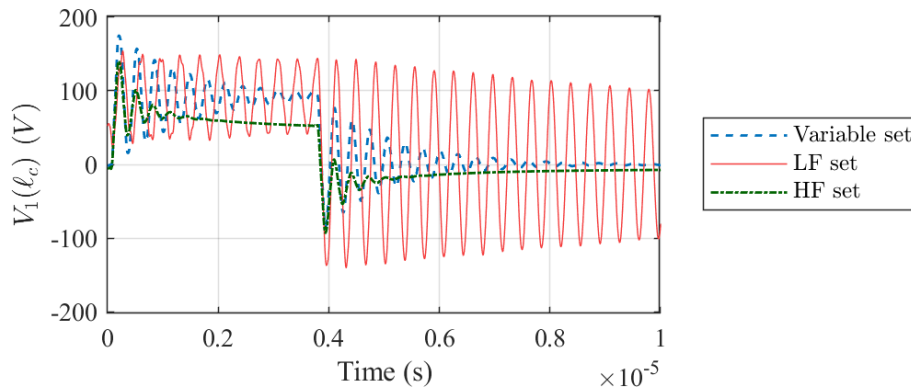


Figure 4.26 – Simulation of  $V_1(\ell_c)$  for three different cable parameter sets

The simulated results for the low frequency parameters have an attenuation coefficient much inferior than the one predicted by the complete model, because the losses at the resonance frequencies of the cable are much superior to its DC losses. For the same reason, the attenuation coefficient with the high frequency set of parameters is superior than the one of the complete model, because the losses at  $20 \text{ MHz}$  are bigger than the losses at the resonance frequency.

Moreover, for “HF” results, the final value of the voltage at the end of first phase of the switching period is considerably lower than expected. This value depends mainly on the DC losses of the cable, and therefore the high losses in the “HF” set of parameters causes this error.

The importance of representing the frequency dependence of the loss-related parameters is clear in this example. Only the parameter set variable on frequency is capable of correctly predict the behavior of a lossy cable in which resonances take place.

#### 4.5.b The wave traveling delay

A second advantage of the model proposed in this work is the correct modeling of the time delay of a traveling wave in a long cable.

To demonstrate it, a simulation of a  $100\text{ m}$  long cable excited by a step voltage (simulated with a trapezoidal signal of long period:  $T_0 = 10\text{ ms}$ ) was performed. The cable parameters used in the simulation are those of the  $2.5\text{ mm}^2$  two-conductor cable, plotted in Fig. 2.33. The simulated input and output voltages in the cable are plotted in Fig. 4.27. A time delay of around  $700\text{ ns}$  can be measured.

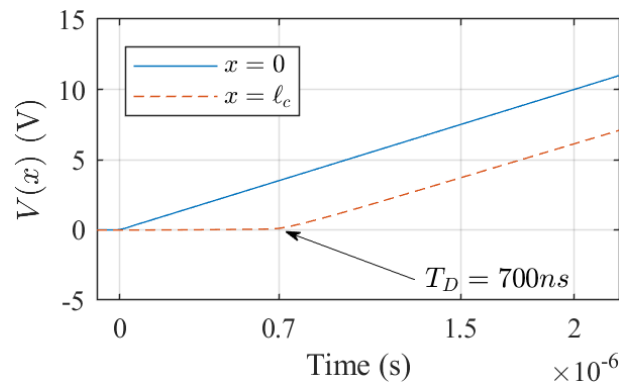


Figure 4.27 – Voltage pulse sent into a  $\ell_c = 100\text{ m}$  long cable

To verify that this delay is coherent, the propagation speed for the  $2.5\text{ mm}^2$  two-conductor cable is plotted in Fig. 4.28. In high frequencies, the mean propagation speed is around  $1.4 \times 10^8\text{ m/s}$ . That gives an approximated time delay of  $T_D = \ell_c/v = 715\text{ ns}$ , what corresponds to the simulation results.

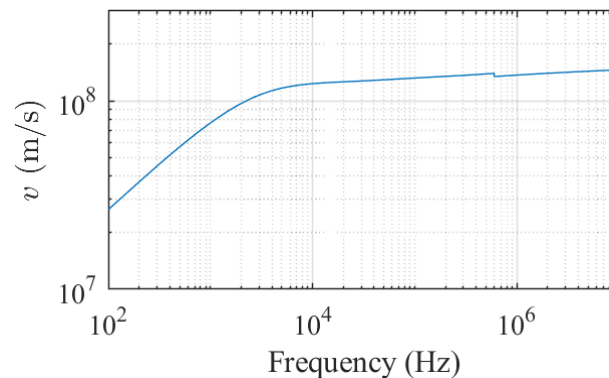


Figure 4.28 – Propagation speed in the  $2.5\text{ mm}^2$  two-conductor cable

It is important to note that the dependence of the propagation speed with the frequency is inherent of lossy lines. For example, it is responsible for the deformation of the input signal on time domain.

### 4.5.c Advantages of the frequency domain model

The principal advantage of solving the transmission line equations in the frequency domain is the fact that no extra approximations are needed to represent the frequency dependency of cable p.u.l. parameters, in opposition to time domain models. The later are always based on approximations to represent phenomena such as proximity and skin effect.

The high accuracy of the simulation on the frequency domain, using the Fourier and the phasor representation series to perform the transform to time domain, is demonstrated in section 4.4.

Moreover, the method has a good computational performance, having a computation time that does not increase with the cable length, but instead depends mainly on the number of points  $x$  along the line where the voltage is to be calculated, and the number of frequency harmonics to be taken into account and the sampling rate on time domain. Therefore, the method is particularly interesting in the applications where the input and output voltages and currents are the only variables of interest, what is the case for most of the applications in the literature.

In terms of computational effort, when modeling a multiconductor cable of  $n + 1$  conductors, the simulation tool requires the calculation of its modeling matrix  $\Phi$ , and the solution of a linear system of order  $2n$ , for each harmonic. Once the frequency domain simulation is performed, a summation of harmonics of the results is needed. These operations demand low computational effort, principally when compared to the time domain simulation of the series association of basic cells, with T-ladder networks emulating the frequency-dependent behavior of the cable losses (cf. 4.2.b)

Also, another advantage in comparison to the equivalent T-ladder networks model is that the frequency domain solution guarantees that the magnetic couplings parameters (p.u.l. mutual inductance) can vary with frequency, a representation that is not possible with the T-ladder networks (cf. 4.2.b).

In conclusion, the frequency domain simulation followed by a Fourier series based time domain transform is an efficient modeling technique, well adapted to represent the building cabling. Indeed, this assertion is reinforced by the fact that the devices connected to a building network can be represented by periodical sources, as they are either alternative (50/60Hz) or have a power converter with a periodic switching on their inputs. One limitation brought by the model based on the signal periodicity is that the lightning phenomena cannot be represented by it, and would need a separate simulation to be taken into account.

## 4.6 Conclusion

In this chapter a time domain simulation tool has been built, using the frequency domain tools developed in the previous chapter and the Fourier series to represent the system on the frequency domain. The results of this simulation tool have been experimentally validated.

The choice to perform time domain simulation passing through the frequency domain guarantees the accurate description of the cable losses, crucial to the resonance phenomenon modeling, at the same time it simplifies the cable losses representation.

Moreover, the accuracy of the results is remarkable. The oscillations observed on the time domain due to resonance are reproduced in the theoretical results within the accuracy of the measurement instruments, and the shape of these oscillations is more realistic than what is more

commonly obtained with time domain simulations.

The proposed frequency domain algorithm is efficient, and as the transform to time domain does not cost much in computing time, the whole simulation tool is not time-consuming computationally.

The proposed time domain simulation tool is well adapted for the simulation of a real industrial or building cabling network, and can be the key to correcting the EMI problems in these networks in the future work.

CONTENTS

---

5.1	INTRODUCTION . . . . .	114
5.2	METHODOLOGY TO DETECT RESONANCE PROBLEMS IN A GIVEN SYSTEM . . . . .	114
5.3	INDUCTION MOTOR FED WITH ELECTRICALLY LONG CABLE . . . . .	115
5.4	DC LINK WITH ELECTRICALLY LONG CABLE . . . . .	123
5.4.a	DC link - differential mode . . . . .	123
5.4.b	DC link - common and differential mode . . . . .	128
5.5	FILTER DESIGN TAKING RESONANCE PHENOMENA INTO ACCOUNT . . . . .	135
5.6	CONCLUSION . . . . .	143

---

**Abstract**

*In this chapter, the MTL simulation is applied to specific systems susceptible to resonance in long cables. A methodology to analyze the resonance potential damage is proposed, and applied in practical examples. Three system are studied with the simulator proposed in this work: an electric machine activated with a variable frequency drive through a long cable, a DC link with voltage elevation for transmission of power in a long distance, and a long connection between a battery and switched device. In the last section, the resonance surface response introduced in chapters 2 and 3 are applied to the design of minimal EMI filter in an embedded system.*

## 5.1 Introduction

In this section the time domain simulation tool developed in the previous chapter will be used to analyze different applications. These examples will show the efficiency and adaptability of the proposed tool.

In addition, the simulation tool allows an analysis in the frequency domain able to predict the resonance behavior of a cable in a given system, what is useful to design systems robust against this phenomenon.

In section 5.2, a straight-forward methodology to analyze the resonance behavior in a given system is described. The efficiency of this methodology is demonstrated in each of the applications studied in this chapter, where the resonance behavior of the given system is characterized. In section 5.3 the well-known case where an induction motor is fed through an electrically long cable is studied. In section 5.4, two DC systems with long cables are studied, the first exclusively in differential mode, in section 5.4.a, and the second in differential and common mode, in section 5.4.b. In section 5.5 the resonance behavior of a cable is taken into account on the designing of a minimal EMI filter taking the resonance phenomenon into account.

## 5.2 Methodology to detect resonance problems in a given system

Resonance problems may arise in any system in which the harmonics injected in a transmission line are of frequency higher than  $f > v/4\ell_c$  — or, equivalently, are of a wavelength smaller than  $\lambda < 4\ell_c$  — where  $v$  is the propagation speed in the line and  $\ell_c$  the line length.

An accurate frequency domain model, defined as described in chapters 2 and 3, is very handy to predict the resonant behavior of any system containing an electrically long cable, i.e., a cable longer than  $\lambda/4$ , for the harmonic of the smallest wavelength circulating in the system.

In this section, a methodology of analysis able to characterize the resonant behavior of a transmission line in a given system is defined. This methodology will be applied in the practical examples described in sections 5.3 and 5.4.

The methodology consists in the determination of the transfer function of a system relative to the perturbation sources.

To that end, first consider that the Frequency domain simulation tool is based on the solution of the system of equations (3.22), repeated here for convenience.

$$\left\{ \begin{array}{l} \begin{bmatrix} \mathbf{V}(\ell_c, f) \\ \mathbf{I}(\ell_c, f) \end{bmatrix} = \mathbf{\Phi}(\ell_c, f) \begin{bmatrix} \mathbf{V}(0, f) \\ \mathbf{I}(0, f) \end{bmatrix} \\ \mathbf{I}(0, f) = \mathbf{S}_S(f) - \mathbf{Y}_S(f)\mathbf{V}(0, f) \\ \mathbf{I}(\ell_c, f) = \mathbf{S}_L(f) - \mathbf{Y}_L(f)\mathbf{V}(\ell_c, f) \end{array} \right.$$

The transfer function relative to a given scalar source  $S$  can be obtained by setting the value of this source to  $1V$  or  $1A$ , and canceling all the other sources in the system.

Using the transfer functions, the resonance frequencies of the cable can be determined by comparing the voltages or currents along the cable to the ones at the cable input. The resonance potential to cause damage can also be estimated.

In addition, the resonance behavior of a system can be used as an additional information in the design of the input/output filters connected to the cable. Indeed, the resonance surface

response introduced in sections 2.5.b and 3.5.b can be adapted to map the resonant behavior of a system, in function of any two variables. These variables can be the real and imaginary part of an impedance, as done previously, or the value of an inductance and a capacitance, what is useful for filter design. An example of an EMI filter design which takes into account the resonance behavior of the cable is described in section 5.5.

### 5.3 Induction motor fed with electrically long cable

The most common EMI problem due to voltage resonance in the literature is the case when long cables are used to connect an induction machines to its drive [52], [20], [35], [41], [45], [15], as mentioned in chapter 1. This well-known application will be studied in this section, as one of the examples for which the time domain simulation tool described in 4.3.c can be useful.

Induction motors are usually driven and controlled with variable frequency drives. The structure of these drives commonly has an inverter on its output. The output filter of drive is often not present, due to the facts that its cost is high and the highly inductive impedance of the motor in low frequencies make it redundant. However, in the absence of the output filter the square pulse-width modulated voltage imposed by the inverter propagates in the line, with its rich harmonic content. It is very likely that the switching harmonics will excite the natural frequencies of a few meters long cable, and the resonance-due harmonic amplification may cause dangerous over-voltages in the system.

These over-voltages due to cable resonance can also be explained on time domain: the inverter imposes a voltage with high  $dV/dt$  in the cable input, and the voltage front is nearly fully reflected at the cable terminals. Indeed, at the cable terminal connected to the electric machine, the wave is reflected because the input impedance of the electric machine is at least an order of magnitude higher than the characteristic impedance of the cable  $Z_c$  for most of the low to medium frequency band. In the inverter terminal, the equivalent impedance of the switching cell is low, as the switching devices have low internal resistance, and the inverter output impedance is at least one order of magnitude lower than  $Z_c$  for most of the frequency band. The reflection at both ends of the cable lead to stationary waves that when superposed cause a significant resonance-due over-voltages at the cable end that may damage the induction machine.

With the advent of wide-band gap semiconductors, the resonance problems will appear for smaller cables [45]. Many practical solutions to this problem are synthesized in [15].

The time domain simulation tool will be used to analyze the system in Fig. 5.1. It consists in an induction motor driven by a variable frequency drive, and connected to it through a long four-conductor cable. The cable has a tinned cooper wire shield that is taken into account by the conductor “4” in Fig. 5.1.

The electrical machine in this example is a Leroy Somer three-phase induction motor, of power  $1.5\text{ kW}$ . The input impedance of the motor was measured following the procedure described by Revol [41], [40]. Assuming that the motor has three identical windings, what is true for most three-phase motors in good shape, the motor can be identified with the two measurements shown in Fig. 5.2, performed between points  $a$  and  $b$ .

The details of the experimental setup to perform the measurements in Fig. 5.2 are resumed in appendix H. Also, this identification method was validated with a different experimental approach, this validation is detailed in appendix I.

The input impedances  $Z_{PP}$  and  $Z_{PG}$  measured in the chosen motor are presented in Fig. 5.3.



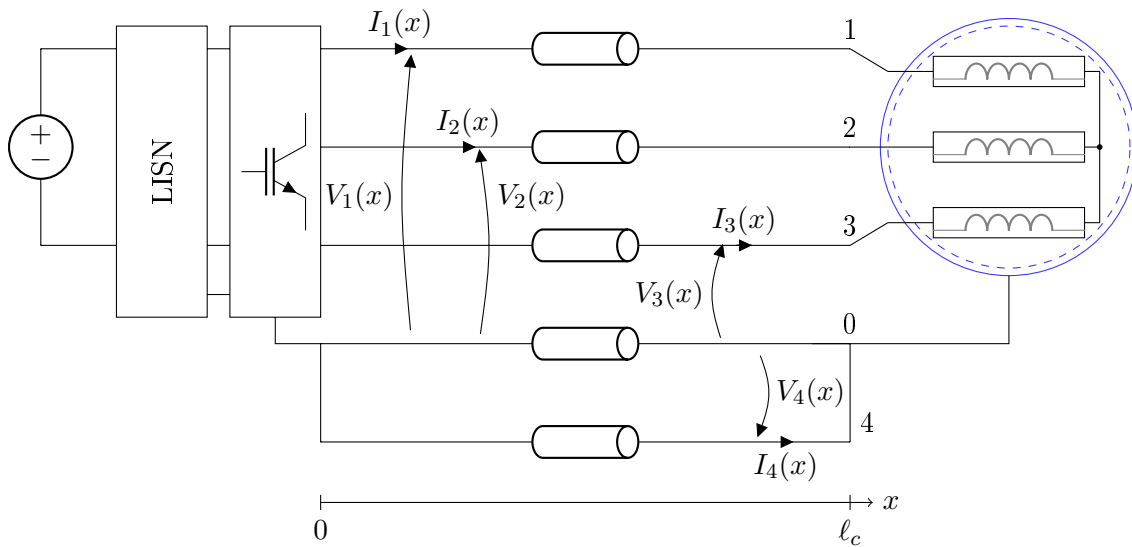
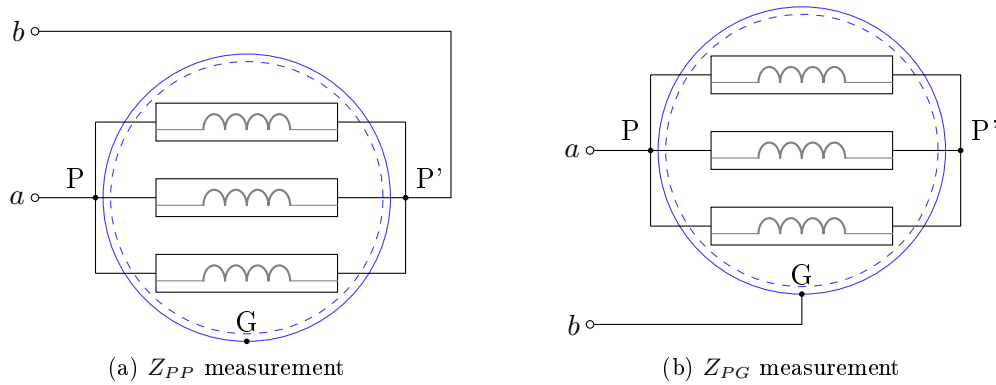


Figure 5.1 – Induction motor fed with long cable

Figure 5.2 – Measurement schematics to characterize the three-phase motor: input impedance measured between points  $a$  and  $b$ 

To obtain an input admittance matrix for the three-phase motor, it is supposed that input impedance of each phase can be presented by the equivalent circuit in Fig. 5.4. In this circuit,  $Z_b$  represents the impedance of one winding, and  $Z_g$  the stray elements between the windings and the motor carcass. It is supposed that the motor is symmetric to common mode, i.e., the stray elements between points  $P$  and  $G$  are the same as the elements between points  $P'$  and  $G$ , and can be represented by the same impedance  $Z_g$ . Indeed, the rotor of an induction motor behaves as a Faraday cage in high frequency, what allows the impedance  $Z_g$  to be constant independent of the rotor position, and symmetric to points  $P$  and  $P'$ .

Impedances  $Z_b$  and  $Z_g$  are obtained from the two measurements in Fig. 5.3 by solving the equations (5.2).

$$Z_b = 3Z_{PP} \frac{(4Z_{GP} - Z_{PP})}{(4Z_{GP} - 2Z_{PP})} \quad (5.2a)$$

$$Z_g = 3\left(2Z_{GP} - \frac{Z_{PP}}{2}\right) \quad (5.2b)$$

The machine is represented in the simulation model by its admittance input impedance  $Y_{motor}$ ,

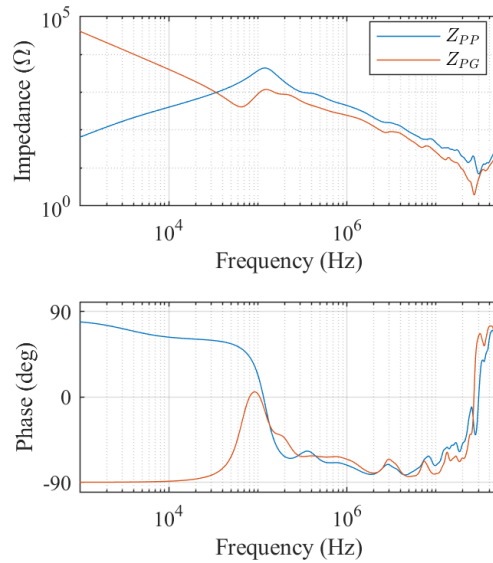


Figure 5.3 – Motor Leroy Somer 1.5 kW measured impedances

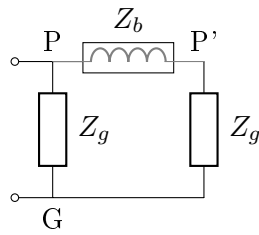


Figure 5.4 – Equivalent circuit of one phase of the motor

a matrix that satisfy the relation (5.3)

$$\begin{bmatrix} I_1(\ell_c) \\ I_2(\ell_c) \\ I_3(\ell_c) \end{bmatrix} = \mathbf{Y}_{\text{motor}} \begin{bmatrix} V_1(\ell_c) \\ V_2(\ell_c) \\ V_3(\ell_c) \end{bmatrix} \quad (5.3)$$

By representing the three phases of the motor in parallel, each phase given by the equivalent circuit in the schematic in Fig. 5.4, the matrix  $\mathbf{Y}_{\text{motor}}$  can be deduced. It is given in (5.4).

$$Y_b = Z_b^{-1} \quad (5.4a)$$

$$Y_g = Z_g^{-1} \quad (5.4b)$$

$$Y_{\text{diag}} = 2Y_b^2 + 6Y_b Y_g + 3Y_g^2 \quad (5.4c)$$

$$\mathbf{Y}_{\text{motor}} = \frac{1}{3(Y_g + Y_b)} \begin{bmatrix} Y_{\text{diag}} & -Y_b^2 & -Y_b^2 \\ -Y_b^2 & Y_{\text{diag}} & -Y_b^2 \\ -Y_b^2 & -Y_b^2 & Y_{\text{diag}} \end{bmatrix} \quad (5.4d)$$

The couplings between the windings of the motor are taken into account in this model. Indeed, this is shown by the fact that the motor is represented by a full admittance matrix, and that  $\mathbf{Y}_{\text{motor}}$  remains a full matrix even if the stray common-mode admittance  $Y_g$  is considered an

open circuit.

The cable is composed of four stranded wire conductors of section  $1.5\text{ mm}^2$  with a tinned cooper wire outer shield, its cross-section is represented in Fig. 5.5 and its p.u.l. parameters are available in appendix G. The cable is  $70\text{ m}$  long, three of its conductors are used for each of the three phases, and the fourth is used as the protective earth (PE) conductor. The PE is connected to the variable-frequency drive carcass at  $x = 0$  and to the motor carcass at  $x = \ell_c$ .

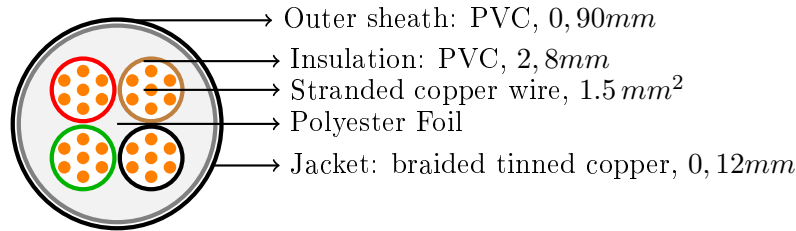


Figure 5.5 – Cross-section of the  $4 \times 1,5\text{ mm}^2$  cables

The cable parameters have been identified experimentally, following the protocol described in section 3.3. The protection conductor PE is taken as the reference conductor 0, as labeled in Fig. 5.1. Naturally, any other conductor could have been chosen as the reference, the PE was the one preferred by the author.

The representation of the voltage inverter on the frequency domain requires a linearization. This necessity arises in the frequency representation of any power converter. However, it is possible to obtain an equivalent frequency domain behavior by representing the switching cell with a trapezoidal pulse source, corresponding either to a voltage or a current in one of the semiconductors, depending on the structure of the power converter under study. This modeling technique has been introduced in the literature in [44], [41], [40].

The inverter chosen for this study is a two-level structure with sinusoidal intersection Pulse Width Modulation (PWM). The inverter is represented in the schematic in Fig. 5.6a, and its parameters are listed in table 5.1. For a power inverter, as introduced in [41], the frequency domain equivalent model is obtained by substituting each switching cell by a voltage source that corresponds to the voltage imposed at the midpoint of the cell, as drawn in Fig. 5.6. Each voltage source  $V_a, V_b, V_c$  is defined as a trapezoidal signal representing the voltage at the terminals of the switch in the low side of each inverter leg. The capacitances  $C_{p0}$  to  $C_{p4}$  represent the stray capacitances in the inverter structure. The LISN on the inverter input is simplified to its  $50\ \Omega$  equivalent impedances in the inverter model.

Table 5.1 – Parameters of two-level voltage inverter

$V_{DC}$	800 V	$R_p$	20 m $\Omega$	$C_{p2}$	50 pF
$C$	1 mF	$C_{p0}$	200 pF	$C_{p3}$	50 pF
$L_p$	50 nH	$C_{p1}$	50 pF	$C_{p4}$	200 pF

With this modeling technique, the upper point of the inverter legs is not fully represented. This is an intrinsic limitation of the model.

The complete equivalent model of the system adapted to frequency-domain simulation is shown in Fig. 5.7.

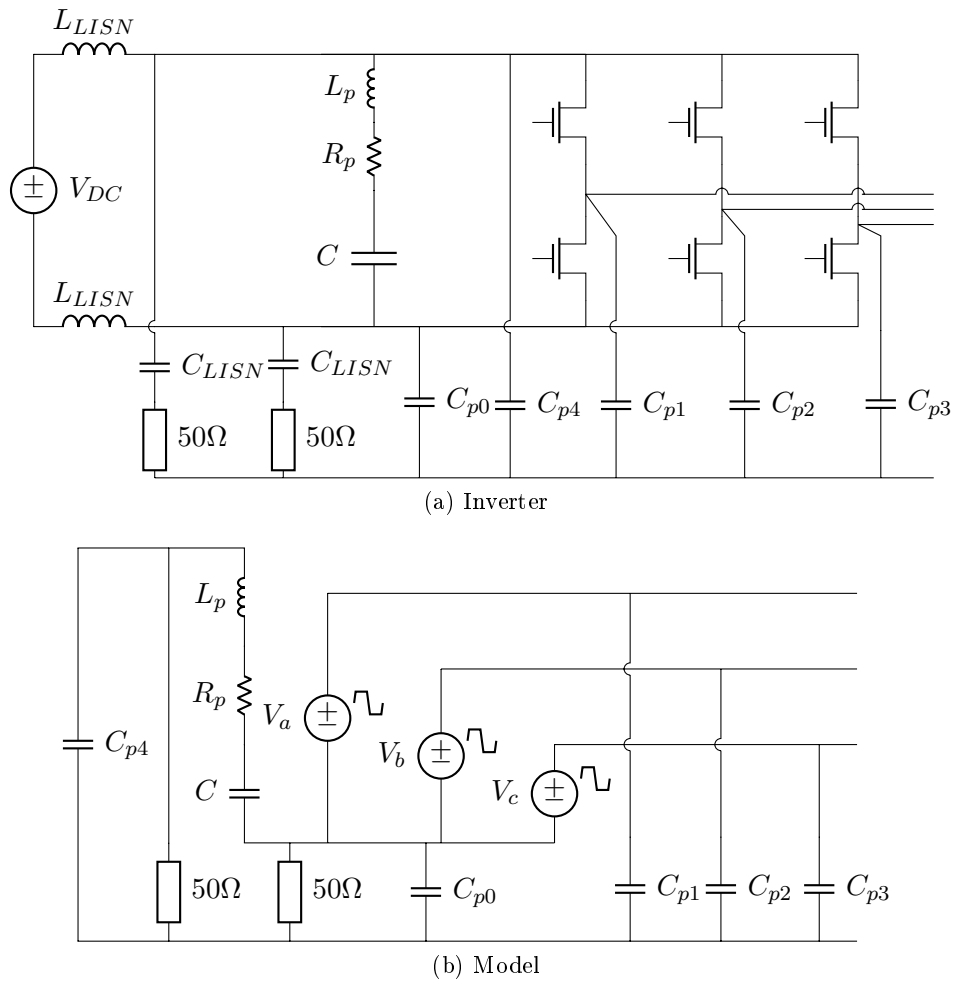


Figure 5.6 – Two-level inverter model, with LISN

The model in Fig. 5.7 allows the analysis of the frequency response of the system. To obtain the transfer functions relative to each one of the sources  $V_a$ ,  $V_b$  and  $V_c$ , three distinct analysis have been performed. In each of them, the voltage of one of the sources was defined as  $1\text{ V}$  for the whole frequency band, while the other sources were short-circuited. The results are plotted in Figs. 5.8 to 5.10.

The resonance frequencies of the cable can be observed in Figs. 5.8 to 5.10. The first, with the biggest amplification, takes place around  $500\text{ kHz}$ . It amplifies up to 4.8 times the amplitude of the harmonic on the cable input.

The symmetry of the problem is visible by comparing the transfer functions relative to  $V_a$  and  $V_c$ , which are equivalent with the voltages  $V_1(\ell_c)$  and  $V_3(\ell_c)$  interchanged.

The likelihood of this resonance to amplify the input signal will be studied by defining the “amplification frequency band” as the bandwidth where the resonance amplification is higher than a half of its peak value. Figs. 5.8 to 5.10 show that the amplification frequency band is a few hundreds of  $\text{kHz}$  large. Considering that most variable frequency drives work with switching frequencies around  $10\text{ kHz}$ , it is likely that there will be switching harmonics in the amplification frequency band, and that resonance-due oscillations will occur.

The time domain simulation of this system is performed with the time domain simulation

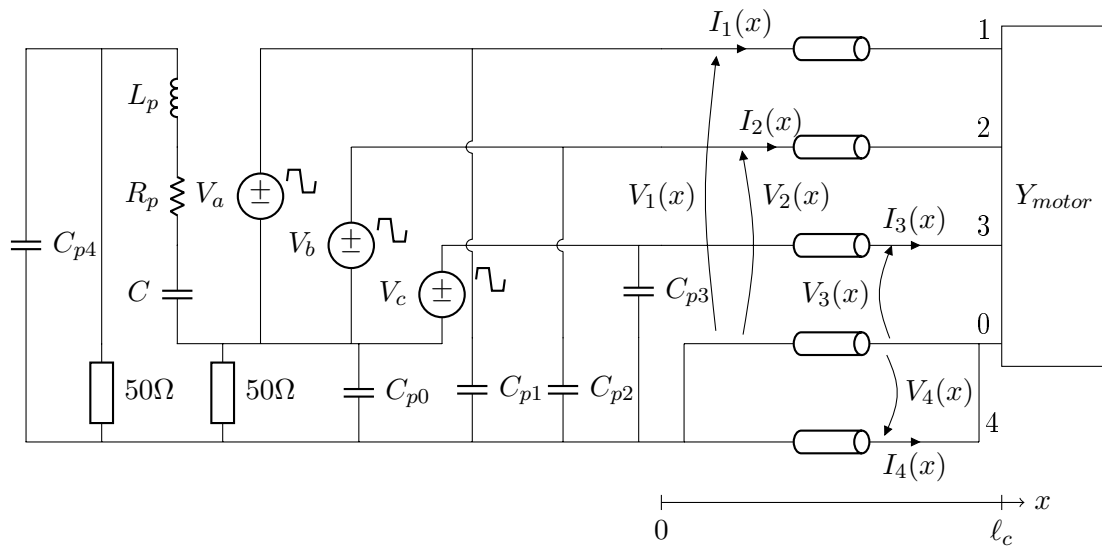
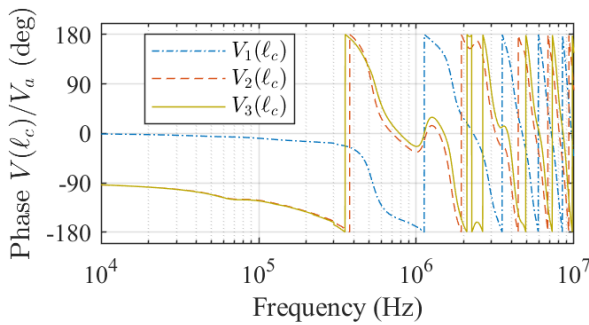
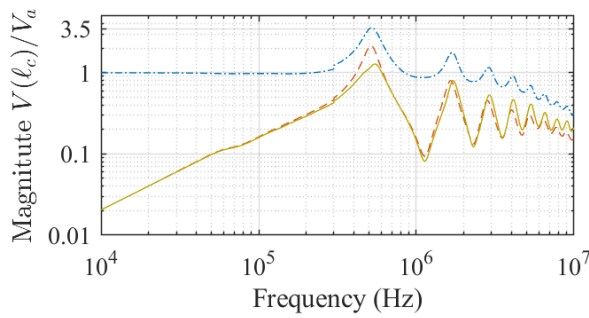
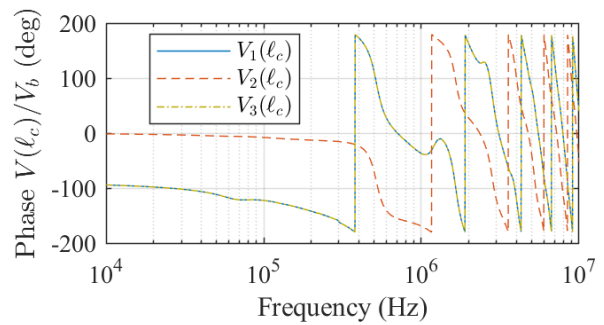
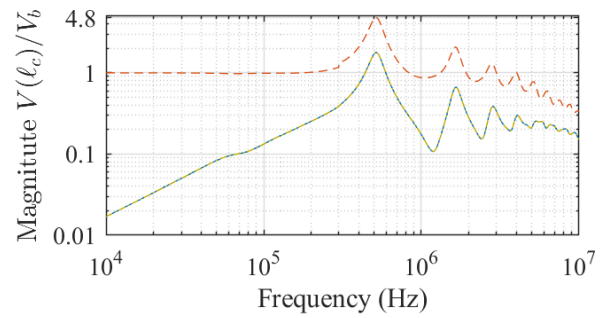


Figure 5.7 – Simulation model - Induction motor fed with long cable

Figure 5.8 – Frequency response relative to  $V_a$ ,  $\ell_c = 70m$ Figure 5.9 – Frequency response relative to  $V_b$ ,  $\ell_c = 70m$ 

tool described in section 4.3. The voltage sources  $V_a$ ,  $V_b$ , and  $V_c$  are defined as ideal trapezoidal sources, with rise time  $t_r$  and fall time  $t_f$ . They are represented in Fig. 5.11. They are calculated supposing that the inverter uses the sinusoidal intersection technique to build the PWM modulation. The switching frequency of the inverter  $f_{switch}$  was set to  $10 kHz$ , the output alternative current has a frequency of  $50 Hz$ , and the duty cycle of the voltages  $V_a$ ,  $V_b$ , and  $V_c$  are calculated for the time instant  $t_{sin} = 4 ms$  of the sinusoidal references of the three-phase system. The frequency domain representation of the sources uses the Fourier series decomposition in (4.20) (cf. Fig. 4.6). The parameters chosen for the time domain simulations are listed in table 5.2.

The time domain simulations were performed for three different cable lengths:  $1 m$ ,  $12 m$ ,

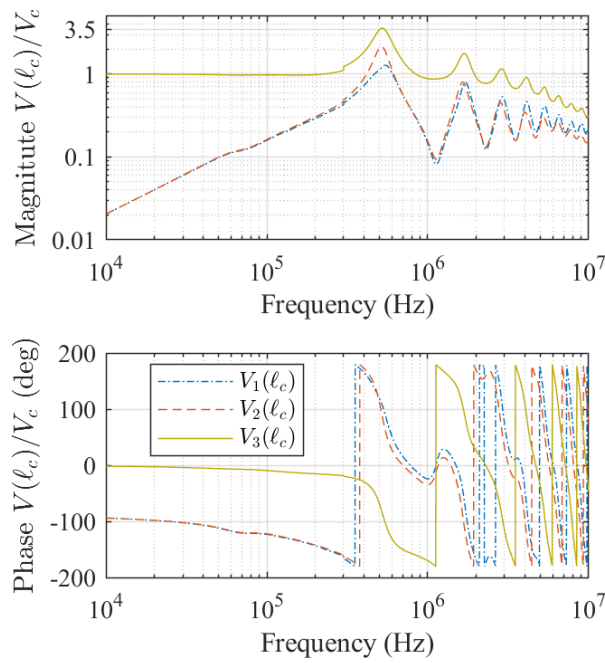
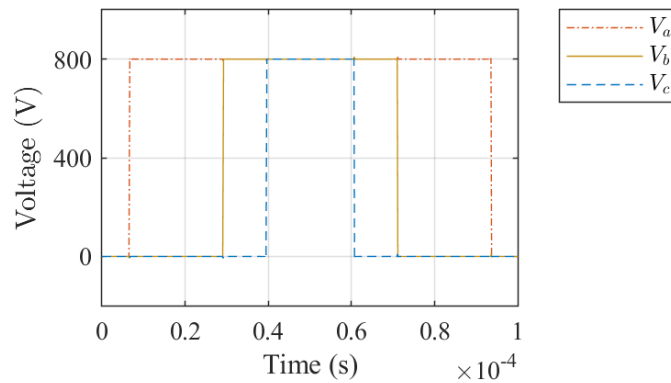
Figure 5.10 – Frequency response relative to  $V_c$ ,  $\ell_c = 70m$ Figure 5.11 – Voltage sources  $V_a$ ,  $V_b$ ,  $V_c$ 

Table 5.2 – Time domain simulation parameters

$f_{switch}$	10 kHz	$t_r$	200 ns
$t_{sin}$	4 ms	$t_f$	150 ns

and 70 m. The simulation results are plotted in Figs. 5.12 to 5.14.

The phase-to-phase voltages at the motor input for  $\ell_c = 70m$ , in Fig. 5.12a, present the oscillations at the resonance frequency predicted by frequency analysis: 500 kHz (cf. Figs. 5.8 to 5.10). Also, the oscillation peak is up to nearly two times the value of step voltage imposed at  $x = 0$ , corresponding to the behavior described in the literature [20]: the maximum over-voltage at the cable extremity is not greater than 2 times the input voltage imposed by the inverter if the oscillations are attenuated before the subsequent PWM pulse.

These oscillations do not take place for an 1 m long cable, as shows Fig. 5.13, and are of smaller amplitude and higher frequency for the 12 m long cable, as shows Fig. 5.14. This behavior

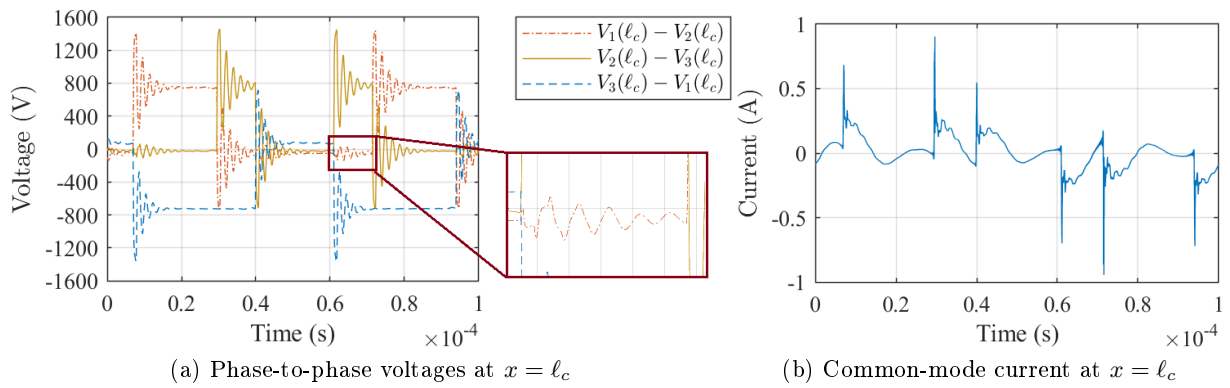


Figure 5.12 – Results of the time domain simulation for  $\ell_c = 70 m$

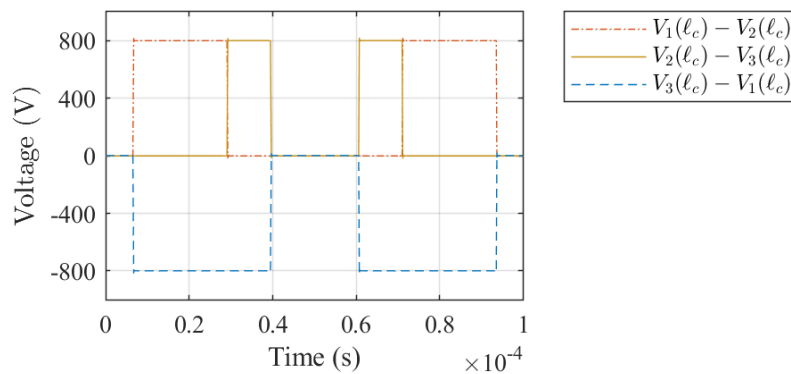


Figure 5.13 – Phase-to-phase voltages at  $x = \ell_c$  for  $\ell_c = 1 m$

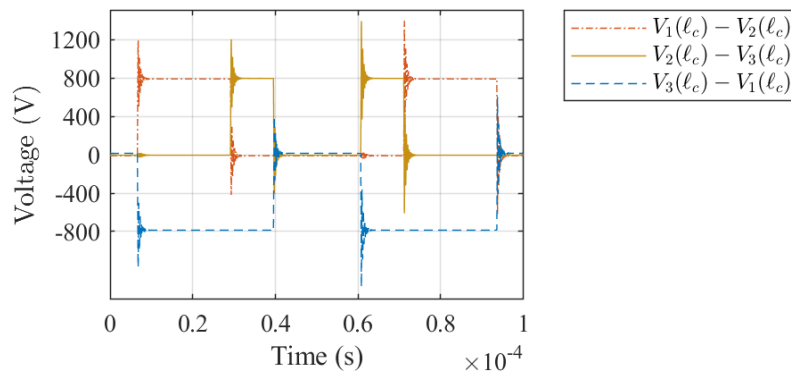


Figure 5.14 – Phase-to-phase voltages at  $x = \ell_c$  for  $\ell_c = 12 m$

corresponds to the one described in the literature [20, 52], and shows that the over-voltages are indeed a resonance-due amplification that occur in electrically long cables.

An interesting result on this solution is that the common-mode current circulating in the motor can be easily predicted, and is plotted for the system with  $\ell_c = 70 m$  in Fig. 5.12b. If this current is too high the machine can suffer insulation faults, and a drastic reduction on the useful life of the machine bearings [29, 36, 46]. Therefore, the prediction of these currents can avoid material damage.

The oscillations induced in one phase by the switching voltage in the other two phases can also be predicted, and can be seen in the zoom in Fig. 5.12a. These oscillations were not mentioned

in the reviewed literature, and they are predictable by the proposed model because it includes coupling elements between the three phases in the cable and in the motor models.

In conclusion, the simulation tool proposed in this work can efficiently model this case study. The coupling between the phases is represented, and the common-mode current in the induction motor carcass can be directly obtained from the simulation results. The resonance in the long cable was predicted with the proposed methodology based on a frequency domain analysis, and the time domain simulation results corresponds to the predicted behavior. The efficiency of the different solutions to avoid resonance-due overvoltages [15] could also be easily determined with this model.

## 5.4 DC link with electrically long cable

In this section, two different systems consisting of a DC link between a battery, or a battery pack, and its load are simulated with the simulation tool described in section 4.3.c.

In system in section 5.4.a we suppose that the stray currents on common mode are neglected. In section 5.4.b the common-mode currents are taken into account, but are supposed to circulate exclusively through a third conductor, used as PE.

### 5.4.a DC link - differential mode

The first DC link to be analyzed is represented on the schematic in Fig. 5.15. In this system, the voltage of a battery is elevated with a boost converter, to reduce the losses in the transmission of its energy through a 200 m long cable. At the cable output, a buck converter is connected to reduce the voltage to the nominal voltage of the load, represented by the impedance  $Z_L$ .

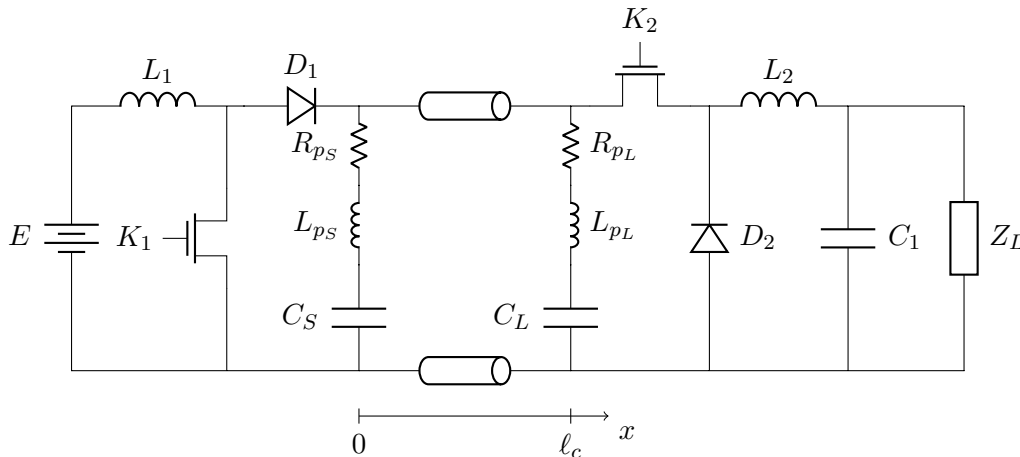


Figure 5.15 – Schematic of the DC link with voltage elevation: boost converter at the cable input and buck converter at the cable output

The boost converter switching cell is the association of the MOSFET  $K_1$  and the diode  $D_1$ , and its switching frequency is  $f_S = 40 \text{ kHz}$ . The capacitor  $C_S$  is its output filter. The capacitor is not ideal, and its imperfections are taken into account with the series parasitic resistance and inductance.

The buck converter switching cell is formed by the diode  $D_2$  and the MOSFET  $K_2$ , switching with at frequency of  $f_L = 100 \text{ kHz}$ . The capacitor  $C_L$  guarantees the stability of its input



voltage, and the same way as the former, it is not ideal, and the series parasitic resistance and inductance represent its imperfections.

The cable in this simulation is a two-conductor  $2.5 \text{ mm}^2$  cable, its cross-section is represented in Fig. 5.16, and its per-unit-length (p.u.l.) parameters are plotted in function of the frequency in Fig. 2.33.

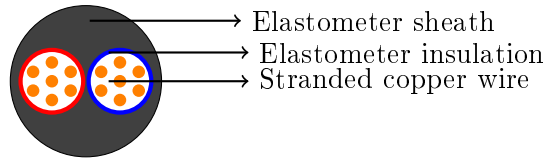


Figure 5.16 – Cross-section of the two-conductor  $2.5 \text{ mm}^2$  cable

As done for the inverter in the previous section, the power converters at each of the cable extremities will be represented in the frequency domain with an equivalent model, where the switching cell is replaced by periodic trapezoidal source [40, 41, 44]. The development of the equivalent model of the buck and boost converters is detailed in the first chapter of [10].

In differential mode, the switching cell of the DC-DC converters is substituted by a current source, as show by the schematic presented in Fig. 5.17. Each source corresponds to the current at the switching cell input. Source  $I_S$  corresponds to the forward current at the diode  $D_1$ , and source  $I_L$  corresponds to the source-drain current in the MOSFET  $K_2$ .

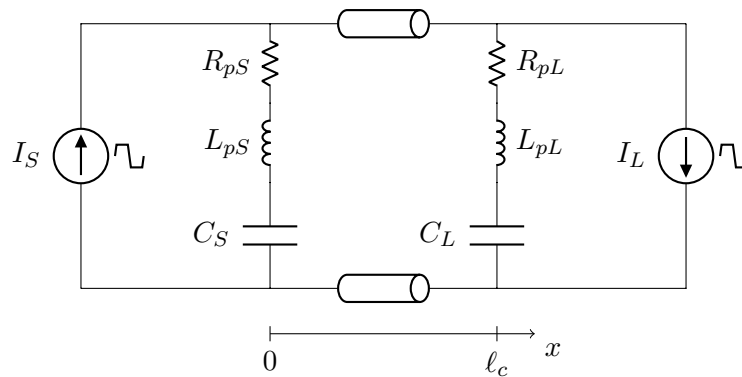


Figure 5.17 – Schematic of the simulated model of the DC link with voltage elevation

Table 5.3 resumes the parameters of the system shown in Fig. 5.17.

Table 5.3 – Parameters of the differential mode DC link model (cf. Fig. 5.17)

$f_S$	$40 \text{ kHz}$	$f_L$	$100 \text{ kHz}$
$C_S$	$10 \mu F$	$C_L$	$10 \mu F$
$R_{pS}$	$10 \text{ m}\Omega$	$R_{pL}$	$10 \text{ m}\Omega$
$L_{pS}$	$10 \text{ nH}$	$L_{pL}$	$10 \text{ nH}$

With the frequency domain simulation model defined (Fig. 5.17), it is possible to perform the frequency response analysis of this system. For this purpose, we calculate the currents on the line at  $x = 0$  and  $x = \ell_c$  for an excitation  $I_S = 1 \text{ A}$  in the whole frequency band, with the source

$I_L$  canceled. The results are presented in Fig. 5.18. The system is symmetric, so the transfer function relative to  $I_L$  has the same behavior.

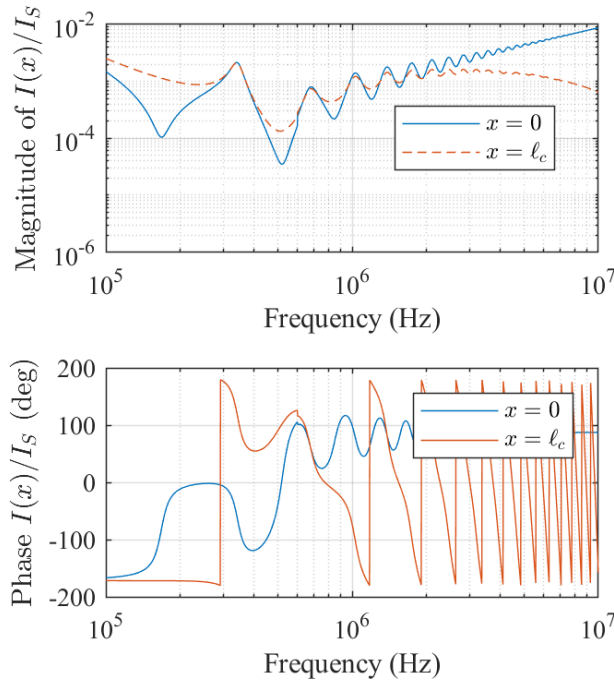


Figure 5.18 – Transfer function of the currents at the line extremities, relative to  $I_S$

From Fig. 5.18 it can be seen that, for the whole frequency band, the responses  $I(0)/I_S$  and  $I(l_c)/I_S$  are not greater than 1. On the resonance frequencies, its amplitudes are the same at both terminals of the cable. For that reason, there is no over-currents or over-voltages due to resonance in the cable.

This can be easily explained by comparing the impedances of the filter and the input impedance of the cable. In other words, the comparison between the impedance of the capacitor  $C_S$ , taking into account its imperfections, and the input impedance  $Z(0)$ , calculated with the capacitor  $C_L$  as load to the cable. Both of these impedances are plotted in Fig. 5.19.

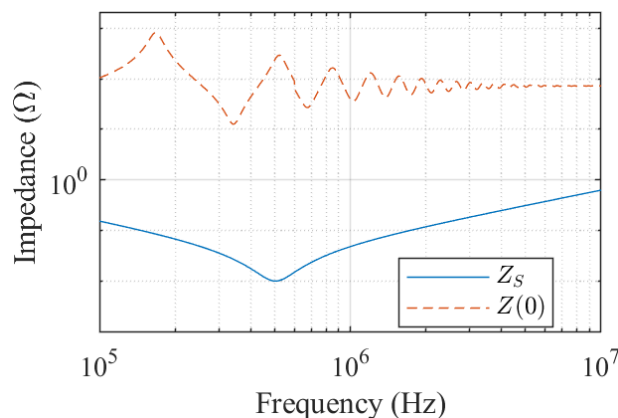


Figure 5.19 – Input impedances of the cable and the capacitor

The impedance of the capacitor is one order of magnitude lower than the input impedance of the cable,  $Z(0)$ . Therefore, the perturbations injected by  $I_S$  circulate preferably through the

capacitor, reducing the amplitude of the harmonics circulating in the cable.

To visualize this conclusion on time domain, a simulation was done following the procedure detailed in section 4.3.

In this simulation, the DC value of the variables could not be simulated. It corresponds to the steady-state value of each variable, and it is an indirect input of the model, dependent on the mean value of the sources  $I_S$  and  $I_L$ . In this case, as both of the converters are represented by a current source, it is not possible to obtain the correct DC components. To explain this fact, consider the current source  $I_L$ : it represents the switched current absorbed by the buck converter, and its DC component should represent the power absorbed by the load  $Z_L$ . Indeed, if the power injected by source  $I_S$  is not completely absorbed by the source  $I_L$ , the power unbalance in the model induces a big error on the DC simulation. Moreover, as the currents represented by  $I_S$  and  $I_L$  are approximated by an ideal trapezoidal signal, it is certain that the power balance in the simulated system (Fig. 5.17) is not the same as the one in the real system (represented in Fig. 5.15). This is a limitation of the proposed model, and it is the reason why the DC components will not be simulated in this case study.

The time domain signals representing the sources  $I_S$  and  $I_L$  are plotted in Fig. 5.20. Recalling that the DC component of the signals is not included in the simulation, and for that reason is not included on the plot. The frequency domain representation of sources  $I_S$  and  $I_L$  uses the Fourier series decomposition in (4.20) (cf. Fig. 4.6).

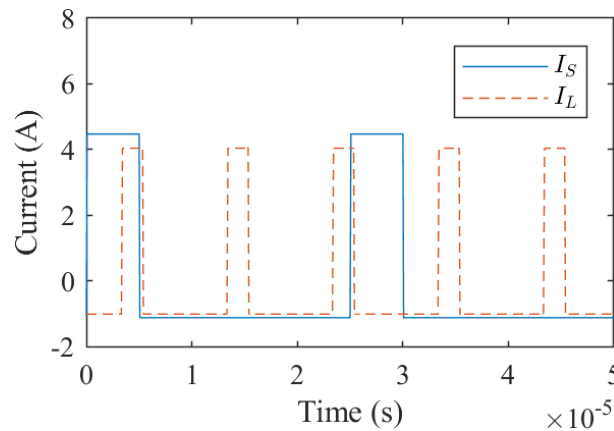


Figure 5.20 – Current sources modeling the DC-DC converters, without DC component

The two power converters have different switching frequencies. As aforementioned, the boost converter has a switching frequency of  $40\text{ kHz}$ , and the buck converter, of  $100\text{ kHz}$ . In systems with two different fundamental frequencies, there is an intrinsic oscillation on the frequency correspondent to the greatest common divisor (gcd) of the two switching frequencies. In our example, the gcd frequency is  $20\text{ kHz}$ .

The  $20\text{ kHz}$  frequency corresponds to a period of  $50\text{ }\mu\text{s}$ , the period represented in Fig. 5.20. It corresponds to five repetitions of the  $100\text{ kHz}$  period, and 2 repetitions of the  $40\text{ kHz}$  period. At  $t_0 + 50\text{ }\mu\text{s}$ , the relative delay between the pulses of each signal is the same as it was at  $t_0$ . From this comes the intrinsic oscillation on  $20\text{ kHz}$  of the system: it is derived of the superposition of the two exciting signals.

It is important to reinforce the fact that the  $20\text{ kHz}$  oscillation comes from the superposition of the harmonics of the two sources, and that there is no harmonic at  $20\text{ kHz}$  circulating in the

system. Equivalently, the frequency domain simulation does not have the  $gcd\ 20\ kHz$  included on the frequencies to which the simulation is effectuated.

The results of the frequency domain simulation converted to time domain are presented in Fig. 5.21.

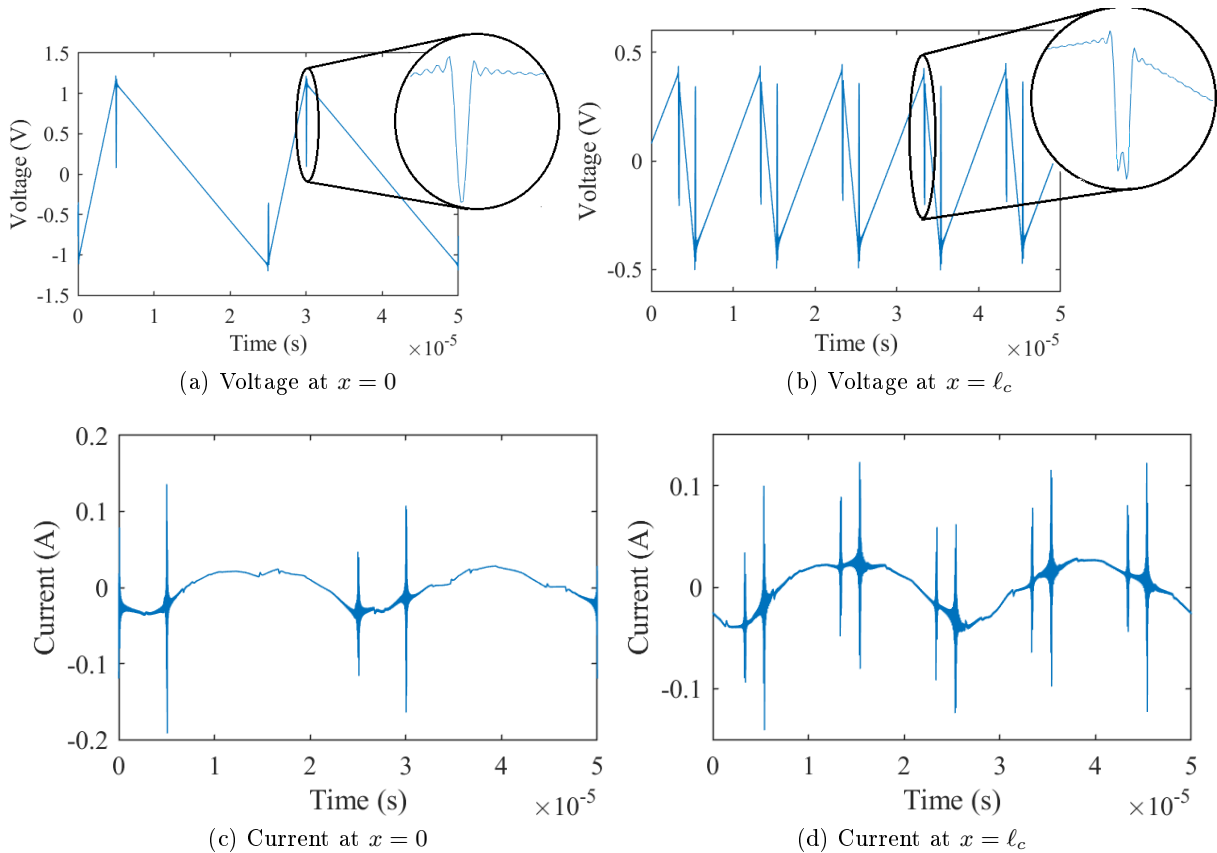


Figure 5.21 – Results of the simulation converted to time domain, without DC component

The oscillations observed on the voltages at the line extremities, plotted in Fig.5.21, are small. It corresponds to the voltage oscillations at the switching frequency, typical of a DC-DC converter. However, fast oscillations right after each switching event are also visible, and are due to the high  $dI/dt$  imposed by the switching cell, after being filtered by the capacitor.

The voltage waveform seem to be periodic with the switching frequencies, with the voltage at  $x = 0$  having an apparent period of  $25\ \mu s$ , in Fig. 5.21a, and an apparent period of  $10\ \mu s$  at  $x = \ell_c$ , in Fig. 5.21b. However, the periodicity of the system with the  $gcd\ 20\ kHz$  is visible in the currents, which have a waveform that does not repeat itself the  $50\ \mu s$  period. The current oscillations are also small, as predicted by the frequency response analysis of the system.

In the DC link studied in this section, there are no resonance related problems. The main reason for the stability of the system is the good filtering at the converters output.

In the next subsection a slight different system will be studied, and the analysis will take into account the common mode circulating in the system.

### 5.4.b DC link - common and differential mode

In this section, a different DC link is studied, taking into account the circulation of common mode. The system under study is presented in Fig. 5.22.

In this system, a three-conductor cable of 100 m long connects a battery to its load. The cable has three conductors because, besides the neutral and phase conductors, the protection conductor PE is connected to the carcasses of the devices. The common mode is supposed to circulate exclusively through the PE conductor.

The study is carried with the cable defined as three-conductors cable with conductors of section 2.5 mm<sup>2</sup>, its cross-section is represented in Fig. 5.23 and its parameters are plotted in Fig. 3.19.

The load is a switching device with common-mode filter at its input. The filter has a common-mode choke: the phase and neutral inputs are winded around magnetic core, using the same winding direction, so that the choke impedance is high in common mode, and almost zero in differential mode. Other than the choke, common-mode and differential-mode filtering capacitors are present, with its series parasitic resistances and inductances. The two common-mode capacitors,  $C_2$  and  $C_3$ , must be identical for the filter to be balanced, thus reducing common-mode circulation.

The switching device is a simplified buck converter. The current source  $I_L$  represents the DC current required by the load. The parasitic capacitance between the switching cell midpoint and the carcass is taken into account with the capacitor  $C_{p3}$ . The floating potential of this point makes this capacitance the most dangerous in terms of common-mode interference.

The battery has an internal resistance  $R_{bat}$ , and the parasitic capacitances to its carcass are as well represented.

As done previously, the switching cell will be represented by equivalent sources [40, 41, 44]. The schematic of the model for this system is drawn in Fig. 5.24. In this figure, the switching cell input current is represented by the current source  $I_S$ , and the voltage of the floating-point is represented by the voltage source  $V_k$ . The justification for this model is detailed in the first chapter of [10].

The parameters used in the model are listed in table 5.4.

Table 5.4 – Parameters of the model (Fig. 5.24)

Battery		Filter					Converter		
$E$	120 V	$R_p$	10 mΩ	$C_1$	10 μF	$C_2 = C_3$	22 nF	$C_{p3}$	100 pF
$R_{bat}$	0.25	$L$	1 μH	$R_{p1}$	20 mΩ	$R_{p2} = R_{p3}$	10 mΩ	$f_{switch}$	20 kHz
$C_{p1} = C_{p2}$	100 pF	$M$	0.5 μH	$L_{p1}$	50 nH	$L_{p2} = L_{p3}$	20 nH		

The representation chosen for the switching cell (with sources  $I_s$  and  $V_k$ ) is not completely accurate, notably because the connection of the floating-point to the upper part of the switching cell is not represented. Indeed, the voltage source could be connected either to the upper part or the lower part of the cell, but either way a current path would be missing.

Despite this inaccuracy, the model represents well enough the behavior of the power converter for frequencies equal or higher than its switching frequency [10].

The model represented in Fig. 5.24 allows the determination of the frequency response of the system.

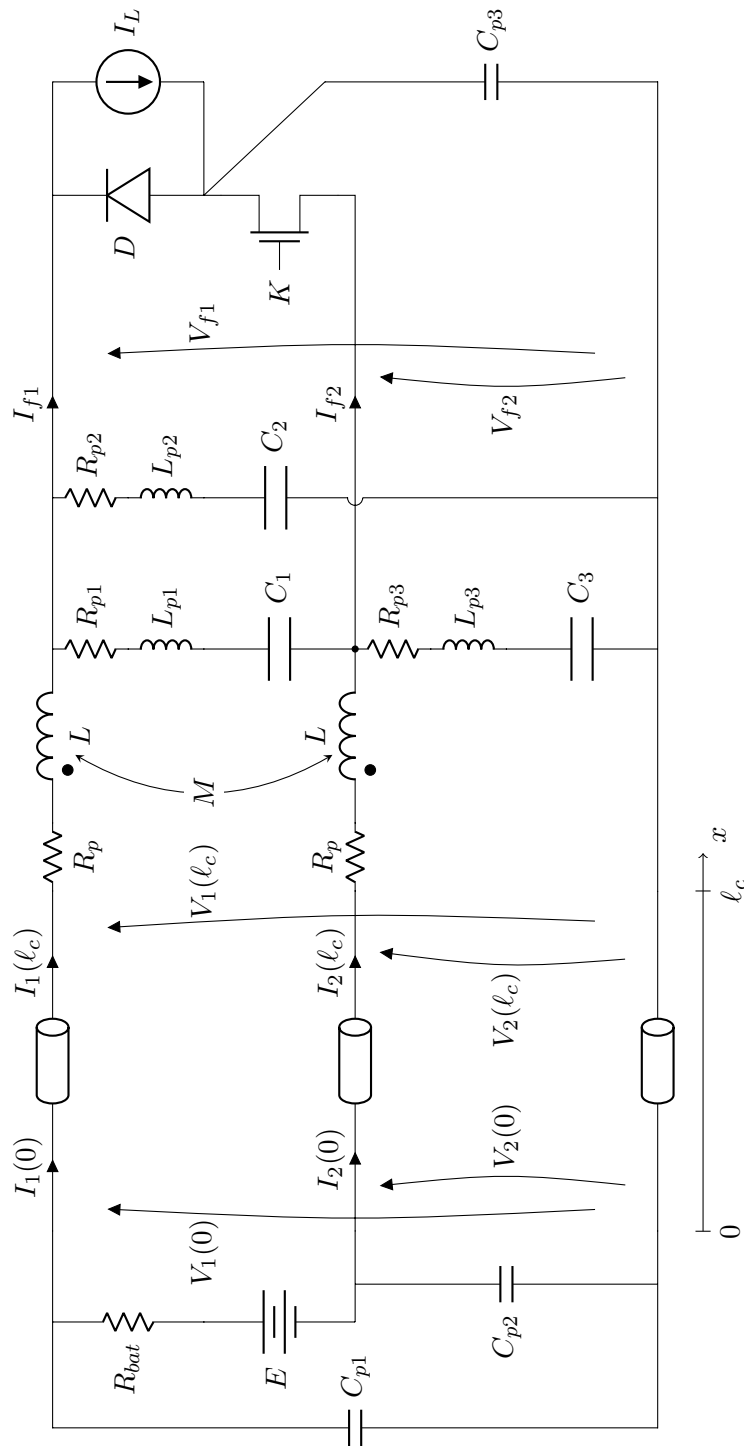


Figure 5.22 – Schematic of the DC link without voltage elevation, with common mode

Source: <http://www.caledonian-cables.co.uk>

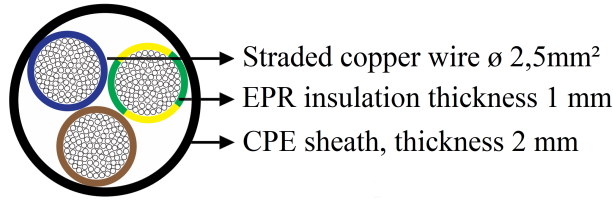


Figure 5.23 – Cross-section of the three-conductor  $2.5\text{ mm}^2$  cable

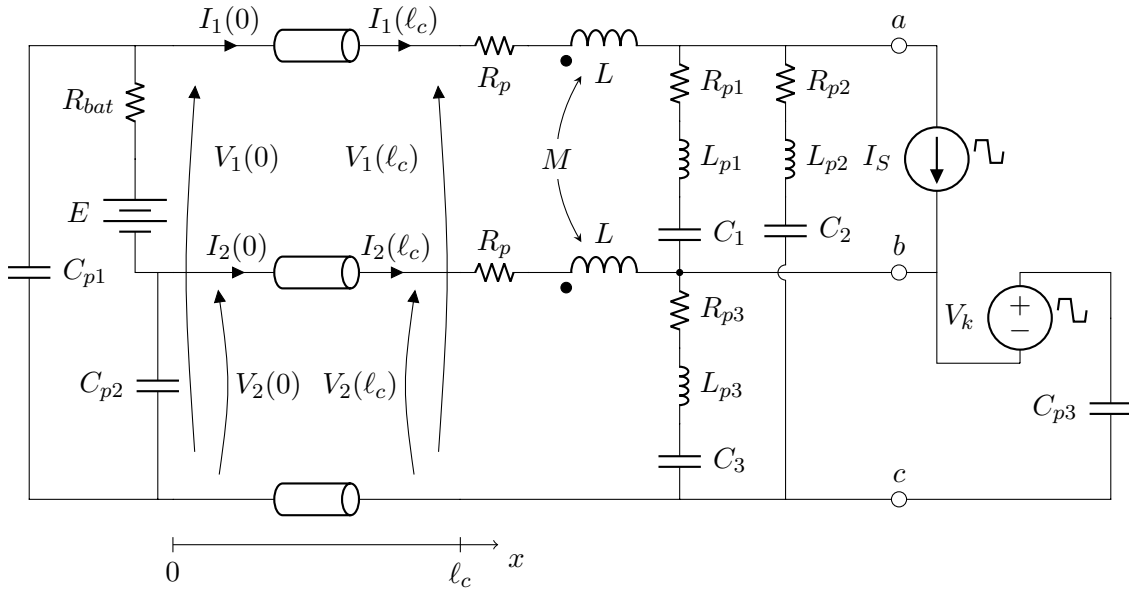


Figure 5.24 – Simulation model of the DC link with common mode

The equivalent model of the switching cell is not balanced. A different equivalent model with decoupled modes could be obtained if desired, and is what is done in section 5.5. For this analysis, the coupled model in Fig. 5.24 was chosen, and as it is not balanced it is simulated in the frequency domain in the physical basis, i.e., in function of  $V_1$ ,  $V_2$ ,  $I_1$  and  $I_2$ , following the steps described in 3.2.c.

However, once the system is solved, it is useful to express the results in the common and differential mode basis, in order to highlight the behavior of the common-mode stray voltage and current in the line. In this analysis, the common and differential modes are defined as follows:

$$V_{DM} = V_1 - V_2 \quad I_{DM} = \frac{I_1 - I_2}{2} \quad (5.5a)$$

$$V_{CM} = \frac{V_1 + V_2}{2} \quad I_{CM} = I_1 + I_2 \quad (5.5b)$$

The transfer functions relative to each of the sources are represented in Fig. 5.25, in terms of the differential-mode and common-mode voltages and currents.

The highest amplification of the voltages and currents occurs around  $5\text{ MHz}$ , for both of the transfer functions relative to  $V_k$  and  $I_S$ . This peak is caused by the interaction between the parasitic capacitance  $C_{p3}$  and the filter elements.

The differential-mode response to the source  $I_S$  in Fig. 5.25a is considerably higher than the

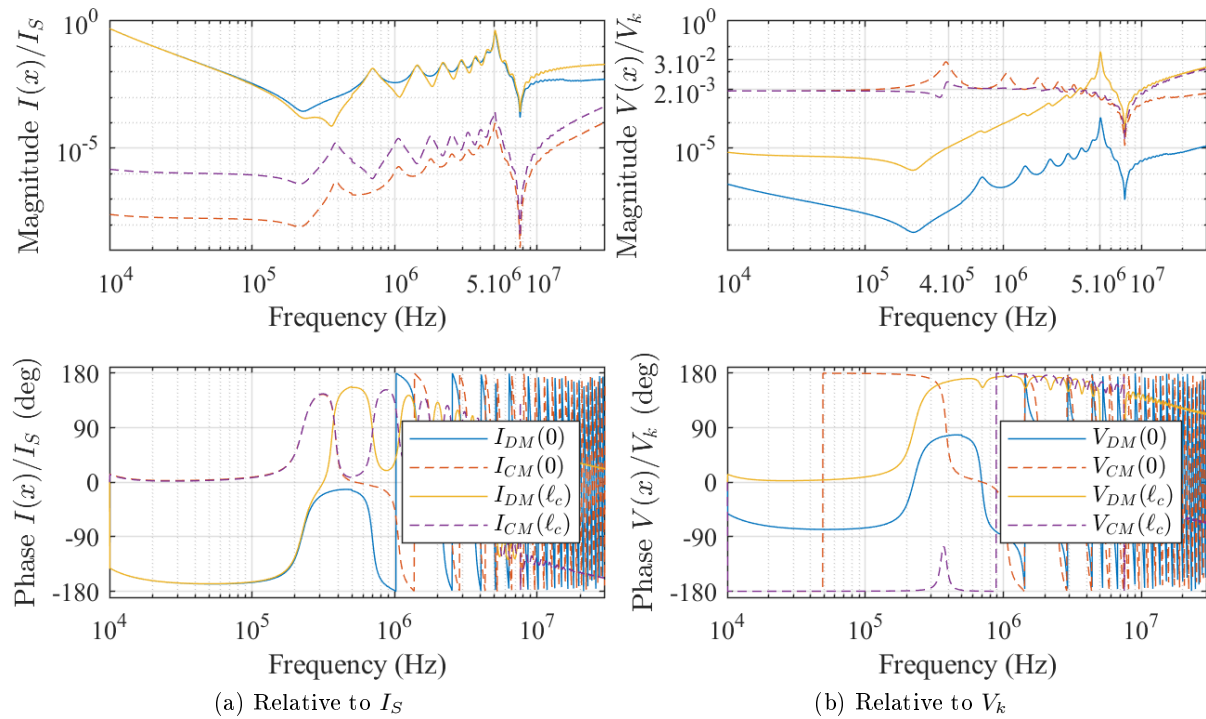


Figure 5.25 – Transfer functions relative to the sources in the system

common mode for whole frequency band. This behavior is expected, as the source  $I_S$  is close to represent the differential-mode excitation in the system.

On the other hand, the common-mode response to the source  $V_k$  in Fig. 5.25b is considerably higher than the differential mode up to a few  $MHz$ . This happens because this source represents the switching voltage imposed at the switching cell middle point, the principal source of common mode in any switching device.

The comparison between the differential-mode voltage magnitudes at both extremities of the line in Fig. 5.25 shows that the differential mode is not amplified at its natural frequencies. This can be explained by comparing the input impedance of the system in differential mode to the impedance of the capacitor filtering the mode,  $C_1$ . The differential mode input impedance  $Z_{DM}$  is calculated from the schematic in Fig. 5.26, between points  $a$  and  $b$ :

The input impedance  $Z_{DM}$  is plotted over the impedance of the non-ideal capacitor  $C_1$  in Fig. 5.27a. It can be seen that, except for a dump around  $1.4MHz$ , the input impedance of the system is larger than the impedance of the filtering capacitor  $C_1$ . For that reason, the harmonics in differential mode generated by the switching cell tend to circulate through the capacitor instead of the line.

A similar analysis can be performed for the common mode. The comparison of the input and output voltages of the line in Fig. 5.25b shows that the common-mode voltage injected at  $x = \ell_c$  is amplified at  $x = 0$ , at the resonance frequencies of the cable, unlike the behavior in differential mode. The first resonance, and thus the one responsible for the highest amplification, is around  $380kHz$ .

This results can be explained, again, by the comparison between the input impedance of the system in common mode compared to its filtering capacitance in common mode: the parallel



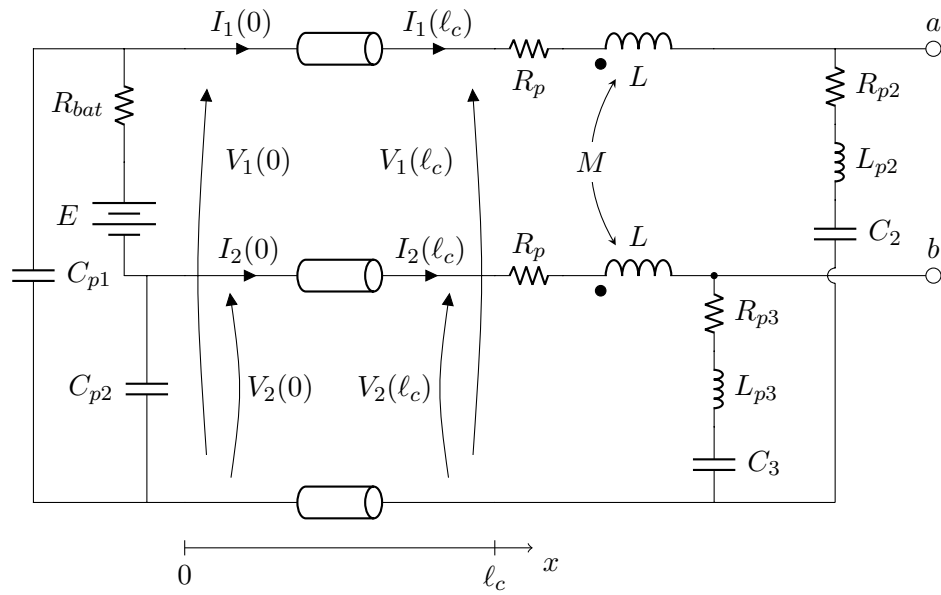


Figure 5.26 – Schematic for the DM input impedance  $Z_{DM}$ , calculated between points  $a$  and  $b$

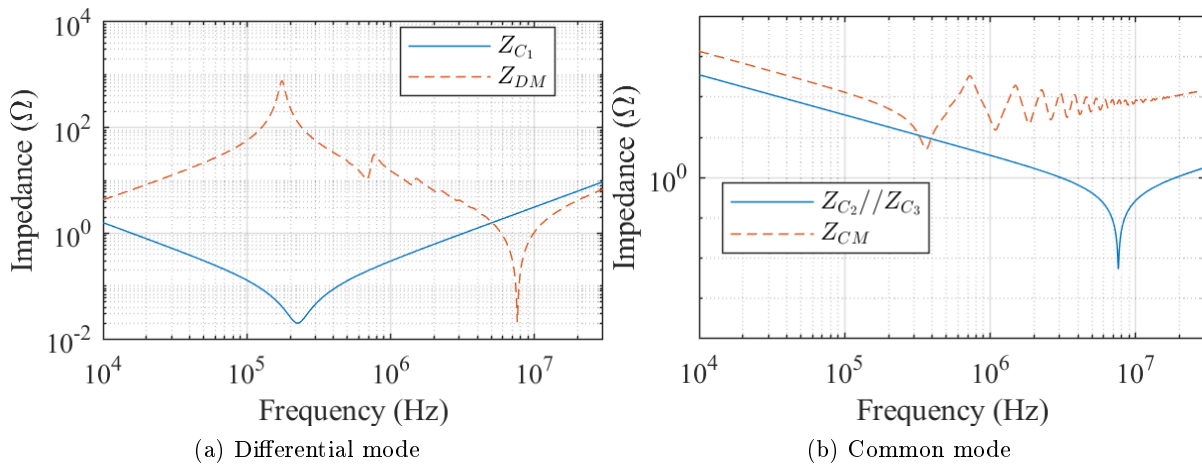


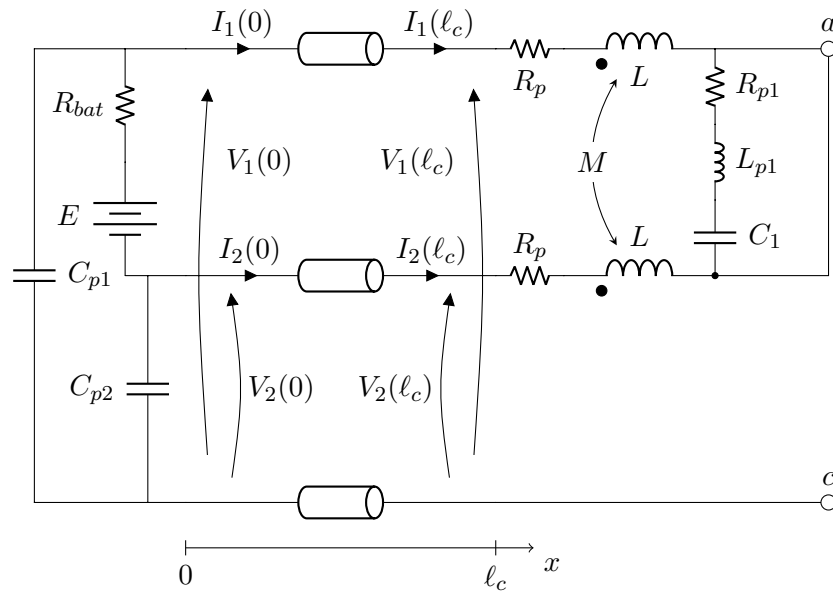
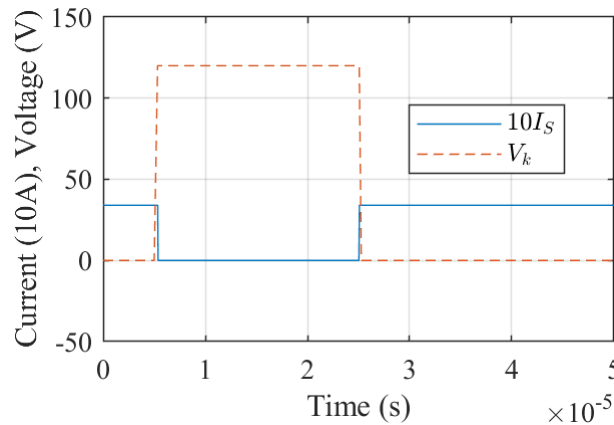
Figure 5.27 – Comparison between the input impedances of the system and the capacitive part of the filter

association of capacitors  $C_2$  and  $C_3$ . The input impedance of the system in common mode  $Z_{CM}$  is calculated with the schematic in Fig. 5.28, between points  $a$  and  $c$ :

The input impedance  $Z_{CM}$  is plotted against the parallel association of the non-ideal capacitors  $C_2$  and  $C_3$  in Fig. 5.27b. The input impedance  $Z_{CM}$  and the filtering capacitors impedance have the same order of magnitude around the first resonance of the cable. For this reason, the common-mode high frequency harmonics generated by the switching cell are not completely filtered, and excite the cable around this resonance frequency.

Now the resonant behavior of the system has been studied, the time domain response will be treated. The time domain simulation is performed as detailed in 4.3. The sources  $I_S$  and  $V_k$  are defined as ideal trapezoidal sources, and are represented in Fig. 5.29. Their frequency domain representation is obtained via the Fourier series defined in (4.20) (see Fig. 4.6).

As done in the previous section, the DC components are not included in this simulation

Figure 5.28 – Schematic for the CM input impedance  $Z_{CM}$ , calculated between points  $a$  and  $c$ Figure 5.29 – Sources  $I_S$  and  $V_k$  — approximated as ideal trapezoidal sources

because with two active sources representing the switching cell the power distribution in DC is susceptible to considerable mistakes. This is due to the fact that the switching cell is composed of elements that do not generate power, and because the approximation of the sources by ideal trapezoidal signals changes slightly power that should be generated, or consumed, by this source in order to fully represent the DC functioning point of the system.

The dynamic behavior of the time domain voltages and currents at both extremities of the line are represented in differential and common mode in Fig. 5.30.

As predicted by the frequency analysis in Fig. 5.25, there are oscillations around  $5\text{ MHz}$  in all the variables, and the biggest one is present in the differential-mode voltage at  $x = \ell_c$ . The common-mode voltage presents an oscillation around  $380\text{ kHz}$  that is amplified at  $x = 0$  due to resonance phenomena, as shows Fig. 5.30b.

The common-mode currents in Fig. 5.30d are small when compared to the differential mode, but they might still cause dysfunctions. Indeed, the common-mode current is more likely to cause EMI problems than the differential mode, mainly because the electric field emitted by it is

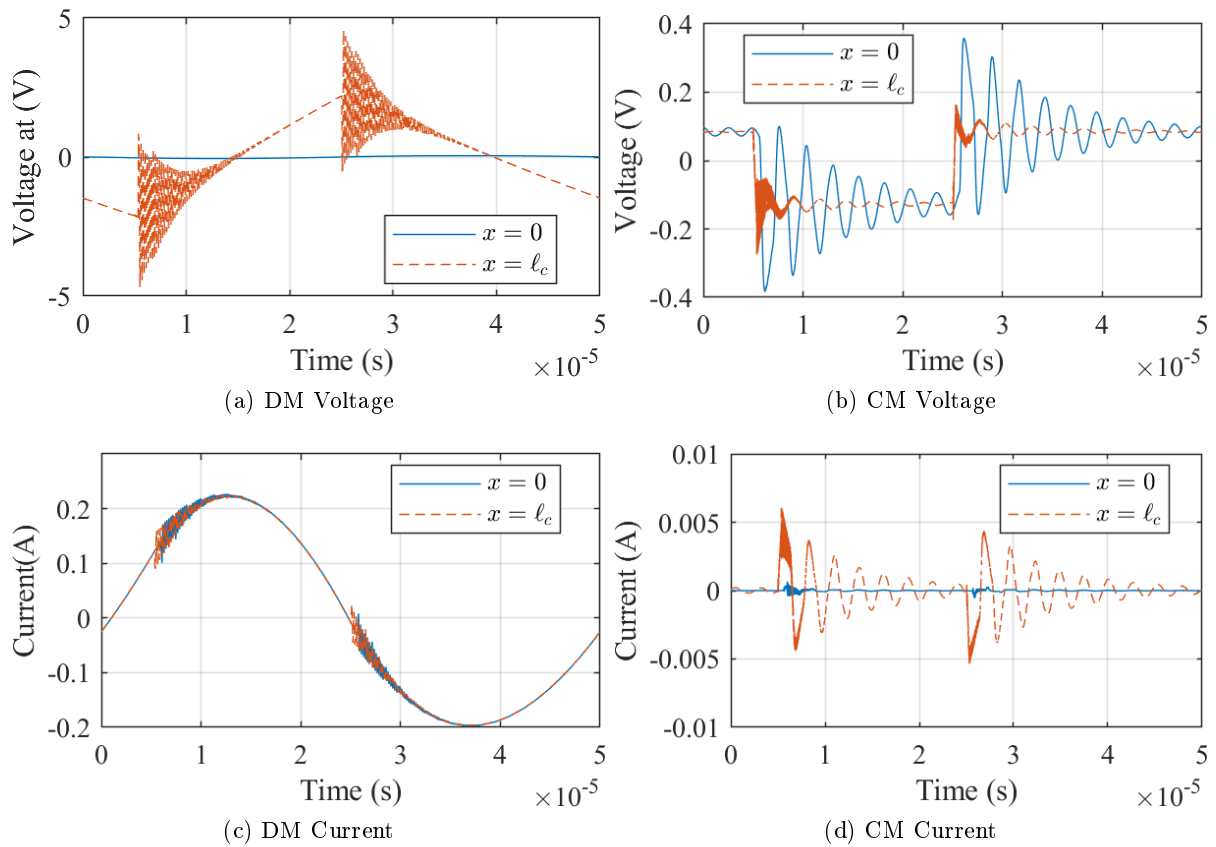


Figure 5.30 – Voltages and currents at the line extremities, without DC component

considerably stronger, as the currents generating it in the cable flow in the same direction [32]. Moreover, the common mode can cause insulation failures.

In the studied case, the common-mode currents are small because most of the common-mode perturbation is filtered by the capacitances  $C_2$  and  $C_3$  and the common-mode choke. To demonstrate the need to filter the common mode, the common-mode capacitances of the filter  $C_2$  and  $C_3$  were both reduced to  $22\text{ pF}$ , and the time domain results were recalculated for this new filter. The results are plotted in Fig. 5.31.

It is clear that the common-mode harmonics are higher, and again these harmonics are amplified at  $x = 0$ . The frequency of the common-mode oscillations changed because of the change of the filter capacitances. Indeed, the resonance frequency of the cable depends on the impedance connected to its terminals, and a change in the common-mode capacitances caused a considerable change in the resonance frequency.

Also, because of the change in the values of  $C_2$  and  $C_3$ , there is a change in high frequency oscillation in the system, which originated by the interaction between the stray capacitance on the switching cell  $C_{p3}$  and the filter elements. In Fig. 5.31, this high frequency oscillation occurs at  $14\text{ MHz}$ , and is better attenuated by the filter than the  $5\text{ MHz}$  oscillation visible in Fig. 5.30.

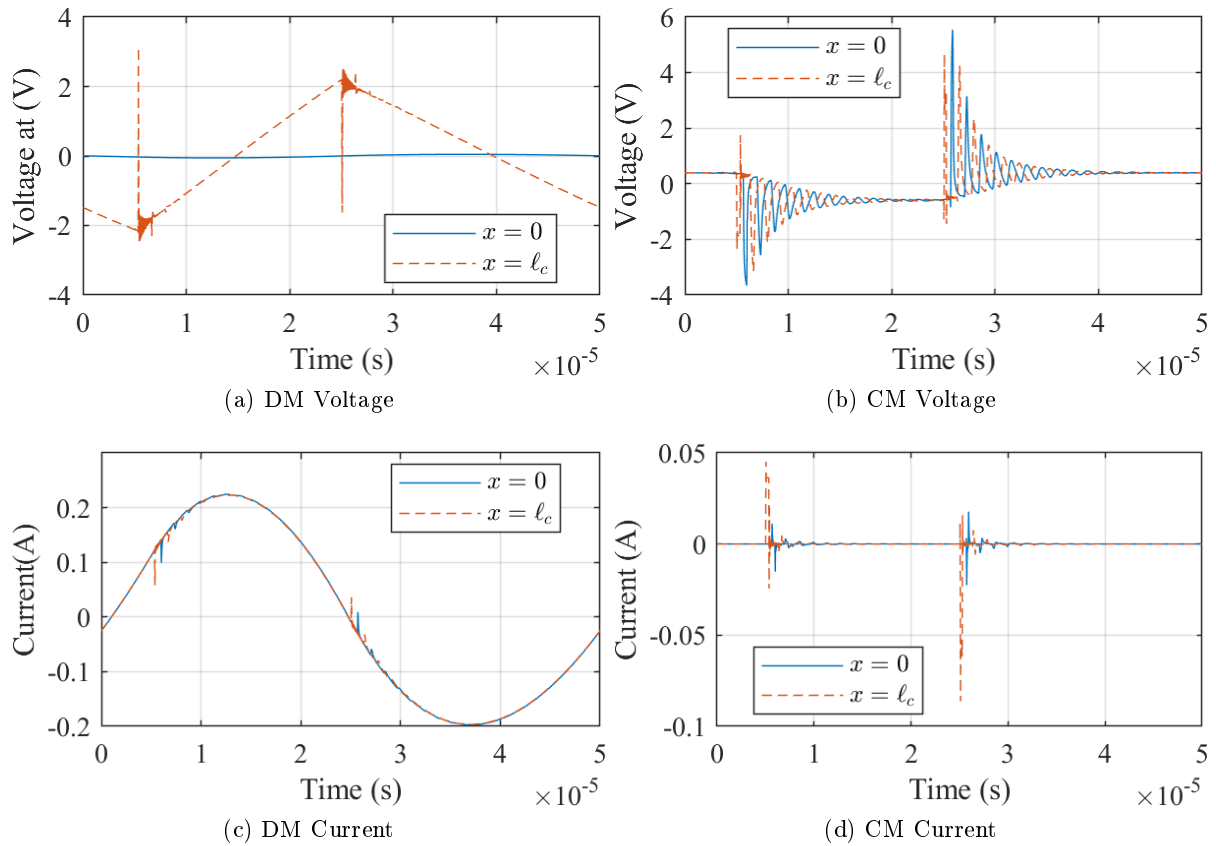


Figure 5.31 – Voltages and currents at the line extremities with  $C_2 = C_3 = 22 \text{ pF}$ , without DC component

## 5.5 Filter design taking resonance phenomena into account

In this section, the surfaces representing the frequency response of the resonance in a transmission line in function of the load connected to its terminals, introduced in sections 2.5.b and 3.5, will be applied to the design of the EMI output filter of a switching device. Indeed, these surfaces, hereafter denominated “resonance surface response”, are most useful in the design phase of a system, when they can predict the resonance behavior of a long cable in function of any two real variables. Resonance in an electrically long cable has the potential to interfere or damage other devices of the system, and designing techniques proposed here guarantees the robustness of the system regarding this phenomenon.

Output filters of EMI polluting devices are usually designed to meet the conducted emissions limits stipulated by international standards. In these standards, the conducted emission are measured with a LISN (Line Impedance Stabilizer Network), a device usually defined to have a normalized  $50 \Omega$  input impedance between each phase and the ground (chassis). Of course, the behavior of a passive filter when connected to the LISN is not the same as when it is connected to a reactive impedance, as is the input impedance of a long cable. New resonance frequencies may be established due to the interaction between the reactive elements of the filter and the cable, and the device emissions may even be amplified instead of attenuated by the filter presence.

Moreover, the resonance in a long cable may considerably amplify the input voltage elsewhere in the cable, and it is possible that even if the high frequency harmonics respect a stipulated limit

on the cable input, this limit is not respected at the other extremity of the cable. To design filter using the resonance surface response, as described by this section, guarantees that a maximum limit for the harmonics will be respected anywhere along the line.

For example, this design technique can be applied to embedded systems because in such applications the whole system is known to the developers, and the cabling network can be properly characterized.

For this example, the system shown in Fig. 5.32 was defined. It consists in a switching device (buck converter) powered by a battery through a long three-conductor cable. The conductors work as phase, neutral and protection PE, and the PE is connected to the device carcasses. The cable is a three-conductor of  $2.5\text{ mm}^2$  stranded cooper wire, its cross-section is represented in Fig. 5.33 and its parameters are plotted in Fig. 3.19. In the system in Fig. 5.32, the cable is  $\ell_c = 30\text{ m}$  long.

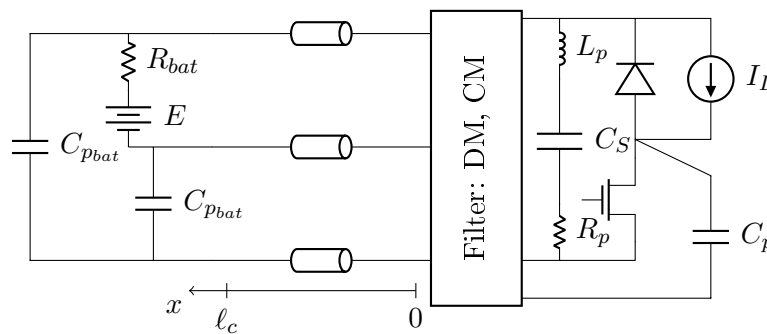


Figure 5.32 – System under study

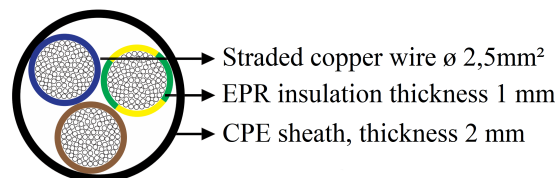


Figure 5.33 – Three-conductor cable cross-section

The battery is modeled with stray capacitances representing the electrical connection to its carcass. The parasitic capacitance of the middle point of the switching cell in the buck converter is also represented, as the high potential variation in this point are the main source of common mode in a switching structure. The numerical values applied to the parameters in the model in Fig. 5.32 are listed in table 5.5.

Table 5.5 – Parameters of the system model

$C_p$	$100\text{ pF}$	$C_{pbat}$	$200\text{ pF}$	$E$	$400\text{ V}$
$C_S$	$10\text{ }\mu\text{F}$	$R_{bat}$	$50\text{ m}\Omega$	$I_L$	$10\text{ A}$
$L_p$	$20\text{ nH}$	$R_p$	$10\text{ m}\Omega$		

The output filter has the structure shown in the schematic in Fig. 5.34. It consists in a common-mode filter close to the switching cell, followed by a differential-mode filter closer to the device output. This is a common filter structure in power converters [51].

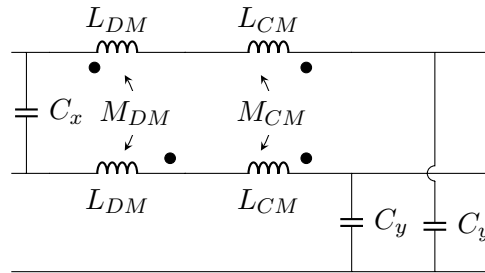


Figure 5.34 – Filter structure

**Classic filter design:** In a classic approach, this filter would be designed to meet the EMI limits stipulated by the concerned standard, with the switching device connected to a LISN. In [39] are defined the guidelines for the most commonly used method for filter design.

For the sake of an example, the guidelines defined in [39] were applied to design the filter given in Fig. 5.34 to meet the standard RTCA DO-160G [42] for airborne devices. The limit for the conducted emissions of a device in the power circuit of an aircraft (Fig. 21-1 in [42]) was applied. The resultant filter parameters are resumed in table 5.6.

Table 5.6 – Filter designed with the classic approach given in [39], to meet the RTCA DO-160G standard

CM	$C_y = 68 \text{ nF}$	$L_{CM} = 107 \text{ } \mu\text{H}$
DM	$C_x = 22 \text{ nF}$	$L_{DM} = 23.5 \text{ } \mu\text{H}$

**Resonance surface response filter design:** To introduce the proposed design method, the definition of a filter attenuation is recalled:

$$Att_V = \frac{V_{output}}{V_{source}} \quad Att_I = \frac{I_{output}}{I_{source}} \quad (5.6)$$

With (5.6), it can be seen that the attenuation of the common-mode filter can be given by the resonance surface response by setting the model sources to  $1 \text{ V}$  or  $1 \text{ A}$ , and calculating the voltages or currents along the system in function of the filter variables:  $C_y$ ,  $L_{CM}$ ,  $C_x$  and  $L_{DM}$ . By storing the highest voltage, or current, after multiple simulations, the resonance surface response maps the highest value of  $Att_V$  or  $Att_I$  provided by the filter anywhere along the cable, for the whole frequency band.

It is important to recall that the resonance surfaces can only be plotted in three-dimensions if the system can be decomposed in the common and differential modes, i.e., two equivalent two-conductor systems (cf. section 3.5). This decomposition will be used in this analysis, and two three-dimensional surfaces will be plotted:

- A common-mode surface, in function of  $C_y$  and  $L_{CM}$ ;
- A differential-mode surface, in function of  $C_x$  and  $L_{DM}$ ;

The frequency band of this study will be  $[150 \text{ kHz}, 35 \text{ MHz}]$ , the lower limit corresponding to the lowest frequency regarded by the conducted emissions international standards, and the higher

limit corresponding to  $3.5/t_r$ , where  $t_r$  was considered  $100\text{ ns}$ , a typical rise time for Silicon-based semiconductors.

In the calculation leading to the resonance surface response there will be 3000 frequency points logarithmic scaled in the aforementioned frequency band. The voltage or current will be calculated every  $1\text{ m}$  along the  $30\text{ m}$  long cable. The numerical values of the variables  $C_y$ ,  $L_{CM}$ ,  $C_x$  and  $L_{DM}$  were also logarithmic scaled. The details of the value range and number of calculation points for each variable are resumed in table 5.7.

Table 5.7 – Parameters of the resonance surface response calculation

	Value range	Number of points	Scale
Frequency $f$	$[150\text{ kHz}, 35\text{ MHz}]$	3000	log
Position $x$	$[0, 30\text{ m}]$	31	linear
$C_y$	$[0.1\text{ nF}, 100\text{ nF}]$	400	log
$L_{CM}$	$[1\text{ }\mu\text{H}, 10\text{ mH}]$	401	log
$C_x$	$[0.1\text{ nF}, 100\text{ nF}]$	400	log
$L_{DM}$	$[1\text{ }\mu\text{H}, 10\text{ mH}]$	401	log

The conducted emission limits for the design using the resonance frequency response will be constant with the frequency, and are given in table 5.8.

Table 5.8 – Conducted emissions limit for the design of filter using the resonance surface response

CM emission limit	$-80\text{ dBV}$
DM emission limit	$-130\text{ dBA}$

With these considerations, the filter design can be performed.

First, the system must be decomposed in the common and differential modes. As aforementioned, the switching cell model introduced in section 5.4 is not balanced. However, this model was derived from the association of two distinct models proposed in [44]: one for differential mode and another for common mode. These separated models will be used in this application.

The equivalent models of the system in Fig. 5.32 are represented in Fig. 5.35, in common mode, and in Fig. 5.36, in differential mode.

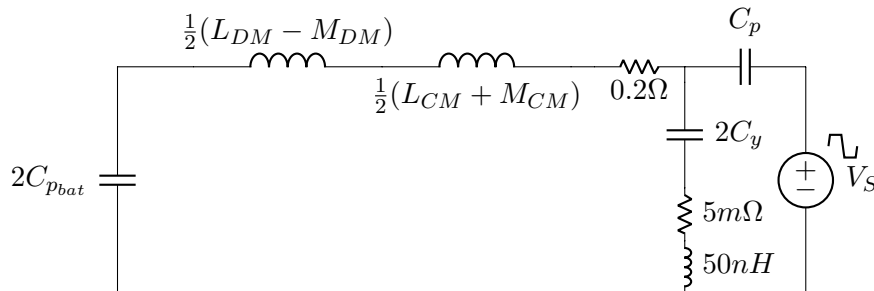


Figure 5.35 – System equivalent circuit in common mode

The parasitic elements of the filter, and the imperfections of the connections between its components, are taken into account in the simulation, because the attenuation of high frequency harmonics is highly dependent on them.

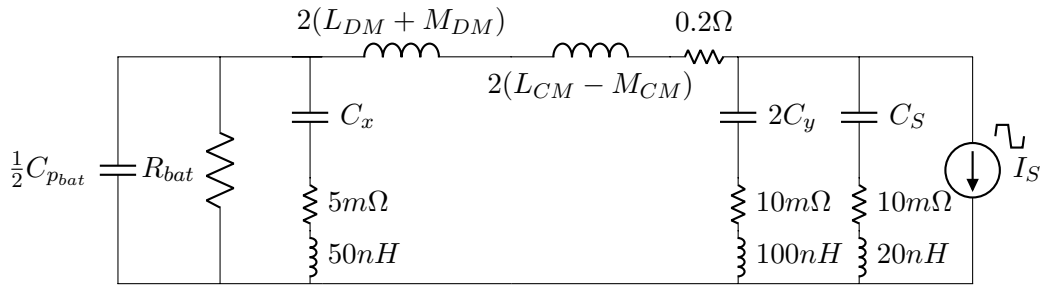


Figure 5.36 – Switching device equivalent circuit in differential mode

The equivalent system in common mode is less influenced by the differential-mode filter elements, and for that reason the common-mode filter will be designed first, using the value pre-designed with the classic approach:  $L_{DM} = 23.5 \mu H$ , given in table 5.6.

The attenuation needed can be calculated with a simulation of the common-mode voltage generated by the buck converter without an output filter. This simulation was done with the common-mode equivalent circuit in the schematic in Fig. 5.35 without the filter elements. The trapezoidal voltage waveform defining the voltage source  $V_S$  is represented in Fig. 5.37a. The common-mode voltage is plotted in Fig. 5.37b.

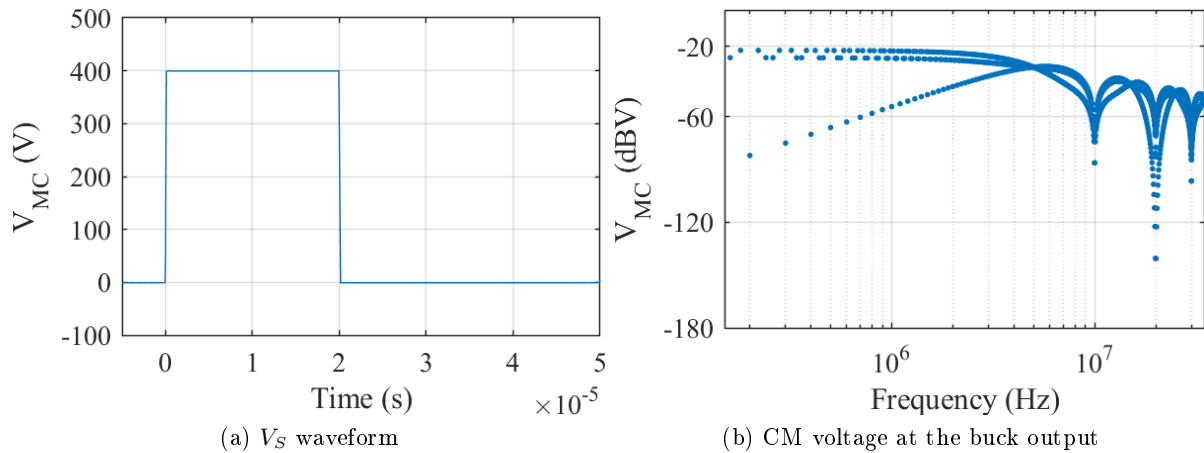


Figure 5.37 – Simulation of the CM voltage generated by the buck converter

In table 5.8 the limit of the common-mode conducted emissions is  $-80 \text{ dBV}$ . Therefore, from Fig. 5.37b, the filter attenuation has to be at least of  $-60 \text{ dB}$ , to successfully attenuate the signal in Fig. 5.37b.

The minimal attenuation of the filter is plotted in function of the filter elements in Fig. 5.38. The frequency to which the minimal attenuation occurred plotted in Fig. 5.39, and the position in Fig. 5.40. In these figures, the pairs  $(L_{CM}, C_y)$  to which the cut-off frequency of the common-mode filter  $1/\sqrt{(1+k)L_{CM}C_y}$  was higher than  $150 \text{ kHz}$  were not taken into account.

There is a zone where the attenuation surface is greater than  $0 \text{ dBV}$ , i.e., greater than 1; it is highlighted in black in Fig. 5.38. In this zone, the harmonics injected by the source, at the correspondent frequencies in Fig. 5.39, would be amplified instead of attenuated. According to the maximum position surface in Fig. 5.40, this maximum would take place at  $x = 26 \text{ m}$ . The pairs  $(C_y, L_{CM})$  that generate this amplification should be avoided.



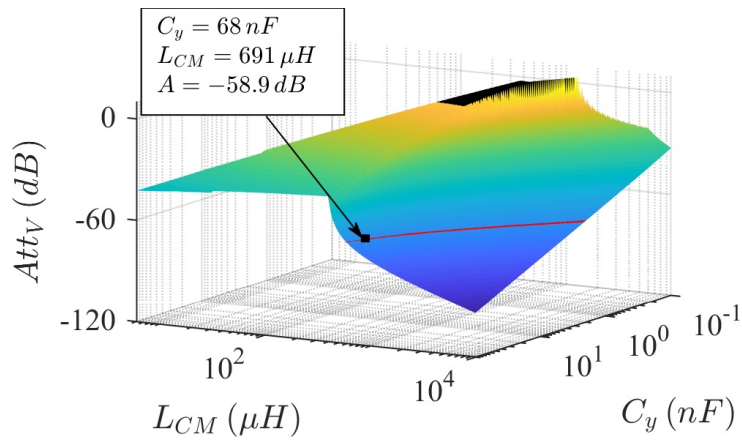


Figure 5.38 – Maximum common-mode voltage along the line in function of  $C_y$  and  $L_{CM}$ ;  $V > 0dBV$  in black,  $V = -60 dBV$  in red

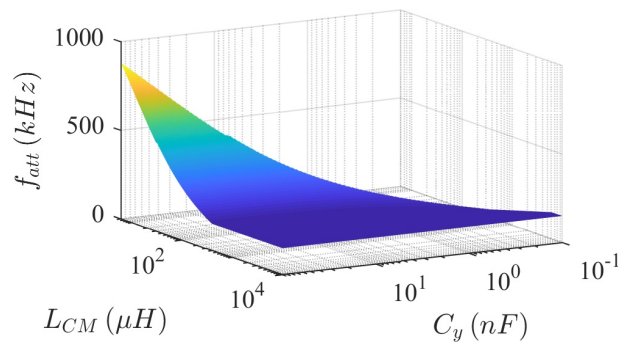


Figure 5.39 – Frequencies of the maximum in common mode

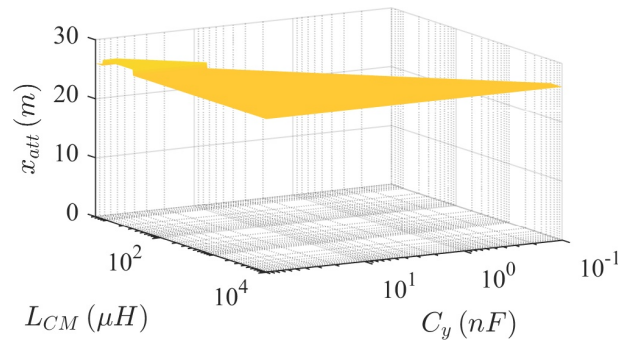


Figure 5.40 – Position of the maximum in common mode

The minimal attenuation required ( $-60 dBV$ ) is highlighted with a red line in the surface in Fig. 5.38. By choosing  $C_y = 68 nF$  (the biggest value in the CMS 1206 packaging), an inductance of  $L_{MC} = 691 \mu H$  would guarantee the required attenuation, for the whole frequency band and in any position along the cable.

These values ( $C_y = 68 nF$ ,  $L_{CM} = 691 \mu H$ ) are used in the evaluation of the differential-mode behavior of the system. Before the DM resonance surface response is built, the attenuation required by the DM filter must be defined.

To that end, the common-mode current at the output of the buck converter must be simulated, with the common-mode filter connected to it. Indeed, the common-mode filter contributes to the

filtering of DM signals, as shown in the schematic in Fig. 5.36. The trapezoidal wave attributed to the current source  $I_S$  is plotted in Fig. 5.41a. The CM current at the output of the CM filter is plotted in function of the frequency in Fig. 5.41b.

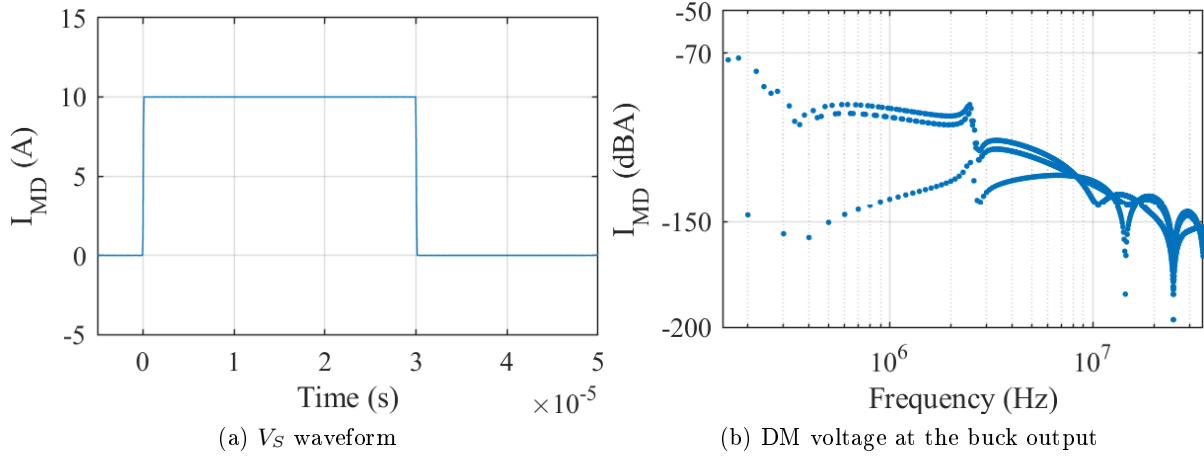


Figure 5.41 – Simulation of the DM current generated by the buck converter with common mode

From Fig. 5.41b that the minimal attenuation the DM filter must introduce can be defined. The filter requirements in table 5.8 demand CM conducted emissions lower than  $-130$  dBA, therefore an attenuation of  $-60$  dBA for the DM filter is sufficient.

The minimal attenuation in the system for each pair  $(C_x, L_{DM})$  is plotted in Fig. 5.42. The frequencies to which each minimum occurred are plotted in Fig. 5.43, and the position along the line where it takes place is plotted in Fig. 5.44. In these figures, the pairs  $(L_{DM}, C_x)$  to which the cut-off frequency of the filter  $1/\sqrt{2(1+k)L_{DM}C_x}$  was higher than  $150$  kHz were not taken into account.

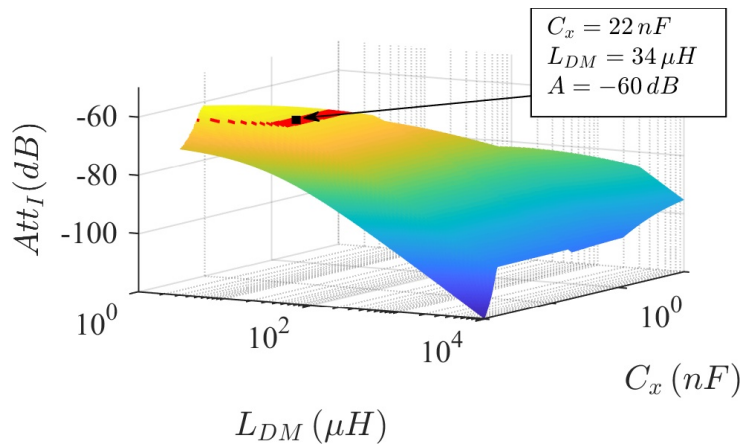


Figure 5.42 – Maximum differential-mode current along the line in function of  $C_x$  and  $L_{DM}$ ;  $I = -60$  dBA in red

The attenuation in differential mode is considerably greater than in common mode, mainly because of the filtering effect of the switching cell associated capacitance, represented by the impedance  $Z_{C_S}$ .

The behavior of the resonance surface for the lowest values of  $C_x$  is an example of what

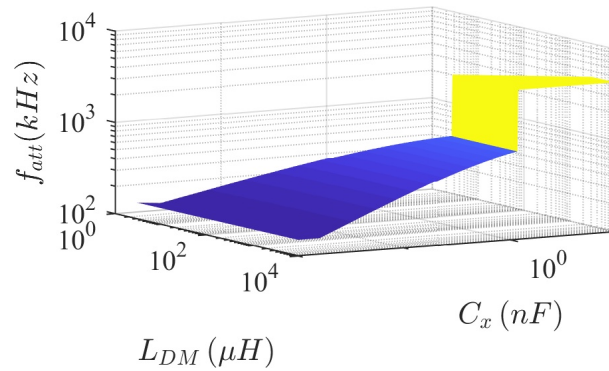


Figure 5.43 – Frequencies of the maximum in differential mode

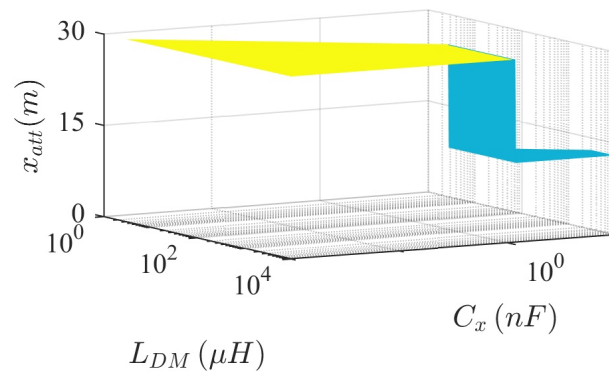


Figure 5.44 – Position of the maximum in differential mode

could not be predicted without applying the transmission line modeling to the long cable. The worst resonance-due amplification takes place near to middle of the cable for a frequency of  $4.13\text{ MHz} \approx \lambda/\ell_c$ , i.e., the second short circuit resonance frequency is more amplified than the others by the association of the filter and the cable. It is shown in section 2.5.c that a non-propagative model could not predict this behavior.

To meet the desired harmonic attenuation of  $-60\text{ dBA}$  the filter passive values should be chosen from the red line in Fig. 5.42. With a capacitance  $C_x = 22\text{ nF}$ , an inductance of  $L_{DM} = 34\text{ }\mu H$  is sufficient to guarantee it, for the whole frequency band, in any position of the line. The filter designed values using the resonance surface response is resumed in table 5.9.

Table 5.9 – Filter designed with resonance surface response

CM	$C_y = 68\text{ nF}$	$L_{CM} = 691\text{ }\mu H$
DM	$C_x = 22\text{ nF}$	$L_{DM} = 34\text{ }\mu H$

The proposed design technique using the resonance surface response can be applied to more complex networks, by concatenating the cabling model proposed in this work (cf. section 3.2.c). This numerical analysis could also be obtained for cables with more conductors, or with coupled common and differential modes, but it would not be able to be visualized.

This design technique offers an alternative to guarantee the EMC robustness in any given system. It is more likely to be useful for embedded applications, such as electric vehicles and aircraft, because the method requires the knowledge of the network to which a switching device

is connected. With the resonance response surface design, it is guaranteed that stray harmonics will not exceed the chosen perturbation limit anywhere along the connection cables.

## 5.6 Conclusion

In this chapter the simulation tool proposed in this work has been used to analyze different systems containing long cables, and determine whether if the resonance phenomenon could cause damage to each of the systems. Also, the resonance surface response obtained with the frequency domain simulation tool was applied to a filter design study.

The frequency domain analysis proposed in section 5.2 has been applied several examples in this chapter, and it has been shown that the proposed model is useful for the prediction of resonance phenomena, and in the design of protection methods against it.

The simulations of the studied systems were performed within a reasonable computation time despite the length of the cables in each system, which were considerably long when compared to the harmonic of the smallest wavelength circulating in the cable. The computational performance of the model is one of its most interesting features, principally it does not depend on of the cable length, but only in the number of positions along the line where the calculations of voltage and current are needed.

To sum up, the cable modeling and simulation method proposed in this work is an interesting contribution to the current literature because it has the potential to accurately predict resonance issues in any system, and be of use in the design phase of such systems to avoid serious damage to its components.



---

## Conclusion

In this thesis was developed an efficient and accurate characterization and modeling method for the EMI parasitic harmonics that may circulate in the cabling network of a large electric system. It is focused on electric systems containing long cables connected to polluting devices, such as power converters.

The simulation method proposed here is based on the frequency domain solution of the telegrapher equations, and consists in a frequency domain simulation using the phasor transform, along with the Fourier Series, as transform between the frequency and time domains. This work was focused on periodic excitation, but the simulator can be extended to the general case via the Fourier transform.

The advantages of the proposed modeling method are numerous. Its numerical efficiency is considerable, what make it useful in the design phase of a system, to predict the EMI problems that may occur in large cabling networks. Moreover, the computational effort does not increase with the cable length. Indeed, the simulation time of the proposed tool depends only on the number of points in which voltage and current must be calculated, and in the number of harmonics to be taken into account. This is convenient to model large cabling systems, in which usually only the connections points need to be taken into account in the simulation.

A second advantage of the proposed method is its accuracy, principally concerning the resonance phenomenon in long cables. Indeed, because the simulations are performed in the frequency domain, the model can represent the exact behavior of the cable parameters, that are frequency dependent. The only source of inaccuracy is the cable parameters identification process. This is an improvement in comparison with the time domain modeling techniques found in the literature: they all need an equivalent representation of the line that intrinsically engender an accuracy loss.

The inconvenient brought by the frequency domain representation is that some structures, such as the power converters themselves, from which the EMI conducted emissions are the main concern of this work, have a non-linear behavior difficult to represent with accuracy in the frequency domain. In this document, equivalent models were used to represent these structures in the frequency domain, but these models have two main inconveniences: they do not represent all the possible current paths in the converter structure, and the steady state behavior of the converter is often an input variable in the model, and thus requiring additional time domain simulations.

Another inconvenient of this simulation method is that its implementation take some effort, and it is not available in the commonly used commercial software. For this study, it had to be completely implemented on Matlab. However, it could be implemented in a simulation adapted

language, such as VHDL-AMS, so it could be spread more easily.

From the work described in this document, there still some interesting perspectives to be explored.

Modeling the common mode path in a given system is one of them. This could be done by considering the common mode stray path as an extra conductor. For instance, from the experiments in chapter 2 to 4 it was deduced that good part of the common mode current in the validation experimental setup circulated through the concrete floor, and for that reason the cable was suspended from the floor with insulating materials. If the path through the concrete floor could be modeled by an extra conductor, the voltage and current circulating in that system could be predicted independently of the position of the cable.

Also, a second interesting perspective would be to further exploit the resonance surface response. For example, the surfaces could also be plotted in function of the cable length, giving information of what length would be more dangerous in terms of voltage amplification. With this analysis, the geometric arrangement of a large system could be designed to minimize EMI problems. Also, the resonance surface with more response than three dimensions capable of representing any system is still to be exploited.

Least of all, the resonance surface response could also be used in optimization process. It would require an interpolation of the surface, or other equivalent representation method, but it can be a useful tool in the optimization of EMI filters in embedded systems.

---

## Bibliography

- [1] A. K. Agrawal, H. M. Fowles, and L. D. Scott. Experimental characterization of multi-conductor transmission lines in inhomogeneous media using time-domain techniques. *IEEE Transactions Electromagnetic Compatibility*, 21, feb 1979.
- [2] A. K. Agrawal, K.-M. Lee, L. D. Scott, and H. M. Fowles. Experimental characterization of multiconductor transmission lines in the frequency domain. *IEEE Transactions Electromagnetic Compatibility*, 21, feb 1979.
- [3] A. K. Agrawal and H. J. Price. Experimental characterization of partially degenerate three-conductor transmission lines in the time domain. *IEEE Transactions Electromagnetic Compatibility*, 23, aug 1981.
- [4] B. K. ans P. A. A. F. Wouters and E. F. Steennis. High frequency modeling of a shielded four-core low voltage underground power cable. *IEEE Transactions on Dielectrics and Electrical Insulation*, 22, apr 2015.
- [5] Ansoft LLC. Simplorer, version 8,0 [software]. Simplorer On-Line Help.
- [6] J. A. Brandão and M. G. das Neves. Basic principles concerning the experimental evaluation of the frequency-dependent parameters of shielded and unshielded three-phase symmetric cables. *IEEE Transactions on Power Delivery*, 26, apr 2011.
- [7] X. Chu, F. Lin, and Z. Yang. The analysis of time-varying resonances in the power supply line of high speed trains. In *International Power Electronics Conference*, 2014.
- [8] S. Cristina and M. Feliziani. A finite element technique for multiconductor cable parameters calculation. *IEEE Transactions on Magnetics*, 25, jul 1989.
- [9] EMTP-EMTPWorks. Frequency dependent line: Fd m-phase. help topics EMTP software, 2003.
- [10] G. Frantz. *Approche système pour l'étude de la compatibilité électromagnétique des réseaux embarqués*. PhD thesis, Université Grenoble Alpes - Grenoble, France, 2015. <NNT : 2015GREAT048>. <tel-01218578>.
- [11] D. A. Frickey. Conversions Between S, Z, Y, h, ABCD, and T Parameters which are Valid for Complex Source and Load Impedances. *IEEE transactions on microwave theory and techniques*, 1994.



- [12] Z. Gao, R. Ji, X. Zhang, X. Yuan, and D. Li. Finite-element modeling and impedance characteristics analysis of two parallel cables in aircraft power system. In *2016 IEEE/CSAA International Conference on Aircraft Utility Systems (AUS)*, oct 2016.
- [13] G. G. Gentili and M. Salazar-Palma. The definition and computation of modal characteristic impedance in quasi-tem coupled transmission lines. *IEEE Transactions on Microwave Theory and Techniques*, feb 1995.
- [14] S. Habib and B. Kordi. Calculation of multiconductor underground cables high-frequency per-unit-length parameters using electromagnetic modal analysis. *IEEE Transactions on Power Delivery*, 28, jan 2013.
- [15] J. He, G. Y. Sizov, P. Zhang, and N. A. O. Demerdash. A review of mitigation methods for overvoltage in long-cable-fed PWM AC drives. In *2011 IEEE Energy Conversion Congress and Exposition*, Sept. 2011.
- [16] B. Honarbakhsh and S. Asadi. Analysis of multiconductor transmission lines using the cn-fdtd method. *IEEE Transactions Electromagnetic Compatibility*, 59, jan 2017.
- [17] M. Hosoya. The simplest equivalent circuit of a multi-terminal network. *Bulletin of the College of Science, University of the Ryukyus*, 70, 2000.
- [18] N. Idir, Y. Weens, and J. J. Franchaud. Skin effect and dielectric loss models of power cables. *IEEE Transactions on Dielectrics and Electrical Insulation*, 16, Feb. 2009.
- [19] W. C. Johnson. *Transmission lines and networks*. McGRAW book company, 1950.
- [20] R. J. Kerkman, D. Leggate, and G. L. Skibinski. Interaction of drive modulation and cable parameters on AC motor transients. *IEEE Transactions on Industry Applications*, 33, May 1997.
- [21] Keysight Technologies. *Impedance measurement handbook*, 5th edition edition, 2015. Available in <https://literature.cdn.keysight.com/litweb/pdf/5950-3000.pdf>. Accessed 18-october-2018.
- [22] Keysight Technologies. 16314a balanced/unbalanced 4 -terminal converter. [www.keysight.com/en/pd-100000503%3Aeps%3Apro-pn-16314A/balanced-unbalanced-4-terminal-converter?cc=FR&lc=fr](http://www.keysight.com/en/pd-100000503%3Aeps%3Apro-pn-16314A/balanced-unbalanced-4-terminal-converter?cc=FR&lc=fr), 2006. [Online; accessed 30-August-2018].
- [23] J.-H. Kim, D. Oh, and W. Kim. Accurate characterization of broadband multiconductor transmission lines for high-speed digital systems. *IEEE Transactions on Advanced Packaging*, 33, nov 2010.
- [24] J. Knockaert, J. Peuteman, J. Catrysse, and R. Belmans. A vector impedance meter method to characterize multiconductor transmission-line parameters. *IEEE Transactions Electromagnetic Compatibility*, 52, nov 2010.
- [25] M. Kuschke and K. Strunz. Transient cable overvoltage calculation and filter design: application to onshore converter station for hydrokinetic energy harvesting. *IEEE Transactions on Power Delivery*, 28, jul 2013.

- [26] B. Lathi. *Linear Systems and Signals*. Oxford University Press, 2002.
- [27] O. Magdun, A. Binder, C. Purcarea, A. Rocks, and B. Funieru. Modeling of asymmetrical cables for an accurate calculation of common mode ground currents. In *2009 IEEE Energy Conversion Congress and Exposition*, Sept. 2009.
- [28] J. R. Marti. Accurate Modelling of Frequency-Dependent Transmission Lines in Electromagnetic Transient Simulations. *IEEE Transactions on Power Apparatus and Systems*, Jan. 1982.
- [29] F. Medard. *Contribution à la modélisation prédictive des comportements hautes fréquences des moteurs de traction*. PhD thesis, Université Grenoble Alpes, 2015.
- [30] T. Ming, S. Jianyang, G. Jianzhao, L. Hongjie, Z. Wei, and L. Deliang. Time-Domain Modeling and Simulation of Partial Discharge on Medium-Voltage Cables by Vector Fitting Method. *IEEE Transactions on magnetics*, 50, Feb. 2014.
- [31] S. J. Orfanidis. *Electromagnetic waves and antennas*. Rutgers University, 2016.
- [32] C. Paul. *Introduction to Electromagnetic compatibility*. Wiley, second edition edition, 2006.
- [33] C. Paul. *Analysis of multiconductor transmission lines*. IEEE Press, 2008.
- [34] C. R. Paul. Decoupling the multiconductor transmission line equations. *IEEE Transactions on Microwave Theory and Techniques*, 44, aug 1996.
- [35] H. D. Paula, D. A. de Andrade, M. L. R. Chaves, J. L. Domingos, and M. A. A. de Freitas. Methodology for cable modeling and simulation for high-frequency phenomena studies in pwm motor drives. *IEEE Transactions Power Electronics*, 23, mar 2008.
- [36] H. d. Paula, M. V. C. Lisboa, J. F. R. Guilherme, M. L. R. Chaves, and W. P. d. Almeida. Characterization of cable arrangements in terms of the generated high-frequency quantities in PWM motor drives. In *2009 Brazilian Power Electronics Conference*, Sept. 2009.
- [37] L. A. Pipes. Matrix theory of multiconductor transmission lines. *The London, Edinburgh, and Dublin Philosophical Magazine and Journal of Science*, 24, 1937.
- [38] PSpice Application Notes. Transmission line applications in pspice. [www.pspice.com/resources/application-notes/transmission-lines-applications-pspice](http://www.pspice.com/resources/application-notes/transmission-lines-applications-pspice), 2016. [Online; accessed 08-September-2018].
- [39] K. Raggl, T. Nussbaumer, and J. W. Kolar. Guideline for a Simplified Differential-Mode EMI Filter Design. *IEEE Transactions on Industrial Electronics*, 57, Mar. 2010.
- [40] B. Revol. *Modélisation et optimisation des performances CEM d'une association variateur de vitesse - machine asynchrone*. PhD thesis, Université Joseph-Fourier - Grenoble, France, 2003. <tel-00006396>.
- [41] B. Revol, J. Roudet, J.-L. Schanen, and P. Loizelet. Emi study of three-phase inverter-fed motor drives. *IEEE Transactions on Industry Applications*, 47, Jan. 2011.

- [42] RTCA, Inc., Washington, DC, USA. *DO-160G: Environmental Conditions and Test Procedures for Airborne Equipment*, 2010.
- [43] S. Zhang, S. Jiang, X. Lu, B. Ge, and F. Z. Peng. Resonance Issues and Damping Techniques for Grid-Connected Inverters With Long Transmission Cable. *IEEE Transactions on power electronics*, 2014.
- [44] R. Scheich. *Caractérisation et prédétermination des perturbations électromagnétiques conduites dans les convertisseurs de l'électronique de puissance*. PhD thesis, Institut National Polytechnique de Grenoble - Grenoble, France, 1993.
- [45] M. J. Scott, J. Brockman, B. Hu, L. Fu, L. Xu, J. Wang, and R. D. Zamora. Reflected wave phenomenon in motor drive systems using wide bandgap devices. In *2014 IEEE Workshop on Wide Bandgap Power Devices and Applications*, Oct. 2014.
- [46] G. Skibinski, J. Erdman, J. Pankau, and J. Campbell. Assessing AC motor dielectric withstand capability to reflected voltage stress using corona testing. In *Conference Record of the 1996 IEEE Industry Applications Conference, 1996. Thirty-First IAS Annual Meeting, IAS '96*, volume 1, Oct. 1996.
- [47] I. Stevanović, B. Wunsch, G. L. Madonna, and S. Skibin. High-frequency behavioral multi-conductor cable modeling for emi simulations in power electronics. *IEEE Transactions on Industrial Informatics*, may 2014.
- [48] A. Sugiura and Y. Kami. Generation and Propagation of Common-Mode Currents in a Balanced Two-Conductor Line. *IEEE Transactions Electromagnetic Compatibility*, 54, Apr. 2012.
- [49] TDA systems. *Practical characterization of lossy transmission lines using TDR*, 2001.
- [50] Tektronix. *TDS3000C Series Digital Phosphor Oscilloscopes*, 2013.
- [51] B. Touré, J. Schanen, L. Gerbaud, T. Meynard, J. Roudet, and R. Ruelland. EMC Modeling of Drives for Aircraft Applications: Modeling Process, EMI Filter Optimization, and Technological Choice. *IEEE Transactions on Power Electronics*, 28, Mar. 2013.
- [52] L. Wang, C. N.-M. Ho, F. Canales, and J. Jatskevich. High-Frequency Modeling of the Long-Cable-Fed Induction Motor Drive System Using TLM Approach for Predicting Overvoltage Transients. *IEEE Transactions on Power Electronics*, 25, Oct. 2010.
- [53] Y. Weens, N. Idir, R. Bausiere, and J. Franchaud. Modeling and simulation of unshielded and shielded energy cables in frequency and time domains. *IEEE Transactions on Magnetics*, 42, July 2006.
- [54] D. F. Williams. Multiconductor transmission line characterization. *IEEE Transactions on Components, Packaging and Manufacturing Technology*, 20, may 1997.
- [55] B. Wunsch, I. Stevanović, and S. Skibin. Length-scalable multi-conductor cable modeling for emi simulations in power electronics. *IEEE Transactions Power Electronics*, apr 2016.

- 
- [56] C.-S. Yen, Z. Fazarinc, and R. L. Wheeler. Time-domain skin-effect model for transient analysis of lossy transmission lines. *Proceedings of the IEEE*, 70, July 1982.
- [57] J. Zhang, J. L. Drewniak, D. J. Pommerenke, M. Y. Koledintseva, R. E. DuBroff, W. Cheng, Z. Yang, Q. B. Chen, and A. Orlandi. Causalrlgc( $f$ ) models for transmission lines from measured-parameters. *IEEE Transactions on Electromagnetic Compatibility*, 52, Feb 2010.



### Papers published on International journals

- T.G. Bade, J. Roudet, JM. Guichon, P. Kuo-Peng, C.A.F. Sartori, JL. Schanen, A. Derby. “Frequency Domain Modeling of Unshielded Multiconductor Power Cables for Periodic Excitation with New Experimental Protocol for Wide Band Parameter Identification”. *Electrical engineering* — Springer, 2019.
- (submitted)

### Papers presented on international conferences

- T.G. Bade, J. Roudet, JM. Guichon, P. Kuo-Peng, C.A.F. Sartori. “Experimental evaluation of voltage resonance on industrial cables”. *IEEE 3rd Global Electromagnetic Compatibility Conference (GEMCCON)*, 2017.
- E. Clavel, J. Roudet, T.G. Bade, P. Joyeux, Z. Gouichiche. “Analysis of lightning propagation inside building via grounding system”. *IEEE 3rd Global Electromagnetic Compatibility Conference (GEMCCON)*, 2017.



In table A.1 are resumed the hyperbolic identities used along the main document.

Table A.1 – Hyperbolic function definitions and identities

<b>Hyperbolic identities</b>
$\cosh(a) = \frac{e^a + e^{-a}}{2}$
$\sinh(a) = \frac{e^a - e^{-a}}{2}$
$\tanh(a) = \frac{e^a - e^{-a}}{e^a + e^{-a}}$
$\cosh(a) + \sinh(a) = e^a$
$\cosh(a \pm jb) = \cosh(a) \cos(b) \pm j \sinh(a) \sin(b)$
$\cosh(a + jn\pi) = (-1)^n \cosh(a)$
$\sinh(a + jn\pi) = (-1)^n \sinh(a)$
$\cosh(a + j(2n - 1)\frac{\pi}{2}) = j(-1)^n \sinh(a)$
$\sinh(a + j(2n - 1)\frac{\pi}{2}) = j(-1)^n \cosh(a)$





In this appendix, the theoretical development of analytical solutions for specific systems with two-conductor cables are detailed. They are based on the definition of a frequency domain model given in section 2.2.a. The first is the case where one of the devices connected to the two-conductor cable is a simple load. The second includes the presence of a scope connected along the cable.

### Equations modeling a two-conductor cable fed through one single terminal ( $S_L = 0$ )

In section 2.2.a is defined the frequency domain simulator for a two-conductor cable connected to two generic devices at its terminals, as shown in Fig B.1, repeated here for convenience. The simulator is given as the solution of the system of equations (B.1).

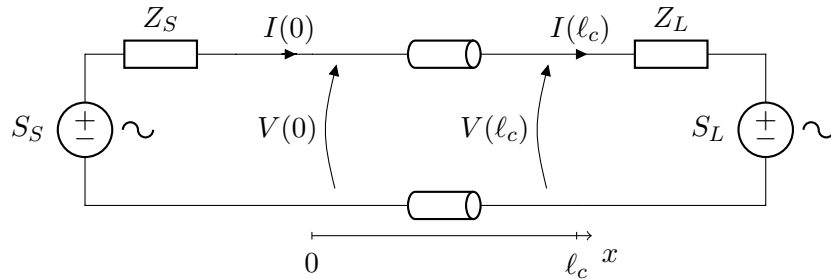


Figure B.1 – Schematic of the generalized frequency domain model for two-conductor cables

$$\begin{cases} \begin{bmatrix} V(\ell_c, f) \\ I(\ell_c, f) \end{bmatrix} = \Phi(\ell_c, f) \begin{bmatrix} V(0, f) \\ I(0, f) \end{bmatrix} & \text{(B.1a)} \\ V(0, f) = S_S - Z_S I(0, f) & \text{(B.1b)} \\ V(\ell_c, f) = S_L + Z_L I(\ell_c, f) & \text{(B.1c)} \end{cases}$$

Along this work, it is more usual than the one where the devices connected to the cable are a simple load that do not inject power in the cable, i.e. systems with  $S_L = 0$ . This simplified system is represented in Fig. B.2.

This simplification allows an easy analytical solution of the system of equations (B.1). This solution has been directly implemented on Matlab during this work, and the theoretical development of this implementation is detailed here.

Equations (B.1) with  $S_L = 0$  can be solved as follows.

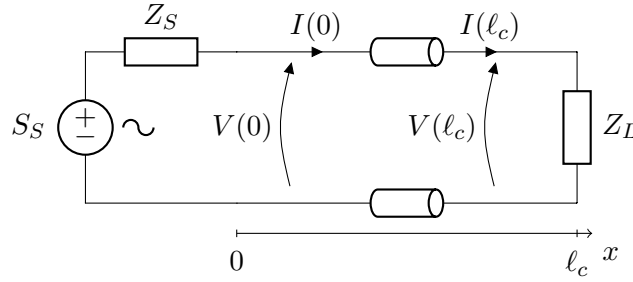


Figure B.2 – Schematic of two-conductor system with passive load

The input impedance of the cable is  $Z(0)$  as in (B.2).

$$Z(0) = Z_c \frac{Z_L + Z_c \tanh(\gamma \ell_c)}{Z_c + Z_L \tanh(\gamma \ell_c)} \quad (\text{B.2})$$

Therefore, the current at the cable input  $I(0)$  can be calculated with (B.3)

$$I(0) = \frac{V_S}{Z_S + Z(0)} \quad (\text{B.3})$$

What gives an input voltage  $V(0)$  as in (B.4)

$$V(0) = V_S - Z_S I(0) = V_S \frac{Z(0)}{Z_S + Z(0)} \quad (\text{B.4})$$

The voltage and current along a two conductor line can be obtained with equation (B.5), as shown in section 2.2.

$$\begin{bmatrix} V(x) \\ I(x) \end{bmatrix} = \begin{bmatrix} \cosh(x\gamma) & -Z_c \sinh(x\gamma) \\ -\frac{1}{Z_c} \sinh(x\gamma) & \cosh(x\gamma) \end{bmatrix} \begin{bmatrix} V(0) \\ I(0) \end{bmatrix} \quad (\text{B.5})$$

With equations (B.3) (B.4), and (B.5), the analytical solution for the voltage and currents in the system in Fig. B.2 is given by (B.6):

$$V(x) = V_S \frac{Z(0)}{Z_S + Z(0)} \left[ \cosh(\gamma x) - \frac{Z_c}{Z(0)} \sinh(\gamma x) \right] \quad (\text{B.6a})$$

$$I(x) = V_S \frac{1}{Z_S + Z(0)} \left[ \cosh(\gamma x) - \frac{Z(0)}{Z_c} \sinh(\gamma x) \right] \quad (\text{B.6b})$$

These are the equations implemented on the frequency domain simulator for this specific case, on Matlab. In the following section, the implementation of this same system with a scope connected to the cable is discussed.

## Taking the connection of a scope into account

A second recurrent system in this work is a two-conductor cable with scope connected to it at position  $x = x_M$ , as shown in Fig. B.3.

In the cases where the impact of the presence of the scope is not negligible, the scope has to be included in the model, represented by its input impedance. The input impedance  $Z_{scope}$  of a voltage probe connected to a scope, while the scope is turned off, was measured using an

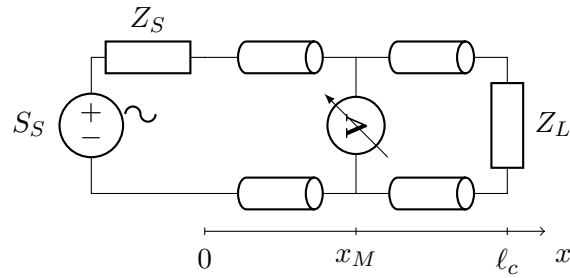


Figure B.3 – Schematic of the two-conductor cable with scope in the middle

impedance analyzer and is represented in Fig. B.4.

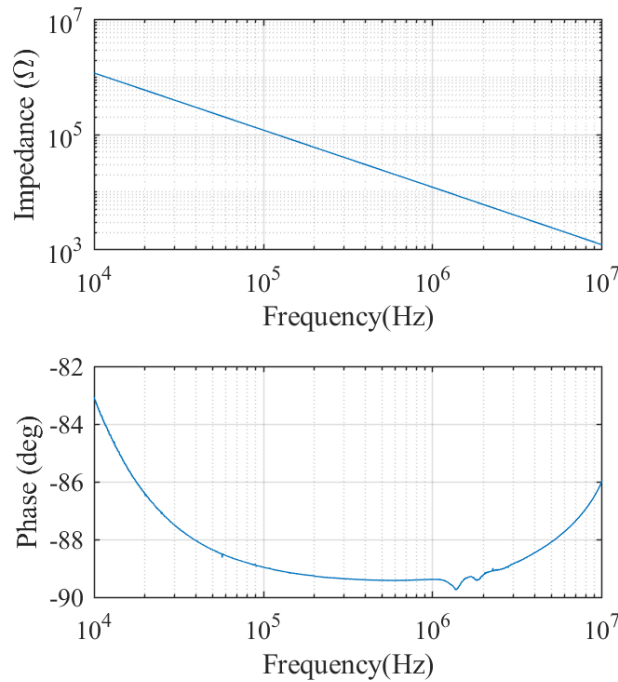


Figure B.4 – Input impedance of scope voltage probe Tektronix P3010 —  $Z_{scope}$

To model the connection of the impedance  $Z_{scope}$  to the cable, the cable has to be divided in two parts: the portion between the source and the scope, and the portion after the scope. Each of these parts is modeled by as a distinct transmission line.

The portion between  $x = 0$  and  $x = x_M$  is modeled as a cable of length  $\ell_1 = x_M$ . The second part of the cable, between  $x = x_M$  and  $x = \ell_c$  is modeled as a cable of length  $\ell_2 = \ell_c - x_M$ .

The current and voltage in the first portion of the cable, of length  $\ell_1$ , can be obtained as follows:

Let  $Z_{\ell_2}(0)$  be the input impedance of the portion of the cable between  $x = x_M$  and  $x = \ell_c$ :

$$Z_{\ell_2}(0) = Z_c \frac{Z_L + Z_c \tanh(\gamma \ell_2)}{Z_c + Z_L \tanh(\gamma \ell_2)} \quad (\text{B.7})$$

Let  $Z_{eq1}$  be the parallel association of the impedances  $Z_{scope}$  and  $Z_{\ell_2}(0)$ :

$$Z_{eq1} = Z_{\ell_2}(0) \parallel Z_{scope} \quad (\text{B.8})$$

The input impedance of the system  $Z_{\ell_1}(0)$  can be calculated with:

$$Z_{\ell_1}(0) = Z_c \frac{Z_{eq1} + Z_c \tanh(\gamma \ell_1)}{Z_c + Z_{eq1} \tanh(\gamma \ell_1)} \quad (\text{B.9})$$

With that, the voltage and current between  $x = 0$  and  $x = x_M$  can be obtained with (B.10)

$$V_{\ell_1}(x) = V_S \frac{Z_{\ell_1}(0)}{Z_S + Z_{\ell_1}(0)} \left[ \cosh(\gamma x) - \frac{Z_c}{Z_{\ell_1}(0)} \sinh(\gamma x) \right] \quad \forall x \in [0, x_M] \quad (\text{B.10a})$$

$$I_{\ell_1}(x) = V_S \frac{1}{Z_S + Z_{\ell_1}(0)} \left[ \cosh(\gamma x) - \frac{Z_{\ell_1}(0)}{Z_c} \sinh(\gamma x) \right] \quad \forall x \in [0, x_M] \quad (\text{B.10b})$$

With these equations, the voltage at  $x = x_M$  can be calculated:

$$V(x_M) = V_S \frac{Z_{\ell_1}(0)}{Z_S + Z_{\ell_1}(0)} \left[ \cosh(\gamma x_M) - \frac{Z_c}{Z_{\ell_1}(0)} \sinh(\gamma x_M) \right] \quad (\text{B.11})$$

This voltage can be compared to the experimental data measured by the scope.

If the voltage in the second portion of the cable is needed, the portion of length  $\ell_2$ , it is more easily calculated using the voltage  $V(x_M)$ . Indeed, it corresponds to the input voltage of the second portion of the cable. The input current of this part of the cable is  $\frac{V(x_M)}{Z_{\ell_2}(0)}$ , and the voltage and current along the cable can be calculated with (B.12).

$$V_{\ell_2}(x) = V(x_M) \left[ \cosh(\gamma(x - x_M)) - \frac{Z_c}{Z_{\ell_2}(0)} \sinh(\gamma(x - x_M)) \right] \quad \forall x \in [x_M, \ell_c] \quad (\text{B.12a})$$

$$I_{\ell_2}(x) = \frac{V(x_M)}{Z_{\ell_2}(0)} \left[ \cosh(\gamma(x - x_M)) - \frac{Z_{\ell_2}(0)}{Z_c} \sinh(\gamma(x - x_M)) \right] \quad \forall x \in [x_M, \ell_c] \quad (\text{B.12b})$$

Another option to calculate the voltage and current in the portion of length  $\ell_2$  would be to represent the system seen from  $x = x_M$  towards  $x = 0$  by its Thévenin equivalent. However, because  $V(x_M)$  is usually calculated, to use equation (B.12) is a more simple and numerical efficient option.

In this appendix, the resonance surface response introduced in section 2.5.b are exploited. These surfaces are three-dimensional plots characterizing the resonant behavior of a transmission line.

In the following section, the resonance phenomena is studied in function of the conductors cross section. Afterwards, it is studied in function of the cable length.

### C.1 Comparison between the resonance behavior of two-conductor cables of different cross-section

The resonance surface response introduced in section 2.5.b (Figs. 2.39 to 2.41) completely characterize the resonance behavior of the two-conductor cable of section  $2.5\text{ mm}^2$  for a cable  $11\text{ m}$  long. It is interesting to compare the resonance behavior of this cable with other cables with different properties, and principally, different losses. As explained in section 2.5.a, the cable losses are the limiting factor of the resonance-voltage and current amplifications.

To that end, the same analysis described in section 2.5.b has been performed for other two cables, one of section  $0.75\text{ mm}^2$ , and other of section  $1.5\text{ mm}^2$ , for portions of cable with the same length, i.e.  $\ell_c = 11\text{ m}$ . The resonance surface response characterizing the cable of section  $0.75\text{ mm}^2$  are plotted in figures C.1 to C.3, and the ones characterizing the cable of section  $1.5\text{ mm}^2$  are plotted in figures C.4 to C.6.

From these figures, the maximal voltage amplifications estimated for each cable are listed in table C.1.

Table C.1 – Maximal voltage amplification for different two-conductor cables

Cable	Max Voltage Amplification
$0.75\text{ mm}^2$	13.47
$1.5\text{ mm}^2$	18
$2.5\text{ mm}^2$	15.83

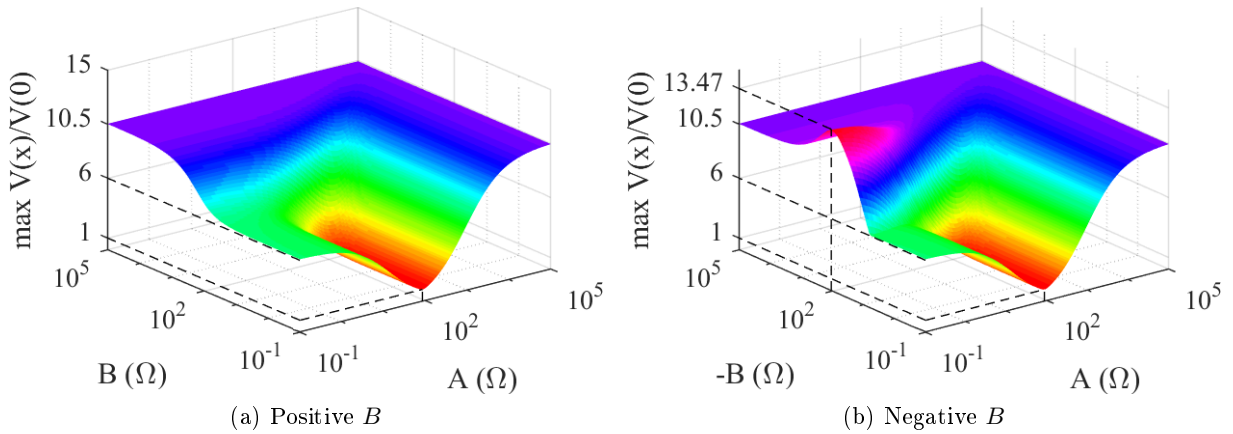


Figure C.1 – Maximum voltage in function of  $Z_L = A + jB$ , cable of section  $0.75 \text{ mm}^2$

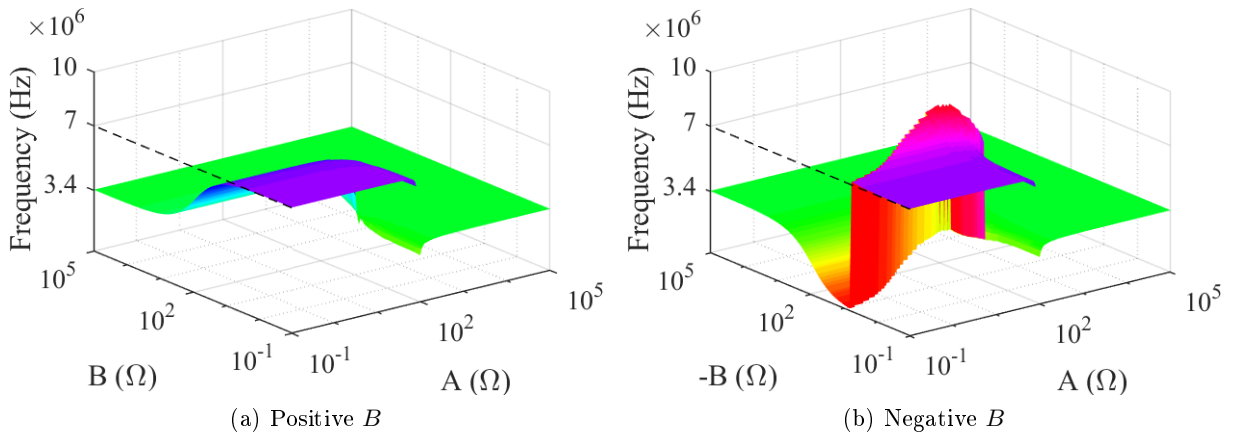


Figure C.2 – Resonance frequency in function of  $Z_L = A + jB$ , cable of section  $0.75 \text{ mm}^2$

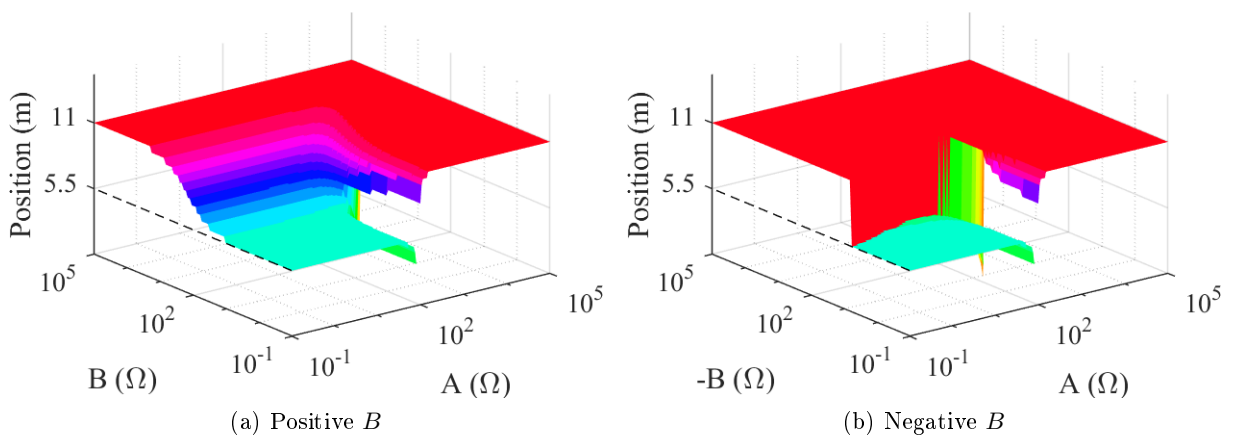


Figure C.3 – Position of the maximum voltage in function of  $Z_L = A + jB$ , cable of section  $0.75 \text{ mm}^2$

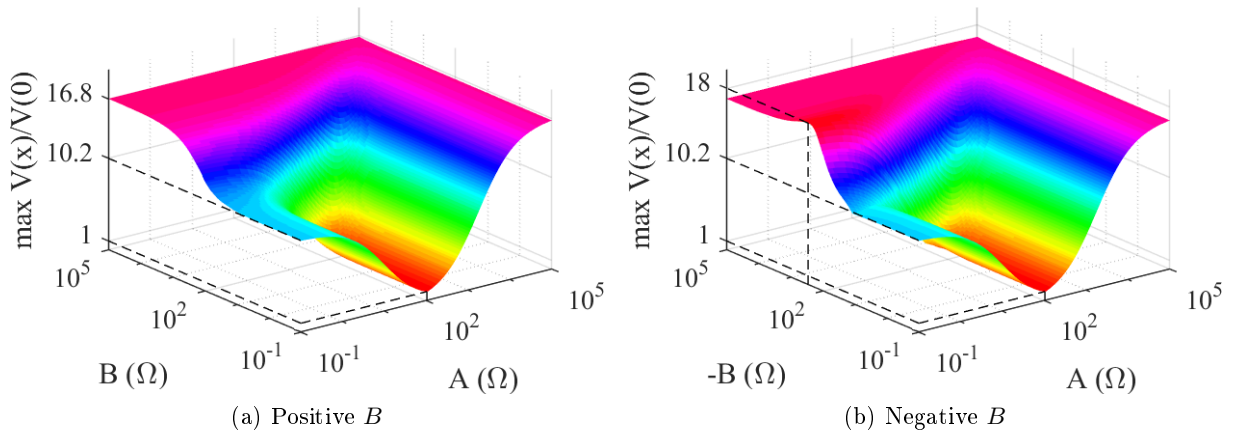


Figure C.4 – Maximum voltage in function of  $Z_L = A + jB$ , cable of section  $1.5 \text{ mm}^2$

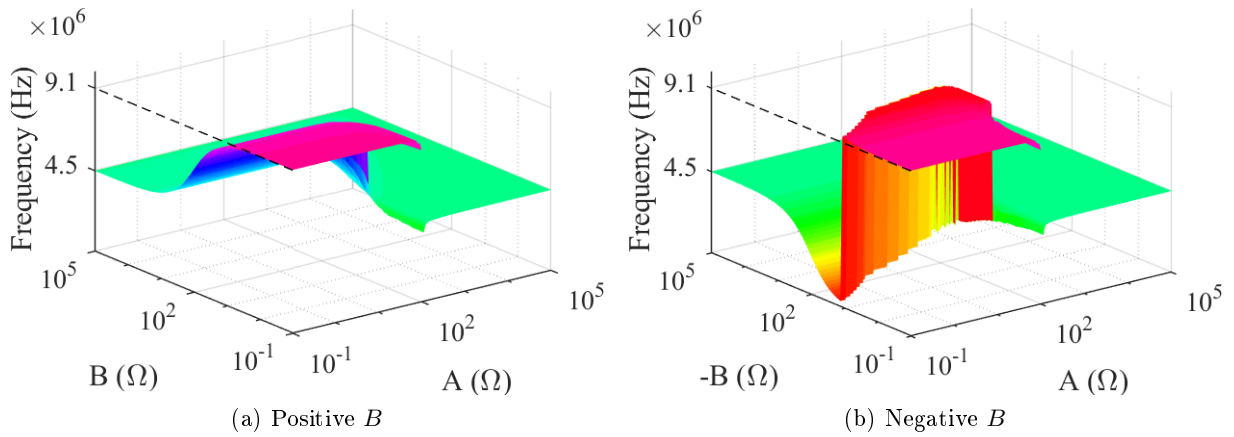


Figure C.5 – Resonance frequency in function of  $Z_L = A + jB$ , cable of section  $1.5 \text{ mm}^2$

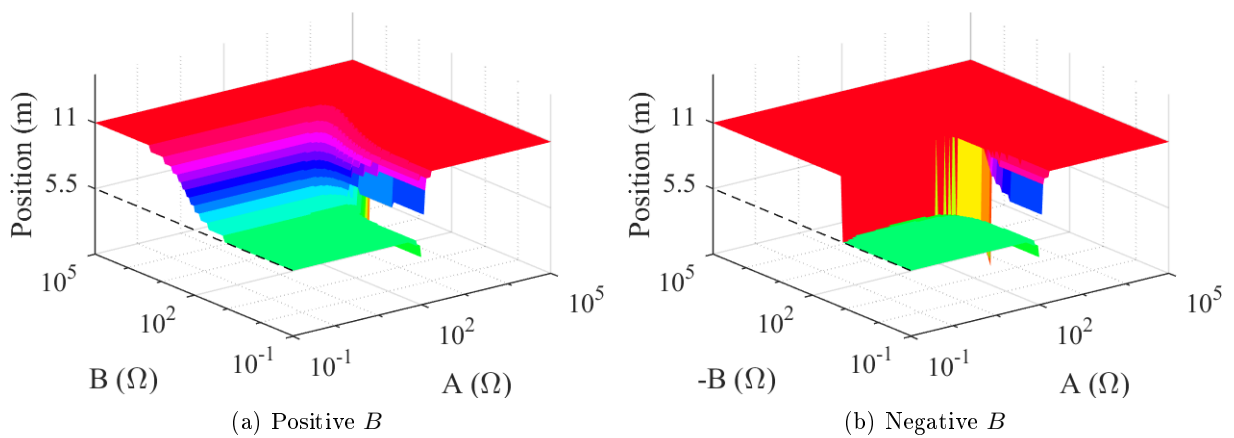


Figure C.6 – Position of the maximum voltage in function of  $Z_L = A + jB$ , cable of section  $1.5 \text{ mm}^2$



Normally, one would expect that the cable with section of  $2.5\text{ mm}^2$  would present the highest voltage amplification, because its p.u.l. resistance should be the smallest among the three cables. To understand the causes of behavior presented in table C.1, we must take a look at the loss related parameters of each one of the studied cables.

The p.u.l. resistance  $r$  and conductance  $g$  of each one of the cables are plotted in Fig. C.7.

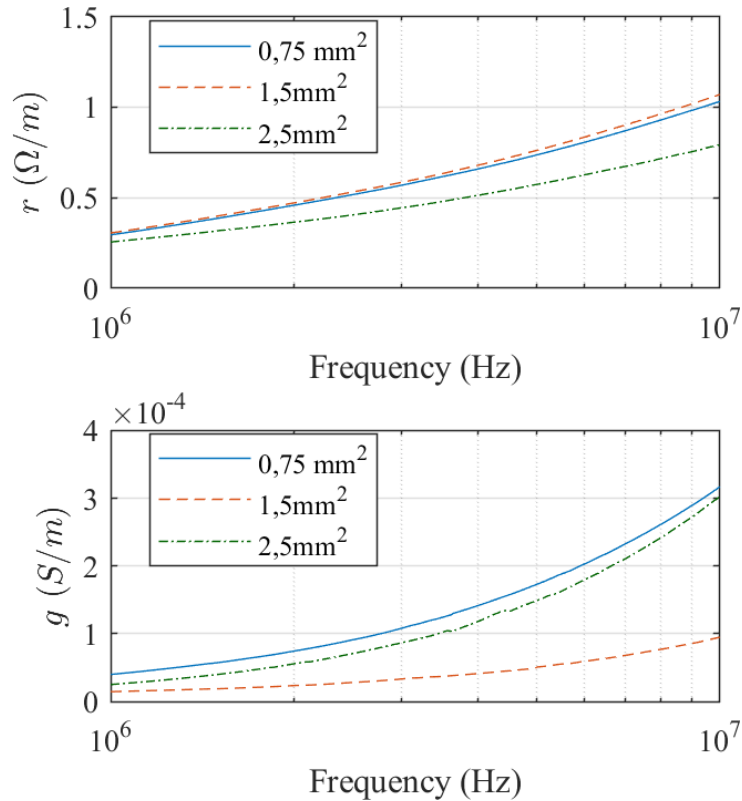


Figure C.7 – Two-conductor cables loss related parameters

It is shown in Fig. C.7 that the p.u.l. conductance of the  $1.5\text{ mm}^2$  is much smaller than the one of the other two cables. Therefore, as both of the loss related parameters  $r$  and  $g$  are determinant on the resonance-due voltage amplification, the amplification for the  $1.5\text{ mm}^2$  is higher than for the other two cables because the combined effect of the losses due to  $r$  and  $g$  in this cable are smaller.

## C.2 Comparison of the resonance behavior of the same cable with different lengths

In the previous sections, the length of the cables under study was kept constant. This section gives an idea of the behavior of the resonance in a cable when its length changes.

When the length of a given cable increases, there are two concurrent phenomena that interfere in the new resonance behavior:

1. A longer cable may increase the total losses of the cable, simply because it is longer.
2. The resonance frequencies of a longer cable are smaller, and as a consequence, the p.u.l. losses of the cable are smaller.

If the p.u.l. loss-related parameters  $r$  and  $g$  were constant with frequency, the total losses of the cable would increase linearly, thus reducing the maximal resonance-due voltage and current amplifications in the cable. But because these losses are frequency dependent, a different behavior is predicted.

The resonance surfaces characterizing the resonance behavior of the two-conductor cable of section  $2.5\text{ mm}^2$ , its cross-section represented in Fig. 2.29, has been predicted for cables with lengths  $50\text{ m}$  and  $200\text{ m}$ . The maximal voltage amplifications and resonance frequency surfaces are plotted in Figs. C.8 to C.11. The surfaces describing the position where the maximal voltage amplification takes place have been omitted in this section because they are very similar to the ones that have been presented before, for the  $11\text{ m}$  long cable, **but are available in appendix C**. As expected, the longer the cable, the smaller the resonance frequency, as well demonstrated

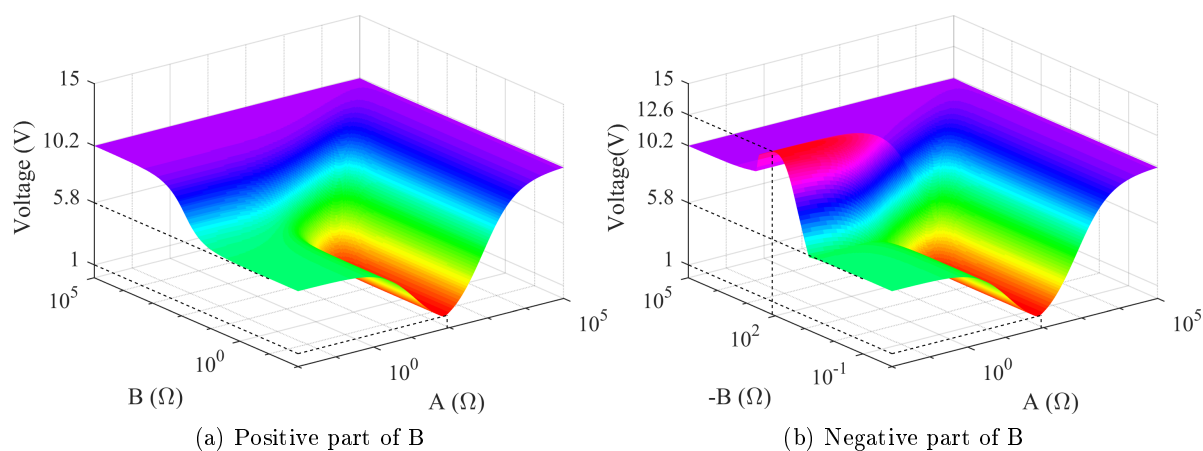


Figure C.8 – Maximal voltage amplification of the two-conductor  $2.5\text{ mm}^2$  cable of length  $50\text{ m}$ , in function of the load

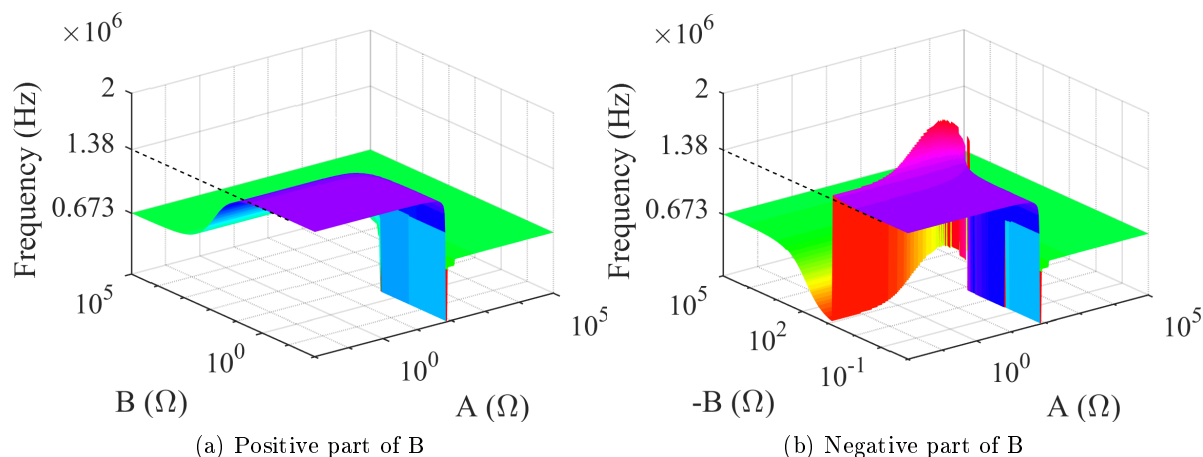


Figure C.9 – First resonance frequencies of the two-conductor  $2.5\text{ mm}^2$  cable of length  $50\text{ m}$ , in function of the load

in Figs. C.9 and C.11.

Curiously, the maximal voltage amplification didn't change much for the different cable lengths. In both Figs. C.8 and C.10 the maximal voltage amplification for high impedance is around 10 times the input voltage, against 14 for the  $11\text{ m}$  long cable, as shown in Fig. 2.39.

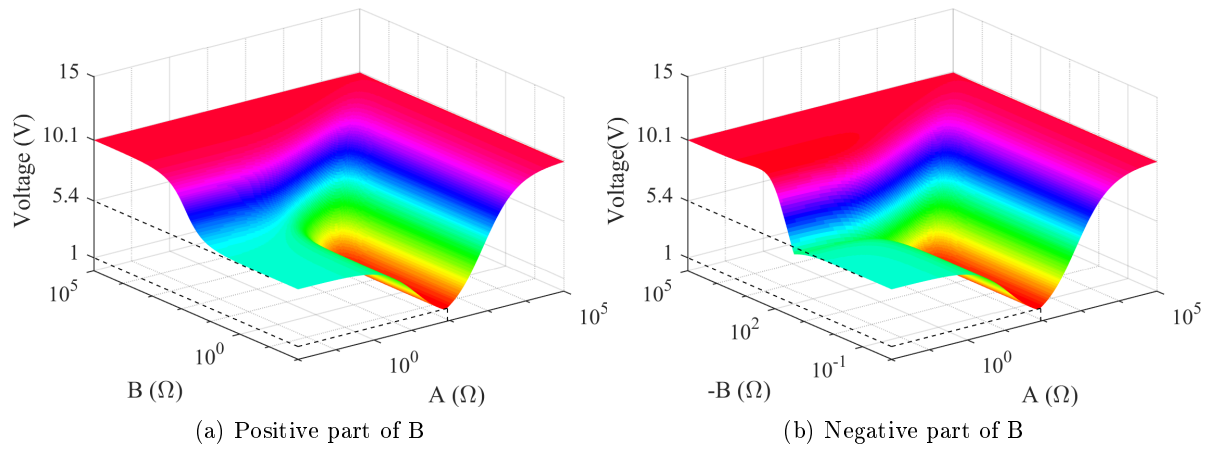


Figure C.10 – Maximal voltage amplification of the two-conductor  $2.5 \text{ mm}^2$  cable of length  $200 \text{ m}$ , in function of the load

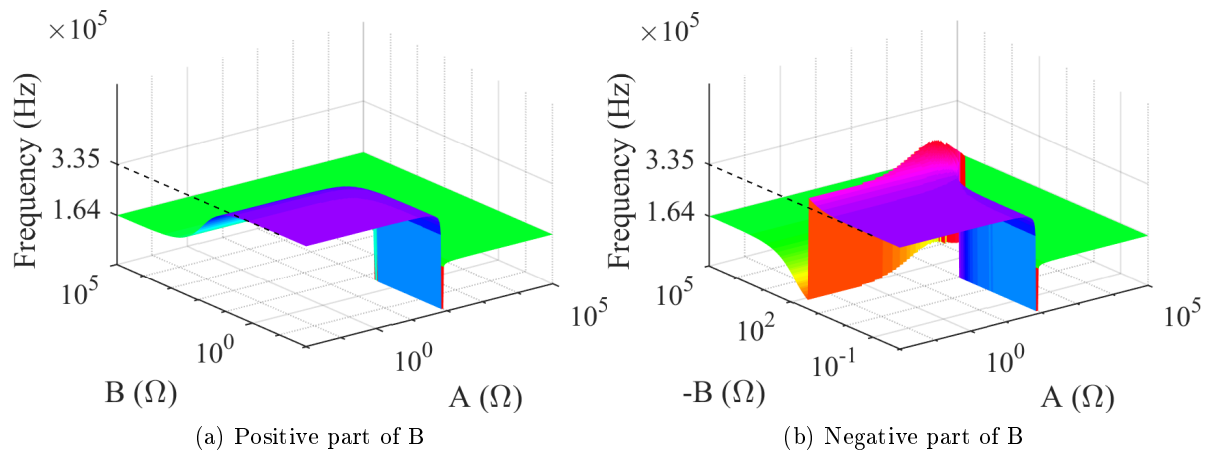


Figure C.11 – First resonance frequencies of the two-conductor  $2.5 \text{ mm}^2$  cable of length  $200 \text{ m}$ , in function of the load

It seems that, for the cable lengths chosen in this study, the two phenomena that impact the amplifications due to resonance, listed above, compensate each other.

A two-port device, as the one presented in Fig. D.1, can be modeled in matrix form using different definitions. The most common are defined in this appendix, and the conversion identities between these models are resumed in table D.1.

The two-port device most common matrix models are the following:

1. Impedance matrix:

$$\begin{bmatrix} V_1 \\ V_2 \end{bmatrix} = \mathbf{Z} \begin{bmatrix} I_1 \\ -I_2 \end{bmatrix} \quad (\text{D.1})$$

2. Admittance matrix:

$$\begin{bmatrix} I_1 \\ -I_2 \end{bmatrix} = \mathbf{Y} \begin{bmatrix} V_1 \\ V_2 \end{bmatrix} \quad (\text{D.2})$$

3. Transmission matrix

$$\begin{bmatrix} V_1 \\ I_1 \end{bmatrix} = \mathbf{T} \begin{bmatrix} V_2 \\ I_2 \end{bmatrix} \quad (\text{D.3})$$

4. Chain matrix

$$\begin{bmatrix} V_2 \\ I_2 \end{bmatrix} = \mathbf{\Phi} \begin{bmatrix} V_1 \\ I_1 \end{bmatrix} \quad (\text{D.4})$$

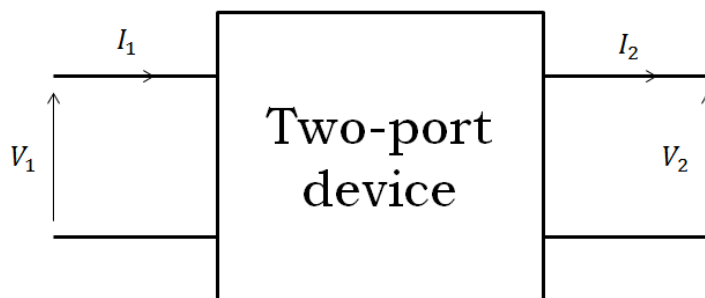


Figure D.1

Table D.1 – Conversion between the two-port devices models

	<b>Z</b>	<b>Y</b>	<b>T</b>	<b>Φ</b>
<b>Z</b>	$\begin{bmatrix} Z_{11} & Z_{12} \\ Z_{21} & Z_{22} \end{bmatrix}$	$\frac{1}{ \mathbf{Y} } \begin{bmatrix} Y_{22} & -Y_{12} \\ -Y_{21} & Y_{11} \end{bmatrix}$	$\frac{1}{C} \begin{bmatrix} A &  \mathbf{T}  \\ 1 & D \end{bmatrix}$	$\frac{1}{ \Phi_{21} } \begin{bmatrix} \Phi_{22} & 1  \\  \Phi  & \Phi_{11} \end{bmatrix}$
<b>Y</b>	$\frac{1}{ \mathbf{Z} } \begin{bmatrix} Z_{22} & -Z_{12} \\ -Z_{21} & Z_{11} \end{bmatrix}$	$v \begin{bmatrix} Y_{11} & Y_{12} \\ Y_{21} & Y_{22} \end{bmatrix}$	$\frac{1}{B} \begin{bmatrix} D & - \mathbf{T}  \\ -1 & A \end{bmatrix}$	$\frac{1}{ \Phi_{12} } \begin{bmatrix} -\Phi_{11} & 1  \\  \Phi  & -\Phi_{22} \end{bmatrix}$
<b>T</b>	$\frac{1}{Z_{21}} \begin{bmatrix} Z_{11} &  \mathbf{Z}  \\ 1 & Z_{22} \end{bmatrix}$	$\frac{1}{Y_{21}} \begin{bmatrix} Y_{22} & -1 \\ - \mathbf{Y}  & -Y_{11} \end{bmatrix}$	$\begin{bmatrix} A & B \\ C & D \end{bmatrix}$	$\frac{1}{ \Phi } \begin{bmatrix} \Phi_{22} & -\Phi_{12}  \\ -\Phi_{21} & \Phi_{11} \end{bmatrix}$
<b>Φ</b>	$\frac{1}{Z_{12}} \begin{bmatrix} Z_{22} & - \mathbf{Z}  \\ -1 & Z_{11} \end{bmatrix}$	$\frac{1}{Y_{12}} \begin{bmatrix} Y_{11} & 1 \\  \mathbf{Y}  & -Y_{22} \end{bmatrix}$	$\frac{1}{ \mathbf{T} } \begin{bmatrix} D & -B \\ -C & A \end{bmatrix}$	$\begin{bmatrix} \Phi_{11} & \Phi_{12} \\ \Phi_{21} & \Phi_{22} \end{bmatrix}$

\* $|\mathbf{A}|$  is the determinant of matrix  $\mathbf{A}$

In this appendix is described a study of the balun used in the measurements of the input impedance of cables. The balun balances the output voltage, and mitigate common mode in the impedance measurement if the devices under test is also balanced.

The cables studied along this work are balanced devices, either if they are short-circuited or open-ended. For this reason, the balun was used to mitigate the common mode in the cable input impedance measurements, used for the cable parameter identification. Refer to section 2.3.b-ii for more details.

The cable parameters presented in the examples along this document were all obtained using the balun Minicircuits T6-4T. In section E.1, the balun itself is experimentally characterized, and in section E.2 a practical analysis of the results gives the frequency band in which the measurements performed with the balun are valid.

## E.1 The balun experimental identification

The practical schematic of the balun under study is drawn in Fig. E.1.

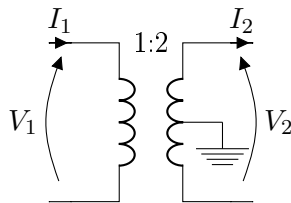


Figure E.1 – Schematic balun

The balun has been experimentally identified as four-port device, in form given in (E.1). This model allows the frequency domain analysis of the balun behavior.

$$\begin{bmatrix} V_1 \\ I_1 \end{bmatrix} = \begin{bmatrix} A & B \\ C & D \end{bmatrix} \begin{bmatrix} V_2 \\ I_2 \end{bmatrix} \quad (\text{E.1})$$

To obtain the ABCD parameters in the equation above, first the impedance matrix in (E.2) was obtained from impedance measurements.

$$\begin{bmatrix} V_1 \\ V_2 \end{bmatrix} = \begin{bmatrix} Z_{11} & Z_{12} \\ Z_{21} & Z_{22} \end{bmatrix} \begin{bmatrix} I_1 \\ I_2 \end{bmatrix} \quad (\text{E.2})$$

The impedance matrix can be obtained with three impedance measurements of the balun: with the balun open-ended  $Z_{OC}$ , short-circuited  $Z_{SC}$ , and connected to a  $50\Omega$  load  $Z_{50}$ . The

elements of the impedance matrix are obtained with (E.3)

$$Z_{11} = Z_{OC} \quad (\text{E.3a})$$

$$Z_{22} = -50 \frac{Z_{50} - Z_{OC}}{Z_{50} - Z_{SC}} \quad (\text{E.3b})$$

$$Z_{12} = Z_{21} = \sqrt{50(Z_{SC} - Z_{OC}) \frac{Z_{50} - Z_{OC}}{Z_{50} - Z_{SC}}} \quad (\text{E.3c})$$

The ABCD parameters can be found from the impedance matrix with (E.4) (cf. appendix D).

$$A = \frac{Z_{11}}{Z_{21}} \quad (\text{E.4a})$$

$$B = -Z_{12} + Z_{11} \frac{Z_{22}}{Z_{21}} \quad (\text{E.4b})$$

$$C = \frac{1}{Z_{21}} \quad (\text{E.4c})$$

$$D = \frac{Z_{22}}{Z_{21}} \quad (\text{E.4d})$$

The ABCD parameters obtained for the Minicircuits T6-4T balun are plotted in Fig. E.2.

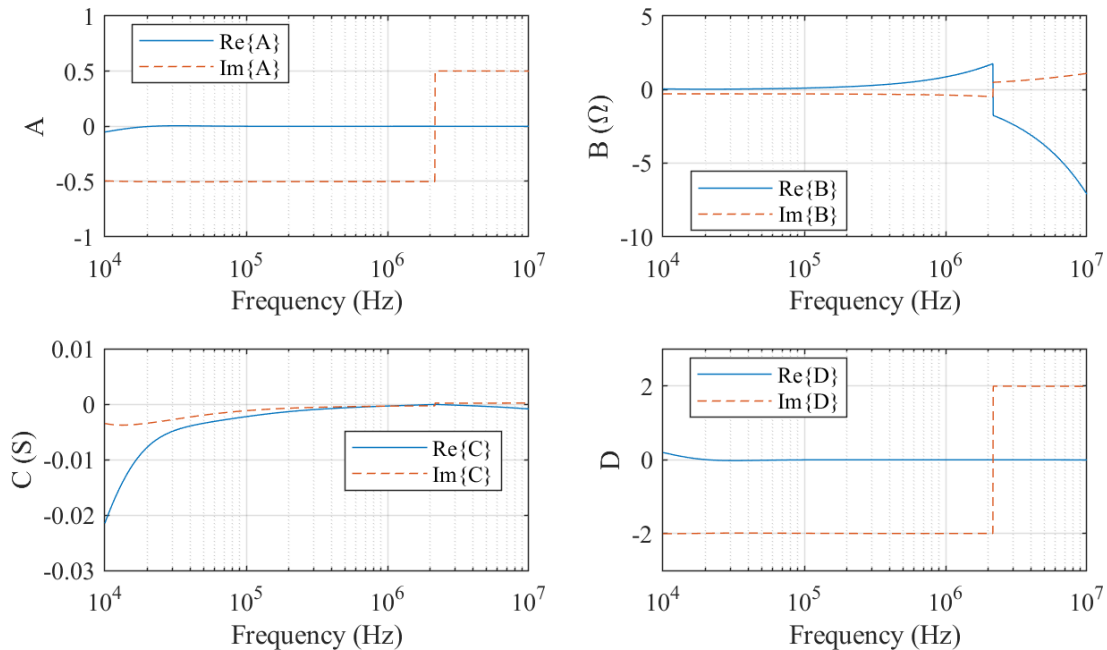


Figure E.2 – ABCD parameters of the Minicircuits T6-4T balun

If the balun behaved ideally, these parameters would have the following values:

$$\begin{bmatrix} A & B \\ C & D \end{bmatrix} = \begin{bmatrix} \frac{1}{2} & 0 \\ 0 & 2 \end{bmatrix} \quad (\text{E.5})$$

In Fig. E.2 it can be seen that the absolute values of the parameters approach these ideal values for a specific frequency band. Indeed, balun are devices designed to be effective in narrow band. Its main applications are RF systems which are not wide band, such as antennas.

It is necessary to determine the frequency band in which the impedance measurements done

with the balun are reliable. The following section discusses this problem.

## E.2 Determination of useful frequency band

As mentioned in the former section, baluns are designed to be performant in narrow frequency bands. In this section, the frequency band where the impedance measurements performed with balun are reliable will be determined.

The impedance measurements are performed after the balun is compensated with three measurements (Open, Short, Load), with the compensation method of the impedance analyzer. The efficiency of this compensation depends on the behavior of the balun, and on the impedance of the device under test (DUT).

If the contribution of the balun on the current measured by the analyzer is higher than the contribution of the DUT, the impedance measurement would have a poor accuracy. For this reason, a simplified method is proposed to determine the frequency band of reliable measurements, using the DUT input impedance.

The analyze proposed here is based in the following facts:

- The absolute value of the input impedance of an open-ended cable decreases logarithmic with frequency, for frequencies lower than its resonance frequency.
- The absolute value of the input impedance of a short-circuited cable increases logarithmic with frequency for frequencies lower than its resonance frequency, but high enough so the inductive behavior of the cable is preponderant before its DC behavior.

The behavior described above can be seen in the input impedance measurement results plotted in Fig. E.3.

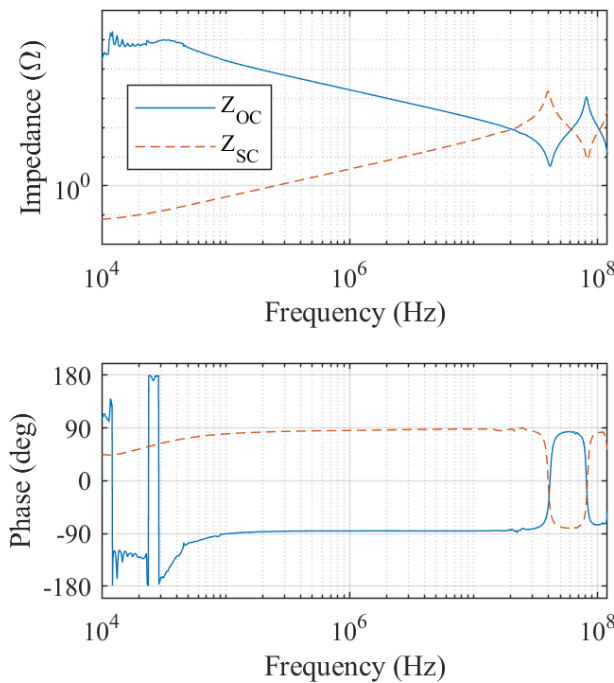


Figure E.3



For the frequencies around a few tens of  $kHz$ , it can be seen that the open-ended cable input impedance does not correspond to the theoretical behavior. This may come from the combination of two difficulties: the impedance is too high to be measured, and the impedance introduced by the balun in this frequency band is much smaller than the DUT impedance. In Fig. E.2, it can be seen that the balun is not ideal in this frequency band, what makes the measurement more difficult.

To determine the lower limit of the frequency band in which these impedance measurements are valid, the logarithmic differentiation of the input impedances in Fig. E.3 will be used.

Theoretically, the logarithmic derivation of  $|Z_{OC}|$  and  $|Z_{SC}|$  with frequency should be constant for frequencies lower than the resonance frequency.

In the logarithmic derivative with frequency of the absolute values of both impedances are plotted in Fig. E.4. Over the derivative plot, a 10% error bar is plotted, and the lowest frequencies to which the derivative is not inside the error bar are marked with black dotted line.

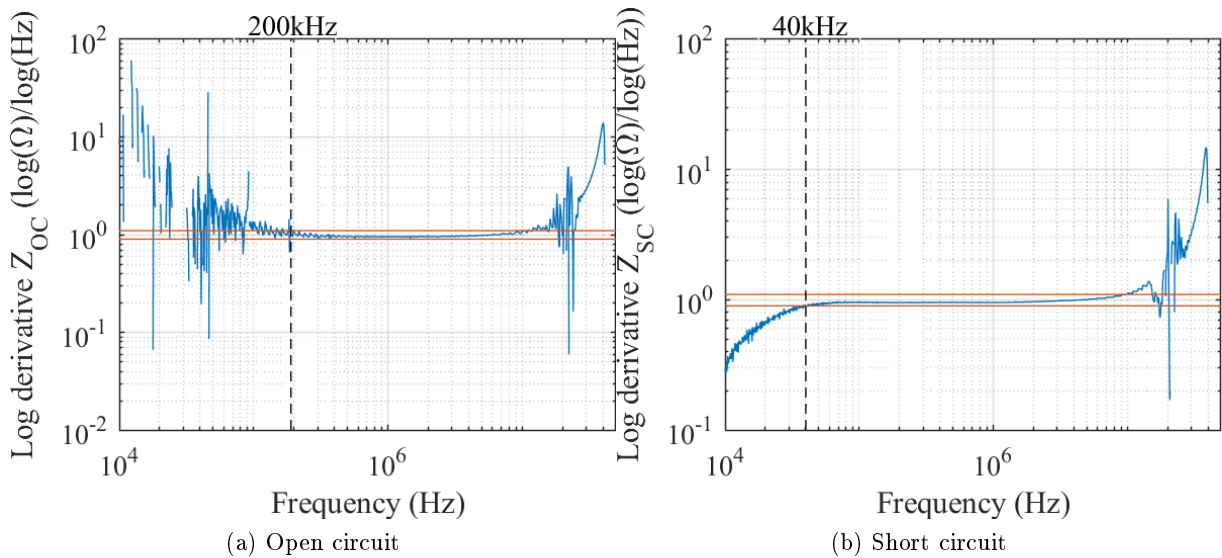


Figure E.4 – Logarithmic derivative of the measured input impedance of the cable, the lowest frequency to which they can be considered constant is marked with dotted line

From Fig.E.4, it can be determined that the impedance measurements with balun should be used for frequencies higher than  $200 kHz$ .

This analysis is not sufficient to determine the high limit of the frequency band, because of the resonance in the sample cable.

The general solution for a Multiconductor Transmission Line is resumed in section 3.2. This solution allows the representation of the MTL as a  $2(n + 1)$ -pole device given in (3.22) on page 57.

This representation can be rewritten by defining  $\sqrt{\mathbf{ZY}}$  as propagation matrix, as follows:

$$\begin{bmatrix} \mathbf{V}(z) \\ \mathbf{I}(z) \end{bmatrix} = \begin{bmatrix} \Phi_{11}(z) & \Phi_{21}(z) \\ \Phi_{21}(z) & \Phi_{22}(z) \end{bmatrix} \begin{bmatrix} \mathbf{V}(0) \\ \mathbf{I}(0) \end{bmatrix} \quad (\text{F.1})$$

$$\Phi_{11}(z) = \cosh(z\sqrt{\mathbf{ZY}}) \quad (\text{F.2})$$

$$\Phi_{21}(z) = -\mathbf{Y}_c \sinh(z\sqrt{\mathbf{ZY}}) \quad (\text{F.3})$$

$$\Phi_{12}(z) = -\sinh(z\sqrt{\mathbf{ZY}})\mathbf{Z}_c \quad (\text{F.4})$$

$$\Phi_{22}(z) = \mathbf{Y}_c \cosh(z\sqrt{\mathbf{ZY}})\mathbf{Z}_c \quad (\text{F.5})$$



This appendix presents the cable parameters of the cable of four conductors of section  $1.5\text{ mm}^2$  with an outer shield of tinned copper wire, its cross-section is represented in Fig. 5.5.

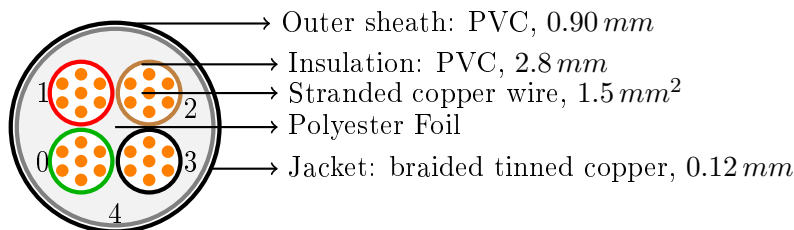


Figure G.1 – Cross-section of the  $4 \times 1.5\text{ mm}^2$  cables, with labeled conductors

The cable has been characterized with the impedance measurements of two sample cables:

- Up to  $300\text{ kHz}$ : a  $8.8\text{ m}$  long sample cable;
- From  $300\text{ kHz}$  to  $10\text{ MHz}$ : a  $1.35\text{ m}$  long sample cable, and the measurements were performed with a balun.

Its p.u.l. parameters are plotted in Fig. G.2. The discrepancies at the change between the two sample cables are bigger than for the former conductors. The authors believe they are due to common-mode circulation in the low frequency sample, of length  $8.8\text{ m}$ . The default Keysight adapter 16047E was used in this measurement, and it is possible that the distance between the extremities of the conductors that were not being measured and the connector contributed to the common-mode circulation.

There are two p.u.l. conductance and capacitance that are considerably smaller than the others:  $G_{20}$ ,  $G_{13}$ ,  $C_{20}$  and  $G_{13}$ . They correspond to the p.u.l. capacitance and conductance of two wires placed diagonally from each other. Because they are smaller, the accuracy in their determination was prejudiced, and for that reason they assume negative values in parts of the frequency band. This inaccuracy did not prejudice the results presented in section 5.3, because the behavior of the cable is mainly determined by the cable p.u.l. parameters of higher value, between two conductors side-by-side or one conductor and the shield.

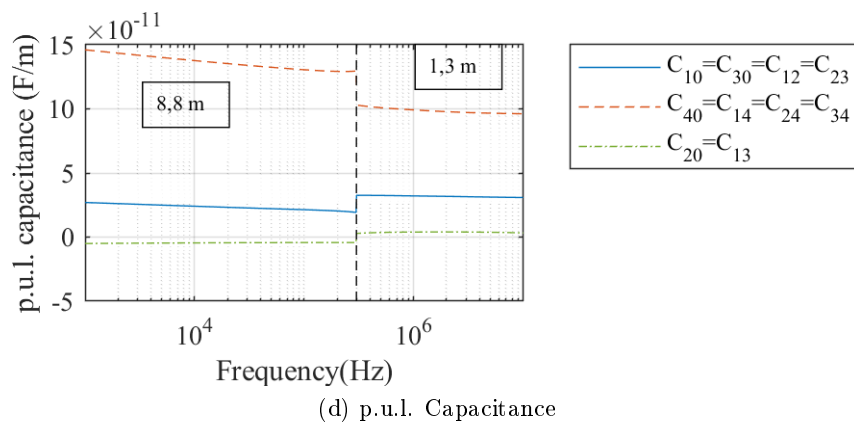
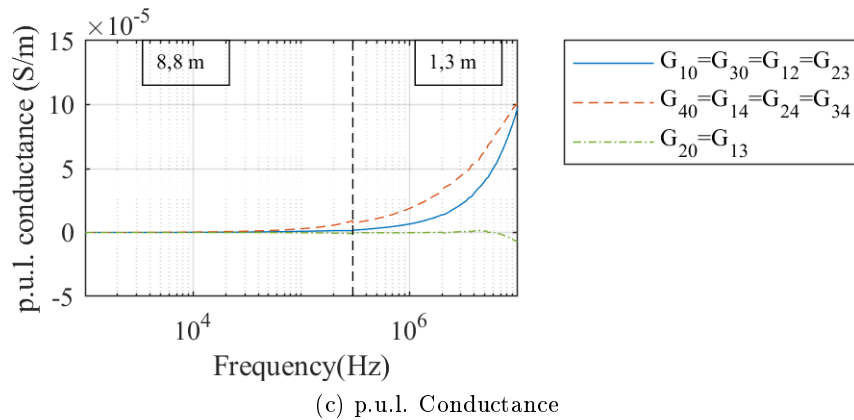
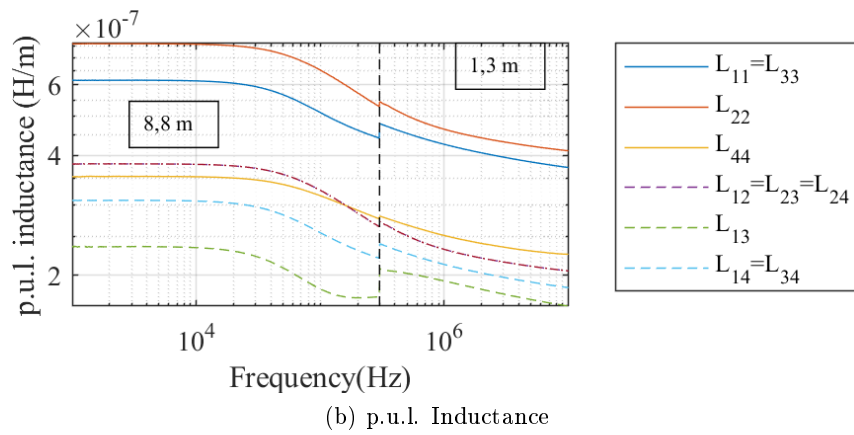
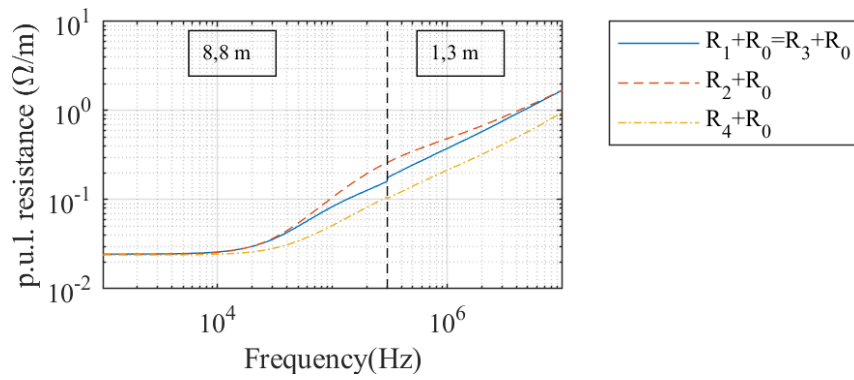


Figure G.2 – Parameters of the shielded cable with 4 conductors of section  $1.5 \text{ mm}^2$

The input impedance of the three-phase motor Leroy Somer 1.5 kW used in section 5.3 was measured with the impedance analyzer Keysight E4990A, and this appendix shows the setup that allowed the measurement. The measurements to be performed are based on the work of Revol [40], and are resumed in the schematics in Fig. H.1.

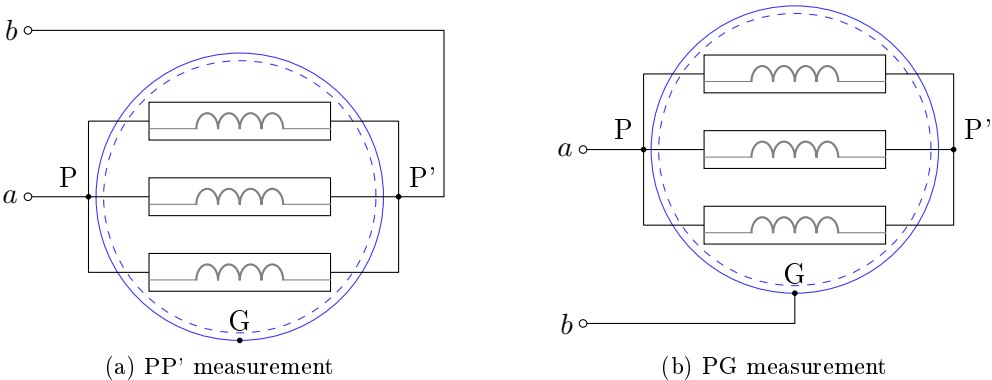


Figure H.1 – Measurement schematics to characterize the three-phase motor: input impedance measured between points *a* and *b*

To reduce measurement errors, the connection between the motor and the analyzer was made with the smallest portion of wire possible. To that end, the analyzer was placed over a platform, as shown in Fig. H.2, to approximate its terminals to the motor terminals. Stranded cooper wire of  $2.5\text{ mm}^2$  was used in the connection.

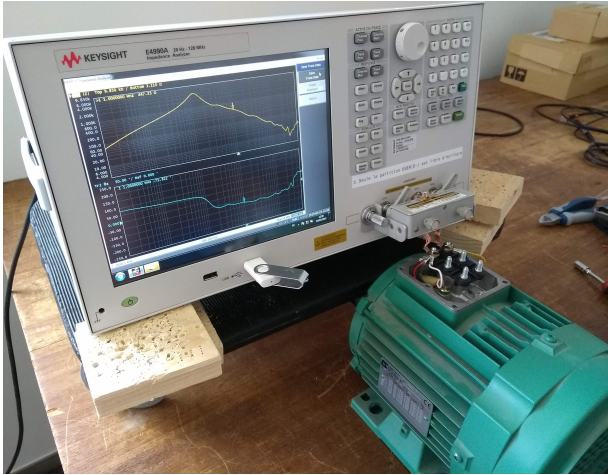


Figure H.2 – Motor input impedance measurement setup

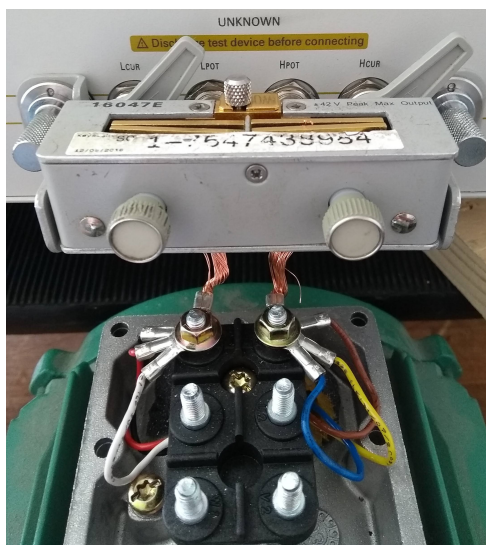
The compensation of the measurement circuit was performed using the insulating support of

the motor terminals. The SHORT compensation is shown in Fig. H.3: the winding connectors were removed, and a copper plate was used to perform the short circuit between the measuring terminals. The OPEN compensation was performed with the measuring terminals at the same position, but without the copper plate.

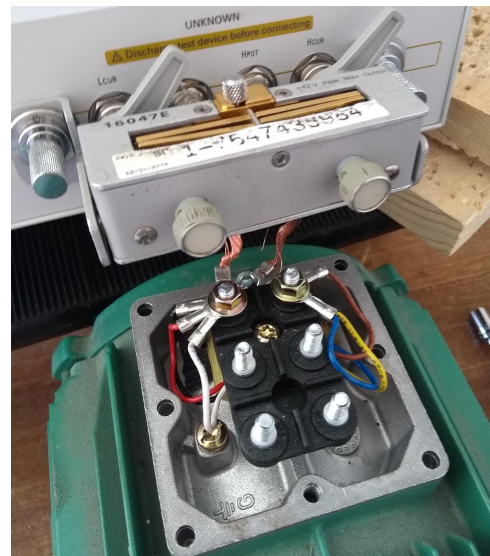


Figure H.3 – Motor input impedance measurement setup: compensation SHORT

Once the compensation is performed, the P-P' measurement is performed as shown in Fig. H.4a, and the P-G measurement as shown in Fig. H.4b.



(a) P-P' measurement,  $Z_{PP}$



(b) P-G measurement,  $Z_{PG}$

Figure H.4 – Motor input impedance measurement setup: connections for measurements

The measurement results are presented in Fig. 5.3.

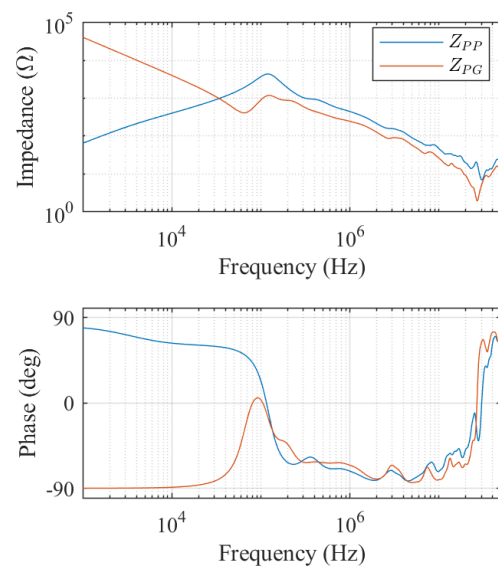


Figure H.5 – Impedances  $Z_{PP}$  and  $Z_{PG}$ , measured with impedance analyzer





The electric motor characterization using the impedance analyzer that was presented in the previous appendix was validated with a second impedance measurement set. This second set, hereafter denominated six-measurement identification, does not use the symmetry hypothesis that were taken previously.

The validation set of measurements consists on characterizing the three-phase motor as a four port generic device, with the three windings connected in star. A schematic of the motor connection is given in Fig. I.1.

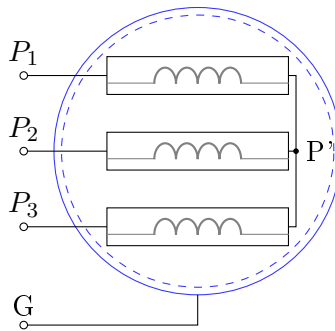


Figure I.1 – Schematic of the three-phase motor as a 4 input device

The input impedance was measured between all the possible combinations between the motor terminals. That gives six input impedances, as listed in table I.1

Table I.1 – Input impedance measured for motor characterization

Terminals	Impedance	Terminals	Impedance
$P_1 - G$	$Z_{P_1G}$	$P_1 - P_2$	$Z_{P_1P_2}$
$P_2 - G$	$Z_{P_2G}$	$P_1 - P_3$	$Z_{P_1P_3}$
$P_3 - G$	$Z_{P_3G}$	$P_2 - P_3$	$Z_{P_2P_3}$

The input impedance matrix  $\mathbf{Z}$  can be built for the three-phase motor following the steps described in section 3.3, what results in the following equations:

$$\mathbf{Z} = \begin{bmatrix} Z_{11} & Z_{12} & Z_{13} \\ Z_{12} & Z_{22} & Z_{23} \\ Z_{13} & Z_{23} & Z_{33} \end{bmatrix} \quad (\text{I.1})$$

$$Z_{11} = Z_{P_1G} \quad Z_{12} = \frac{1}{2}(Z_{P_1G} + Z_{P_2G} - Z_{P_1P_2}) \quad (\text{I.2})$$

$$Z_{22} = Z_{P_2G} \quad Z_{13} = \frac{1}{2}(Z_{P_1G} + Z_{P_3G} - Z_{P_1P_3}) \quad (\text{I.3})$$

$$Z_{33} = Z_{P_3G} \quad Z_{23} = \frac{1}{2}(Z_{P_2G} + Z_{P_3G} - Z_{P_2P_3}) \quad (\text{I.4})$$

$$(\text{I.5})$$

To verify that this identification technique is equivalent to the 2-measurement identification described in H, two different impedances were compared using the matrices issued from each of the identification techniques: the common-mode impedance  $Z_{CM}$ , measured between the short-circuited terminals  $P_1$ ,  $P_2$  and  $P_3$  and the carcass  $G$ ; and the mutual impedance  $Z_{P_1P_2}$ . They can be calculated as follows:

$$Z_{CM} = \mathbf{Y} \begin{bmatrix} 1 \\ 1 \\ 1 \end{bmatrix} \quad (\text{I.6})$$

$$\begin{bmatrix} V_1 \\ V_2 \\ V_3 \end{bmatrix} = \mathbf{Z} \begin{bmatrix} 1 \\ -1 \\ 0 \end{bmatrix} \quad (\text{I.7a})$$

$$Z_{P_1P_2} = V_1 - V_2 \quad (\text{I.7b})$$

The impedances calculated with each identification are plotted over the experimental data in Fig. I.2.

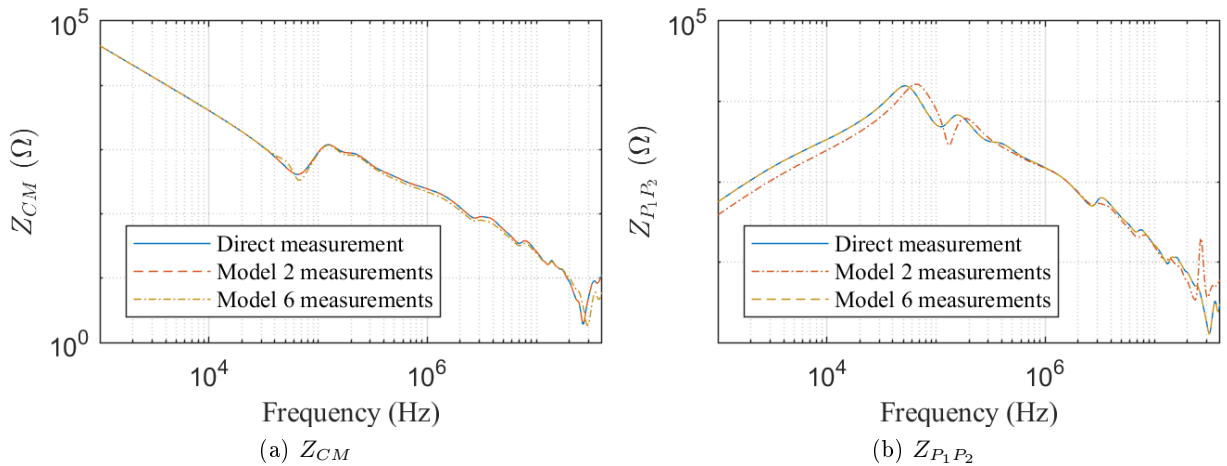


Figure I.2 – Comparison of the two motor experimental characterizations

The results in Fig. I.2 show that the two motor identification methods are equivalent, the

discrepancies between the input impedances being negligible. In Fig. I.2a the two-measurement model fit perfectly the experimental data because it is based on this measurement, the same goes for Fig. I.2b where it is the impedance calculated from the six-measurement identification that fits perfectly the experimental data.



# LIST OF FIGURES

1	The two most used voltage-current representation in circuit schematics . . . . .	xv
2	Source symbols used in this document . . . . .	xv
1.1	Schematic to show the loss impact on resonance-due voltage amplification . . . . .	6
1.2	Voltage amplification at $x = \ell_c$ for three different loss characteristics . . . . .	7
2.1	Two-conductor transmission line, variable definition . . . . .	10
2.2	Elementary cell of two-conductor transmission lines, with its per-unit-length parameters . . . . .	11
2.3	Schematic of the generalized frequency domain model for two-conductor cables . . . . .	12
2.4	Frequency domain simulation tool inputs and outputs — two-conductor cables . . . . .	13
2.5	$\gamma = \alpha + j\frac{\omega}{v}$ in function of frequency . . . . .	14
2.6	$Z_c$ in function of frequency . . . . .	15
2.7	Time-domain reflectometer (TDR) . . . . .	17
2.8	VNA measurement . . . . .	17
2.9	The input impedance of the cable . . . . .	19
2.10	Two-conductor cable characteristic impedance identification for different lengths . . . . .	20
2.11	Example of common-mode measurement corruption due to common-mode current [21] . . . . .	22
2.12	Solution to avoid common-mode-due error [21] . . . . .	23
2.13	Common-mode analysis of balun-isolated measurement . . . . .	23
2.14	Configuration “A”: avoids common-mode circulation . . . . .	24
2.15	Configuration “B”: common-mode enhancing configuration . . . . .	24
2.16	Cross-section of the two-conductor $0.75\text{ mm}^2$ cable . . . . .	24
2.17	E4990A adapter designed by the authors . . . . .	25
2.18	Cross-section of two-conductor $0.75\text{ mm}^2$ cable . . . . .	27
2.19	Schematic of the validation resonance-based experiment . . . . .	28
2.20	Connection of the voltage probe along the line . . . . .	28
2.21	Voltage probe input impedance . . . . .	29
2.22	Frequency domain voltage simulation . . . . .	29
2.23	Input impedance comparison . . . . .	30
2.24	Theoretical input impedance calculation . . . . .	31
2.25	Input impedance comparison, theoretical calculations using parameters obtained from identification with and without balun . . . . .	31
2.26	Input impedance comparison, theoretical calculations using parameters obtained from identification with or without balun, identification without balun on ideal configuration . . . . .	32

2.27	Cross-section of the two-conductor $0.75 \text{ mm}^2$ cable . . . . .	34
2.28	Per-unit-length parameters of the $0.75 \text{ mm}^2$ cable . . . . .	35
2.29	Cross-section of the two-conductor $2.5 \text{ mm}^2$ cable . . . . .	35
2.30	Parameters of the cable of section $0.75 \text{ mm}^2$ . . . . .	36
2.31	Per-unit-length parameters of the cable of section $0.75 \text{ mm}^2$ . . . . .	36
2.32	Parameters of the cable of section $2.5 \text{ mm}^2$ . . . . .	37
2.33	Per-unit-length parameters of the cable of section $2.5 \text{ mm}^2$ . . . . .	37
2.34	Schematics for the resonance analysis . . . . .	38
2.35	Voltage and current envelopes of a short-circuited resonant line . . . . .	39
2.36	Voltage and current envelopes of an open-ended resonant line . . . . .	40
2.37	Voltage envelope in function of frequency for the short-circuited two-conductor cable of section $2.5 \text{ mm}^2$ , with variations on the attenuation constant $\alpha$ . . . . .	41
2.38	Schematics for the resonance analysis . . . . .	42
2.39	Maximum voltage in function of $Z_L = A + jB$ , positive and negative parts of $B$ . . . . .	43
2.40	Resonance frequency in function of $Z_L = A + jB$ , positive and negative parts of $B$ . . . . .	44
2.41	Position of the maximum voltage in function of $Z_L = A + jB$ , positive and negative parts of $B$ . . . . .	45
2.42	The given RLC load . . . . .	46
2.43	The intersection of the load impedance and the resonance frequency surface . . . . .	46
2.44	Voltage amplifications and positions corresponding to the two intersections . . . . .	46
2.45	The maximum voltage amplification possible due to resonance phenomena . . . . .	47
2.46	A possible load for the desired voltage amplification . . . . .	47
2.47	The resonance frequency and maximum amplification position for the maximum amplification possible . . . . .	48
2.48	Representation of an electrically short line, with load $Z_L$ . . . . .	48
2.49	The chosen load $Z_L$ . . . . .	49
2.50	Input impedance of the line under study . . . . .	49
2.51	Input impedance of the open-ended line . . . . .	50
3.1	Multiconductor transmission line, variables definition . . . . .	53
3.2	Elementary cell of multiconductor transmission lines, with its p.u.l. parameters . . . . .	53
3.3	$(n + 1)$ -port equivalent circuit . . . . .	59
3.4	Multiconductor transmission line, variables definition . . . . .	60
3.5	Frequency domain simulation tool inputs and outputs — multiconductor cables . . . . .	61
3.6	Program flowchart of the frequency domain simulation tool — multiconductor cables . . . . .	63
3.7	Self impedance measurement setup . . . . .	65
3.8	Mutual-impedance measurement setup . . . . .	65
3.9	Three-conductor cable cross-section . . . . .	66
3.10	Schematic: resonance-based validation experiment . . . . .	67
3.11	Connection of the voltage probe along the line . . . . .	67
3.12	Frequency domain voltage simulation . . . . .	68
3.13	Experimental validation : resonance-due voltage amplification . . . . .	69
3.14	Schematic: input impedance validation experiment . . . . .	69
3.15	Theoretical input impedance calculation . . . . .	70
3.16	Experimental validation : input impedance . . . . .	71

3.17	Cross-section of the three-conductor $2.5\text{ mm}^2$ cable . . . . .	71
3.18	Three-conductor cable complex parameters . . . . .	73
3.19	Three-conductor p.u.l. parameters . . . . .	73
3.20	Schematic for numerical resonance analysis . . . . .	74
3.21	Differential and common-mode currents . . . . .	76
3.22	Schematic for numerical resonance analysis, $\ell_c = 12\text{ m}$ . . . . .	78
3.23	Voltage amplification due to resonance on the three-conductor cable, in differential and common mode, in function of the modal load . . . . .	80
3.24	Resonance frequencies of the three-conductor cable, in differential and common mode, in function of the modal load . . . . .	80
3.25	Position of the maximal voltage amplification on the three-conductor cable, in differential and common mode, in function of the modal load . . . . .	81
3.26	Load used for this example . . . . .	82
3.27	Intersection of the modal impedances with the resonance frequency surfaces. . . . .	83
3.28	Points of intersection on the voltage amplification resonance surfaces . . . . .	83
3.29	Points of intersection on the position of maximal amplification due to resonance surfaces . . . . .	83
3.30	Voltage at $x = \ell_c$ , common/differential modes . . . . .	84
3.31	Voltage at $x = \ell_c$ , physical base . . . . .	84
4.1	T-ladder network to represent the cable losses . . . . .	92
4.2	Equivalent network to represent the cable inductance . . . . .	93
4.3	Basic cell for time domain simulation of a MTL, parameter variable on frequency . . . . .	93
4.4	Schematic of the multiconductor transmission line . . . . .	97
4.5	Flowchart of the complete model . . . . .	98
4.6	Parameters of periodical trapezoidal source . . . . .	100
4.7	Photo of the experimental setup . . . . .	100
4.8	Schematic for the time domain validation experiment . . . . .	101
4.9	Connection of the voltage probe along the line . . . . .	101
4.10	The RL series load chosen for the experimental validation . . . . .	102
4.11	The RL series load connected to the two-conductor $2.5\text{ mm}^2$ cable . . . . .	102
4.12	Results of the validation experiment with series RL load . . . . .	103
4.13	RL series C parallel load connected to the $0.75\text{ mm}^2$ cable . . . . .	103
4.14	Load used in the three-conductor cable time domain validation experiment . . . . .	103
4.15	Short line model of the system, valid for low frequencies . . . . .	104
4.16	The voltage along the line on the frequency domain . . . . .	105
4.17	Validation results for the RL series C parallel load . . . . .	105
4.18	Validation results for the RL series C parallel load, zoom on the $6,4\text{ MHz}$ resonance . . . . .	105
4.19	Cross-section of the three-conductor $2.5\text{ mm}^2$ cable . . . . .	106
4.20	Schematic for the three-conductor cable time domain validation experiment . . . . .	106
4.21	Load used in the three-conductor cable time domain validation experiment . . . . .	107
4.22	Voltage $V_1(\ell_c)$ . . . . .	107
4.23	Voltage $V_2(\ell_c)$ . . . . .	108
4.24	Current $I_1(0)$ . . . . .	108
4.25	Current $I_2(0)$ . . . . .	108



4.26	Simulation of $V_1(\ell_c)$ for three different cable parameter sets . . . . .	109
4.27	Voltage pulse sent into a $\ell_c = 100\text{ m}$ long cable . . . . .	110
4.28	Propagation speed in the $2.5\text{ mm}^2$ two-conductor cable . . . . .	110
5.1	Induction motor fed with long cable . . . . .	116
5.2	Measurement schematics to characterize the three-phase motor: input impedance measured between points $a$ and $b$ . . . . .	116
5.3	Motor Leroy Somer $1.5\text{ kW}$ measured impedances . . . . .	117
5.4	Equivalent circuit of one phase of the motor . . . . .	117
5.5	Cross-section of the $4 \times 1,5\text{ mm}^2$ cables . . . . .	118
5.6	Two-level inverter model, with LISN . . . . .	119
5.7	Simulation model - Induction motor fed with long cable . . . . .	120
5.8	Frequency response relative to $V_a, \ell_c = 70\text{ m}$ . . . . .	120
5.9	Frequency response relative to $V_b, \ell_c = 70\text{ m}$ . . . . .	120
5.10	Frequency response relative to $V_c, \ell_c = 70\text{ m}$ . . . . .	121
5.11	Voltage sources $V_a, V_b, V_c$ . . . . .	121
5.12	Results of the time domain simulation for $\ell_c = 70\text{ m}$ . . . . .	122
5.13	Phase-to-phase voltages at $x = \ell_c$ for $\ell_c = 1\text{ m}$ . . . . .	122
5.14	Phase-to-phase voltages at $x = \ell_c$ for $\ell_c = 12\text{ m}$ . . . . .	122
5.15	Schematic of the DC link with voltage elevation: boost converter at the cable input and buck converter at the cable output . . . . .	123
5.16	Cross-section of the two-conductor $2.5\text{ mm}^2$ cable . . . . .	124
5.17	Schematic of the simulated model of the DC link with voltage elevation . . . . .	124
5.18	Transfer function of the currents at the line extremities, relative to $I_S$ . . . . .	125
5.19	Input impedances of the cable and the capacitor . . . . .	125
5.20	Current sources modeling the DC-DC converters, without DC component . . . . .	126
5.21	Results of the simulation converted to time domain, without DC component . . . . .	127
5.22	Schematic of the DC link without voltage elevation, with common mode . . . . .	129
5.23	Cross-section of the three-conductor $2.5\text{ mm}^2$ cable . . . . .	130
5.24	Simulation model of the DC link with common mode . . . . .	130
5.25	Transfer functions relative to the sources in the system . . . . .	131
5.26	Schematic for the DM input impedance $Z_{DM}$ , calculated between points $a$ and $b$ . . . . .	132
5.27	Comparison between the input impedances of the system and the capacitive part of the filter . . . . .	132
5.28	Schematic for the CM input impedance $Z_{CM}$ , calculated between points $a$ and $c$ . . . . .	133
5.29	Sources $I_S$ and $V_k$ — approximated as ideal trapezoidal sources . . . . .	133
5.30	Voltages and currents at the line extremities, without DC component . . . . .	134
5.31	Voltages and currents at the line extremities with $C_2 = C_3 = 22\text{ pF}$ , without DC component . . . . .	135
5.32	System under study . . . . .	136
5.33	Three-conductor cable cross-section . . . . .	136
5.34	Filter structure . . . . .	137
5.35	System equivalent circuit in common mode . . . . .	138
5.36	Switching device equivalent circuit in differential mode . . . . .	139
5.37	Simulation of the CM voltage generated by the buck converter . . . . .	139

5.38	Maximum common-mode voltage along the line in function of $C_y$ and $L_{CM}$ ; $V > 0dBV$ in black, $V = -60dBV$ in red . . . . .	140
5.39	Frequencies of the maximum in common mode . . . . .	140
5.40	Position of the maximum in common mode . . . . .	140
5.41	Simulation of the DM current generated by the buck converter with common mode . . . . .	141
5.42	Maximum differential-mode current along the line in function of $C_x$ and $L_{DM}$ ; $I = -60dBA$ in red . . . . .	141
5.43	Frequencies of the maximum in differential mode . . . . .	142
5.44	Position of the maximum in differential mode . . . . .	142
B.1	Schematic of the generalized frequency domain model for two-conductor cables . . . . .	3
B.2	Schematic of two-conductor system with passive load . . . . .	4
B.3	Schematic of the two-conductor cable with scope in the middle . . . . .	5
B.4	Input impedance of scope voltage probe Tektronix P3010 — $Z_{scope}$ . . . . .	5
C.1	Maximum voltage in function of $Z_L = A + jB$ , cable of section $0.75 mm^2$ . . . . .	8
C.2	Resonance frequency in function of $Z_L = A + jB$ , cable of section $0.75 mm^2$ . . . . .	8
C.3	Position of the maximum voltage in function of $Z_L = A + jB$ , cable of section $0.75 mm^2$ . . . . .	8
C.4	Maximum voltage in function of $Z_L = A + jB$ , cable of section $1.5 mm^2$ . . . . .	9
C.5	Resonance frequency in function of $Z_L = A + jB$ , cable of section $1.5 mm^2$ . . . . .	9
C.6	Position of the maximum voltage in function of $Z_L = A + jB$ , cable of section $1.5 mm^2$ . . . . .	9
C.7	Two-conductor cables loss related parameters . . . . .	10
C.8	Maximal voltage amplification of the two-conductor $2.5 mm^2$ cable of length $50 m$ , in function of the load . . . . .	11
C.9	First resonance frequencies of the two-conductor $2.5 mm^2$ cable of length $50 m$ , in function of the load . . . . .	11
C.10	Maximal voltage amplification of the two-conductor $2.5 mm^2$ cable of length $200 m$ , in function of the load . . . . .	12
C.11	First resonance frequencies of the two-conductor $2.5 mm^2$ cable of length $200 m$ , in function of the load . . . . .	12
D.1	. . . . .	13
E.1	Schematic balun . . . . .	15
E.2	ABCD parameters of the Minicircuits T6-4T balun . . . . .	16
E.3	. . . . .	17
E.4	Logarithmic derivative of the measured input impedance of the cable, the lowest frequency to which they can be considered constant is marked with dotted line . . . . .	18
G.1	Cross-section of the $4 \times 1.5 mm^2$ cables, with labeled conductors . . . . .	21
G.2	Parameters of the shielded cable with 4 conductors of section $1.5 mm^2$ . . . . .	22
H.1	Measurement schematics to characterize the three-phase motor: input impedance measured between points $a$ and $b$ . . . . .	23
H.2	Motor input impedance measurement setup . . . . .	23

---

H.3	Motor input impedance measurement setup: compensation SHORT . . . . .	24
H.4	Motor input impedance measurement setup: connections for measurements . . . . .	24
H.5	Impedances $Z_{PP}$ and $Z_{PG}$ , measured with impedance analyzer . . . . .	25
I.1	Schematic of the three-phase motor as a 4 input device . . . . .	27
I.2	Comparison of the two motor experimental characterizations . . . . .	28

# List of Tables

2.1	Characteristic Impedance Distortions Due to Resonance . . . . .	21
2.2	Maximum difference between the impedance measured using configurations “A” and “B”, relative to the measurement in config. “A” . . . . .	25
2.3	Maximum difference between the impedance measured in configurations A and B, relative to the impedance measured in config. “A”; impedance analyzer powered through a LISN . . . . .	26
2.4	Frequency-Domain Model Resonance Frequency and Amplitude Relative Errors .	30
2.5	Two-conductor $2.5\text{ mm}^2$ cable parameters, at the resonance frequencies of the short-circuited line (cf. Fig. 2.33) . . . . .	39
2.6	Two-conductor $2.5\text{ mm}^2$ cable parameters, at the resonance frequencies of the open-ended line (cf. Fig. 2.33) . . . . .	40
2.7	Range of values used in the numerical analysis of the resonance . . . . .	42
2.8	Characteristics of the predicted resonances . . . . .	47
3.1	Frequency-Domain Model Resonance Frequency and Amplitude Relative Errors .	68
3.2	Range of values used in the numerical analysis of the resonance . . . . .	79
3.3	Resonance characteristics - modal base . . . . .	82
4.1	Characteristics of the predicted resonance . . . . .	102
4.2	Trapezoidal source parameters . . . . .	102
4.3	Trapezoidal source parameters . . . . .	104
4.4	Characteristics of the predicted resonances . . . . .	104
4.5	Trapezoidal source parameters . . . . .	106
4.6	Fixed cable parameters for resonance analysis . . . . .	109
5.1	Parameters of two-level voltage inverter . . . . .	118
5.2	Time domain simulation parameters . . . . .	121
5.3	Parameters of the differential mode DC link model (cf. Fig. 5.17) . . . . .	124
5.4	Parameters of the model (Fig. 5.24) . . . . .	128
5.5	Parameters of the system model . . . . .	136
5.6	Filter designed with the classic approach given in [39], to meet the RTCA DO-160G standard . . . . .	137
5.7	Parameters of the resonance surface response calculation . . . . .	138
5.8	Conducted emissions limit for the design of filter using the resonance surface response	138
5.9	Filter designed with resonance surface response . . . . .	142
A.1	Hyperbolic function definitions and identities . . . . .	1

C.1	Maximal voltage amplification for different two-conductor cables . . . . .	7
D.1	Conversion between the two-port devices models . . . . .	14
I.1	Input impedance measured for motor characterization . . . . .	27

# CHARACTERIZATION OF THE CABLING ON INDUSTRIAL POWER NETWORKS FOR EMI SIMULATION

**Abstract** This work analyses the EMI problems that may arise in the large electric networks on industrial plants, taking into account the switching harmonics injected in these systems by power converters. The harmonics were studied in the frequency band from DC up to a few tens of  $MHz$ . To model the propagation of the switching harmonics in long electric cables, an accurate and computationally efficient simulation method is proposed. It is fit to simulate the behavior of medium frequency parasitic signals in large cabling networks, e.g. on industrial plants, buildings, and others. This method can be useful in the designing of such systems, contributing to the development of protection measures against dysfunction or damage that may be caused by EMI phenomena in the network.

**Keywords** *Cabling, EMI in industrial power systems, Power converters EMI, EMI long cable model, Frequency-domain simulation*

---

# CARACTÉRISATION DU CÂBLAGE DES RÉSEAUX INDUSTRIELS DE PUISSANCE EN VUE DE LA SIMULATION CEM

**Resumé** Dans cette thèse sont analysés les problèmes liés à la CEM qui peuvent se produire dans un réseau électrique industriel de grandes dimensions, prenant en compte les harmoniques introduits dans le système par le découpage des convertisseurs de puissance. Les harmoniques ont été étudiés dans la bande de fréquence entre DC et quelques dizaines de  $MHz$ . Pour modéliser la propagation des harmoniques de découpage dans les longs câbles électriques, une méthode de simulation précise et de bas coût computationnel a été proposée. Cette méthode est adaptée pour simuler le comportement des signaux parasite dans les câblages longs présents dans les réseaux industriels, des bâtiments ou autre, et peut être utile pour le dimensionnement de ces réseaux, en vue du développement de méthodes de protection contre des dysfonctionnements et dommages qui peuvent être causés par des phénomènes d'interférence électromagnétique.

**Mots clés** *Câblage, CEM en réseaux industriels de puissance, Interférence électromagnétique générée par des convertisseurs de puissance, Modèle CEM pour câbles longs, Simulation dans le domaine de la fréquence*